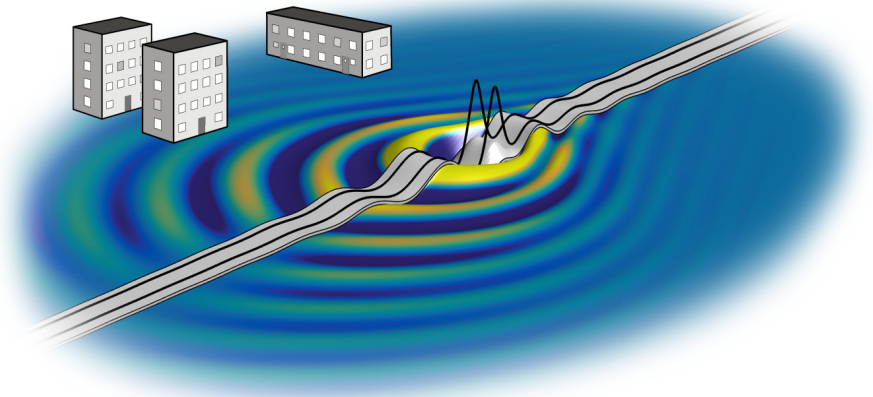




LUND
UNIVERSITY



VIBRATIONS FROM RAILWAY TRAFFIC

Computational Modeling and Analysis

JENS MALMBORG

Structural
Mechanics

Doctoral Thesis

DEPARTMENT OF CONSTRUCTION SCIENCES

DIVISION OF STRUCTURAL MECHANICS

ISRN LUTVDG/TVSM--22/1033--SE (1-209) | ISSN 0281-6679

ISBN 978-91-8039-374-4 (print) | ISBN 978-91-8039-373-7 (pdf)

DOCTORAL THESIS

VIBRATIONS FROM RAILWAY TRAFFIC
Computational Modeling and Analysis

JENS MALMBORG

Copyright © Jens Malmberg 2022.

Printed by V-husets tryckeri LTH, Lund, Sweden, September 2022 (*PI*).

For information, address:

Division of Structural Mechanics,
Faculty of Engineering LTH, Lund University, Box 118, SE-221 00 Lund, Sweden.

Homepage: www.byggmek.lth.se

Acknowledgements

I would like to express my gratitude towards my supervisor Prof. Kent Persson for giving me the opportunity to become a PhD student and for giving me the freedom to explore an interesting field. I would also like to thank my co-supervisor Dr. Peter Persson, for carefully reading and commenting on my manuscripts. Dr. Ola Flodén became my co-supervisor during the final year. Thanks are directed to all supervisors for their encouragement and support with various matters during my studies. I am also grateful to Dr. Andrew Peplow for our cooperation on Paper F and for interesting discussions. I thank Mr. Bo Zadig for his excellent work with many of the illustrations in the thesis.

Thanks to Prof. Lars Vabbersgaard Andersen at Aarhus University and his former student Dr. Paulius Bucinkas for helpful advice regarding semi-analytical modeling of dynamic ground response. I am grateful to both for pleasant company during conferences in faraway lands.

Furthermore, I would like to thank my good friend and colleague Linus Andersson. We were colleagues already in 2010, and sort of encouraged each other to become PhD students. I appreciate all the fun, and sometimes even fruitful, discussions we have had.

I thank my mom and dad, Birgitta and Bo, for always supporting me and for making life easier by helping out with all sorts of things from babysitting to woodworking.

Finally, I thank my wife Stina and our wonderful children Torsten and Maj, for constantly reminding me about what is truly important and I apologize for occasionally forgetting.

September 2022
Jens Malmborg

Abstract

The population is growing, and an increasing proportion of the population lives in urban areas. As a consequence, human exposure to noise and vibrations is increasing; two major sources being railway and road traffic. Larger and denser cities lead to a higher amount of traffic close to where people work and live. Land close to railways and heavily trafficked roads, previously left unexploited, are now being used for dwellings and offices. Vibrations are often accompanied by noise, to which long-term exposure is known to have serious health effects. Furthermore, some buildings such as hospitals and research facilities contain instruments that are highly sensitive to vibrations, and require proper vibration isolation to ensure safe operation. To address the problems of noise and vibrations, their generation and propagation need to be understood.

The vibrations next to a railway track are caused by the forces exerted on the track by the passing train. These forces are the sum of a quasi-static part due to the deadweight of the train, and a dynamic part. The dynamic part is caused by various phenomena resulting in time-dependent train–track interaction forces. The vibrations generated at the track propagate through the underlying and surrounding soil as elastic waves of various types. The mechanical properties of the soil strongly influence the wave propagation and the resulting vibrations registered by a receiver at some distance from the track. For a building structure next to the track, the vibrations inside the building furthermore depend on the mechanical and geometrical properties of the building's structural elements.

In the thesis, numerical models and modeling strategies for predicting ground-borne vibrations from railway tracks have been developed. Various techniques to calculate the wave propagation in the soil have been implemented and used for studying different phenomena, such as the vibrations at the soil surface and in a building next to the track, caused by a train running over an uneven rail. Furthermore, the mitigation of train-induced ground vibrations and so called “critical velocity” effects, i.e. high-speed trains moving faster than the wave speed in the underlying soil, were studied. In addition, models developed in the the thesis were utilized to compare the dynamic responses of a heavyweight concrete building and a lightweight wooden building, when excited by ground vibrations induced by a train moving over an uneven rail.

Populärvetenskaplig sammanfattning

En ökande andel av befolkningen bor i urbana miljöer, där störande ljud och vibrationer är vanligt förekommande. Två huvudsakliga källor till dessa störningar är tung trafik från väg och järnväg. Större och tätare städer leder till ökad trafik där människor bor och arbetar. Mark nära järnväg och tungt trafikerad väg, som tidigare lämnats oexploaterad, används för både bostäder och kontorsbyggnader. Vibrationer ackompanjeras ofta av buller som har kända negativa hälsoeffekter. Vidare innehåller somliga byggnader, såsom sjukhus och forskningsanläggningar, vibrationskänslig utrustning som behöver skyddas för att dess funktion ska upprätthållas. För att kunna angripa problemen med störande buller och vibrationer krävs förståelse för deras uppkomst och utbredning.

Vibrationerna bredvid ett järnvägsspår orsakas av krafterna som genereras av tåget på spåret. Dessa krafter består av en kvasi-statisk del orsakad av tågets egenvikt, och en dynamisk del. De dynamiska krafterna orsakas av olika fenomen, t.ex. att rälsen inte är helt jämn och att markens styvhet varierar längs spåret. Vibrationerna som genereras vid spåret sprids genom den under och omkringliggande marken som elastiska vågor av olika typer. Markens egenskaper påverkar vågutbredningen och har stor betydelse för vilka vibrationsnivåer som registreras bredvid spåret. För en byggnad bredvid spåret beror vibrationsnivåerna vidare på byggnadens utformning och material.

I avhandlingen utvecklas beräkningsmodeller och modelleringsstrategier för att prediktera markvibrationer orsakade av spårbunden trafik. Olika numeriska tekniker för att beräkna vågutbredningen i marken har implementerats i datormodeller och använts för att studera olika fenomen, såsom vibrationerna på markytan och i en byggnad, till följd av ett förbipasserande tåg körandes på en ojämn räls. För höghastighetståg kan ett fenomen uppstå då tågets hastighet närmar sig vågutbredningshastigheten i den underliggande marken, som yttrar sig i kraftigt förhöjda vibrationsnivåer både i och jämte spåret. I avhandlingen används de utvecklade numeriska modellerna för att studera höghastighetsfenomenet och möjliga vibrationsreducerande åtgärder i form av jordförstärkningar.

Contents

I	Introduction and Overview	xiii
1	Introduction	1
1.1	Background	1
1.2	Aims and objectives	1
1.3	Limitations	2
1.4	Outline	2
2	Environmental Vibrations	5
2.1	General remarks	5
2.2	Effects of ground-borne vibrations	6
2.3	Ground vibrations	7
2.3.1	Wave propagation	7
2.3.2	Ground response to stationary and moving loads	10
2.3.3	Vibration reduction methods	12
3	Structural Dynamics and Elastic Waves	15
3.1	Equations of motion	15
3.2	Structural dynamics	16
3.2.1	Free vibration	17
3.2.2	Steady-state response to harmonic loading	19
3.2.3	Frequency-independent damping	20
3.3	Elastic waves	22
3.3.1	Wave propagation in structural elements	22
3.3.2	Wave propagation in an elastic continuum	24
3.4	Soil–structure interaction	28
3.4.1	General remarks	28
3.4.2	Substructure theorem	28
4	Numerical Solution Methods	31
4.1	The finite element method	31
4.1.1	General remarks	31
4.1.2	Finite element equations for 3D elasticity	32
4.1.3	Formulation in a moving frame of reference	34
4.1.4	FE formulation in 2.5D	35
4.1.5	Perfectly matched layers	39
4.2	The layer transfer matrix method	42

4.2.1	General remarks	42
4.2.2	Flexibility matrix of a horizontally layered half-space	43
4.2.3	Formulation in a moving frame of reference	46
4.2.4	Dispersion curves	47
5	Predicting Vibrations from Railway Traffic	51
5.1	General remarks	51
5.2	Excitation mechanisms	51
5.3	Numerical modeling	52
5.4	Track models in appended papers	55
5.4.1	A coupled 3D track–soil model	57
5.4.2	A coupled 2.5D track–soil model	60
5.4.3	A 2.5D FE–PML model	66
5.4.4	Discussion	67
6	Summary of Appended Papers	71
6.1	Paper A	71
6.2	Paper B	72
6.3	Paper C	73
6.4	Paper D	74
6.5	Paper E	75
6.6	Paper F	76
7	Concluding Remarks	77
7.1	Conclusions and contributions	77
7.2	Suggestions for future work	78
	References	81
II	Appended Publications	87

Paper A

Modeling train-induced ground-borne vibrations using FEM in a moving frame of reference.

J. Malmberg, K. Persson, P. Persson.

In proceedings of COMPDYN 2019, 7:th International Conference on Computational Methods in Structural Dynamics and Earthquake Engineering, Crete, Greece, 2019.

Paper B

Evaluating the effect of vibration isolation mats on train-induced ground vibrations.

J. Malmberg, K. Persson, P. Persson.

In proceedings of SEMC 2019, 7:th International Conference on Structural Engineering, Mechanics and Computation, Cape Town, South Africa, 2019.

Paper C

Effects of modeling strategies for a slab track on predicted ground vibrations.

J. Malmborg, P. Persson, K. Persson.

Soil Dynamics and Earthquake Engineering 136: 106254, 2020.

Paper D

Numerical investigation of railway subgrade stiffening: Critical speed and free-field vibrations.

J. Malmborg, P. Persson, K. Persson.

Transportation Geotechnics 34: 100748, 2022.

Paper E

Numerical study of train-induced vibrations in light and heavy building systems.

J. Malmborg, O. Flodén, P. Persson, K. Persson.

Submitted for publication.

Paper F

Numerical modelling applied to wave-propagation analysis for arbitrary frequency and layer depths within infinite elastic media.

A. Peplow, J. Malmborg, P. Persson.

Submitted for publication.

Part I

Introduction and Overview

1 Introduction

1.1 BACKGROUND

The population is growing. Currently (year 2022), 89% of the Swedish population live in urban areas. For the population worldwide, the figure is 56%. These numbers are increasing [1].

As a consequence of the urban densification, human exposure to noise and vibrations is increasing, two major sources being railway and road traffic. Larger and denser cities lead to a higher amount of traffic close to where people work and live. Land close to railways and heavily trafficked roads, previously left unexploited, are now being used for dwellings and offices. Vibrations are often accompanied by noise, which is known to cause serious health effects. Furthermore, some buildings such as hospitals and research facilities contain instruments that are highly sensitive to vibrations, and require proper vibration isolation to ensure safe operation.

To address the problems of noise and vibrations, their generation and propagation need to be known. When the physics behind the observed phenomena is understood, appropriate mitigation measures may be undertaken. To describe the physics in detail, mathematical models are required. These models are generally so complex that they need to be solved using computers. Such models can then be used to evaluate the efficacy of different design alternatives, by numerically predicting the outcome of different scenarios. They can therefore be helpful in making better decisions during the early stages of design of, for example, a new building close to a railway track.

1.2 AIMS AND OBJECTIVES

The long-term aim of the work presented in this thesis is to reduce noise and vibrations for residents close to railways and heavily trafficked roads, and to enable safe operation of sensitive equipment and instruments in such areas. To accomplish the long-term aim, tools are needed to understand and predict the generation and propagation of such vibrations.

The objective of the work is to investigate and develop efficient numerical techniques and mod-

els that can be used in engineering practice for predicting ground-borne vibrations emanating from railway traffic. Apart from being able to properly represent the transmission of the vibrations through the ground, and into a building structure, such models need to include the source of the vibrations.

In this thesis, various numerical techniques are employed to predict the free-field ground vibrations caused by a train running on a railway track. The influence of different modeling strategies regarding the railway track is investigated, and the change in response due to a mitigation measure under the track is studied. The effect of high speed trains moving on soft soils and possible response mitigation through soil stiffening is investigated using numerical simulations. Furthermore, the developed models are utilized to compare the dynamic responses of a heavyweight concrete building and a lightweight wooden building, when excited by ground vibrations induced by a train moving over an uneven rail.

1.3 LIMITATIONS

Vibrations from a train running at constant speed along a straight railway track with constant geometry is considered. Vibrations due to rail curvature, rail joints/switches, transition zones, varying subgrade stiffness, etc. are not accounted for. However, vertical unevenness of the rail is considered as a source of dynamic excitation. Furthermore, the high-speed phenomenon that is encountered when the train speed approaches the speed of the elastic waves in the ground is studied. A linear-elastic material behaviour is assumed for all components (track, soil and buildings) throughout this work.

1.4 OUTLINE

This thesis is divided into two parts:

Part I is divided into seven chapters and contains an overview of the work and an introduction to the research area of environmental vibrations, with particular emphasis on the physics and the numerical modeling of ground-borne vibrations. In Chapter 2, some general concepts regarding the generation and propagation of ground vibrations are introduced, together with a brief summary of vibration mitigation measures. Chapter 3 provides the basics of the physics that govern the dynamics of structural systems, and different wave types in structural elements and an elastic continuum are derived. Two numerical methods used extensively in the present work are described in Chapter 4, namely the Finite Element Method and the Layer Transfer Matrix method. How these methods can be used for efficiently evaluating the response of moving loads is given special attention. In Chapter 5 the numerical prediction of train-induced vibrations is discussed. The excitation mechanisms behind ground vibrations generated by railway traffic are introduced, with a short review of different computational modeling strategies aiming to simulate some of these mechanisms and the resulting wavefield in the ground. Three

different computational models that have been implemented and presented in the appended papers are described along with a small example case. A summary of the appended papers are given in Chapter 6, and finally some concluding remarks are given in Chapter 7. Part II contains the appended papers.

2 Environmental Vibrations

2.1 GENERAL REMARKS

In the urban environment, there is a vast number of sources producing vibrations. Heavily trafficked roads, railways, and construction work (e.g. pile driving), are a few examples of external sources that can generate vibrations perceptible inside a building. Rotating machinery, ventilation systems, walking people, closing doors, are examples of internal vibration sources.

The current work is focused on models for predicting vibrations generated by external sources, where the vibrations are generated in one location and transmitted to a second location through the ground. The process of vibration transmission is often described in terms of a source, a medium and a receiver. The receiver can be a building, a part of a building structure, equipment or a person inside the building. The medium, or transmission path, where the vibrations are transferred as elastic waves, includes the ground but could also, depending on the receiver, include the building; see Figure 2.1.

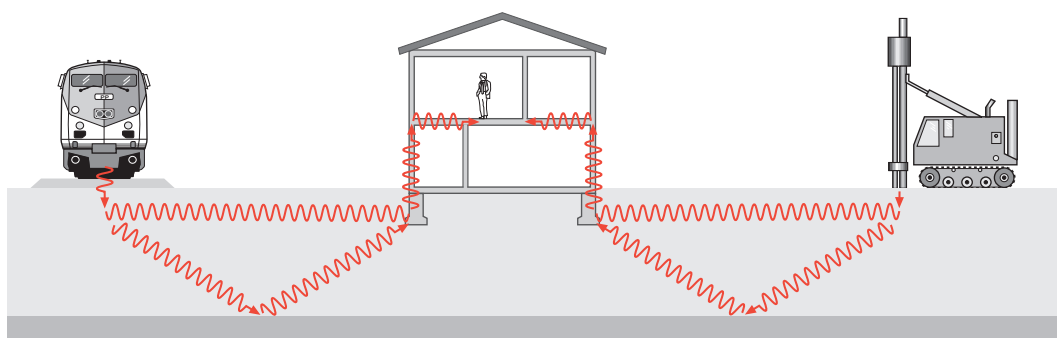


Figure 2.1: Vibration transmission from the source, via the transmission path, to the receiver.

2.2 EFFECTS OF GROUND-BORNE VIBRATIONS

Ground-borne vibrations may cause annoyance to humans, through perceptible motion of building floors and radiated noise. Ground-borne vibrations from pile driving and blasting during construction may also lead to structural damage of buildings, however such effects from road and railway traffic are very rare [2]. Furthermore, the operation of sensitive equipment in for example hospitals or research facilities may be adversely affected by ground-borne vibrations.

Vibration is an oscillatory motion around a static equilibrium, and such a motion may be described or quantified in many different ways using different descriptors. The amplitude of the vibration may be described in terms of the maximum displacement, velocity or acceleration during the event, or in terms of an “effective value” calculated as the root-mean-square (RMS). Further, a vibration may consist of a single harmonic motion or have a broad frequency content.

In the frequency range 20 – 250 Hz, vibrations inside buildings may lead to acoustic radiation heard as a rumbling noise. Furthermore, the vibrations may excite resonance frequencies of structural members and furniture inside the building, producing a rattling noise [3]. At low frequencies (< 80 Hz), humans are sensitive to whole-body vibrations, but how the vibrations are perceived also depends on the amplitude and the duration of the vibration [2]. There are studies suggesting that environmental noise contributes to cardiovascular risk of coronary artery disease, hypertension, stroke and heart failure [4].

The international standard ISO 2631 [5] specifies vibration criteria guidelines for different applications in terms of allowable RMS values of vibration velocity in 1/3 octave bands. These

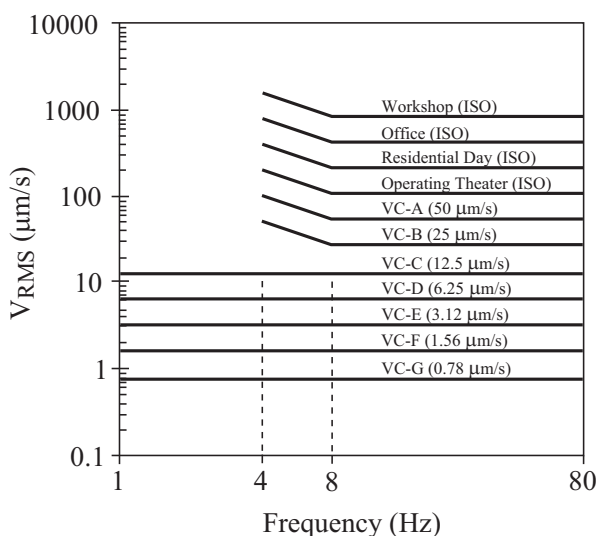


Figure 2.2: Vibration requirements. ISO guidelines and VC curves.

are shown in Figure 2.2, together with so called Vibration Criterion (VC) curves, that are frequently used by manufacturers of sensitive equipment to specify maximum allowable vibration levels.

2.3 GROUND VIBRATIONS

2.3.1 Wave propagation

Ground vibrations propagate as elastic waves. In an infinite, homogeneous, elastic medium (a so called full-space), only two different types of waves exist; the P-wave and the S-wave, which propagate independently of each other. The P-waves are also called pressure, dilational, longitudinal, irrotational or primary waves. P-waves are the fastest moving waves, and the particle movement is parallel with the wave propagation direction. The S-waves are also called shear, rotational, equivoluminal or secondary waves, and are characterized by a particle movement that is perpendicular to the wave propagation direction. However, in a homogeneous, elastic semi-infinite medium involving a free surface (a so called half-space), the P- and S-waves interact at the surface, resulting in a surface wave called the Rayleigh wave, propagating with a slightly lower velocity than the S-wave. The particle motion is elliptical, and the amplitude decreases with depth. At the surface, the particle motion is retrograde. At depths larger than about 1.5 wavelengths, the particle displacement amplitude is only a few percents of the maximum value, see further Section 3.3.2. The P-, S- and Rayleigh waves are shown schematically in Figure 2.3.

For a harmonic excitation, the wavelength λ of the resulting waves are $\lambda = c/f$, where c is the wave propagation speed (the so called phase velocity) of the respective wave type and f is the frequency, in Hz, of the harmonic load. The wavenumber is defined as $k = 2\pi/\lambda$ and is

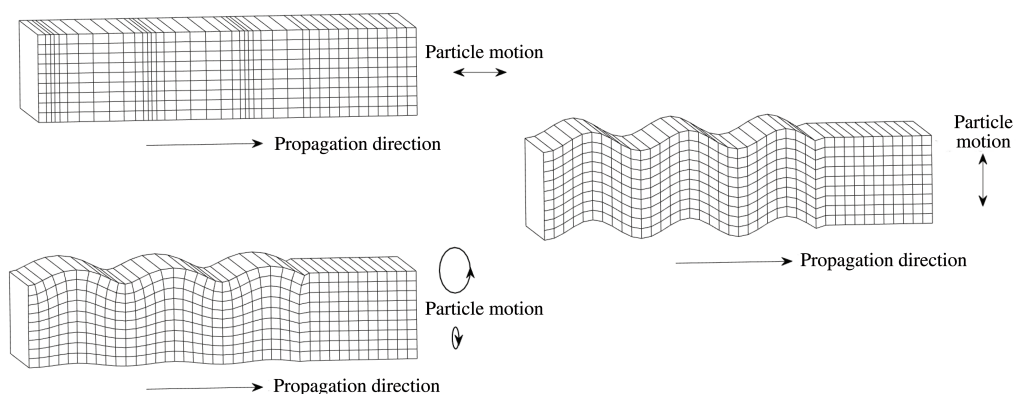


Figure 2.3: P-, S- and Rayleigh waves.

the space domain equivalent of the angular frequency ω in time domain ($\omega = 2\pi f = 2\pi/T$).

Disregarding any energy dissipation due to material damping, the total energy within a traveling wave remains constant. However, since the wavefront increases in size with increasing distance from the source, the energy density decreases, causing an attenuation of the particle displacement amplitude. Contrary to the P- and S-waves, that propagate away from a point source with spherical wavefronts, the Rayleigh wave propagates only along the surface with a circular wavefront. Therefore, the attenuation is weaker for the Rayleigh wave than for the P- and S-waves. The Rayleigh wave carries about 2/3 of the energy transmitted into the ground from a vertical oscillatory load on the surface of an elastic half-space [6]. Furthermore, due to the lower attenuation of the Rayleigh wave, the particle displacement on the soil surface is often primarily due to the Rayleigh wave, especially at longer distances.

The earth is not a homogeneous half-space. All soils are layered to some extent, with different material properties within and between the different layers. Hence, waves propagate with different velocities in the different layers. When a wave arrives at an interface between two layers with different elastic properties, the wave is partially reflected and partially refracted. Similarly to the case of P- and S-waves interacting at the free surface of a homogeneous half-space, interaction between the two waves takes place along an interface between two different materials. The layering also introduces surface waves other than the fundamental Rayleigh wave. These are often called P-SV waves, indicating that they stem from interacting P- and vertically polarized S-waves. In fact, the depth and material properties of the different soil layers have a huge impact on the vibration response. Some typical wave speeds of P- and S-waves in different soil materials are shown in Figure 2.4.

As will be shown in Section 3.3.2, the speeds with which the P-, S- and Rayleigh waves propagate (c_p , c_s and c_R) within a homogeneous material are independent of frequency. Such waves are called non-dispersive. In a layered soil, with homogeneous layers, the surface waves become dispersive due to the fact that the wavefronts potentially span several soil layers with different mechanical properties. For very low frequencies, i.e. long wavelengths, the velocity of the sur-

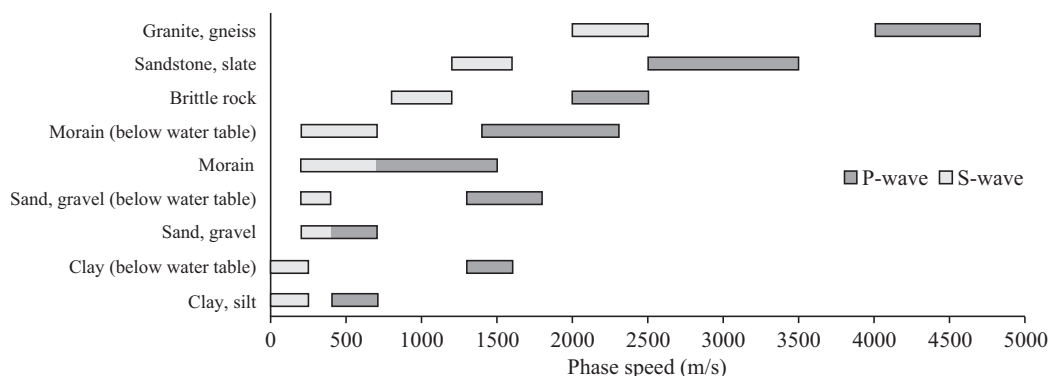


Figure 2.4: Phase velocities of P- and S-waves in some typical ground materials [7].

face wave is generally governed by the phase velocity in the lower soil layers. On the contrary, for higher frequencies, i.e. short wavelengths, when most of the surface wave is contained in the upper layer(s), the phase velocity of the Rayleigh wave in the upper layer(s) governs the velocity of the surface wave. This is illustrated in Figure 2.5, showing the so called dispersion diagrams of the P-, S- and Rayleigh waves for the two materials of a layered ground consisting of a 4 m deep clay shale layer, overlaying a half-space. The dispersion curves of the stiffer half-space material are shown in blue, whereas the corresponding curves for the soil layer are shown in red. The curves are shown in a wavenumber–frequency diagram, so that the phase velocity of each wavetype is given by the inverse of the slope in the diagram ($c = \omega/k$). The lines have a constant slope, i.e. the same phase velocity regardless of frequency. The curves are displayed over a contour plot showing the amplitude of vertical response due to a vertical harmonic excitation of the soil surface, where black indicates high response and white indicates low response. For excitation frequencies over about 15 Hz, the response for a given frequency is dominated by wavenumbers around the Rayleigh wave of the top soil material, meaning that the fundamental surface wave is practically unaffected by the higher phase velocities in the underlying half-space. An increasing number of higher order waves, faster than the fundamental surface wave, emerge for increasing frequencies. For frequencies below 5 Hz, the response on the soil surface is dominated by lower wavenumbers pertaining to the phase velocity in the underlying half-space, and in the range of about 5–15 Hz the velocity of the wave dominating the response is affected by both the top soil layer and the half-space.

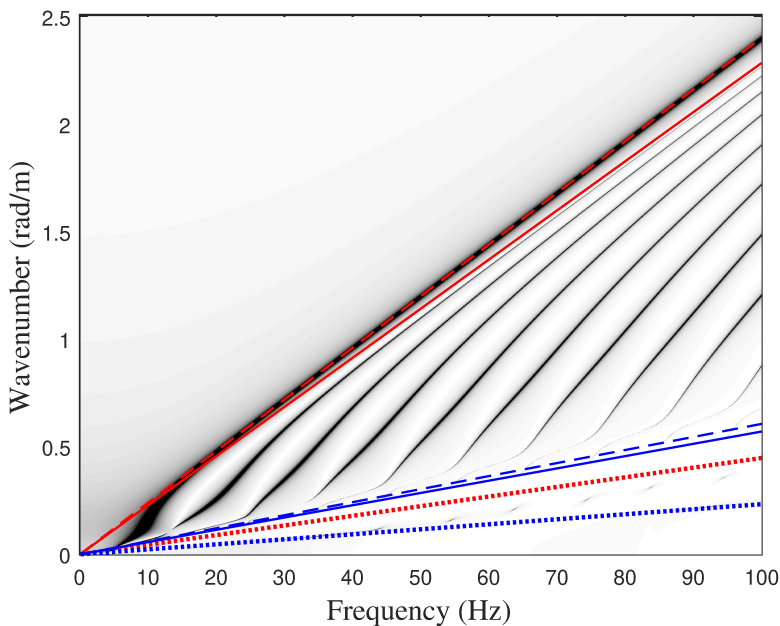


Figure 2.5: Dispersion curves for a layered half-space. Straight lines represent P-waves (dotted), S-waves (solid) and Rayleigh-waves (dashed) of the top soil (red) and the half-space material (blue).

In reality soil is not a homogeneous, linearly elastic medium. Soil is a granular material that typically displays a highly non-linear behavior. However, for the frequencies of interest in environmental vibrations, the wavelengths are much longer than the typical particle size, which makes a continuum model reasonable. For most problems relating to environmental vibrations, the strain levels remain relatively low, especially at some distance from the source, justifying a linear elastic approach. In all forthcoming sections and chapters, a linear elastic continuum approach is assumed for the soil in the numerical predictions of ground vibrations. Further, it is assumed that the soil is horizontally stratified, i.e. that it consists of horizontal layers.

2.3.2 Ground response to stationary and moving loads

The response of the ground to a dynamic load depends, apart from the site conditions (i.e. soil stratification and elastic properties), on the load distribution in space and time. The distribution in time, i.e. the load time-history signal, can be decomposed into its spectral components through a Fourier transform. The analysis of single harmonic excitation components, in contrast to a transient time-history analysis, is sometimes preferred both due to computational efficiency and physical insight.

When a harmonic load with frequency f is stationary, i.e. remains in the same position on the soil surface, the response in a stationary receiver anywhere on the soil surface is also harmonic with the same frequency. If the load is moving with a constant velocity on the soil surface, the response in a receiver moving with the same velocity is also harmonic with the frequency of the load. However, if the receiver position remains fixed and the load is moving (or vice versa), the response in the receiver becomes transient. The response amplitude increases as the load approaches the receiver, and decreases as the load recedes away from the receiver. Furthermore, the response in the stationary receiver contains more frequencies than the excitation frequency f of the moving load. When the load is approaching the receiver, the wavelengths of the waves reaching the receiver are compressed, and instead elongated as the load moves away from the receiver. This is known as the Doppler effect. This phenomenon is illustrated in Figure 2.6, for a unit harmonic load at $f = 40$ Hz distributed over a circular area ($r = 0.5$ m) on the soil surface. Figure 2.6 (a) shows the wavefield on the soil surface when the load is stationary, whereas in (b) the load is moving with a velocity of $v = 0.38c_R = 100$ m/s along the positive x -axis. The time-history response of a stationary point, located at $(x, y) = (0, 15)$, is shown in Figure 2.7, for the case of a stationary load (a), and for the case of the moving load (b). In figure (b), for the moving load, the time $t = 0$ corresponds to when the load is located at $(x, y) = (0, 0)$. The difference in time periods for one cycle of vibration in the beginning and the end of the event is clearly seen.

A moving load generates vibrations in a stationary receiver even when the load is constant. This is because the constant load causes a deflection of the soil surface that follows the moving load, and as the deflected soil surface passes the receiver a transient movement is registered. The response of the soil surface when the constant load moves at a velocity of $v = 0.38c_R$,

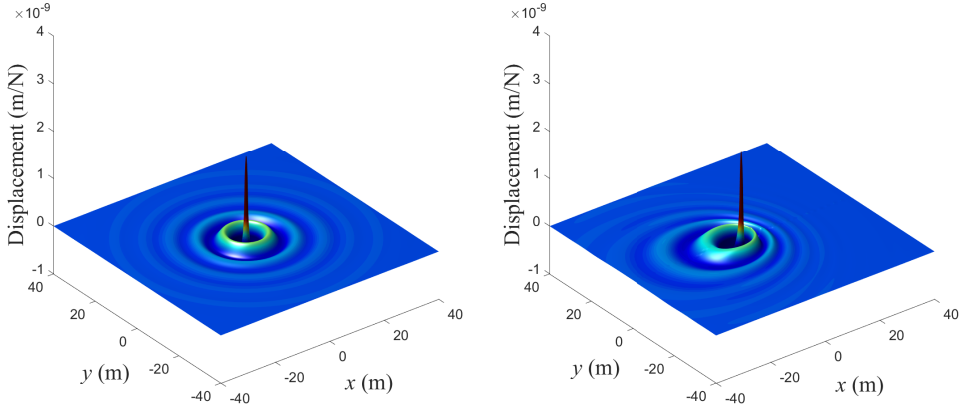


Figure 2.6: Wavefield generated by a harmonic unit load at $f = 40$ Hz that is stationary (a), and moving along the x -axis at the speed $v = 0.38c_R = 100$ m/s (b) .

well below the Rayleigh wave speed in the soil material, is shown in Figure 2.8 (a). When the load velocity approaches the Rayleigh wave speed, the soil displacement increases as shown in Figure 2.8 (b). When the load velocity exceeds the Rayleigh wave speed, a number of waves are generated behind the load, as shown in Figure 2.8 (c). High-speed trains on poor soil conditions, moving at critical speed, close to or faster than the wave speed of the soil material, generating high vibration amplitudes in the track and the surrounding soil, is a well-known phenomenon and has been studied by several researchers. A famous example from Sweden is that of Ledsgård, where the passenger train X-2000 generated very high ground vibrations due to poor soil conditions [8]. A numerical study concerning critical speed and its mitigation through soil stiffening is presented in appended Paper D.

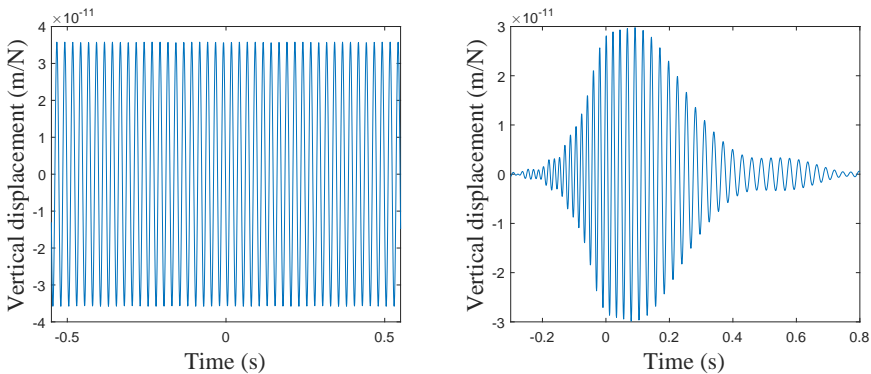


Figure 2.7: Time-history of the displacements in a stationary point 15 m from a harmonic unit load at $f = 40$ Hz that is stationary (a), and moving along the x -axis at the speed $v = 0.38c_R = 100$ m/s (b) .

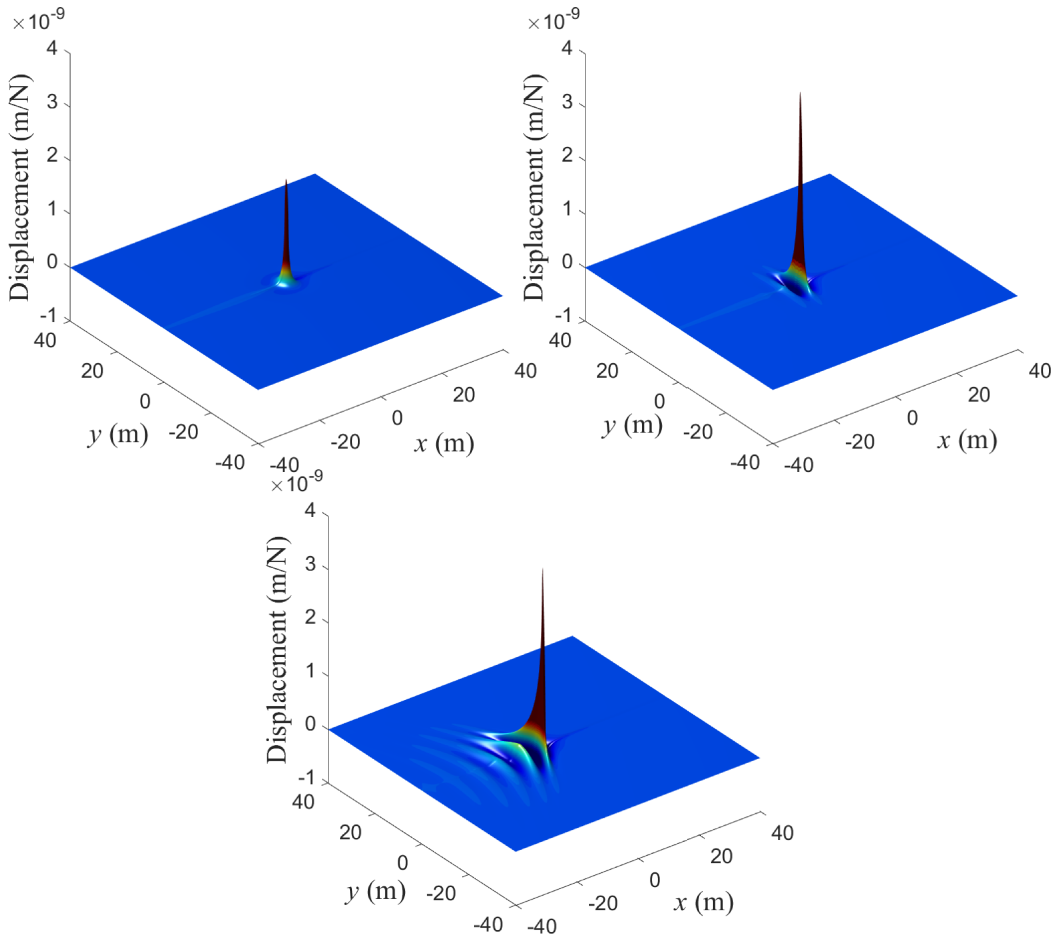


Figure 2.8: Constant unit load moving along the x -axis at the speeds $v = 0.38c_R$ (a), $v = 1.0c_R$ (b) and $v = 1.15c_R$ (c).

2.3.3 Vibration reduction methods

With reference to Figure 2.1, measures to reduce the ground-borne vibrations experienced by a receiver may be directed to the source, the transmission path or the receiver.

When vibration mitigation measures are directed to the source, the general idea is to reduce the forces transmitted from the source to the ground. This may be achieved by introducing a resilient element under the source that modifies the transmissibility, i.e. the ratio of the transmitted force to the applied force. This concept is illustrated in Figure 2.9, showing the transmissibility of a single-degree-of-freedom (SDoF) system subjected to a harmonic load. Depending on the relation between the frequency of the applied load, ω , and the resonance frequency of the SDoF system, ω_n , different amounts of the applied load P_0 are transferred to the support. Hence, when a resilient element is introduced under the source, the resonance

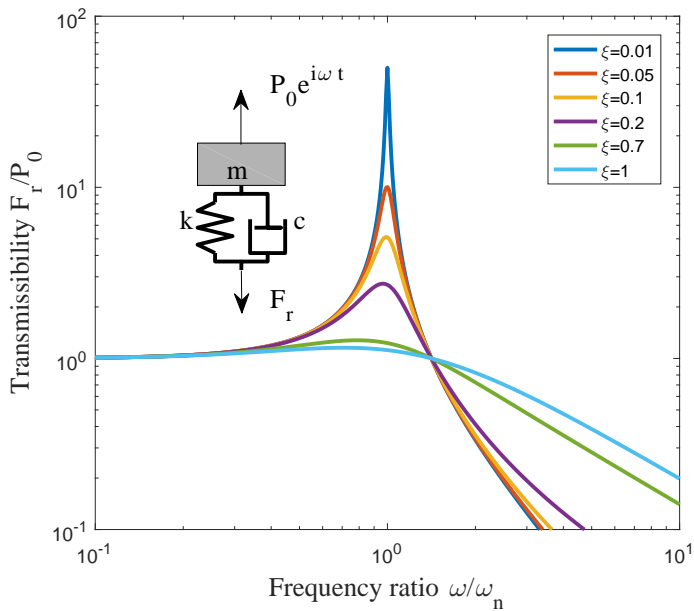


Figure 2.9: Transmissibility for harmonic excitation, for different factors of critical damping ξ . After [9].

frequency of the system decreases, increasing the ratio ω/ω_n . For loading frequencies higher than the new resonance frequency of the system, the transmissibility decreases, thereby dynamically isolating the mass. This comes at the cost, however, of an increased transmissibility around the new resonance frequency. Apart from the elastic properties of the resilient element, the transmissibility is governed also by the damping properties, as indicated by the difference between the curves in the diagram.

For railway tracks an example of a resilient element is an elastic mat placed under the ballast, a so called under-ballast mat, in the case of a conventional ballasted track, or underneath the slab in the case of a slab track resulting in a so called floating slab. Resilient elements may also be introduced higher up in the track structure, e.g. in the rail fasteners. However, to dynamically isolate the track for frequencies relevant to ground vibration (< 80 Hz), a large portion of the track mass should be located over the resilient element [10]. The resilient element should, with reference to Figure 2.9, provide a resonance frequency as low as possible for the track structure. A lower limit exists due to limitations in the maximum allowable static deflection. Another way of addressing train-induced ground vibrations at the source, is to improve the soil conditions under the track.

Ground-borne vibrations may also be reduced by modifications in the transmission path between the source and the receiver. Typical examples include trenches and solid barriers, where the idea is to shield an area containing the receiver(s) from incoming waves; see Figure 2.10.

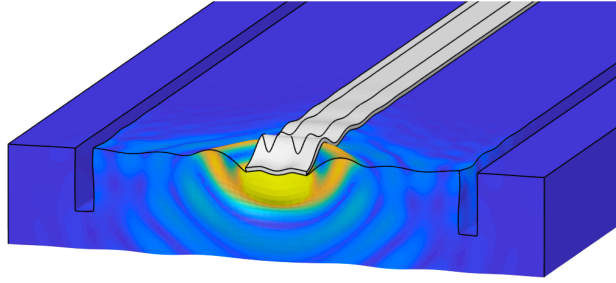


Figure 2.10: A trench between the source and receiver may be an effective means of reducing vibrations.

Similarly to the case of introducing a resilient layer underneath the source, the receiver may be dynamically isolated through the use of a resilient support. It can be shown that the curves presented in Figure 2.9 for the force transmissibility are identical to those for acceleration transmissibility. In the latter case, the input to the SDOF system is a harmonic acceleration at the support, and the measured response is the acceleration of the mass. In regions prone to earthquakes, seismic base isolation of entire buildings is often based on this principle. However, in the case of environmental vibrations, a more common use of the principle is to dynamically isolate sensitive equipment. Great reductions in the response of the receiver can be achieved by introducing a resilient element at its support. Again, the drawback is the increased transmissibility for excitation frequencies close to the resonance frequency of the isolated receiver.

When evaluating mitigation efforts, the concept of insertion loss (IL) is often used for quantifying the vibration reduction. The insertion loss is expressed in decibels and signifies the difference in power of two signals. The kinetic energy, and hence power p , of a vibrating mechanical system, is proportional to the squared displacement u , i.e.

$$\text{IL} = 10\log\left(\frac{p_{\text{ref}}}{p_{\text{iso}}}\right) = 10\log\left(\frac{u_{\text{ref}}^2}{u_{\text{iso}}^2}\right) = 20\log\left(\frac{u_{\text{ref}}}{u_{\text{iso}}}\right), \quad (2.1)$$

where u_{ref} denotes the displacement obtained for the reference case, without any installed mitigation measure, and u_{iso} denotes the displacement obtained after the installation of a mitigation measure.

3 Structural Dynamics and Elastic Waves

3.1 EQUATIONS OF MOTION

By studying the forces acting on an infinitesimal cube within a continuum and applying Newton's second law, it can be shown that independently of the stress–strain behavior of the continuum, equilibrium requires that

$$\frac{\partial \sigma_{ij}}{\partial x_j} + b_i = \rho \frac{\partial^2 u_i}{\partial t^2}, \quad (3.1)$$

which is the Cauchy equation of motion. Here $\sigma_{ij} = \sigma_{ij}(x_1, x_2, x_3, t)$ is the Cauchy stress tensor, $u_i = u_i(x_1, x_2, x_3, t)$ is the displacement in direction i , $b_i = b_i(x_1, x_2, x_3, t)$ is the body forces per unit volume in direction i . Further, $\rho = \rho(x_1, x_2, x_3)$ is the material density, t denotes time and x_j is the coordinate in direction j of the Cartesian space. Note that Eq. (3.1) actually contains three equations, one for each coordinate-direction $i = 1, 2, 3$. As will be shown in Section 4.1, these equations are the starting point when formulating the FE equations for a solid continuum.

Assuming small strains and a linear elastic material behavior, the stress-strain relationship follows Hooke's law,

$$\sigma_{ij}(x_1, x_2, x_3, t) = E_{ijkl} \epsilon_{kl}, \quad (3.2)$$

where E_{ijkl} is the elasticity tensor and the small-strain tensor is

$$\epsilon_{ij} = \epsilon_{ij}(x_1, x_2, x_3, t) = \frac{1}{2} \left(\frac{\partial u_i}{\partial x_j} + \frac{\partial u_j}{\partial x_i} \right). \quad (3.3)$$

For a homogeneous material with linear elastic properties, the stress tensor can be written as

$$\sigma_{ij}(x_1, x_2, x_3, t) = \lambda \Delta \delta_{ij} + 2\mu \epsilon_{ij}, \quad (3.4)$$

where λ and μ are the Lamé' parameters defined as functions of Young's modulus E and Poisson's ratio ν , as

$$\lambda = \frac{\nu E}{(1+\nu)(1-2\nu)}, \quad \mu = \frac{E}{2(1+\nu)}. \quad (3.5)$$

Further, δ_{ij} is the Kronecker delta function, and Δ is the dilation defined as

$$\Delta = \Delta(x_1, x_2, x_3, t) = \epsilon_{11} + \epsilon_{22} + \epsilon_{33} = \frac{\partial u_k}{\partial x_k}. \quad (3.6)$$

It can be shown that these definitions together with Eq. (3.1) lead to the Navier equations

$$(\lambda + \mu) \frac{\partial^2 u_j}{\partial x_i \partial x_j} + \mu \frac{\partial^2 u_i}{\partial x_j \partial x_j} + b_i = \rho \frac{\partial^2 u_i}{\partial t^2}, \quad (3.7)$$

which can also be written as

$$(\lambda + \mu) \frac{\partial \Delta}{\partial x_i} + \mu \nabla^2 u_i + b_i = \rho \frac{\partial^2 u_i}{\partial t^2}, \quad (3.8)$$

with the Laplacian operator ∇^2 defined as

$$\nabla^2 = \frac{\partial^2}{\partial x_1^2} + \frac{\partial^2}{\partial x_2^2} + \frac{\partial^2}{\partial x_3^2} = \frac{\partial^2}{\partial x_j \partial x_j}. \quad (3.9)$$

3.2 STRUCTURAL DYNAMICS

A linearly elastic mechanical system can be described by its mass, elastic and damping properties. The simplest possible system having all these three properties is the so called single-degree-of-freedom (SDoF) system shown in Figure 3.1, consisting of a mass, a (weightless) spring and a (weightless) viscous damper (dashpot). The degree-of-freedom (DoF) refers to the possible movement of the mass, which in this example is constrained to the horizontal axis. The elastic force in the spring is proportional to the displacement u of the mass and the spring stiffness k , i.e. $f_e = ku$, whereas the force in the dashpot is proportional to the velocity \dot{u} of the mass and the damping coefficient c , i.e. $f_d = c\dot{u}$. Using d'Alembert's principle, the inertia force of the mass m is proportional to the acceleration \ddot{u} , i.e. $f_i = m\ddot{u}$ and acting in the opposite direction of the acceleration. When a time dependent external load $p(t)$ is applied to the mass,

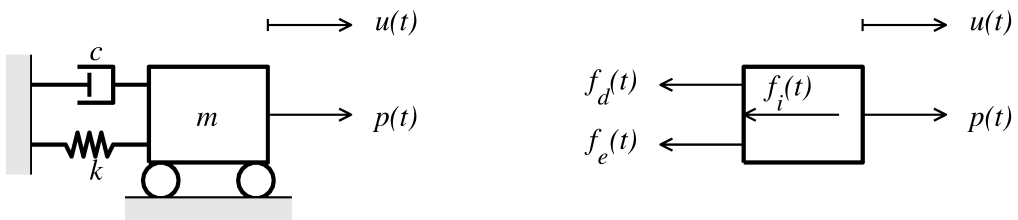


Figure 3.1: Single-degree-of-freedom system subjected to a time-dependent force $p(t)$. After [11].

the equation of motion for the mass is obtained by expressing the equilibrium of the forces acting on it, as

$$f_i(t) + f_d(t) + f_e(t) = p(t), \quad (3.10)$$

which, by using the previous expressions for the individual components, can be written as

$$m\ddot{u}(t) + c\dot{u}(t) + ku(t) = p(t). \quad (3.11)$$

For a multi-degree-of-freedom (MDoF) system involving several components, the equation of motion for that system can be written as

$$\mathbf{M}\ddot{\mathbf{u}}(t) + \mathbf{C}\dot{\mathbf{u}}(t) + \mathbf{K}\mathbf{u}(t) = \mathbf{p}(t), \quad (3.12)$$

where \mathbf{M} , \mathbf{C} and \mathbf{K} are the systems mass, damping and stiffness matrices, respectively. Further, $\ddot{\mathbf{u}}(t)$, $\dot{\mathbf{u}}(t)$, $\mathbf{u}(t)$, and $\mathbf{p}(t)$ denote vectors containing the acceleration, velocity, displacement and external loading, respectively, for each DoF. In fact, this is also the system of equations that is solved when applying the FE method as described in Section 4.1.

3.2.1 Free vibration

When no external loading acts on the SDoF system, the solution $u(t)$ to the homogeneous equation

$$m\ddot{u}(t) + c\dot{u}(t) + ku(t) = 0, \quad (3.13)$$

is found on the form

$$u(t) = Ge^{st}, \quad (3.14)$$

where G is an arbitrary complex constant. By noting that $\dot{u}(t) = sGe^{st}$ and $\ddot{u}(t) = s^2Ge^{st}$, insertion into Eq. (3.13) yields

$$(ms^2 + cs + k)Ge^{st} = 0. \quad (3.15)$$

Non-trivial solutions require that $ms^2 + cs + k = 0$, which can be written as

$$s^2 + \frac{c}{m}s + \omega_n^2 = 0, \quad (3.16)$$

where the variable

$$\omega_n = \sqrt{\frac{k}{m}}, \quad (3.17)$$

has been introduced. The solutions s to Eq. (3.16) are found as

$$s_{1,2} = -\frac{c}{2m} \pm \sqrt{\left(\frac{c}{2m}\right)^2 - \omega_n^2}. \quad (3.18)$$

If no damping is present, i.e. $c = 0$, then

$$s_{1,2} = \pm\sqrt{-\omega_n^2} = \pm i\omega_n, \quad (3.19)$$

where i is the imaginary unit, $i = \sqrt{-1}$, and it can be shown [11] that the resulting motion $u(t)$ may be written as

$$u(t) = A \cos(\omega_n t + \phi), \quad (3.20)$$

where the real constant A and the phase angle ϕ depend on the initial conditions. Further, it is seen that ω_n is the frequency of vibration, i.e. the natural frequency of the undamped SDoF system.

When damping is present, the nature of the solution depends on the relation of the damping coefficient c to the mass m and stiffness k . When the expression under the square root sign in Eq. (3.18) becomes zero, i.e.

$$c = c_c = 2m\omega_n, \quad (3.21)$$

the system is said to be critically damped, and the resulting free vibration does not contain any oscillations, but returns asymptotically to rest as

$$u(t) = (A + Bt)e^{-\omega_n t}, \quad (3.22)$$

where A and B are real constants determined from the initial conditions [11].

The damping ratio ξ is defined as

$$\xi = \frac{c}{c_c}. \quad (3.23)$$

When $\xi < 1$, the system is said to be underdamped and the free vibration is obtained as

$$u(t) = A \cos(\omega_D t + \phi) e^{-\xi \omega_n t}, \quad (3.24)$$

where $\omega_D = \omega_n \sqrt{1 - \xi^2}$ is the damped frequency of vibration, and the real constant A and phase angle ϕ are determined from the initial conditions.

For the undamped case of the MDoF system, the homogeneous differential equation

$$\mathbf{M}\ddot{\mathbf{u}}(t) + \mathbf{K}\mathbf{u}(t) = 0, \quad (3.25)$$

is solved by assuming a harmonic solution of the form $\mathbf{u}(t) = \mathbf{\Phi} \hat{U} e^{i\omega t}$, where $\mathbf{\Phi}$ is a constant vector, \hat{U} is a complex amplitude and ω is the angular frequency of vibration. Inserting the assumed solution into Eq. (3.25) yields

$$(-\omega^2 \mathbf{M} + \mathbf{K}) \mathbf{\Phi} \hat{U} e^{i\omega t} = 0, \quad (3.26)$$

and non-trivial solutions require that

$$\det(-\omega^2 \mathbf{M} + \mathbf{K}) = 0. \quad (3.27)$$

If the system has N DoFs, then N solutions to Eq. (3.27) exist, with the eigenvalues (natural frequencies) $\omega_i = \omega_1, \dots, \omega_N$ and corresponding eigenvectors (natural modes, eigenmodes)

$\Phi_i = \Phi_1, \dots, \Phi_N$. The modes can be used as base vectors for describing any displacement of the system as

$$\mathbf{u}(t) = \sum_{i=1}^{i=N} q_i(t) \Phi_i, \quad (3.28)$$

where $q_i(t)$ is the modal coordinate. Further, the modes are mass and stiffness orthogonal, and can be used for diagonalizing the mass and stiffness matrices, providing a set of N uncoupled equations. Hence, the response of each mode can be solved separately, analogously to a SDoF system and the total system response is obtained by Eq. (3.28). This is also true for a damped MDoF system, if so called classical damping is utilized, meaning that the modes also diagonalize the damping matrix.

3.2.2 Steady-state response to harmonic loading

When a SDoF system is subjected to a harmonic load, i.e. $p(t) = \hat{p}e^{i\omega t}$, the steady-state solution to Eq. (3.11) is found by assuming that the response is also harmonic with the excitation frequency, i.e. $u(t) = \hat{u}e^{i\omega t}$. Insertion into Eq. (3.11) yields

$$(-\omega^2 m + i\omega c + k)\hat{u} = \hat{p}, \quad (3.29)$$

or equivalently

$$\hat{u} = \frac{\hat{p}}{(-\omega^2 m + i\omega c + k)}. \quad (3.30)$$

Using Eq. (3.21) and Eq. (3.23), this can be written as

$$\hat{u} = \frac{\hat{p}}{k(1 - \frac{\omega^2}{\omega_n^2} + 2i\frac{\omega}{\omega_n}\xi)}. \quad (3.31)$$

The steady-state forces in the spring and dashpot are $f_e = ku = k\hat{u}e^{i\omega t}$ and $f_d = c\dot{u} = i\omega c\hat{u}e^{i\omega t}$, respectively, and hence the total reaction force becomes

$$f_r = f_e + f_d = \frac{(k + i\omega c)\hat{p}}{k(1 - \frac{\omega^2}{\omega_n^2} + 2i\frac{\omega}{\omega_n}\xi)} = \frac{(1 + 2i\xi\frac{\omega}{\omega_n})\hat{p}}{(1 - \frac{\omega^2}{\omega_n^2} + 2i\frac{\omega}{\omega_n}\xi)}. \quad (3.32)$$

When divided by \hat{p} , this provides the transmissibility of the SDoF system, i.e. the ratio of the reaction force to the applied force. In Figure 2.9 this expression is plotted for different values of ω/ω_n and ξ .

The transfer function $H(\omega)$, or frequency response function (FRF), of the SDoF system is obtained by dividing Eq. (3.31) by \hat{p} ,

$$H(\omega) = \frac{\hat{u}}{\hat{p}} = \frac{1}{k(1 - \frac{\omega^2}{\omega_n^2} + 2i\frac{\omega}{\omega_n}\xi)}, \quad (3.33)$$

giving the complex displacement response of the SDoF system due to a unit load of frequency ω . Clearly, for zero damping, $\xi = 0$, the response goes to infinity for $\omega = \omega_n$.

For the MDoF system, governed by Eq. (3.12), subjected to harmonic loading, $\mathbf{p}(t) = \hat{\mathbf{p}}e^{i\omega t}$, harmonic response is assumed as $\mathbf{u}(t) = \hat{\mathbf{u}}e^{i\omega t}$. Here, each element of the vectors $\hat{\mathbf{p}}$ and $\hat{\mathbf{u}}$ are complex numbers. Similarly to the SDoF system, the following equation is obtained by insertion of the assumed solution into Eq. (3.12),

$$(-\omega^2\mathbf{M} + i\omega\mathbf{C} + \mathbf{K})\hat{\mathbf{u}} = \mathbf{D}(\omega)\hat{\mathbf{u}} = \hat{\mathbf{p}}, \quad (3.34)$$

where the dynamic stiffness matrix, $\mathbf{D}(\omega) = (-\omega^2\mathbf{M} + i\omega\mathbf{C} + \mathbf{K})$ has been introduced. The solution $\hat{\mathbf{u}}$ is obtained as

$$\hat{\mathbf{u}} = \mathbf{D}^{-1}(\omega)\hat{\mathbf{p}}. \quad (3.35)$$

The inverse of the dynamic stiffness matrix, $\mathbf{D}^{-1}(\omega)$, contains transfer functions between the different DoFs; i.e. element (i, j) of $\mathbf{D}^{-1}(\omega)$ contains the response in DoF i , due to a unit harmonic load applied at DoF j .

3.2.3 Frequency-independent damping

Damping generally refers to a mechanism in which mechanical energy is being dissipated, causing a reduction of the vibration response. Material damping, more specifically, refers to the dissipation of mechanical energy within the material due to internal mechanisms. To model such energy dissipation mathematically, the stress in the material is assumed to consist of an elastic part depending on the strain level, and a viscous part depending on the strain-rate. Using the analogy of a SDoF system, the elastic part refers to the force in the spring and the viscous part refers to force in the dashpot. With harmonic displacement loading, i.e.

$$u = u_0e^{i\omega t}, \quad (3.36)$$

the sum of the elastic and viscous force can be written as

$$f_r = (ku_0 + i\omega cu_0)e^{i\omega t}. \quad (3.37)$$

One cycle of vibration generates an ellipse in the force–displacement diagram, the hysteresis loop, as indicated in Figure 3.2. The area within the hysteresis loop signifies the energy dissipated over the cycle. The dissipated energy over one cycle of vibration is calculated as

$$\Delta W = \int_0^{2\pi/\omega} f_r \frac{\partial u}{\partial t} dt = \pi c\omega u_0^2. \quad (3.38)$$

The maximum strain energy stored during one cycle is $W_s = \frac{1}{2}ku_0^2$, and it can be shown [12] that the dissipated energy ΔW is related to the damping factor ξ through the maximum strain energy W_s as

$$\xi = \frac{1}{4\pi} \frac{\Delta W}{W_s} = \frac{c\omega}{2k}. \quad (3.39)$$

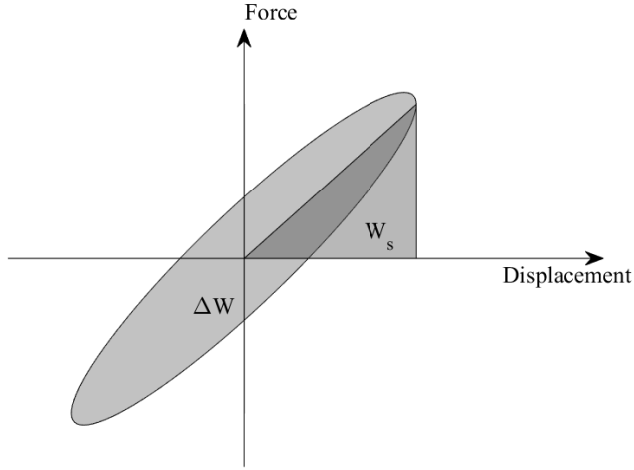


Figure 3.2: Hysteresis loop showing the dissipated energy ΔW during one cycle of vibration and the maximum strain energy W_s .

Here it is seen that the damping factor is proportional to the frequency of the loading ω . To obtain a frequency-independent damping, the damping coefficient c is expressed using Eq. (3.39), as

$$c = \frac{2k\xi}{\omega}. \quad (3.40)$$

Insertion of this expression for c into Eq. (3.37) yields

$$f_r = (ku_0 + i\omega cu_0)e^{i\omega t} = k(1 + 2i\xi)u_0e^{i\omega t} = k^*u_0e^{i\omega t}. \quad (3.41)$$

Here, $k^* = k(1 + 2i\xi) = k(1 + i\eta)$ is the complex stiffness, and $\eta = 2\xi$ is known as the loss factor. Now, Eq.(3.40) can be written as

$$c = \frac{k\eta}{\omega}. \quad (3.42)$$

Generalizing Eq. (3.42) to a MDoF system gives

$$\mathbf{C} = \mathbf{K} \frac{\eta}{\omega}, \quad (3.43)$$

which inserted into Eq. (3.34) provides

$$\left(-\omega^2 \mathbf{M} + i\omega \mathbf{C} + \mathbf{K} \right) \hat{\mathbf{u}} = \left(-\omega^2 \mathbf{M} + \mathbf{K}(1 + i\eta) \right) \hat{\mathbf{u}} = \mathbf{D}(\omega) \hat{\mathbf{u}} = \hat{\mathbf{p}}, \quad (3.44)$$

with the dynamic stiffness defined as $\mathbf{D}(\omega) = -\omega^2 \mathbf{M} + \mathbf{K}(1 + i\eta)$. This type of frequency-independent damping is sometimes referred to as structural damping.

3.3 ELASTIC WAVES

3.3.1 Wave propagation in structural elements

A disturbance of the static equilibrium of a structural element causes a stress field to propagate through the member as elastic waves. Different wave types propagate with different phase velocities that may or may not depend on the frequency. When the phase velocity depends on the frequency, the waves are called dispersive. When waves are dispersive, a pulse of waves with different frequencies will spread, or disperse, due to the different propagation velocities.

Longitudinal waves in an infinite rod

First, a simple case of an infinite rod with constant Young's modulus E , section area A and density ρ is considered. The equation for the rod can be written as

$$EA \frac{\partial^2 u(x, t)}{\partial x^2} + p(x, t) = \rho A \frac{\partial^2 u(x, t)}{\partial t^2}, \quad (3.45)$$

where $u = u(x, t)$ is the displacement of the rod at position x and time t , and $p(x, t)$ denotes an external force. The homogeneous equation, i.e. without external force, can then be written as

$$EA \frac{\partial^2 u(x, t)}{\partial x^2} - \rho A \frac{\partial^2 u(x, t)}{\partial t^2} = 0, \quad (3.46)$$

or equivalently

$$\frac{\partial^2 u(x, t)}{\partial x^2} - \frac{1}{c^2} \frac{\partial^2 u(x, t)}{\partial t^2} = 0. \quad (3.47)$$

Here, the variable $c = \sqrt{\frac{E}{\rho}}$ has been introduced. This is the one-dimensional wave equation. It is easily checked that both the functions $\phi(x - ct)$ and $\psi(x + ct)$ satisfy the equation. The shape of the functions $\phi(x - ct)$ and $\psi(x + ct)$ do not change. They represent a displacement field that propagates as a wave along the x -axis in the positive and negative direction, respectively, with the speed c [13]. Hence, for the rod, waves propagate with the so called phase velocity $c = \sqrt{\frac{E}{\rho}}$. Now, it is assumed that the solution is harmonic in time, i.e. a complex solution is prescribed as $u(x, t) = \tilde{u}(x)e^{i\omega t}$. Here, ω is the circular frequency of vibration. Insertion into Eq. (3.46) and rearranging yields

$$\frac{\partial^2 \tilde{u}(x)}{\partial x^2} + \frac{\rho}{E} \omega^2 \tilde{u}(x) = 0. \quad (3.48)$$

This is a second-order differential equation, and solutions are of the form $\tilde{u}(x) = Ce^{ikx}$. Using this expression in Eq. (3.48) yields the dispersion relation,

$$k^2 - \frac{\rho}{E} \omega^2 = 0, \quad (3.49)$$

which has two roots. Both roots are real, $k_{1,2} = \pm\omega\sqrt{\frac{\rho}{E}} = \pm k_L$. The general solution to Eq. (3.46) is therefore

$$u(x, t) = C_1 e^{(i\omega t + ik_L x)} + C_2 e^{(i\omega t - ik_L x)}, \quad (3.50)$$

where the two terms represent harmonic waves propagating in the negative and positive directions, respectively, of the x -axis. This becomes clear if the phase of the first exponential is studied. For a certain time t_0 and position along the rod x_0 , the phase is

$$\xi = \omega t_0 + k_L x_0. \quad (3.51)$$

At a later instant in time, $t_1 = t_0 + \Delta t$, this phase is found at $x_1 = x_0 + \Delta x$, i.e

$$\xi = \omega(t_0 + \Delta t) + k_L(x_0 + \Delta x). \quad (3.52)$$

Subtracting Eq. (3.51) from Eq. (3.52) yields

$$\Delta x = -\frac{\omega}{k_L} \Delta t. \quad (3.53)$$

Since k_L is positive and real, Δx is negative, i.e. the wave has propagated in the negative x -direction, and it has done so with the phase velocity $c_L = \omega/k_L = \sqrt{E/\rho}$. The term k_L is called the longitudinal wavenumber and it is related to the wavelength λ_L as $k_L = 2\pi/\lambda_L$.

The fact that the phase velocity does not depend on the frequency ω , means that the longitudinal waves are non-dispersive. As shown in the next section, the situation is different for flexural waves.

Transversal waves in an infinite Bernoulli beam

For a uniform Bernoulli–Euler beam, the homogeneous equation can be written as

$$EI \frac{\partial^4 w(x, t)}{\partial x^4} + \rho A \frac{\partial^2 w(x, t)}{\partial t^2} = 0, \quad (3.54)$$

where EI is the bending stiffness, ρ is the mass density, A is the cross-section area and w is the vertical displacement. As for the rod in the previous section, a harmonic solution is assumed as $w(x, t) = \tilde{w}(x)e^{i\omega t}$. Insertion into Eq. (3.54) yields

$$\frac{\partial^4 \tilde{w}(x)}{\partial x^4} + \frac{\rho A}{EI} \omega^2 \tilde{w}(x) = 0, \quad (3.55)$$

to which solutions are of the form $\tilde{w}(x) = C e^{ikx}$. Using this expression in Eq. (3.55) yields the dispersion relation,

$$k^4 - \frac{\rho A}{EI} \omega^2 = 0. \quad (3.56)$$

This equation has two real and two imaginary roots; $k_{1,2} = \pm k_B$ and $k_{3,4} = \pm ik_B$ where $k_B = \sqrt{\omega} \left(\frac{\rho A}{EI} \right)^{1/4}$ is the flexural wavenumber. The general solution to Eq. (3.54) is therefore

$$w(x, t) = C_1 e^{(i\omega t + ik_B x)} + C_2 e^{(i\omega t - ik_B x)} + C_3 e^{(i\omega t - k_B x)} + C_4 e^{(i\omega t + k_B x)}. \quad (3.57)$$

Here, the terms involving C_1 and C_2 represent propagating waves, whereas the two remaining terms represent evanescent waves. The phase velocity is $c_B = \frac{\omega}{k_B} = \sqrt{\omega} \left(\frac{EI}{\rho A} \right)^{1/4}$. The phase velocity is frequency-dependent, i.e. the flexural waves are dispersive.

3.3.2 Wave propagation in an elastic continuum

In Section 3.1 the Navier equations, expressing the equation of motion for a homogeneous, linearly elastic continuum, was presented. Disregarding body forces, the Navier equations become

$$(\lambda + \mu) \frac{\partial^2 u_j}{\partial x_i \partial x_j} + \mu \frac{\partial^2 u_i}{\partial x_j \partial x_j} = \rho \frac{\partial^2 u_i}{\partial t^2}. \quad (3.58)$$

For a homogeneous infinite domain, i.e. a so called full-space, there are two different solutions to this equation: the dilational P-wave and the equivoluminal S-wave. These are called body waves. However, for a homogeneous domain with a free surface, i.e. a so called half-space, a coupling occurs between the P-wave and the S-wave. This coupling results in a surface wave, the Rayleigh wave, propagating in a direction parallel with the surface.

The P-wave

It can be shown [6] that by taking the divergence of Eq. (3.58), a scalar wave equation is obtained in terms of the previously defined dilation $\Delta(x_1, x_2, x_3, t)$, as

$$\frac{\partial^2 \Delta}{\partial x_k \partial x_k} = \frac{1}{c_p^2} \frac{\partial^2 \Delta}{\partial t^2}, \quad (3.59)$$

with

$$c_p = \sqrt{\frac{\lambda + 2\mu}{\rho}}. \quad (3.60)$$

This means that the solution to Eq. (3.59) represents a wave where the dilation Δ propagates with the velocity c_p . This wave is frequently called the P-wave, pressure wave, or primary wave, where primary refers to the fact that it is the fastest traveling wave and hence the first wave to arrive at a receiver.

The S-wave

Taking the rotation of Eq. (3.58), leads to the following three-dimensional wave equation [6]

$$\frac{\partial^2 w_i}{\partial x_j \partial x_j} = \frac{1}{c_s^2} \frac{\partial^2 w_i}{\partial t^2}, \quad (3.61)$$

where $w_i = w_i(x_1, x_2, x_3, t)$ denotes the rotation of the displacement field, defined as

$$w_1 = \frac{1}{2} \left(\frac{\partial u_3}{\partial x_2} - \frac{\partial u_2}{\partial x_3} \right), \quad w_2 = \frac{1}{2} \left(\frac{\partial u_1}{\partial x_3} - \frac{\partial u_3}{\partial x_1} \right), \quad w_3 = \frac{1}{2} \left(\frac{\partial u_2}{\partial x_1} - \frac{\partial u_1}{\partial x_2} \right), \quad (3.62)$$

and

$$c_s = \sqrt{\frac{\mu}{\rho}}. \quad (3.63)$$

The solution to Eq. (3.61) describes the propagation of a pure rotational wave, with the phase speed c_s . This wave is usually called the S-wave, shear wave or secondary wave. The particle motion is perpendicular to the propagation direction. Often the S-wave is divided into two components of horizontal and vertical motion, referred to as SH- and SV-waves.

The Rayleigh wave

Here, a plane surface wave propagating in the positive x_1 -direction of a homogeneous half-space is considered. The depth coordinate, x_3 , is pointing into the interior of the half-space. The particle displacement is independent of the x_2 -coordinate. The displacements in the x_1 - and x_3 -directions are now expressed in terms of two potential functions Φ and Ψ :

$$u_1 = \frac{\partial \Phi}{\partial x_1} + \frac{\partial \Psi}{\partial x_3}, \quad u_3 = \frac{\partial \Phi}{\partial x_3} - \frac{\partial \Psi}{\partial x_1}, \quad (3.64)$$

which inserted into Eq. (3.58) yields the two equations [6]

$$\nabla^2 \Phi = \frac{1}{c_p^2} \frac{\partial^2 \Phi}{\partial t^2}, \quad \nabla^2 \Psi = \frac{1}{c_s^2} \frac{\partial^2 \Psi}{\partial t^2}. \quad (3.65)$$

The wavefield is allowed to propagate along the x_1 -axis only. Harmonic solutions to Eqs. (3.65) are therefore sought in the form

$$\Phi = F(x_3) e^{i(\omega t - k_R x_1)}, \quad \Psi = G(x_3) e^{i(\omega t - k_R x_1)}, \quad (3.66)$$

where $F(x_3)$ and $G(x_3)$ are amplitude functions, and k_R is the wavenumber of the Rayleigh wave, $k_R = 2\pi/\lambda_R$. Insertion of these expressions into Eq. (3.65) leads to the following ordinary differential equations for F and G ,

$$\frac{d^2 F(x_3)}{dx_3^2} - \gamma_p^2 F(x_3) = 0, \quad \frac{d^2 G(x_3)}{dx_3^2} - \gamma_s^2 G(x_3) = 0, \quad (3.67)$$

where $\gamma_p^2 = k_R^2 - k_p^2$ and $\gamma_s^2 = k_R^2 - k_s^2$. The solution to Eqs. (3.67) are sought on the form

$$F(x_3) = A_1 e^{(-\gamma_p x_3)} + B_1 e^{(\gamma_p x_3)}, \quad G(x_3) = A_2 e^{(-\gamma_s x_3)} + B_2 e^{(\gamma_s x_3)}. \quad (3.68)$$

The constants $B_1 = B_2 = 0$, since an amplitude increasing to infinity with the depth coordinate x_3 is physically invalid. Hence, from Eqs. (3.66) and (3.68), the following expressions are obtained for the potential functions

$$\Phi = A_1 e^{(-\gamma_p x_3)} e^{i(\omega t - k_R x_1)}, \quad \Psi = A_2 e^{(-\gamma_s x_3)} e^{i(\omega t - k_R x_1)}. \quad (3.69)$$

The free surface is traction free, i.e. $\sigma_{33} = \sigma_{13} = 0$. Using these boundary conditions, with the expression for the stress tensor in Eq. (3.4), the displacements in Eq. (3.64), and the potentials in Eq. (3.69), the following relations are obtained

$$\begin{aligned} \frac{A_1}{A_2} \frac{(\lambda + 2\mu)\gamma_p^2 - \lambda k_R^2}{2i\mu k_R \gamma_s} - 1 &= 0, \\ \frac{A_1}{A_2} \frac{2\gamma_p i k_R}{\gamma_s^2 + k_R^2} + 1 &= 0. \end{aligned} \quad (3.70)$$

It can be shown [6] that from these relations, the following expression may be obtained relating the Rayleigh wave velocity c_R and the S-wave velocity c_s ,

$$K^6 - 8K^4 + (24 - 16\alpha^2)K^2 + 16(\alpha^2 - 1) = 0, \quad (3.71)$$

where $K = \frac{c_R}{c_s}$ and $\alpha = \frac{c_s}{c_p}$. The relation between the Poisson's ratio, and the phase velocities of the P-, S- and Rayleigh waves are shown in Figure 3.3 (left). The phase velocity of the Rayleigh wave is frequency independent, i.e. the Rayleigh wave is non-dispersive.

Inserting the potential functions in Eq. (3.69) into Eq. (3.64) yields the following expressions for the displacements,

$$\begin{aligned} u_1 &= -A_1 i k_R e^{(-\gamma_p x_3)} e^{i(\omega t - k_R x_1)} - A_2 \gamma_s e^{(-\gamma_s x_3)} e^{i(\omega t - k_R x_1)}, \\ u_3 &= -A_1 \gamma_p e^{(-\gamma_p x_3)} e^{i(\omega t - k_R x_1)} + A_2 i k_R e^{(-\gamma_s x_3)} e^{i(\omega t - k_R x_1)}. \end{aligned} \quad (3.72)$$

Using the relation between A_1 and A_2 established in Eq. (3.70), these displacements may be written as

$$\begin{aligned} u_1 &= A_1 i k_R \left(-e^{(-\gamma_p x_3)} + \frac{2\gamma_s \gamma_p}{\gamma_s^2 + k_R^2} e^{(-\gamma_s x_3)} \right) e^{i(\omega t - k_R x_1)}, \\ u_3 &= A_1 k_R \left(-\frac{\gamma_p}{k_R} e^{(-\gamma_p x_3)} + \frac{2\gamma_p k_R}{\gamma_s^2 + k_R^2} e^{(-\gamma_s x_3)} \right) e^{i(\omega t - k_R x_1)}. \end{aligned} \quad (3.73)$$

The terms inside the main brackets signify the difference in amplitudes for the horizontal and vertical particle motion. The presence of i in u_1 means that the horizontal particle motion is out-of-phase with the vertical motion by 90° , indicating that the particle movement follows an elliptical path. The relative amplitudes of the horizontal and vertical particle motion is shown in Figure 3.3 (right), for various values of Poisson's ratio.

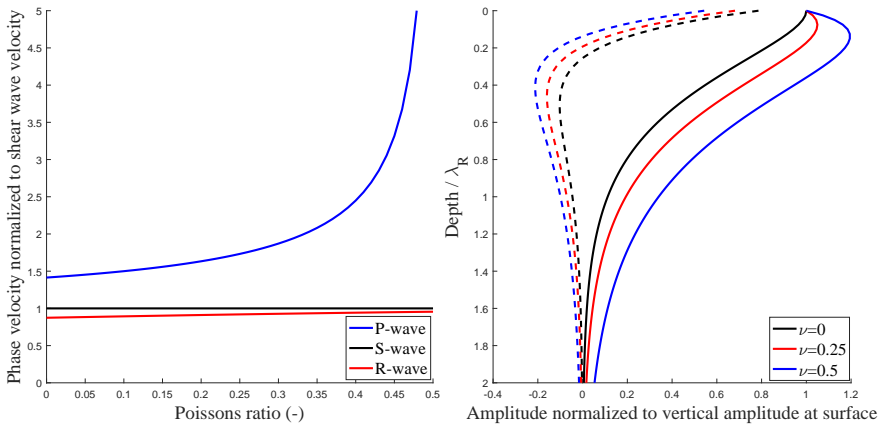


Figure 3.3: Left: Relation between Poisson’s ratio and phase velocities of the P-, S- and Rayleigh (R-) wave. Right: Relative amplitudes of vertical (solid) and horizontal (dashed) particle motion in Rayleigh wave for various Poisson’s ratio.

Damping

For soils, material damping effects occur due to friction between particles and structural rearrangement of the particles. Experimental studies suggests that the damping ratio is rather insensitive to the frequency of vibration. Hence, in computational models, soil material damping is most often introduced as a loss factor by using complex stiffness values as described in Section 3.2.3.

Another form of “damping” relevant for ground vibrations, is the attenuation of the vibration response at an increasing distance from the source, which is due to the spreading of the energy over a successively larger domain. This is usually called geometrical damping or geometrical attenuation. P- and S-waves originating from a point source on the soil surface spread radially with hemi-spherical wavefronts. At the time t the distance to the wave front, i.e. the radius of the half-sphere, is $r = c \times t$ and the surface area of the half-sphere is $2\pi r^2$. The amount of energy contained in the wavefront does not change, meaning that the energy density is inversely proportional to the wavefront surface area. Hence, the energy of body waves spreads as $1/r^2$. Since the mechanical energy (strain energy + kinetic energy) is proportional to the squared displacements, the displacement amplitude of body waves decreases as $1/r$. However, when the source is a line load, the body waves spread radially with cylindrical wavefronts, and by the same reasoning the energy and displacement amplitude can be shown to decrease as $1/r$ and $1/\sqrt{r}$, respectively. Surface waves that originate from a point source on the soil surface, spread radially along the surface with circular wavefronts, with the energy density being proportional to the wavefront circumference. Hence, the energy of Rayleigh waves decreases as $1/r$, and the displacement amplitude decreases as $1/\sqrt{r}$. In the case of a line load, there is no geometrical attenuation at all of the surface waves [14].

3.4 SOIL–STRUCTURE INTERACTION

3.4.1 General remarks

A modeling approach to calculate the vibrations inside a building excited by an external source, located on the ground surface or inside the soil volume, is to include everything, i.e. the source, the soil and the building structure, in one large numerical model analyzed in time-domain. However, in many cases this approach is impractical and computationally expensive. Kausel [15,16] showed that, if the source is unaffected by the presence of the building structure, the excitation of the building is fully defined by the free-field ground motion calculated or measured at the location of the building. The free-field ground motion can then be used for exciting the building, and obtaining the building response, in a calculation model of the building where the surrounding soil is included only as a dynamic stiffness at the soil–structure interface. This is referred to as the “substructure theorem”, presented in the following section.

3.4.2 Substructure theorem

The building response to the incoming wave field may be determined by applying a frequency domain formulation in which the building is excited by a set of fictitious forces at the soil–structure interface. These fictitious forces are calculated from the free-field response at the soil–structure interface. Kausel et al [15, 16] refer to this as the substructure theorem which can be motivated in the following manner. Figure 3.4 (a) shows a building structure, with an external source exciting the ground. The excitation by the external source causes a displacement \mathbf{u}_i and a traction \mathbf{p}_i along the soil–structure interface, where a sub-index i refers to the interface. In Figure 3.4 (b) the building is extracted from the ground, viewed as a free body in space. Equilibrium requires that the displacements \mathbf{u}_i are identical at the soil-structure boundaries of both sub-systems, and that the tractions \mathbf{p}_i are equal in size but in opposite direction.

In Figure 3.4 (c) the same source is present, but without the building structure; however the soil prism that were to be removed in order to erect the building is highlighted. The displacements and tractions along the soil prism boundary are denoted by \mathbf{u}_i^* and \mathbf{p}_i^* respectively. In Figure 3.4 (d) the soil prism is extracted, and again equilibrium requires that the displacements are equal at the boundaries of both sub-systems, and that the tractions are equal in size but in opposite direction. If the forces and displacements of the outer region in Figure 3.4 (d) are subtracted from Figure 3.4 (b), the external source cancels out, and the displacements and tractions on the open soil-structure interface become $\Delta\mathbf{u}_i = \mathbf{u}_i - \mathbf{u}_i^*$ and $\Delta\mathbf{p}_i = -\mathbf{p}_i - (-\mathbf{p}_i^*) = \mathbf{p}_i^* - \mathbf{p}_i$ respectively. Since the external source has cancelled out, the displacements $\Delta\mathbf{u}_i$ can only be the result of the tractions $\Delta\mathbf{p}_i$, and these two fields are related via the dynamic stiffness of the soil along the soil–structure boundary $\mathbf{Z} = \mathbf{Z}(\omega)$ as

$$\mathbf{Z}\Delta\mathbf{u}_i = \Delta\mathbf{p}_i \rightarrow \mathbf{Z}(\mathbf{u}_i - \mathbf{u}_i^*) = \mathbf{p}_i^* - \mathbf{p}_i. \quad (3.74)$$

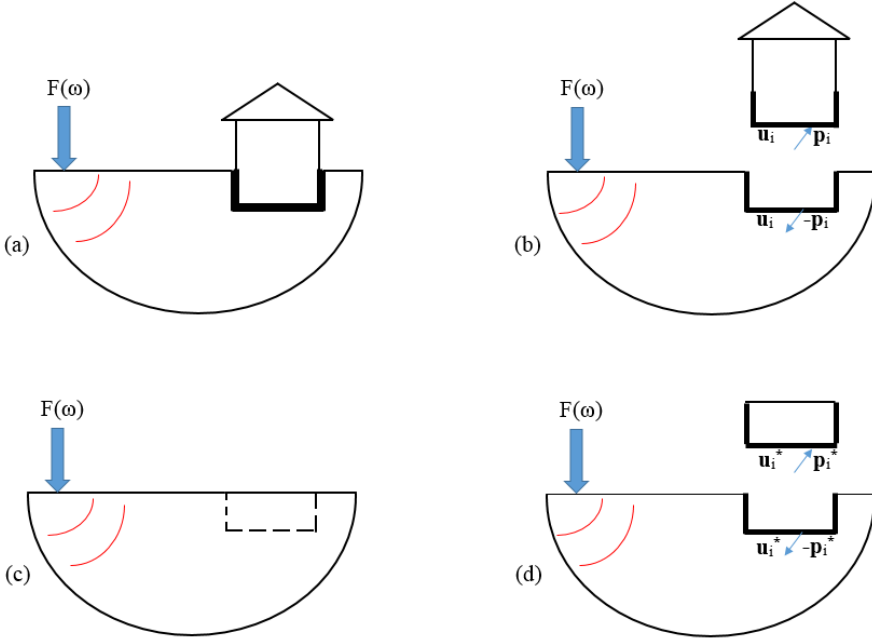


Figure 3.4: Dynamic excitation of the soil surface by the source $F(\omega)$ for the cases with (a and b) and without (c and d) an adjacent building structure.

Referring to the building structure sub-system in Figure 3.4 (b) the forces acting on the building along the soil–structure interface, \mathbf{p}_i , can be obtained from Eq. (3.74) as

$$\mathbf{p}_i = -\mathbf{Z}\mathbf{u}_i + \mathbf{Z}\mathbf{u}_i^* + \mathbf{p}_i^*. \quad (3.75)$$

Letting a subscript b refer to all the degrees of freedom of the structure except those at the soil–structure interface, the dynamic equilibrium of the structure can be written as

$$\begin{bmatrix} \mathbf{D}_{bb} & \mathbf{D}_{bi} \\ \mathbf{D}_{ib} & \mathbf{D}_{ii} \end{bmatrix} \begin{bmatrix} \mathbf{u}_b \\ \mathbf{u}_i \end{bmatrix} = \begin{bmatrix} \mathbf{0} \\ \mathbf{p}_i \end{bmatrix} = \begin{bmatrix} \mathbf{0} \\ -\mathbf{Z}\mathbf{u}_i + \mathbf{Z}\mathbf{u}_i^* + \mathbf{p}_i^* \end{bmatrix}, \quad (3.76)$$

where $\mathbf{D} = \mathbf{D}(\omega)$ is the dynamic stiffness of the building. Moving the first load term to the left-hand side, results in

$$\begin{bmatrix} \mathbf{D}_{bb} & \mathbf{D}_{bi} \\ \mathbf{D}_{ib} & \mathbf{D}_{ii} + \mathbf{Z} \end{bmatrix} \begin{bmatrix} \mathbf{u}_b \\ \mathbf{u}_i \end{bmatrix} = \begin{bmatrix} \mathbf{0} \\ \mathbf{Z}\mathbf{u}_i^* + \mathbf{p}_i^* \end{bmatrix}. \quad (3.77)$$

It is now clear that the building response, due to the external source loading, can be calculated using the free-field displacements and tractions at the soil–structure interface obtained from a calculation model where the presence of the building structure is disregarded. This approach is very convenient as it allows the separation of source and receiver into different models. This is

particularly useful when dealing with building responses due to moving loads. Computational models operating in frequency domain in a moving frame of reference following the moving load can be very efficient, compared to conventional 3D time-domain models, for calculating the free-field ground motion caused by the moving load but such models do not allow for the inclusion of stationary structures, at least not in a straight forward manner. The substructure theorem enables the calculation of the building response in a separate conventional structural model using the free-field response, obtained from a different model, as excitation input. The formulation makes no approximations and is therefore exact, however the necessary assumptions are that the soil response is linear and that the source loading is unaffected by the presence of the building structure. Since the formulation is in frequency domain, Eq. (3.77) is solved for a range of frequencies and if the time-domain response is required, it can be obtained from an inverse discrete Fourier transform.

The dynamic stiffness of the soil along the soil–structure interface, $\mathbf{Z}(\omega)$, can be obtained in several ways. For homogeneous half-spaces and circular footings, analytical expressions exist. For more complex soil profiles and footing geometries, numerical methods such as FEM or semi-analytical techniques can be used. In Paper E, $\mathbf{Z}(\omega)$ was calculated using the Green's function of a layered half-space, obtained using the semi-analytical technique discussed in Chapter 4.

4 Numerical Solution Methods

In the current work, several numerical solution methods have been used for calculating the ground vibrations from loads on a railway track. Various formulations of the finite element method, described in Section 4.1, has been used for modeling the railway track. To model the wave propagation in the ground, a time efficient semi-analytical method described in Section 4.2 has been used as well as finite element modeling of the soil domain. The coupling of the methods used for the track and soil is described in Chapter 5.

4.1 THE FINITE ELEMENT METHOD

4.1.1 General remarks

In physics and engineering, many phenomena are mathematically described by partial differential equations (PDEs). Analytical solutions to such PDEs can usually only be found for very simple geometries, domain properties, boundary conditions and loads. For more complex cases, numerical methods are employed to find approximations to the true solution. One commonly used method is the finite element method (FEM), in which the computational domain is divided into smaller elements forming an element mesh. Each element is geometrically defined by its nodes, and in the general case also by some function defining the element boundary between the nodes. The physical field is discretized onto the nodes, and inside each element the field is assumed to vary according to some predefined function which is usually a simple polynomial function. The method is very versatile and can be formulated to account for very complex behavior such as geometric and material non-linearities etc.

The FE formulation leads to a system of equations where the values of the physical field in the nodes are the unknowns. Smaller elements in general lead to a more accurate solution, since the error due to the assumed variation within each element decreases. At the same time the computational cost increases, because the size of the system of equations increases with increasing number of nodes. For problems where the physical field is a scalar function, e.g. temperature, each node has only one degree-of-freedom (DoF). However, for problems where the physical field is a vector function, such as structural mechanics problems, each node is gen-

erally associated with a number of DoFs, e.g. the displacements in the (x_1, x_2, x_3) -directions. As mentioned in Section 3.2, the system of equations obtained when applying the FE method can be written as

$$\mathbf{M}\ddot{\mathbf{u}}(t) + \mathbf{C}\dot{\mathbf{u}}(t) + \mathbf{K}\mathbf{u}(t) = \mathbf{f}(t). \quad (4.1)$$

Here, \mathbf{M} , \mathbf{C} and \mathbf{K} are the mass, damping and stiffness matrices, respectively. These matrices are $(N \times N)$, where N is the number of DoFs. Further, $\ddot{\mathbf{u}}(t)$, $\dot{\mathbf{u}}(t)$, $\mathbf{u}(t)$, and $\mathbf{f}(t)$ are $(N \times 1)$ column vectors containing the acceleration, velocity, displacement and external loading, respectively, for each DoF. Often, the steady-state response due to harmonic excitation, $\mathbf{f}(t) = \hat{\mathbf{f}}e^{i\omega t}$, is of interest. As mentioned in Section 3.2, this steady-state response is solved by assuming a harmonic response with the same frequency, $\mathbf{u}(t) = \hat{\mathbf{u}}e^{i\omega t}$, resulting in

$$(-\omega^2\mathbf{M} + i\omega\mathbf{C} + \mathbf{K})\hat{\mathbf{u}} = \mathbf{D}(\omega)\hat{\mathbf{u}} = \hat{\mathbf{f}}. \quad (4.2)$$

In Section 4.1.2 below, the standard FE equations for a 3D linear elastic continuum are presented. These equations are also used in Sections 4.1.3–4.1.4 where FE formulations are presented for a moving frame of reference, and for so called 2.5D FEM, respectively. Although presented here only for solid continuum elements, the concepts presented in Sections 4.1.3–4.1.4 apply analogously also to structural elements such as beam and shell elements, whose derivations in the fixed frame of reference can be found in standard textbooks on FEM, e.g. [17]. Section 4.1.5 contains a brief description of perfectly matched layers (PMLs), that are used for artificially attenuating waves at the truncated ends of a FE model.

4.1.2 Finite element equations for 3D elasticity

The Cauchy equation of motion, governing the dynamic equilibrium of a continuum, was presented in Section 3.1 and is repeated here for clarity,

$$\frac{\partial \sigma_{ij}}{\partial x_j} + b_i = \rho \frac{\partial^2 u_i}{\partial t^2}. \quad (4.3)$$

Defining the matrix differential operator $\tilde{\nabla}$, the stress vector $\boldsymbol{\sigma}$, the body force vector \mathbf{b} and the displacement vector \mathbf{u} as

$$\tilde{\nabla}^T = \begin{bmatrix} \frac{\partial}{\partial x_1} & 0 & 0 & \frac{\partial}{\partial x_2} & \frac{\partial}{\partial x_3} & 0 \\ 0 & \frac{\partial}{\partial x_2} & 0 & \frac{\partial}{\partial x_1} & 0 & \frac{\partial}{\partial x_3} \\ 0 & 0 & \frac{\partial}{\partial x_3} & 0 & \frac{\partial}{\partial x_1} & \frac{\partial}{\partial x_2} \end{bmatrix}, \quad (4.4)$$

$$\boldsymbol{\sigma}^T = [\sigma_{11} \quad \sigma_{22} \quad \sigma_{33} \quad \sigma_{12} \quad \sigma_{13} \quad \sigma_{23}], \quad (4.5)$$

$$\mathbf{b}^T = [b_1 \quad b_2 \quad b_3], \quad (4.6)$$

$$\mathbf{u}^T = [u_1 \quad u_2 \quad u_3], \quad (4.7)$$

Eq. (4.3) is written as

$$\tilde{\mathbf{V}}^T \boldsymbol{\sigma} + \mathbf{b} = \rho \frac{\partial^2 \mathbf{u}}{\partial t^2}. \quad (4.8)$$

The weak form is obtained by multiplying Eq. (4.8) by an arbitrary weight function vector $\mathbf{g} = \mathbf{g}(x_1, x_2, x_3)$ and integrating it over the region [17]. The resulting weak form, after partial integration of the first term, becomes

$$\int_V (\tilde{\mathbf{V}} \mathbf{g})^T \boldsymbol{\sigma} dV + \rho \int_V \mathbf{g}^T \frac{\partial^2 \mathbf{u}}{\partial t^2} dV = \int_S \mathbf{g}^T \mathbf{t} dS + \int_V \mathbf{g}^T \mathbf{b} dV, \quad (4.9)$$

where \mathbf{t} is the traction vector.

To obtain the FE formulation, the displacements $\mathbf{u}(x_1, x_2, x_3, t)$ are approximated using the nodal values $\mathbf{a}(t)$ and the shape functions $\mathbf{N}(x_1, x_2, x_3)$ as $\mathbf{u} = \mathbf{N}\mathbf{a}$. The shape function matrix \mathbf{N} is written as

$$\mathbf{N}(x_1, x_2, x_3) = \begin{bmatrix} N_1 & 0 & 0 & N_2 & 0 & 0 & \dots & N_n & 0 & 0 \\ 0 & N_1 & 0 & 0 & N_2 & 0 & \dots & 0 & N_n & 0 \\ 0 & 0 & N_1 & 0 & 0 & N_2 & \dots & 0 & 0 & N_n \end{bmatrix}, \quad (4.10)$$

where n is the number of nodes and $N_i = N_i(x_1, x_2, x_3)$. Further, the stress vector is expressed as $\boldsymbol{\sigma} = \mathbf{D}\boldsymbol{\epsilon} = \mathbf{D}\tilde{\mathbf{V}}\mathbf{u} = \mathbf{D}\tilde{\mathbf{V}}\mathbf{N}\mathbf{a}$. Here, \mathbf{D} is the constitutive matrix for isotropic elasticity,

$$\mathbf{D} = \frac{E}{(1+v)(1-2v)} \begin{bmatrix} 1-v & v & v & 0 & 0 & 0 \\ v & 1-v & v & 0 & 0 & 0 \\ v & v & 1-v & 0 & 0 & 0 \\ 0 & 0 & 0 & \frac{1}{2}(1-2v) & 0 & 0 \\ 0 & 0 & 0 & 0 & \frac{1}{2}(1-2v) & 0 \\ 0 & 0 & 0 & 0 & 0 & \frac{1}{2}(1-2v) \end{bmatrix}. \quad (4.11)$$

Adopting the Galerkin method, the weight function $\mathbf{g}(x_1, x_2, x_3)$ is approximated using the same shape functions as for the displacement field, i.e. $\mathbf{g} = \mathbf{N}\mathbf{c}$. Here, \mathbf{c} is an arbitrary vector. Inserting these approximations for \mathbf{u} and \mathbf{g} into Eq. (4.9) and noting that \mathbf{c} is arbitrary, the mass and stiffness matrices and the load vector, are identified as

$$\begin{aligned} \mathbf{K} &= \int_V (\tilde{\mathbf{V}}\mathbf{N})^T \mathbf{D} (\tilde{\mathbf{V}}\mathbf{N}) dV, \\ \mathbf{M} &= \rho \int_V \mathbf{N}^T \mathbf{N} dV, \\ \mathbf{f}_l &= \int_S \mathbf{N}^T \mathbf{t} dS + \int_V \mathbf{N}^T \mathbf{b} dV. \end{aligned} \quad (4.12)$$

Although the expressions of the matrices in Eqs. (4.12) are for the entire computational domain V with the boundary surface S , they are equally valid, and generally evaluated, for each element separately. This is done by exchanging the integration limits from those of the entire domain (V and S) to those of the individual element (V^e and S^e) and further by changing \mathbf{N} , describing

the shape functions of all the elements, to \mathbf{N}^e , describing the shape functions solely for the individual element. The so obtained element matrices (\mathbf{K}^e , \mathbf{M}^e , \mathbf{f}_1^e) are then assembled into their position of the respective global matrices (\mathbf{K} , \mathbf{M} , \mathbf{f}_1), determined by the global numbering of the element DoFs.

4.1.3 Formulation in a moving frame of reference

When analyzing moving loads, such as a train moving along a railway track, a traditional 3D FE approach can lead to a very large system of equations. Because the load is moving, it will eventually leave the computational domain. Hence, it may be necessary to use a very large model. If the geometry and the material properties are invariant in the direction of the moving load, a computationally more efficient model may be obtained, by formulating the governing equations in a reference frame that follows the moving load at a fixed velocity. In such a formulation, the moving load remains fixed in the same position of the model, enabling the use of a smaller computational domain. Furthermore, the problem can be analyzed using frequency-domain methods instead of time-stepping procedures, which may be beneficial both in terms of computational cost and understanding of physical phenomena.

Here, the load is assumed to move at a fixed speed v along the positive x_1 -axis. A coordinate transformation is introduced as

$$(\tilde{x}_1, \tilde{x}_2, \tilde{x}_3) = (x_1 - vt, x_2, x_3), \quad (4.13)$$

where $\tilde{x}_1, \tilde{x}_2, \tilde{x}_3$ denotes the coordinates in the moving frame of reference. Partial derivatives in the two reference frames are related as [14]

$$\frac{\partial}{\partial x_1} = \frac{\partial}{\partial \tilde{x}_1}, \quad \frac{\partial}{\partial t} \Big|_{x_1} = \frac{\partial}{\partial t} \Big|_{\tilde{x}_1} - v \frac{\partial}{\partial \tilde{x}_1}. \quad (4.14)$$

Applying this coordinate transformation to the Cauchy equation of motion, Eq. (4.3), yields

$$\frac{\partial \tilde{\sigma}_{ij}}{\partial \tilde{x}_j} + \tilde{b}_i = \rho \left(\frac{\partial^2 \tilde{u}_i}{\partial t^2} - 2v \frac{\partial^2 \tilde{u}_i}{\partial t \partial \tilde{x}_1} + v^2 \frac{\partial^2 \tilde{u}_i}{\partial \tilde{x}_1^2} \right), \quad (4.15)$$

where $\tilde{\cdot}$ denotes that a variable is expressed in the moving frame of reference. With a notation analogous to Eq. (4.8), this equation can be written as

$$\tilde{\nabla}^T \tilde{\boldsymbol{\sigma}} + \tilde{\mathbf{b}} = \rho \left(\frac{\partial^2 \tilde{\mathbf{u}}}{\partial t^2} - 2v \frac{\partial^2 \tilde{\mathbf{u}}}{\partial t \partial \tilde{x}_1} + v^2 \frac{\partial^2 \tilde{\mathbf{u}}}{\partial \tilde{x}_1^2} \right). \quad (4.16)$$

Now the ordinary procedure is followed to reach the FE formulation. The weak form is obtained by multiplying with an arbitrary weight function $\mathbf{g} = \mathbf{g}(\tilde{x}_1, \tilde{x}_2, \tilde{x}_3)$ and integrating

over the region, resulting in

$$\begin{aligned} & \int_V (\tilde{\nabla} \mathbf{g})^T \tilde{\boldsymbol{\sigma}} \, dV + \rho \int_V \mathbf{g}^T \frac{\partial^2 \tilde{\mathbf{u}}}{\partial t^2} \, dV - 2\rho v \int_V \mathbf{g}^T \frac{\partial^2 \tilde{\mathbf{u}}}{\partial t \partial \tilde{x}_1} \, dV + \\ & \rho v^2 \int_S \mathbf{g}^T \frac{\partial \tilde{\mathbf{u}}}{\partial \tilde{x}_1} n_x \, dS - \rho v^2 \int_V \frac{\partial \tilde{\mathbf{g}}}{\partial \tilde{x}_1}^T \frac{\partial \tilde{\mathbf{u}}}{\partial \tilde{x}_1} \, dV = \\ & \int_S \mathbf{g}^T \tilde{\mathbf{t}} \, dS + \int_V \mathbf{g}^T \tilde{\mathbf{b}} \, dV, \end{aligned} \quad (4.17)$$

after partial integration of the first term. The displacements $\tilde{\mathbf{u}}(\tilde{x}_1, \tilde{x}_2, \tilde{x}_3, t)$ are approximated using the nodal values $\tilde{\mathbf{a}}(t)$ and the shape functions $\mathbf{N}(\tilde{x}_1, \tilde{x}_2, \tilde{x}_3)$ as $\tilde{\mathbf{u}} = \mathbf{N}\tilde{\mathbf{a}}$. It is emphasized that the nodal values now represent displacements in the moving frame of reference. The weight function $\mathbf{g}(\tilde{x}_1, \tilde{x}_2, \tilde{x}_3)$ is approximated using the same shape functions, i.e. $\mathbf{g} = \mathbf{N}\tilde{\mathbf{c}}$, where $\tilde{\mathbf{c}}$ is an arbitrary vector. Inserting these approximations into Eq. (4.17) yields the mass, damping and stiffness matrices, as well as the load vector, as

$$\begin{aligned} \mathbf{K} &= \int_V (\tilde{\nabla} \mathbf{N})^T \mathbf{D} (\tilde{\nabla} \mathbf{N}) \, dV - \rho v^2 \int_V \frac{\partial \mathbf{N}^T}{\partial \tilde{x}_1} \frac{\partial \mathbf{N}}{\partial \tilde{x}_1} \, dV + \rho v^2 \int_S \mathbf{N}^T \frac{\partial \mathbf{N}}{\partial \tilde{x}_1} n_x \, dS, \\ \mathbf{C} &= -2\rho v \int_V \mathbf{N}^T \frac{\partial \mathbf{N}}{\partial \tilde{x}_1} \, dV, \\ \mathbf{M} &= \rho \int_V \mathbf{N}^T \mathbf{N} \, dV, \\ \mathbf{f}_1 &= \int_S \mathbf{N}^T \tilde{\mathbf{t}} \, dS + \int_V \mathbf{N}^T \tilde{\mathbf{b}} \, dV. \end{aligned} \quad (4.18)$$

Comparing Eqs. (4.18) with Eqs. (4.12) it is seen that due to the coordinate transformation, some velocity dependent terms have arisen in the stiffness matrix and the damping matrix. These terms are called convective terms. It is also emphasized that if the load speed is set to $v = 0$, the expressions in Eqs. (4.18) are identical to Eqs. (4.12). As pointed out in [14], convection may lead to unstable numerical solutions in time domain analyses if the standard Galerkin approach is used, and there are different ways to stabilize the solution. However, in the present work the formulation above is used merely for frequency domain analyses, see Chapter 5 and the appended papers.

4.1.4 FE formulation in 2.5D

When the problem geometry is invariant in one direction, an efficient solution method can be established by Fourier transforming the governing equations with respect to the invariant coordinate axis [18–20]. This is often called 2.5D FEM or wavenumber FEM.

The weak form for 3D elasticity was established in Eq. 4.9 and is repeated here for convenience.

$$\int_V (\tilde{\nabla} \mathbf{g})^T \boldsymbol{\sigma} \, dV + \rho \int_V \mathbf{g}^T \frac{\partial^2 \mathbf{u}}{\partial t^2} \, dV = \int_S \mathbf{g}^T \mathbf{t} \, dS + \int_V \mathbf{g}^T \mathbf{b} \, dV. \quad (4.19)$$

The volume V is now assumed to be limited in the (x_2, x_3) directions by the area A , and to have infinite length in the x_1 -direction. This means that the equation can be written as

$$\int_{-\infty}^{\infty} \int_A (\tilde{\nabla} \mathbf{g})^T \boldsymbol{\sigma} \, dA \, dx_1 + \int_{-\infty}^{\infty} \int_A \mathbf{g}^T \frac{\partial^2 \mathbf{u}}{\partial t^2} \, dA \, dx_1 - \int_{-\infty}^{\infty} \int_A \mathbf{g}^T \mathbf{b} \, dA \, dx_1 - \int_{-\infty}^{\infty} \oint_{\Gamma_A} \mathbf{g}^T \mathbf{t} \, d\Gamma_A \, dx_1 = 0, \quad (4.20)$$

where Γ_A denotes the circumference of the area A . Now, the FE mesh is defined on the surface A in the (x_2, x_3) -plane. The shape function matrix is written as

$$\mathbf{N}(x_2, x_3) = \begin{bmatrix} N_1 & 0 & 0 & N_2 & 0 & 0 & \dots & N_n & 0 & 0 \\ 0 & N_1 & 0 & 0 & N_2 & 0 & \dots & 0 & N_n & 0 \\ 0 & 0 & N_1 & 0 & 0 & N_2 & \dots & 0 & 0 & N_n \end{bmatrix}, \quad (4.21)$$

where n is the number of nodes and $N_i = N_i(x_2, x_3)$. Further, the displacement vector \mathbf{u} ,

$$\mathbf{u}(x_1, x_2, x_3) = [u_1(x_1, x_2, x_3) \quad u_2(x_1, x_2, x_3) \quad u_3(x_1, x_2, x_3)]^T, \quad (4.22)$$

is now approximated using the shape functions and the nodal displacement vector as

$\mathbf{u}(x_1, x_2, x_3) = \mathbf{N}(x_2, x_3)\mathbf{a}(x_1)$, where

$$\mathbf{a}(x_1) = [a_{1x_1}(x_1) \quad a_{1x_2}(x_1) \quad a_{1x_3}(x_1) \quad a_{2x_1}(x_1) \quad \dots \quad a_{nx_3}(x_1)]^T. \quad (4.23)$$

With the Galerkin approach, the weight function vector \mathbf{g} is also approximated using the shape function matrix and an arbitrary nodal displacement vector as $\mathbf{g}(x_1, x_2, x_3) = \mathbf{N}(x_2, x_3)\mathbf{c}(x_1)$. As usual, the stress vector is expressed as $\boldsymbol{\sigma} = \mathbf{D}\boldsymbol{\epsilon} = \mathbf{D}\tilde{\nabla}\mathbf{u} = \mathbf{D}\tilde{\nabla}\mathbf{N}\mathbf{a}$ where \mathbf{D} is the constitutive matrix for isotropic elasticity defined in Eq. (4.11). With the matrix differential

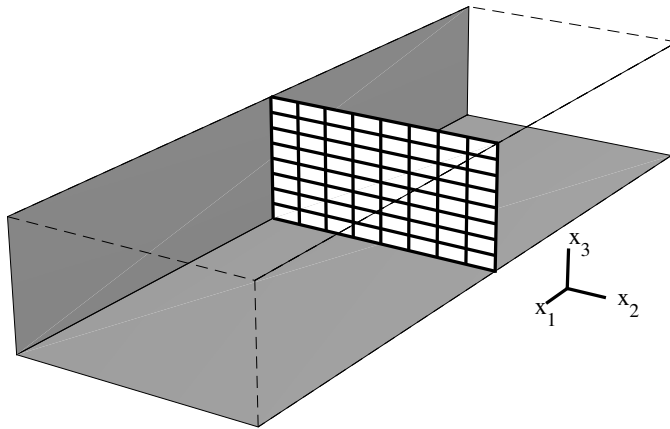


Figure 4.1: A longitudinally invariant structure with a 2D mesh defined in the (x_2, x_3) -plane.

operator $\tilde{\nabla}$ defined by Eq. (4.4),

$$\begin{aligned}\tilde{\nabla}\mathbf{u} &= \tilde{\nabla}(\mathbf{N}\mathbf{a}) = \mathbf{L}_1\mathbf{N}(x_2, x_3)\mathbf{a}(x_1) + \mathbf{L}_2\mathbf{N}(x_2, x_3)\frac{\partial\mathbf{a}(x_1)}{\partial x_1} = \mathbf{B}_1\mathbf{a}(x_1) + \mathbf{B}_2\frac{\partial\mathbf{a}(x_1)}{\partial x_1}, \\ \tilde{\nabla}\mathbf{g} &= \tilde{\nabla}(\mathbf{N}\mathbf{c}) = \mathbf{L}_1\mathbf{N}(x_2, x_3)\mathbf{a}(x_1) + \mathbf{L}_2\mathbf{N}(x_2, x_3)\frac{\partial\mathbf{c}(x_1)}{\partial x_1} = \mathbf{B}_1\mathbf{a}(x_1) + \mathbf{B}_2\frac{\partial\mathbf{c}(x_1)}{\partial x_1},\end{aligned}\quad (4.24)$$

where

$$\mathbf{L}_1^T = \begin{bmatrix} 0 & 0 & 0 & \frac{\partial}{\partial x_2} & \frac{\partial}{\partial x_3} & 0 \\ 0 & \frac{\partial}{\partial x_2} & 0 & 0 & 0 & \frac{\partial}{\partial x_3} \\ 0 & 0 & \frac{\partial}{\partial x_3} & 0 & 0 & \frac{\partial}{\partial x_2} \end{bmatrix}, \quad (4.25)$$

and

$$\mathbf{L}_2^T = \begin{bmatrix} 1 & 0 & 0 & 0 & 0 & 0 \\ 0 & 0 & 0 & 1 & 0 & 0 \\ 0 & 0 & 0 & 0 & 1 & 0 \end{bmatrix}. \quad (4.26)$$

Equation 4.20 can now be written as

$$\begin{aligned}& \int_{-\infty}^{\infty} \int_A \left(\mathbf{B}_1\mathbf{c} + \mathbf{B}_2\frac{\partial\mathbf{c}}{\partial x_1} \right)^T \mathbf{D} \left(\mathbf{B}_1\mathbf{a} + \mathbf{B}_2\frac{\partial\mathbf{a}}{\partial x_1} \right) dA dx_1 + \\ & \int_{-\infty}^{\infty} \int_A (\mathbf{N}\mathbf{c})^T \rho \left(\mathbf{N}\frac{\partial^2\mathbf{a}}{\partial t^2} \right) dA dx_1 - \int_{-\infty}^{\infty} \int_A (\mathbf{N}\mathbf{c})^T \mathbf{b} dA dx_1 - \\ & \int_{-\infty}^{\infty} \oint_{\Gamma_A} (\mathbf{N}\mathbf{c})^T \mathbf{t} d\Gamma_A dx_1 = 0,\end{aligned}\quad (4.27)$$

which, by noting that $\mathbf{a}(x_1)$ and $\mathbf{c}(x_1)$ are independent of (x_2, x_3) and can therefore be placed outside the inner integral, can be written as

$$\begin{aligned}& \int_{-\infty}^{\infty} \mathbf{c}^T \int_A \mathbf{B}_1^T \mathbf{D} \mathbf{B}_1 dA \mathbf{a} dx_1 + \int_{-\infty}^{\infty} \mathbf{c}^T \int_A \mathbf{B}_1^T \mathbf{D} \mathbf{B}_2 dA \frac{\partial\mathbf{a}}{\partial x_1} dx_1 + \\ & \int_{-\infty}^{\infty} \frac{\partial\mathbf{c}}{\partial x_1}^T \int_A \mathbf{B}_2^T \mathbf{D} \mathbf{B}_1 dA \mathbf{a} dx_1 + \int_{-\infty}^{\infty} \frac{\partial\mathbf{c}}{\partial x_1}^T \int_A \mathbf{B}_2^T \mathbf{D} \mathbf{B}_2 dA \frac{\partial\mathbf{a}}{\partial x_1} dx_1 + \\ & \int_{-\infty}^{\infty} \mathbf{c}^T \int_A \mathbf{N}^T \rho \mathbf{N} dA \frac{\partial^2\mathbf{a}}{\partial t^2} dx_1 - \int_{-\infty}^{\infty} \mathbf{c}^T \int_A \mathbf{N}^T \mathbf{b} dA dx_1 - \\ & \int_{-\infty}^{\infty} \mathbf{c}^T \oint_{\Gamma_A} \mathbf{N}^T \mathbf{t} d\Gamma_A dx_1 = 0.\end{aligned}\quad (4.28)$$

Now, a Fourier transform from the x_1 -coordinate to the wavenumber k_1 is performed, and

the following notation is used

$$\begin{aligned}
\hat{\mathbf{a}}(k_1) &= \int_{-\infty}^{\infty} \mathbf{a}(x_1) e^{-ik_1 x_1} dx_1, \\
\hat{\mathbf{c}}(k_1) &= \int_{-\infty}^{\infty} \mathbf{c}(x_1) e^{-ik_1 x_1} dx_1, \\
\hat{\mathbf{b}}(k_1, x_2, x_3) &= \int_{-\infty}^{\infty} \mathbf{b}(x_1, x_2, x_3) e^{-ik_1 x_1} dx_1, \\
\hat{\mathbf{t}}(k_1, x_2, x_3) &= \int_{-\infty}^{\infty} \mathbf{t}(x_1, x_2, x_3) e^{-ik_1 x_1} dx_1.
\end{aligned} \tag{4.29}$$

The derivatives of \mathbf{a} and \mathbf{c} with respect to x_1 , become

$$\begin{aligned}
\mathcal{F}\left(\frac{\partial \mathbf{a}(x_1)}{\partial x_1}\right) &= ik_1 \hat{\mathbf{a}}(k_1), \\
\mathcal{F}\left(\frac{\partial \mathbf{c}(x_1)}{\partial x_1}\right) &= ik_1 \hat{\mathbf{c}}(k_1).
\end{aligned} \tag{4.30}$$

To transform Eq. (4.27), from spatial x_1 - to wavenumber k_1 -domain, Parseval's formula is used:

$$\int_{-\infty}^{\infty} \overline{g(x_1)} m(x_1) dx_1 = \int_{-\infty}^{\infty} \overline{\hat{g}(k_1)} \hat{m}(k_1) d\frac{k_1}{2\pi}. \tag{4.31}$$

Equation (4.31) is now applied on Eq. (4.27), yielding

$$\begin{aligned}
&\int_{-\infty}^{\infty} \overline{\hat{\mathbf{c}}^T} \int_A \mathbf{B}_1^T \mathbf{D} \mathbf{B}_1 dA \hat{\mathbf{a}} d\frac{k_1}{2\pi} + \int_{-\infty}^{\infty} ik_1 \overline{\hat{\mathbf{c}}^T} \int_A \mathbf{B}_1^T \mathbf{D} \mathbf{B}_2 dA \hat{\mathbf{a}} d\frac{k_1}{2\pi} + \\
&\int_{-\infty}^{\infty} -ik_1 \overline{\hat{\mathbf{c}}^T} \int_A \mathbf{B}_2^T \mathbf{D} \mathbf{B}_1 dA \hat{\mathbf{a}} d\frac{k_1}{2\pi} + \int_{-\infty}^{\infty} k_1^2 \overline{\hat{\mathbf{c}}^T} \int_A \mathbf{B}_2^T \mathbf{D} \mathbf{B}_2 dA \hat{\mathbf{a}} d\frac{k_1}{2\pi} + \\
&\int_{-\infty}^{\infty} \overline{\hat{\mathbf{c}}^T} \int_A \mathbf{N}^T \rho \mathbf{N} dA \frac{\partial^2 \hat{\mathbf{a}}}{\partial t^2} d\frac{k_1}{2\pi} - \int_{-\infty}^{\infty} \overline{\hat{\mathbf{c}}^T} \int_A \mathbf{N}^T \hat{\mathbf{b}} dA d\frac{k_1}{2\pi} - \\
&\int_{-\infty}^{\infty} \overline{\hat{\mathbf{c}}^T} \oint_{\Gamma_A} \mathbf{N}^T \hat{\mathbf{t}} d\Gamma_A d\frac{k_1}{2\pi} = 0.
\end{aligned} \tag{4.32}$$

Since $\hat{\mathbf{c}}(k_1)$ is arbitrary, it can be concluded that the following equation must apply for each wavenumber k_1 ,

$$\mathbf{M} \ddot{\hat{\mathbf{a}}}(k_1) + \left(\mathbf{K}_0 + ik_1 \mathbf{K}_1 + k_1^2 \mathbf{K}_2 \right) \hat{\mathbf{a}}(k_1) = \hat{\mathbf{f}}_1(k_1), \tag{4.33}$$

where $\ddot{\mathbf{a}}(k_1) = \frac{\partial^2 \hat{\mathbf{a}}(k_1)}{\partial t^2}$ and

$$\begin{aligned}
 \mathbf{M} &= \int_A \mathbf{N}^T \rho \mathbf{N} \, dA, \\
 \mathbf{K}_0 &= \int_A \mathbf{B}_1^T \mathbf{D} \mathbf{B}_1 \, dA, \\
 \mathbf{K}_1 &= \int_A \mathbf{B}_1^T \mathbf{D} \mathbf{B}_2 \, dA - \int_A \mathbf{B}_2^T \mathbf{D} \mathbf{B}_1 \, dA, \\
 \mathbf{K}_2 &= \int_A \mathbf{B}_2^T \mathbf{D} \mathbf{B}_2 \, dA, \\
 \hat{\mathbf{f}}_1 &= \int_A \mathbf{N}^T \hat{\mathbf{b}} \, dA + \oint_{\Gamma_A} \mathbf{N}^T \hat{\mathbf{t}} \, d\Gamma_A.
 \end{aligned} \tag{4.34}$$

The terms \mathbf{M} , \mathbf{K}_0 , \mathbf{K}_1 and \mathbf{K}_2 are independent of the wavenumber k_1 and only need to be evaluated once. The load vector $\hat{\mathbf{f}}_1$ is in general, however, wavenumber dependent.

For a harmonic load $\hat{\mathbf{f}}_1(k_1, t) = \check{\mathbf{f}}_1(k_1)e^{i\omega t}$, the response is also harmonic, $\hat{\mathbf{a}}(k_1, t) = \check{\mathbf{a}}(k_1)e^{i\omega t}$ leading to,

$$(-\omega^2 \mathbf{M} + \mathbf{K}_0 + ik_1 \mathbf{K}_1 + k_1^2 \mathbf{K}_2) \check{\mathbf{a}}(k_1) = \check{\mathbf{f}}_1(k_1). \tag{4.35}$$

The system of equations given by Eq. (4.35) is solved for a set of discrete values of the wavenumber k_1 , and the nodal displacements in spatial domain $\mathbf{a}(x_1)$ are then obtained by a discrete inverse Fourier transform of $\check{\mathbf{a}}(k_1)$. When solved for N uniformly spaced wavenumbers ranging from $k_1 = -(\frac{N}{2} - 1)\Delta k_1$ to $k_1 = (\frac{N}{2})\Delta k_1$, the displacements $\mathbf{a}(x_1)$ are obtained for N uniformly spaced points on the x_1 -axis, spanning the length $2\pi/\Delta k_1$.

Formulation in a moving frame of reference

Contrary to the full 3D case discussed in Section 4.1.3, no additional integrals are introduced in the FE matrices in the case of 2.5D FE, when the fixed frame of reference is replaced by one moving at velocity v along the x_1 -axis. In wavenumber domain, this change of reference frames becomes particularly simple. Actually, the response is obtained in the moving frame of reference following the load at velocity v , by replacing ω in Eq. (4.35) by $\tilde{\omega} = \omega - k_1 v$. This is shown in Section 4.2.3 for the semi-analytical ground model and, by analogy, applies also to the case of FE in the wavenumber domain.

4.1.5 Perfectly matched layers

Special attention needs to be given to the fictitious boundaries of a truncated FE model in order to avoid spurious reflections of elastic waves. One efficient technique is to truncate the FE model by the use of Perfectly Matched Layers (PMLs) that absorb propagating waves with any angle of incidence. The idea behind PMLs is the introduction of a so called stretched

coordinate. Consider an elastic domain extending from $s = 0$ to $s = s_0$, and a PML region extending from $s = s_0$ to $s = s_t$, see Figure 4.2.

The stretched coordinate is defined as [20, 21]

$$\tilde{s} = \int_0^s \lambda_s(s) ds = s_0 + \int_{s_0}^s \lambda_s(s) ds, \quad (4.36)$$

where $\lambda_s(s)$ is a complex valued stretch function. Partial derivatives with respect to \tilde{s} are written as

$$\frac{\partial}{\partial \tilde{s}} = \frac{1}{\lambda_s(s)} \frac{\partial}{\partial s}. \quad (4.37)$$

Here, a formulation for PMLs in a 2.5D context [20] is considered. Stretching is applied to the x_2 - and x_3 -coordinates by introducing the partial derivatives of the stretched coordinates \tilde{x}_2 and \tilde{x}_3 into the equilibrium equation; see Eq. (4.8). Disregarding body forces and assuming steady-state response with angular frequency ω , this leads to the modified equilibrium equations

$$\hat{\nabla}^T \boldsymbol{\sigma} + \omega^2 \rho \mathbf{u} = 0, \quad (4.38)$$

where

$$\hat{\nabla}^T = \begin{bmatrix} \frac{\partial}{\partial x_1} & 0 & 0 & \frac{1}{\lambda_2} \frac{\partial}{\partial x_2} & \frac{1}{\lambda_3} \frac{\partial}{\partial x_3} & 0 \\ 0 & \frac{1}{\lambda_2} \frac{\partial}{\partial x_2} & 0 & \frac{\partial}{\partial x_1} & 0 & \frac{1}{\lambda_3} \frac{\partial}{\partial x_3} \\ 0 & 0 & \frac{1}{\lambda_3} \frac{\partial}{\partial x_3} & 0 & \frac{\partial}{\partial x_1} & \frac{1}{\lambda_2} \frac{\partial}{\partial x_2} \end{bmatrix}. \quad (4.39)$$

It is shown in [20] that by applying a Galerkin procedure and FE discretization, Eq. (4.35)

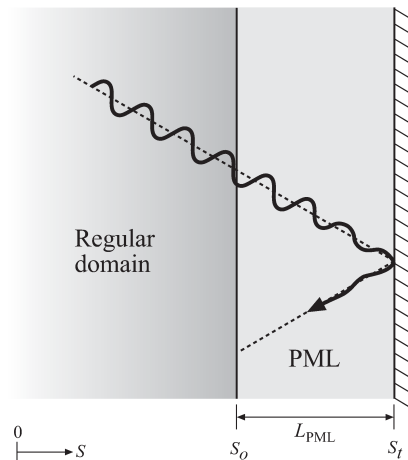


Figure 4.2: An incident wave being attenuated inside the PML.

applies with the following FE matrices for the PML region:

$$\begin{aligned}
\mathbf{M} &= \int_A \lambda_2 \lambda_3 \mathbf{N}^\top \rho \mathbf{N} \, dA, \\
\mathbf{K}_0 &= \int_A \lambda_2 \lambda_3 \mathbf{B}_1^\top \mathbf{D} \mathbf{B}_1 \, dA, \\
\mathbf{K}_1 &= \int_A \lambda_2 \lambda_3 \left(\mathbf{B}_1^\top \mathbf{D} \mathbf{B}_2 - \mathbf{B}_2^\top \mathbf{D} \mathbf{B}_1 \right) \, dA, \\
\mathbf{K}_2 &= \int_A \lambda_2 \lambda_3 \mathbf{B}_2^\top \mathbf{D} \mathbf{B}_2 \, dA, \\
\hat{\mathbf{f}}_1 &= \oint_{\Gamma_A} \lambda_2 \lambda_3 \mathbf{N}^\top \hat{\mathbf{t}} \, d\Gamma_A.
\end{aligned} \tag{4.40}$$

where $\mathbf{B}_1 = \mathbf{L}_1 \mathbf{N}$ and $\mathbf{B}_2 = \mathbf{L}_2 \mathbf{N}$ with

$$\mathbf{L}_1^\top = \begin{bmatrix} 0 & 0 & 0 & \frac{1}{\lambda_2} \frac{\partial}{\partial x_2} & \frac{1}{\lambda_3} \frac{\partial}{\partial x_3} & 0 \\ 0 & \frac{1}{\lambda_2} \frac{\partial}{\partial x_2} & 0 & 0 & 0 & \frac{1}{\lambda_3} \frac{\partial}{\partial x_3} \\ 0 & 0 & \frac{1}{\lambda_3} \frac{\partial}{\partial x_3} & 0 & 0 & \frac{1}{\lambda_2} \frac{\partial}{\partial x_2} \end{bmatrix}, \tag{4.41}$$

and

$$\mathbf{L}_2^\top = \begin{bmatrix} 1 & 0 & 0 & 0 & 0 & 0 \\ 0 & 0 & 0 & 1 & 0 & 0 \\ 0 & 0 & 0 & 0 & 1 & 0 \end{bmatrix}. \tag{4.42}$$

The stretching functions may be selected according to [20, 21] as

$$\lambda_j(x_j) = 1 + f_j^e(x_j) - i \frac{f_j^p(x_j)}{a_0}, \tag{4.43}$$

where $a_0 = \omega L_{\text{PML}}/c_s$ is a dimensionless frequency, with L_{PML} being a characteristic length chosen as the thickness of the PML and c_s is the shear wave velocity in the medium. The functions $f_j^e(x_j)$ and $f_j^p(x_j)$ are attenuation functions, attenuating evanescent (e) and propagating (p) waves, respectively. For $\lambda_2 = \lambda_3 = 1$, it is seen that the matrices in Eq. (4.40) for the PML region equal those in Eq. (4.34) for the regular domain. This should hold at the interface between the regular domain and the PML to avoid an impedance mismatch, i.e. the attenuation functions $f_j^e(x_j)$ and $f_j^p(x_j)$ should equal zero at the interface. It is shown in [20] that using a non-zero attenuation function for the evanescent waves shortens the wavelength of propagating waves inside the PML, necessitating a denser FE mesh.

4.2 THE LAYER TRANSFER MATRIX METHOD

4.2.1 General remarks

Using FEM to analyze wave propagation problems in (semi-)infinite media such as a layered half-space poses a number of potential problems. One issue is that, depending on the problem at hand, often a large computational domain is required. The required number of elements in the computational domain depends on the wavelengths. Typically 6–10 nodes are needed per wavelength to properly resolve a propagating wave. With increasing loading frequency the wavelengths decrease, and hence the number of required elements increases.

However, if visco-elastic properties and a horizontal stratification is assumed, see Figure 4.3, a so called Green's function (a fundamental solution) can be found analytically in frequency–wavenumber domain by the layer transfer matrix (LTM) method. When the solution has been established for a set of wavenumbers, it is brought back to frequency–space domain through a 2D discrete inverse Fourier transform.

The method briefly outlined below, was derived in [22, 23] and is further detailed in [24] and [14].

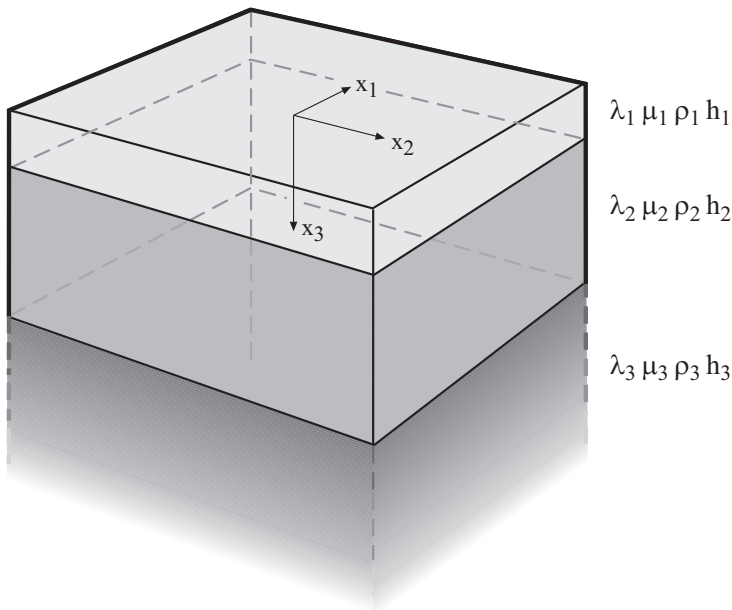


Figure 4.3: Horizontally layered half-space with visco-elastic properties.

4.2.2 Flexibility matrix of a horizontally layered half-space

First, a single soil layer with the Lamé parameters λ and μ and density ρ , is considered. Neglecting body forces, the equilibrium of the soil layer is governed by Navier equations

$$(\lambda + \mu) \frac{\partial^2 u_j}{\partial x_i \partial x_j} + \mu \frac{\partial^2 u_i}{\partial x_j \partial x_j} = \rho \frac{\partial^2 u_i}{\partial t^2}, \quad (4.44)$$

and some boundary conditions on the top and bottom of the layer. Here, $u_i = u_i(x_1, x_2, x_3, t)$ is the displacement in direction i .

Fourier transforming the Navier equations with respect to the horizontal coordinates and time, (x_1, x_2, t) , i.e.

$$U_i(k_1, k_2, x_3, \omega) = \int_{-\infty}^{\infty} \int_{-\infty}^{\infty} \int_{-\infty}^{\infty} u_i e^{-i(k_1 x_1 + k_2 x_2 + \omega t)} dx_1 dx_2 dt, \quad (4.45)$$

yields the Navier equations in frequency–wavenumber domain as

$$(\lambda + \mu) \check{\Delta} i k_1 + \mu \left(\frac{d^2}{dx_3^2} - k_1^2 - k_2^2 \right) U_1 = -\rho \omega^2 U_1, \quad (4.46a)$$

$$(\lambda + \mu) \check{\Delta} i k_2 + \mu \left(\frac{d^2}{dx_3^2} - k_1^2 - k_2^2 \right) U_2 = -\rho \omega^2 U_2, \quad (4.46b)$$

$$(\lambda + \mu) \frac{d\check{\Delta}}{dx_3} + \mu \left(\frac{d^2}{dx_3^2} - k_1^2 - k_2^2 \right) U_3 = -\rho \omega^2 U_3, \quad (4.46c)$$

where k_1 and k_2 are the wavenumbers in the direction of x_1 and x_2 , respectively, and ω is the frequency of vibration. Further, $\check{\Delta} = \check{\Delta}(k_1, k_2, x_3, \omega)$ is the Fourier transform, with respect to the horizontal coordinates and time, of the dilation $\Delta(x_1, x_2, x_3, t)$ defined in Eq. (3.6), i.e.

$$\check{\Delta}(k_1, k_2, x_3, \omega) = \int_{-\infty}^{\infty} \int_{-\infty}^{\infty} \int_{-\infty}^{\infty} \Delta e^{-i(k_1 x_1 + k_2 x_2 + \omega t)} dx_1 dx_2 dt = i k_1 U_1 + i k_2 U_2 + \frac{dU_3}{dx_3}. \quad (4.47)$$

Equation (4.46a) and Eq. (4.46b) are now multiplied by $i k_1$ and $i k_2$ respectively, and Eq (4.46c) is differentiated with respect to x_3 . The sum of the three equations lead to the ordinary homogeneous differential equation for the dilation

$$\left(\frac{d^2}{dx_3^2} - k_1^2 - k_2^2 + \frac{\omega^2}{c_p^2} \right) \check{\Delta} = \left(\frac{d^2}{dx_3^2} - k_1^2 - k_2^2 + k_p^2 \right) \check{\Delta} = \left(\frac{d^2}{dx_3^2} - \alpha_p^2 \right) \check{\Delta} = 0, \quad (4.48)$$

where c_p and k_p is the phase speed and wavenumber, respectively, of the P-wave and the following definitions have been made

$$\alpha_p^2 = k_1^2 + k_2^2 - k_p^2, \quad (4.49a)$$

$$\alpha_s^2 = k_1^2 + k_2^2 - k_s^2. \quad (4.49b)$$

Equation (4.48) has the solution

$$\check{\Delta}(k_1, k_2, x_3, \omega) = a_1 e^{\alpha_p x_3} + a_2 e^{-\alpha_p x_3}, \quad (4.50)$$

where a_1 and a_2 are integration constants. The solution for the dilation is inserted into Eqs. (4.46a–c), leading to three equations for the displacement amplitudes,

$$\frac{d^2 U_1}{dx_3^2} - \alpha_s^2 U_1 = -\left(\frac{\lambda}{\mu} + 1\right) i k_1 (a_1 e^{\alpha_p x_3} + a_2 e^{-\alpha_p x_3}), \quad (4.51a)$$

$$\frac{d^2 U_2}{dx_3^2} - \alpha_s^2 U_2 = -\left(\frac{\lambda}{\mu} + 1\right) i k_2 (a_1 e^{\alpha_p x_3} + a_2 e^{-\alpha_p x_3}), \quad (4.51b)$$

$$\frac{d^2 U_3}{dx_3^2} - \alpha_s^2 U_3 = -\left(\frac{\lambda}{\mu} + 1\right) \alpha_p (a_1 e^{\alpha_p x_3} - a_2 e^{-\alpha_p x_3}). \quad (4.51c)$$

The solutions to Eqs.(4.51) can be written as

$$U_1 = b_1 e^{\alpha_s x_3} + b_2 e^{-\alpha_s x_3} + b_3 e^{\alpha_p x_3} + b_4 e^{-\alpha_p x_3}, \quad (4.52a)$$

$$U_2 = c_1 e^{\alpha_s x_3} + c_2 e^{-\alpha_s x_3} + c_3 e^{\alpha_p x_3} + c_4 e^{-\alpha_p x_3}, \quad (4.52b)$$

$$U_3 = d_1 e^{\alpha_s x_3} + d_2 e^{-\alpha_s x_3} + d_3 e^{\alpha_p x_3} + d_4 e^{-\alpha_p x_3}. \quad (4.52c)$$

It can be shown that only six of the integration constants ($a_1, a_2, b_1, b_2, c_1, c_2$) are independent [14], and that the remaining constants are

$$\begin{aligned} b_3 &= -\frac{i k_1}{k_p^2} a_1, & b_4 &= -\frac{i k_1}{k_p^2} a_2, & c_3 &= -\frac{i k_2}{k_p^2} a_1, & c_4 &= -\frac{i k_2}{k_p^2} a_2, \\ d_1 &= -\left(\frac{i k_1}{\alpha_s} b_1 + \frac{i k_2}{\alpha_s} c_1\right), & d_2 &= \frac{i k_1}{\alpha_s} b_2 + \frac{i k_2}{\alpha_s} c_2, & d_3 &= -\frac{\alpha_p}{k_p^2} a_1, & d_4 &= \frac{\alpha_p}{k_p^2} a_2. \end{aligned} \quad (4.53)$$

Fourier transforming the stress tensor, $\sigma_{jk}(x_1, x_2, x_3, t)$ defined in Eq. (3.4), with respect to the horizontal coordinates and time yields

$$\check{\sigma}_{jk}(k_1, k_2, x_3, \omega) = \int_{-\infty}^{\infty} \int_{-\infty}^{\infty} \int_{-\infty}^{\infty} \sigma_{jk} e^{-i(k_1 x_1 + k_2 x_2 + \omega t)} dx_1 dx_2 dt. \quad (4.54)$$

For a known displacement field (U_1, U_2, U_3), the corresponding traction stresses ($\check{\sigma}_{13}, \check{\sigma}_{23}, \check{\sigma}_{33}$) are calculated as

$$\check{\sigma}_{13} = \mu \left(\frac{dU_1}{dx_3} + i k_1 U_3 \right), \quad (4.55a)$$

$$\check{\sigma}_{23} = \mu \left(\frac{dU_2}{dx_3} + i k_2 U_3 \right), \quad (4.55b)$$

$$\check{\sigma}_{33} = \lambda (i k_1 U_1 + i k_2 U_2 + \frac{dU_3}{dx_3}) + 2\mu \frac{dU_3}{dx_3}. \quad (4.55c)$$

The displacements and the traction stresses are collected in a vector \mathbf{S}

$$\mathbf{S}(k_1, k_2, x_3, \omega) = [\mathbf{U} \quad \mathbf{P}]^T = [U_1 \quad U_2 \quad U_3 \quad \check{\sigma}_{13} \quad \check{\sigma}_{23} \quad \check{\sigma}_{33}]^T. \quad (4.56)$$

For any layer j , the vector \mathbf{S}^j can be written as

$$\mathbf{S}^j(k_1, k_2, x_3, \omega) = \mathbf{A}^j(k_1, k_2, \omega) \mathbf{E}^j(k_1, k_2, x_3, \omega) \mathbf{b}^j. \quad (4.57)$$

The vector \mathbf{b}^j contains the integration constants governed by the boundary conditions at the top and the bottom of the layer,

$$\mathbf{b}^j = [a_1 \quad b_1 \quad c_1 \quad a_2 \quad b_2 \quad c_2]^T. \quad (4.58)$$

The matrix \mathbf{E}^j is defined as

$$\mathbf{E}^j(k_1, k_2, x_3, \omega) = \begin{bmatrix} e^{\alpha_p x_3} & 0 & 0 & 0 & 0 & 0 \\ 0 & e^{\alpha_s x_3} & 0 & 0 & 0 & 0 \\ 0 & 0 & e^{\alpha_s x_3} & 0 & 0 & 0 \\ 0 & 0 & 0 & e^{-\alpha_p x_3} & 0 & 0 \\ 0 & 0 & 0 & 0 & e^{-\alpha_s x_3} & 0 \\ 0 & 0 & 0 & 0 & 0 & e^{-\alpha_s x_3} \end{bmatrix}. \quad (4.59)$$

$\mathbf{A}^j(k_1, k_2, \omega)$ is a (6×6) matrix, where the entries follow from Eqs. (4.52–4.53) and Eq. (4.55). At the top of the j :th layer \mathbf{E}^j is the identity matrix. Now, using the superscript 0 and 1 to refer to the top ($x_3 = 0$) or bottom ($x_3 = h$) of the layer, the vector \mathbf{S}^j is, respectively

$$\mathbf{S}^{j,0} = \mathbf{A}^j \mathbf{E}^{j,0} \mathbf{b}^j = \mathbf{A}^j \mathbf{b}^j, \quad (4.60a)$$

$$\mathbf{S}^{j,1} = \mathbf{A}^j \mathbf{E}^{j,1} \mathbf{b}^j. \quad (4.60b)$$

The vector \mathbf{b}^j of integration constants can be eliminated by expressing the vector \mathbf{S}^j on either side of the layer in terms of the vector \mathbf{S}^j on the other side, e.g.

$$\mathbf{S}^{j,1} = \mathbf{A}^j \mathbf{E}^{j,1} \mathbf{b}^j = \mathbf{A}^j \mathbf{E}^{j,1} (\mathbf{A}^j)^{-1} \mathbf{S}^{j,0} = \mathbf{T}^j \mathbf{S}^{j,0}, \quad (4.61)$$

where

$$\mathbf{T}^j = \mathbf{A}^j \mathbf{E}^{j,1} (\mathbf{A}^j)^{-1}, \quad (4.62)$$

is a propagator matrix for layer j . Due to continuity of displacements and tractions over interfaces between layers, several layers can be assembled in the same manner, forming a relationship between the displacement and stresses at the top of the stratum (layer 1) and at the bottom of the stratum (layer J) as

$$\mathbf{S}^{J,1} = \mathbf{T}^J \mathbf{T}^{J-1} \mathbf{T}^{J-2} \dots \mathbf{T}^1 \mathbf{S}^{1,0}. \quad (4.63)$$

This is the layer transfer matrix approach by Thomson and Haskell [25, 26]. For certain frequencies and stratifications, this method suffers from loss-of-precision. To circumvent these problems, in the current work, the different soil layers are assembled in an orthonormalization procedure [27]. The details are left out, and the interested reader is instead referred to [27]. With known boundary conditions at the lowest interface, a relationship between the traction and the displacement at the surface can be obtained,

$$\mathbf{U}^0(k_1, k_2, \omega) = \mathbf{G}(k_1, k_2, \omega) \mathbf{P}^0(k_1, k_2, \omega), \quad (4.64)$$

where

$$\mathbf{G} = \mathbf{G}(k_1, k_2, \omega) = \begin{bmatrix} G_{11} & G_{12} & G_{13} \\ G_{21} & G_{22} & G_{23} \\ G_{31} & G_{32} & G_{33} \end{bmatrix}, \quad (4.65)$$

is the Green's function for the layered half-space. The Green's function $\mathbf{G}(k_1, k_2, \omega)$, when multiplied by a traction vector for the surface $\mathbf{P}^0(k_1, k_2, \omega)$, gives the displacement vector $\mathbf{U}^0(k_1, k_2, \omega)$ on the surface. The displacement vector is obtained in Cartesian space through a double inverse Fourier transform

$$u_i(x_1, x_2, x_3 = 0, \omega) = \frac{1}{4\pi^2} \int_{-\infty}^{\infty} \int_{-\infty}^{\infty} U_i e^{i(k_1 x_1 + k_2 x_2)} dk_1 dk_2. \quad (4.66)$$

In practice, Eq. (4.64) is evaluated for a set of discrete values of k_1 and k_2 , and Eq. (4.66) is evaluated using an inverse Fast Fourier Transform (iFFT) algorithm. The Green's function is calculated for $N \times N$ uniformly spaced wavenumbers (k_1, k_2) ranging from $k_i = -(\frac{N}{2} - 1)\Delta k$ to $k_i = (\frac{N}{2})\Delta k$. The displacements are then obtained in $N \times N$ uniformly spaced points in Cartesian space (x_1, x_2) , spanning the area $\frac{2\pi}{\Delta k} \times \frac{2\pi}{\Delta k}$. Hence, the spacing between the points where the results are obtained is governed by the wavenumber increment and the number of points used to calculate the Green's function. To obtain accurate results, $\max(k)$ must be high enough to ensure that either $\mathbf{G} \approx 0$ or $\mathbf{P} \approx 0$ for $k > \max(k)$, whereas Δk must be small enough to ensure that high gradients in either \mathbf{G} or \mathbf{P} are resolved.

There are other formulations to obtain the Green's function of a horizontally layered elastic half-space than the LTM approach discussed above. In the Stiffness Matrix Method (SMM) by Kausel and Roesset [28], the Thomson-Haskell layer transfer matrices are used to derive a stiffness matrix for each soil layer, and the stiffness matrices for all layers are assembled into a global stiffness matrix for the whole soil profile. The layer stiffness matrices are formulated in wavenumber domain for the horizontal coordinates, while the depth coordinate is kept in spatial domain, like in the original LTM method. The SMM was first formulated for 2D problems but has since been expanded to cover 3D problems [29]. A variant of the SMM is presented in detail in appended Paper F.

Another method is the Thin Layer Method (TLM) [28,30], which is a stiffness matrix approach where a linear variation of the displacements is assumed in the depth direction. Hence, each soil layer is split into a number of thin layers to make the assumption of linear displacement variations in the depth direction acceptable.

4.2.3 Formulation in a moving frame of reference

In the same manner as for the FE formulation in a moving frame of reference, the coordinate transformation

$$(\tilde{x}_1, \tilde{x}_2, \tilde{x}_3) = (x_1 - vt, x_2, x_3), \quad (4.67)$$

is introduced, where v is the vehicle speed. Applying the transformation to the Navier equations Eq. (4.44) yields

$$(\lambda + \mu) \frac{\partial^2 \tilde{u}_j}{\partial \tilde{x}_i \partial \tilde{x}_j} + \mu \frac{\partial^2 \tilde{u}_i}{\partial \tilde{x}_j \partial \tilde{x}_j} = \rho \left(\frac{\partial^2 \tilde{u}_i}{\partial t^2} - 2v \frac{\partial^2 \tilde{u}_i}{\partial t \partial \tilde{x}_1} + v^2 \frac{\partial^2 \tilde{u}_i}{\partial \tilde{x}_1^2} \right), \quad (4.68)$$

where $\tilde{u}_i = \tilde{u}_i(\tilde{x}_1, \tilde{x}_2, \tilde{x}_3, t)$ is the displacement in the moving frame of reference. Fourier transforming these equations with respect to the horizontal coordinates and time, $(\tilde{x}_1, \tilde{x}_2, t)$, yields the Navier equations in frequency–wavenumber domain as [14]

$$(\lambda + \mu) \tilde{\Delta} i \tilde{k}_1 + \mu \left(\frac{\partial^2}{\partial \tilde{x}_3^2} - \tilde{k}_1^2 - \tilde{k}_2^2 \right) \tilde{U}_1 = \rho (-\omega^2 + 2v\omega \tilde{k}_1 - v^2 \tilde{k}_1^2) \tilde{U}_1, \quad (4.69a)$$

$$(\lambda + \mu) \tilde{\Delta} i \tilde{k}_2 + \mu \left(\frac{\partial^2}{\partial \tilde{x}_3^2} - \tilde{k}_1^2 - \tilde{k}_2^2 \right) \tilde{U}_2 = \rho (-\omega^2 + 2v\omega \tilde{k}_1 - v^2 \tilde{k}_1^2) \tilde{U}_2, \quad (4.69b)$$

$$(\lambda + \mu) \frac{\partial \tilde{\Delta}}{\partial \tilde{x}_3} + \mu \left(\frac{\partial^2}{\partial \tilde{x}_3^2} - \tilde{k}_1^2 - \tilde{k}_2^2 \right) \tilde{U}_3 = \rho (-\omega^2 + 2v\omega \tilde{k}_1 - v^2 \tilde{k}_1^2) \tilde{U}_3. \quad (4.69c)$$

Here, a tilde is used to emphasize that a variable is expressed in terms of the moving $(\tilde{x}_1, \tilde{x}_2, \tilde{x}_3)$ coordinate system, i.e.

$$\tilde{U}_i(\tilde{k}_1, \tilde{k}_2, \tilde{x}_3, \omega) = \int_{-\infty}^{\infty} \int_{-\infty}^{\infty} \int_{-\infty}^{\infty} \tilde{u}_i e^{-i(\tilde{k}_1 \tilde{x}_1 + \tilde{k}_2 \tilde{x}_2 + \omega t)} d\tilde{x}_1 d\tilde{x}_2 dt, \quad (4.70)$$

where \tilde{k}_1 and \tilde{k}_2 are the wavenumbers in the direction of \tilde{x}_1 and \tilde{x}_2 , respectively. Now, with

$$\tilde{\omega} = \omega - \tilde{k}_1 v, \quad (4.71)$$

Eq. (4.69) is written as

$$(\lambda + \mu) \tilde{\Delta} i \tilde{k}_1 + \mu \left(\frac{d^2}{d\tilde{x}_3^2} - \tilde{k}_1^2 - \tilde{k}_2^2 \right) \tilde{U}_1 = -\rho \tilde{\omega}^2 \tilde{U}_1, \quad (4.72a)$$

$$(\lambda + \mu) \tilde{\Delta} i \tilde{k}_2 + \mu \left(\frac{d^2}{d\tilde{x}_3^2} - \tilde{k}_1^2 - \tilde{k}_2^2 \right) \tilde{U}_2 = -\rho \tilde{\omega}^2 \tilde{U}_2, \quad (4.72b)$$

$$(\lambda + \mu) \frac{d\tilde{\Delta}}{d\tilde{x}_3} + \mu \left(\frac{d^2}{d\tilde{x}_3^2} - \tilde{k}_1^2 - \tilde{k}_2^2 \right) \tilde{U}_3 = -\rho \tilde{\omega}^2 \tilde{U}_3. \quad (4.72c)$$

These are the same equations as in Eq. (4.46). Hence, the solution procedure outlined in the previous subsection is applicable also in the moving frame of reference, with the difference being that the frequency is wavenumber dependent as given by Eq. (4.71). The frequency $\tilde{\omega}$ is the frequency of vibration of a material point.

4.2.4 Dispersion curves

Figure 2.5 in Section 2.3.1 shows the dispersion relation for the P-, S- and Rayleigh waves of the two materials of a layered soil profile, displayed over a contour plot showing the amplitude

of vertical response due to a vertical harmonic excitation of the soil surface. This contour plot was created by plotting the (absolute) value of the Green's function matrix element G_{33} , see Eq. (4.65). High values indicate combinations of frequency and wavenumber where a vertical excitation of the soil surface leads to a high vertical response, which indicate the presence of propagating waves. Hence, such a contour plot gives an indication of the dispersion curves of the full soil profile.

The dispersion curves of a layered soil profile can be calculated from an eigenvalue problem formulated using the layer transfer matrices. The problem comes down to finding the wavenumbers and frequencies for which the determinant of a matrix $\mathbf{D}(k_1, k_2 = 0, \omega)$, being a function of the layer transfer matrices (see [31] for details), becomes zero, i.e.

$$\det(\mathbf{D}(k_1, 0, \omega)) = 0. \quad (4.73)$$

The roots to this equation can only be found through search techniques. Starting at a given (low) frequency, the determinant is calculated for a range of wavenumbers. When the determinant is close to zero or changes signs for two consecutive wavenumbers, a refinement of the wavenumber spacing is made and the determinant is calculated again. When the determinant is sufficiently close to zero, this indicates the presence of a propagating wave. The process is repeated for the next frequency increment, and when a propagating wave is found it can either be the continuation of a wave found in the previous frequency increment or it can mark the "cut-on" of a higher order mode. Figure 4.4, from appended Paper D, shows the dispersion curves of a layered ground consisting of a very soft clay layer over a stiffer half-space, obtained in this manner. The dispersion curve of a simplified track model is also indicated in the figure, and from the intersection point of the track and ground dispersion curves an estimation of the so-called critical velocity can be inferred.

There are other more refined methods that can be employed to find the roots to Eq. (4.73) and to trace the continuation of identified dispersion curves for increasing frequencies. Such a method is discussed in appended Paper F.

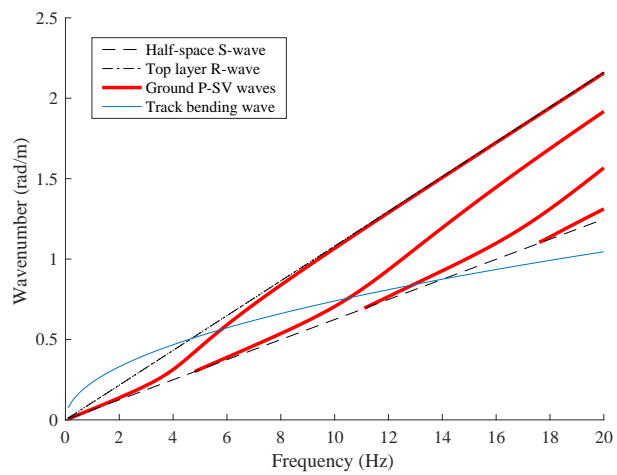


Figure 4.4: Dispersion curves of a layered half-space (Figure 7 in appended Paper D).

5 Predicting Vibrations from Railway Traffic

5.1 GENERAL REMARKS

A prediction model should, based on given input conditions, provide as output an estimation of some sought quantity. Such a model can be empirical, e.g. by using some statistical method of analyzing data, the model predicts the response quantity for given input conditions based on a large set of previously collected data (conditions and response quantities). Generally, such empirical models do not explain the underlying physics of the predicted response, but rely on that the previously collected data covers all the conditions for the situation to be predicted. Nonetheless, such models can be useful and provide satisfactory results in several situations.

Here, however, focus will be on computational methods with the aim of simulating the generation and propagation of ground-borne vibrations, specifically those generated by railway traffic. For a computational model to provide accurate predictions, it needs detailed descriptions of the source (i.e. the train and the excitation mechanisms), the transmission path, and the receiver. The excitation mechanisms are briefly discussed in Section 5.2, and a brief overview of various calculation methods and strategies are given in Section 5.3. In Section 5.4 the track models developed and used in the appended papers are described.

5.2 EXCITATION MECHANISMS

The vibrations generated by a train moving along a railway track can be divided into a quasi-static contribution and a dynamic contribution. The quasi-static contribution refers to the effect of the moving constant dead load of the train that causes a deflection of the soil surface. As described in Section 2.3, this moving static deflection of the soil surface is experienced as a transient vibration by a stationary observer next to the track. The dynamic contribution, however, is much more complex and originates from several different mechanisms.

Since the rail is not perfectly smooth, dynamic contact forces arise in the wheel–rail interfaces as

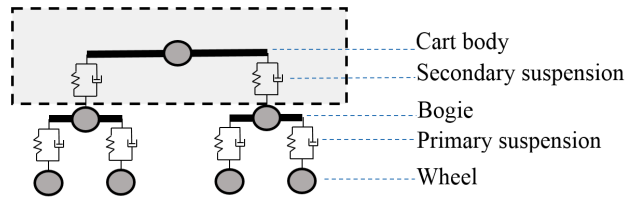


Figure 5.1: Planar vehicle model consisting of lumped masses, springs and dashpots.

the vehicle moves over the rough rail surface. The frequency content of these dynamic contact forces depends on the vehicle speed. A specific rail unevenness component of wavelength λ , generates a dynamic load at frequency $f = v/\lambda$ where v is the vehicle speed. For example, for a vehicle moving at $v = 30$ m/s, dynamic excitation in the frequency range 1–80 Hz result from unevenness wavelengths in the range 0.375–30 m.

Similarly, the wheels are not perfectly round. Out-of-roundness and uneven wear causes periodic dynamic wheel–rail contact forces. These can be severe in the presence of so called wheel-flats. A wheel-flat occurs when the wheel locks during braking or due to slippery conditions, causing a flat spot on the wheel that generates large impact forces for each revolution.

Further, dynamic wheel–rail forces are generated by changes in the conditions under the rail along the track, e.g. varying soil- or ballast stiffness. In addition, in most track systems the rail is discretely supported by sleepers, causing a variation of the rail stiffness over the span of one sleeper bay which in turn generates a dynamic excitation at the sleeper-passing frequency $f = v/d$, where d is the sleeper spacing. Other excitation mechanisms include impact excitation due to switches, crossings, joints, etc.

5.3 NUMERICAL MODELING

The calculation of the train–track interaction forces are often carried out using simple 2D multi-body vehicle models where the features most important for the dynamic behavior, such as unsprung/sprung masses and primary/secondary suspensions, are included, see Figure 5.1. The vehicle model is connected to a model of the railway track that should provide an accurate stiffness of the rail, since this stiffness strongly influences the wheel–rail contact forces. Conventional ballasted tracks usually consist of rails supported by rail pads, sleepers and ballast. In slab tracks, the rail can either be continuously or discretely supported. Track models are often 2D finite element models, comprising Bernoulli–Euler or Timoshenko beams representing the rail. In the case of conventional ballasted tracks, the rail is connected to a series of discrete springs, dashpots and masses, representing rail pads, sleepers, ballast and subsoil [32–35]. In models of slab tracks, the rail is usually connected to beam representations of the slab and support layer, with spring and dashpot connections between the layers [36–38].

Analyses of such track models are typically performed in time domain, in a fixed Cartesian

coordinate system. Time-domain analyses allow for inclusion of non-linear behavior, for example in the contact condition between the vehicle and the rail. Such models have been used by many different authors to study different mechanisms such as rail unevenness, wheel flats, transition zones, etc. These analyses may be used for studying effects on the track or riding comfort in the vehicle, but the forces obtained in any of the interfaces (e.g. wheel–rail or track–subsoil) may also be used in a subsequent model to study the ground-vibrations generated by these forces, see e.g. [35, 39, 40]. Some authors [36, 41–43] have used similar track models formulated in a moving frame of reference following the vehicle at a fixed speed, by applying a Galilean coordinate transformation to the governing equations. A benefit of such an approach is that the vehicle never leaves the computational domain, enabling the use of a smaller model. Also, the wheel–rail contact formulation becomes less complicated because the wheels interact with the same rail elements throughout the analysis. The coordinate transformation implies that the track is invariant in the track direction, so for example discrete rail supports are modeled as being continuously distributed and track stiffness variation cannot be treated in a straight-forward manner. However, it has been shown [44] that the contribution to the interaction forces, and the resulting free-field vibrations, by the track stiffness variation is much smaller than the contribution from track unevenness. From the excitation mechanisms described in Section 5.2, track unevenness is the one most often accounted for in predictions of ground-borne vibrations.

The wave propagation in the ground resulting from the dynamic loads on the track can be calculated using numerous numerical techniques. FEM offers a large flexibility regarding modeling capabilities in terms of geometrical conditions and material properties. However, the need for discretizing a large soil volume, under and between the source and the receiver, can generate very large systems of equations that are time-consuming or practically impossible to solve. The maximum element size is governed by the wavelengths of the propagating waves, and for moving loads these wavelengths decrease in front of the load, requiring a finer mesh. Furthermore, special techniques need to be employed at the fictitious boundaries of the truncated soil volume to avoid spurious reflections of waves. So called impedance boundary conditions [45], which are basically tuned dashpot dampers, can be used to cancel out P- and S-waves impinging orthogonally to the boundary—however, surface waves and P- and S-waves impinging with an angle are partially reflected, compromising the solution, especially close to the truncated ends of the domain. A more recent technique to avoid reflecting waves is the use of a so called perfectly matched layer (PML), which uses a complex coordinate stretching to artificially dampen the incoming waves over a few elements [21].

The boundary element method (BEM) overcomes some of the shortcomings of FEM. For instance, non-reflecting boundaries are inherent to the governing boundary integrals. Furthermore, the soil interior domain does not need to be modeled explicitly, if only the response of the soil surface is required. BEM uses a Green's function (fundamental solution) as a weight function. In the simplest case, the Green's function of a homogeneous full-space is used, requiring discretization of (introduction of elements to) every soil layer interface. Assembling the system matrices is a much more complex and time-consuming procedure than in FEM. For every node of the model, the Green's function for displacement and traction are integ-

rated over the entire boundary. Due to singularities of the Green's functions, this matter is not straight-forward. Furthermore, the system matrices become fully populated. 3D models employing FE or/and BE have been used by a number of researchers to study train-induced vibrations [46–49], and can be used for both time domain and frequency domain analysis.

By assuming constant geometry in the load travel direction, computational savings can be made by applying a so called 2.5D technique, where only a cross section of the soil and railway track is discretized. By means of a Fourier transform with respect to time and the track direction coordinate, a sequence of 2D problems are solved for a number of discrete wavenumbers, and the 3D response is recovered by an inverse Fourier transform of the wavenumber domain response. Such a methodology has been applied to both FE and BE formulations, and mixed BE–FE models, by several authors, see e.g. [18, 19, 50–53].

If the soil is assumed to consist of horizontally oriented visco-elastic layers, a (semi-)analytical approach can be used to obtain the response for a given load in frequency–wavenumber domain, by applying a Fourier transform on the governing equations with respect to the horizontal coordinates and time, as described in Section 4.2. The response is then obtained in spatial coordinates by an inverse Fourier transform of the wavenumber domain solution. Generally, the solution can be obtained at rather large distances from the load, at a much lower computational effort than with FEM or BEM. Figures 2.5–2.8 were produced using this technique. A track model can be incorporated into such a semi-analytical model [22, 23, 31, 54], and the effect of a vehicle running over an uneven rail can be analyzed in frequency domain by describing the unevenness in terms of its wavenumber content and summing the responses from the excitation from a number of discrete wavenumbers, in the moving frame of reference.

While 2.5D models allow for fast computation of the 3D ground response, the necessary assumption of geometrical invariance in the track direction makes it impossible to include a regular building in the model. Therefore, a common approach to calculate building responses to train-induced ground vibrations is to first calculate the free-field ground response at the location of the building and then use this free-field response to excite the building in a separate model [55–61]. This is also the approach followed in appended Paper E.

Regardless of the choice of numerical method, large uncertainties are generally associated with predicted ground-borne vibration levels, due to the limited knowledge of the values of the governing parameters. In addition, simplifications are necessary to produce practically feasible models. However, if the most important characteristics of the vibration excitation and transmission path can be identified and modeled, numerical predictions can nevertheless be meaningful for evaluating different designs and mitigation measures.

5.4 TRACK MODELS IN APPENDED PAPERS

As discussed in Section 5.3, several numerical techniques can be employed to predict the ground vibrations next to a railway track. In the appended Papers A–C a 3D model that combines the FE method and the LTM method, in a moving frame of reference following the vehicle, is utilized. In appended Paper D a 2.5D FE–PML model is used for modeling both the track and the surrounding soil. Further, a model employing 2.5D FE for the railway track and the LTM method for the soil is presented in appended Paper E. The computational code for these models were implemented in FORTRAN by the author, utilizing Intel Math Kernel Library [62] for some of the mathematical operations. Below follows a thorough description and a comparison of these models for a specific case.

For the following presentation of the different models, a slab track consisting of a concrete slab, rails and rail pads, is considered. The slab width and thickness is $w = 3.0$ m and $t = 0.2$ m, respectively. The track is assumed to rest on a 14 m deep stiff clay till layer overlaying a half-space. The soil conditions corresponds to a site near the research facility MAX IV Laboratory in Lund, Sweden. The track, however, is hypothetical. All models are established in the moving reference frame following the load, implying that the track and soil are assumed invariant in the running direction. Hence, the discrete rail supports are considered as distributed. The track and soil properties are given in Tables 5.1 and 5.2, respectively.

Here, the rail displacements and the ground surface response 10 m from the track center line is studied, as a harmonic point load runs on the track with a velocity of $v = 30$ m/s (= 108 km/h). Two frequencies of excitation are considered, $f = 40$ Hz and $f = 80$ Hz.

The 3D model used in the appended Papers A–C is briefly recapitulated in Section 5.4.1. The coupled 2.5D model, used in Paper E, is described in Section 5.4.2. The 2.5D FE–PML model, used in Paper D, is described in Section 5.4.3. Finally, the response obtained with the three different models for the particular case studied here is presented and discussed in Section 5.4.4.

Table 5.1: Track properties.

	Parameter	Value
Rail	Mass (kg/m)	60
	Young's modulus (GPa)	210
	Second moment of inertia (m ⁴)	3.217×10^{-5}
	Loss factor (-)	0.01
	Track gauge (m)	1.435
Rail	Stiffness (MN/m ²)	250
pads	Damping (kNs/m ²)	22.5
Slab	Density (kg/m ³)	2500
	Young's modulus (GPa)	30
	Poisson's ratio	0.2
	Width (m)	3.0
	Thickness (m)	0.2
	Loss factor (-)	0.04

Table 5.2: Ground properties.

Layer	Parameter	Value
Soil	Depth (m)	14
	Young's modulus (MPa)	475
	Poisson's ratio	0.48
	Density (kg/m ³)	2125
	Loss factor (-)	0.14
Bedrock (half-space)	Depth (m)	∞
	Young's modulus (MPa)	8800
	Poisson's ratio	0.40
	Density (kg/m ³)	2600
	Loss factor (-)	0.04

5.4.1 A coupled 3D track–soil model

In this specific example, the track slab is modeled using 3D solid elements, following the formulation in the moving frame of reference as described in Section 4.1.3. The soil is described by a dynamic stiffness matrix for a set of nodes where the slab interacts with the ground. These nodes are referred to as soil-structure interaction (SSI) nodes.

The soil dynamic stiffness matrix is derived from the Green's function of the layered soil in the moving reference frame, as described in Section 4.2.3, and can be interpreted as a super-element to which the track structure is coupled. The total system of equations is then solved and the forces in the slab–soil interface, i.e. the SSI nodes, are obtained. Finally, the Green's function is used for establishing the total displacement response in the free-field as a summation of contributions from each individual SSI node.

FE model of track

The track slab is modeled using 3D solid continuum elements, for which the formulation in a moving frame of reference was given in Section 4.1.3. Fully integrated linear brick elements with 8 nodes and 3 translational DoFs per node are used. Six elements are used in the thickness direction of the slab, and an element length of $0.15 \text{ m} \times 0.15 \text{ m}$ in the (x_1, x_2) -plane is used. The rails are represented by Bernoulli–Euler beam elements with two nodes, each node having a rotational DoF and a vertical translational DoF. The beam elements are coupled to the solid elements through visco-elastic interface elements, composed of continuously distributed springs and dashpots, representing the rail pads. The formulation of these elements are presented in both Paper A and Paper C. Damping is introduced into the slab and the rails by the use of complex Young's moduli, $E^* = E(1 + i\eta)$, where η is the loss factor, leading to a frequency independent damping as described in Section 3.2.3. Assuming a harmonic excitation with the

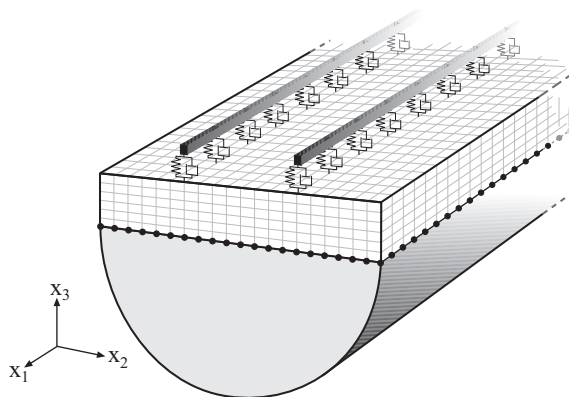


Figure 5.2: Illustration of 3D FE mesh of a railway track coupled to a horizontally layered half-space.

angular frequency $\omega = 2\pi f$, the governing equations for the track can be written as

$$(-\omega^2 \mathbf{M}_t + i\omega \mathbf{C}_t + \mathbf{K}_t) \hat{\mathbf{u}}_t = \mathbf{D}_t(\omega) \hat{\mathbf{u}}_t = \hat{\mathbf{f}}_t, \quad (5.1)$$

where \mathbf{M}_t , \mathbf{C}_t and \mathbf{K}_t is the mass, damping and (complex) stiffness matrix, respectively, for the total track system (excluding the underlying soil). Further, $\mathbf{D}_t(\omega)$ is the corresponding dynamic stiffness matrix. The vector $\hat{\mathbf{u}}_t$ contains the displacements in the track DoFs, and the vector $\hat{\mathbf{f}}_t$ contains the externally applied loads.

Soil dynamic stiffness matrix

Assuming that the track structure contains m nodes on the soil interface, each with three translational DoFs, a $(3m \times 3m)$ dynamic stiffness matrix $\mathbf{D}_s(f)$ for the soil super-element, i.e. the m SSI nodes, is to be determined. Here, advantage is taken of the assumed invariability of the soil in the horizontal directions.

The first step involves calculating the soil response due to a unit harmonic load, with frequency f , moving along the x_1 -axis on the soil surface with velocity v . The unit load is evenly distributed over a rectangular area, the size of which is chosen as equal to the element size of the connecting track. Hence, with reference to Sections 4.1.3 and 4.2.3, the traction is distributed over a rectangular area centered in the origin of the moving coordinate system $(\tilde{x}_1, \tilde{x}_2, \tilde{x}_3)$, as

$$p_j(\tilde{x}_1, \tilde{x}_2, \omega) = \begin{cases} 1/(4ab), & -a < \tilde{x}_1 < a, \quad -b < \tilde{x}_2 < b \\ 0, & \text{otherwise} \end{cases}, \quad (5.2)$$

where $2a$ and $2b$ is the width in the \tilde{x}_1 and \tilde{x}_2 directions, respectively. In the current example, $2a = 2b = 0.15$. In wavenumber domain the traction becomes

$$\hat{p}_j(\tilde{k}_1, \tilde{k}_2, \omega) = \frac{\sin(\tilde{k}_1 a)}{\tilde{k}_1 a} \frac{\sin(\tilde{k}_2 b)}{\tilde{k}_2 b}. \quad (5.3)$$

The soil surface displacement response is calculated in frequency–wavenumber domain $(\tilde{k}_1, \tilde{k}_2, \omega)$, for $N \times N$ wavenumbers, using the LTM method in accordance with Section 4.2. After a discrete inverse Fourier transform the soil surface response, in terms of complex displacements $(\tilde{u}_1, \tilde{u}_2, \tilde{u}_3)$, is obtained in $N \times N$ points in the moving coordinate system $(\tilde{x}_1, \tilde{x}_2, \tilde{x}_3)$. In the moving frame of reference, the response in each point of the soil surface is harmonic with the frequency of the excitation. The area spanned by the response surface depend on the wavenumber increment, and the spacing between the response points depend on the number of points N , as described in Section 4.2.2. In the current example $N = 4096$ and $\max(\tilde{k}_1) = \max(\tilde{k}_2) = 2\pi/0.15$ rad/m, which has been found to be sufficient in the case studied here. Figure 5.3 shows a response surface of the vertical displacement due to a vertical unit harmonic load.

The soil surface displacements are calculated separately for a unit load in each of the three $(\tilde{x}_1, \tilde{x}_2, \tilde{x}_3)$ directions, i.e. nine response surfaces are obtained, here denoted $U(i, j, \tilde{x}_1, \tilde{x}_2)$

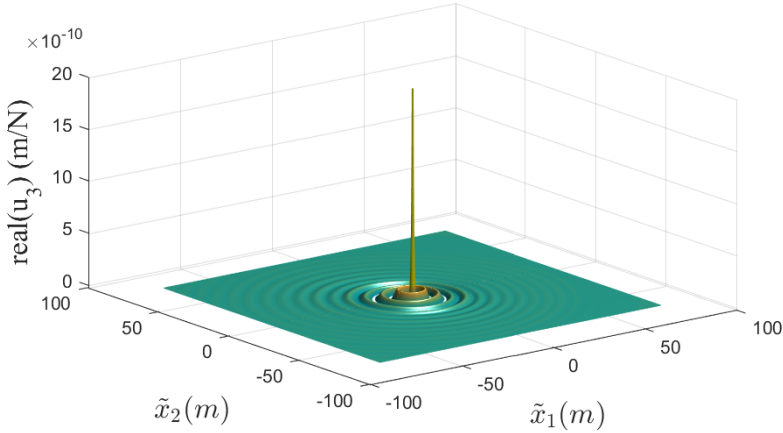


Figure 5.3: Response surface showing the real part of the vertical displacement due to a rectangular vertical unit load with $f = 40$ Hz and $v = 30$ m/s.

where $i (= 1, 2, 3)$ is the load direction and $j (= 1, 2, 3)$ is the displacement direction. A $(3m \times 3m)$ flexibility matrix for the m SSI nodes, $\mathbf{H}_s(\omega)$, is established by interpolating from the nine response surfaces.

Let DoF q_j denote the displacement in direction j of node q . Similarly, let DoF r_i denote the displacement in direction i of node r . Element (q_j, r_i) of the flexibility matrix contains the complex displacements in DoF q_j due to a unit load in DoF r_i . Letting $\Delta\tilde{x}_1$ and $\Delta\tilde{x}_2$ denote the distance between nodes q and r in the \tilde{x}_1 - and \tilde{x}_2 -directions, then the flexibility matrix element (q_j, r_i) is obtained as

$$H_{q_j r_i} = U(i, j, \Delta\tilde{x}_1, \Delta\tilde{x}_2). \quad (5.4)$$

Finally, the dynamic stiffness matrix of the soil is obtained as the inverse of the flexibility matrix, i.e. $\mathbf{D}_s(\omega) = \mathbf{H}_s^{-1}(\omega)$, and the following equation applies for the soil super-element,

$$\mathbf{D}_s(\omega)\hat{\mathbf{u}}_s = \hat{\mathbf{f}}_s, \quad (5.5)$$

where the vector $\hat{\mathbf{u}}_s$ contains the displacements in the SSI DoFs, and the vector $\hat{\mathbf{f}}_s$ contains the externally applied loads.

Solution of global equations

When the dynamic stiffness matrices of the track and the soil, \mathbf{D}_t and \mathbf{D}_s , have been determined, they are assembled in a standard FE manner forming a total dynamic stiffness for the track and soil system, \mathbf{D}_g .

The following equation applies to the coupled track and soil system,

$$\mathbf{D}_g(\omega)\hat{\mathbf{u}}_t = \hat{\mathbf{f}}_t. \quad (5.6)$$

The load vector $\hat{\mathbf{f}}_t$ is zero except for the rows corresponding to the rail loading points DoFs. The SSI DoFs $\hat{\mathbf{u}}_s$ are a subset of the track DoFs $\hat{\mathbf{u}}_t$. Hence, when Eq. (5.6) has been solved, the corresponding forces in the SSI DoFs are obtained as

$$\hat{\mathbf{f}}_s = \mathbf{D}_s(\omega)\hat{\mathbf{u}}_s. \quad (5.7)$$

Now, a second flexibility matrix $\mathbf{H}_{s,f}(\omega)$ is defined, again by using the response surfaces $U(i, j, \tilde{x}_1, \tilde{x}_2)$ in a procedure similar to the one described above, to express the displacements in a number of points in the free-field due to loading of the SSI DoFs. The free-field displacements are then obtained as $\mathbf{u}_f = \mathbf{H}_{s,f}(\omega)\mathbf{f}_s$.

5.4.2 A coupled 2.5D track–soil model

By combining the 2.5D FE method with the semi-analytical soil representation a very time efficient model is obtained. Here, the track cross-section in the (x_2, x_3) -plane is represented by a 2D mesh comprising 2.5D elements. For each discrete wavenumber k_1 in the x_1 -direction, a dynamic stiffness matrix for the track is calculated, which is coupled to a dynamic stiffness matrix representing the soil, calculated from the Green's function of the layered half-space using the LTM method.

FE model of track

The track slab cross-section is modeled using 2.5D solid elements in the (x_2, x_3) -plane. The governing FE equations for such elements were presented in Section 4.1.4. Here, fully integrated 4-node isoparametric quadrilateral elements with linear shape functions are used. Six elements are used in the thickness direction of the slab, and an element length of 0.15 m is

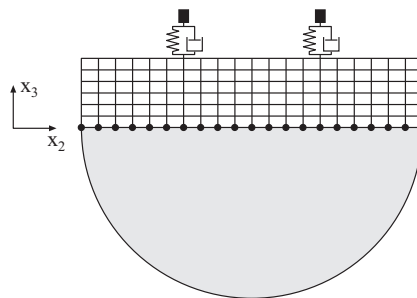


Figure 5.4: Illustration of a 2D FE mesh coupled to a horizontally layered half-space.

used in the x_2 -direction. As described in Section 4.1.4, the calculations are performed in the moving frame of reference following the load at velocity v , by evaluating the stiffness matrices for the frequency $\tilde{\omega} = \omega - k_1 v$, where ω is the actual frequency of excitation by the moving harmonic load. A dynamic stiffness matrix for the track slab, $\mathbf{D}_p(\tilde{k}_1, \tilde{\omega})$, is established in accordance with Eq. (4.35). The rail and rail pads, for which the dynamic stiffness is derived below, is coupled to the slab.

Each rail is represented by a Bernoulli–Euler beam of infinite length, with bending stiffness $(EI)_r$ and mass m_r , continuously supported by distributed springs and dashpots representing the rail pads, with stiffness k_P and damping c_P . The rail is subjected to a harmonic load P_0 with circular frequency ω , moving in the positive x_1 -direction with the velocity v . The governing equation for the rail can be written as

$$(EI)_r \frac{\partial^4 u_r}{\partial x^4} + m_r \frac{\partial^2 u_r}{\partial t^2} + k_P (u_r - u_s) + c_P \left(\frac{\partial u_r}{\partial t} - \frac{\partial u_s}{\partial t} \right) = \delta(x - vt) P_0 e^{i\omega t}. \quad (5.8)$$

Here, $u_r = u_r(x_1, t)$ is the vertical displacement of the rail and $u_s = u_s(x_1, t)$ is the vertical displacement of the slab directly under the rail. The equation is obtained in the frame of reference following the load by applying the coordinate transformation in Eq. (4.13),

$$(EI)_r \frac{\partial^4 \tilde{u}_r}{\partial \tilde{x}^4} + m_r \left(\frac{\partial^2 \tilde{u}_r}{\partial t^2} - 2v \frac{\partial^2 \tilde{u}_r}{\partial \tilde{x} \partial t} + v^2 \frac{\partial^2 \tilde{u}_r}{\partial \tilde{x}^2} \right) + k_P (\tilde{u}_r - \tilde{u}_s) + c_P \left(\frac{\partial \tilde{u}_r}{\partial t} - v \frac{\partial \tilde{u}_r}{\partial \tilde{x}} - \left(\frac{\partial \tilde{u}_s}{\partial t} - v \frac{\partial \tilde{u}_s}{\partial \tilde{x}} \right) \right) = \delta(\tilde{x}) P_0 e^{i\omega t}, \quad (5.9)$$

where, again, $\tilde{\cdot}$ denotes that a variable is expressed in the moving frame of reference. Fourier transforming Eq. (5.9) with respect to \tilde{x} yields

$$(EI)_r \tilde{k}_1^4 \bar{u}_r + m_r \left(\frac{\partial^2 \bar{u}_r}{\partial t^2} - 2iv\tilde{k}_1 \frac{\partial \bar{u}_r}{\partial t} - v^2 \tilde{k}_1^2 \bar{u}_r \right) + k_P (\bar{u}_r - \bar{u}_s) + c_P \left(\left(\frac{\partial \bar{u}_r}{\partial t} - iv\bar{u}_r \right) - \left(\frac{\partial \bar{u}_s}{\partial t} - iv\bar{u}_s \right) \right) = P_0 e^{i\omega t}, \quad (5.10)$$

with $\bar{u} = \bar{u}(\tilde{k}_1, t) = \int_{-\infty}^{\infty} \tilde{u}(\tilde{x}, t) e^{-i\tilde{k}_1 \tilde{x}} d\tilde{x}$, and \tilde{k}_1 denotes the wavenumber in the direction of \tilde{x} .

Further, assuming steady-state vibration with circular frequency ω , i.e. $\bar{u}(\tilde{k}_1, t) = \check{u}(\tilde{k}_1) e^{i\omega t}$ and setting $\tilde{\omega} = \omega - \tilde{k}_1 v$ yields

$$(EI)_r \tilde{k}_1^4 \check{u}_r - \tilde{\omega}^2 m_r \check{u}_r + k_P (\check{u}_r - \check{u}_s) + i\omega c_P (\check{u}_r - \check{u}_s) = P_0. \quad (5.11)$$

Based on the above equation, a one-dimensional element similar to a simple Kelvin-Voigt element can be formulated for the rail and rail pad in \tilde{k}_1 -domain, governed by

$$\begin{bmatrix} (EI)_r \tilde{k}_1^4 - \tilde{\omega}^2 m_r + k_P + i\tilde{\omega} c_P & -(k_P + i\tilde{\omega} c_P) \\ -(k_P + i\tilde{\omega} c_P) & k_P + i\tilde{\omega} c_P \end{bmatrix} \begin{bmatrix} \check{u}_r \\ \check{u}_s \end{bmatrix} = \begin{bmatrix} P_0 \\ 0 \end{bmatrix}, \quad (5.12)$$

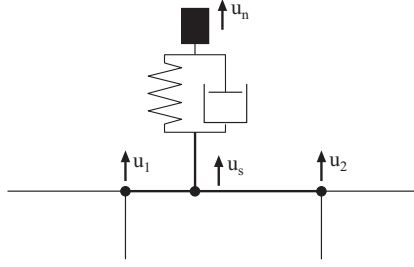


Figure 5.5: Coupling of rail and rail pad element to underlying slab element.

which can be written as $\mathbf{D}_r \check{\mathbf{u}}_r = \check{\mathbf{f}}_r$.

In the general case, the rail element is not located directly over a node of the track slab mesh. Hence, the vertical displacement at the contact point between the rail and the slab, \check{u}_s , is expressed in terms of the shape functions and vertical displacements of the two nodes spanning the edge of the connecting slab element, as

$$\check{u}_s = N_1 \check{u}_1 + N_2 \check{u}_2, \quad (5.13)$$

where the shape functions N_1 and N_2 are evaluated at the coordinate of the slab–rail contact point. It can be shown that this leads to the following dynamic stiffness matrix for the rail element,

$$\mathbf{D}_r = \begin{bmatrix} (EI)_r \tilde{k}_1^4 - \tilde{\omega}^2 m_r + k_P + i\tilde{\omega} c_P & -N_1(k_P + i\tilde{\omega} c_P) & -N_2(k_P + i\tilde{\omega} c_P) \\ -N_1(k_P + i\tilde{\omega} c_P) & N_1^2(k_P + i\tilde{\omega} c_P) & N_1 N_2(k_P + i\tilde{\omega} c_P) \\ -N_2(k_P + i\tilde{\omega} c_P) & N_1 N_2(k_P + i\tilde{\omega} c_P) & N_2^2(k_P + i\tilde{\omega} c_P) \end{bmatrix}, \quad (5.14)$$

with the corresponding DoFs $(\check{u}_r, \check{u}_1, \check{u}_2)$. The dynamic stiffness matrices for slab and the two rails can now be assembled into one for the whole track structure, \mathbf{D}_t , pertaining to the displacements of all the track DoFs $\check{\mathbf{u}}_t$. Damping is introduced into the slab and the rails by the use of complex Young's moduli, $E^* = E(1 + i \operatorname{sgn}(\tilde{\omega})\eta)$, where sgn is the sign function and η is the loss factor, leading to a frequency independent damping as described in Section 3.2.3.

Soil dynamic stiffness matrix

To derive the dynamic stiffness matrix of the soil, the slab–soil interface is discretized into n strips with a uniform width, where n is the number of elements in the slab. Hence, the width of a single strip is $\Delta = w/n$, where w is the slab width.

First, a single strip centered around the \tilde{x}_2 -axis, with a unit harmonic force in direction j is considered. In this section, the argument $\tilde{\omega}$ has been dropped for brevity; it is understood that a harmonic response with the angular frequency $\tilde{\omega} = \omega - \tilde{k}_1 v$ is considered. The strip stress

is

$$p_j(\tilde{x}_1, \tilde{x}_2) = \begin{cases} \frac{1}{\Delta}, & -\Delta/2 < \tilde{x}_2 < \Delta/2 \\ 0, & \text{otherwise} \end{cases}. \quad (5.15)$$

In wavenumber domain the interface stress becomes

$$\hat{p}_j(\tilde{k}_1, \tilde{k}_2) = \frac{\sin(\tilde{k}_2\Delta/2)}{\tilde{k}_2\Delta/2}. \quad (5.16)$$

The soil surface displacement in direction i due to the soil surface stress in direction j is denoted \hat{u}_{ij} . From Eq. (4.64) this displacement is obtained as $\hat{u}_{ij}(\tilde{k}_1, \tilde{k}_2) = G_{ij}(\tilde{k}_1, \tilde{k}_2)\hat{p}_j(\tilde{k}_1, \tilde{k}_2)$ (no summation on repeated indices).

By performing an inverse Fourier transform with respect to wavenumber \tilde{k}_2 , the soil displacement at an arbitrary \tilde{x}_2 -coordinate is obtained as

$$\begin{aligned} \check{u}_{ij}(\tilde{k}_1, \tilde{x}_2) &= \frac{1}{2\pi} \int_{-\infty}^{\infty} \hat{u}_{ij}(\tilde{k}_1, \tilde{k}_2) e^{i\tilde{k}_2\tilde{x}_2} d\tilde{k}_2 = \frac{1}{2\pi} \int_{-\infty}^{\infty} G_{ij}(\tilde{k}_1, \tilde{k}_2) \hat{p}_j(\tilde{k}_1, \tilde{k}_2) e^{i\tilde{k}_2\tilde{x}_2} d\tilde{k}_2 \\ &= \frac{1}{2\pi} \int_{-\infty}^{\infty} G_{ij}(\tilde{k}_1, \tilde{k}_2) \frac{\sin(\tilde{k}_2\Delta/2)}{\tilde{k}_2\Delta/2} e^{i\tilde{k}_2\tilde{x}_2} d\tilde{k}_2 = \check{H}_{ij}(\tilde{k}_1, \tilde{x}_2). \end{aligned} \quad (5.17)$$

$\check{H}_{ij}(\tilde{k}_1, \tilde{x}_2)$ is a transfer function, expressing the displacements at \tilde{x}_2 due to a unit load at the strip centered around $\tilde{x}_2 = 0$. Due to the translational invariability of the soil, $\check{H}_{ij}(\tilde{k}_1, \tilde{x}_2)$ can be used for calculating the soil displacement at any distance along the \tilde{x}_2 -axis from any loaded strip, by replacing the coordinate \tilde{x}_2 with the distance between the mid-points of the “source strip” and the “receiver strip”. Hence, for each wavenumber \tilde{k}_1 , a flexibility matrix, linking the displacements and forces in all the n strips, is established as

$$\begin{bmatrix} \check{H}_{11}(0) & \check{H}_{12}(0) & \dots & \check{H}_{13}(-(n-1)\Delta) \\ \check{H}_{21}(0) & \check{H}_{22}(0) & \dots & \check{H}_{23}(-(n-1)\Delta) \\ \check{H}_{31}(0) & \check{H}_{32}(0) & \dots & \check{H}_{33}(-(n-1)\Delta) \\ \check{H}_{11}(\Delta) & \check{H}_{12}(\Delta) & \dots & \check{H}_{13}(-(n-2)\Delta) \\ \vdots & \vdots & \dots & \vdots \\ \check{H}_{31}((n-1)\Delta) & \check{H}_{32}((n-1)\Delta) & \dots & \check{H}_{33}(0) \end{bmatrix} \begin{bmatrix} \check{f}_{1x} \\ \check{f}_{1y} \\ \vdots \\ \check{f}_{nz} \end{bmatrix} = \begin{bmatrix} \check{u}_{1x} \\ \check{u}_{1y} \\ \vdots \\ \check{u}_{nz} \end{bmatrix}, \quad (5.18)$$

where the argument \tilde{k}_1 has been dropped for brevity. Equation (5.18) can be written as $\check{\mathbf{H}}_s \check{\mathbf{f}}_s = \check{\mathbf{u}}_s$, where $\check{\mathbf{u}}_s$ and $\check{\mathbf{f}}_s$ are vectors containing displacements and forces respectively. Hence, the dynamic stiffness matrix is obtained as $\mathbf{D}_s = \check{\mathbf{H}}_s^{-1}$. For the discretized soil interface, the following equation relates the total forces on each strip to the displacements in the mid-point of each strip,

$$\mathbf{D}_s \check{\mathbf{u}}_s = \check{\mathbf{f}}_s. \quad (5.19)$$

It is emphasized that Eq. (5.19) applies for a given wavenumber \tilde{k}_1 and frequency $\tilde{\omega}$, i.e. $\mathbf{D}_s = \mathbf{D}_s(\tilde{k}_1, \tilde{\omega})$, $\check{\mathbf{u}}_s = \check{\mathbf{u}}_s(\tilde{k}_1, \tilde{\omega})$, and $\check{\mathbf{f}}_s = \check{\mathbf{f}}_s(\tilde{k}_1, \tilde{\omega})$. For each \tilde{k}_1 , however, a loop over a set of wavenumbers \tilde{k}_2 in the \tilde{x}_2 -direction is necessary for the evaluation of the Green's function and Eq. (5.17).

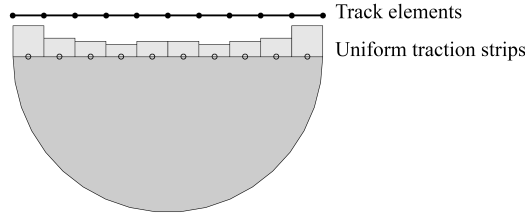


Figure 5.6: Strips of uniform traction on the soil. The nodes and edges of the connecting track elements are also shown.

Coupling of track and soil

The “interaction points” of the discretized soil interface are located at the mid-point of each strip, whereas the nodes of the track elements at the interface are located in the strip end-points. The two domains are initially uncoupled. To couple the two domains, a transformation matrix is used to enforce displacement compatibility between the mid-point of each soil strip and the corresponding point of the FE mesh. A similar procedure was followed in [51] to couple 2.5D boundary elements to a FE mesh. The displacements in the soil strip mid-points, $\check{\mathbf{u}}_s$, are expressed in terms of the displacements of the track nodes at the interface, $\check{\mathbf{u}}_{st}$ as

$$\check{\mathbf{u}}_s = \mathbf{T}\check{\mathbf{u}}_{st}, \quad (5.20)$$

where the transformation matrix \mathbf{T} depends on the element shape functions in the track elements. Because linear elements are used for the track, and the soil strip mid-points are located in the center of each corresponding track element, Eq. (5.20) states that the displacements of each soil strip mid-point equal the average displacements in the two nodes spanning the edge of the connecting element. The same transformation matrix is used to relate the forces from the soil strips to the actual track nodes,

$$\check{\mathbf{f}}_{st} = \mathbf{T}^T \check{\mathbf{f}}_s, \quad (5.21)$$

Hence, in terms of the track DoFs of the track–soil interface, the dynamic equilibrium for the soil can be written as

$$\mathbf{D}_{st}\check{\mathbf{u}}_{st} = \check{\mathbf{f}}_{st}, \quad (5.22)$$

with $\mathbf{D}_{st} = \mathbf{T}^T \mathbf{D}_s \mathbf{T}$.

Solution of global equations

The dynamic stiffness matrices for the soil, \mathbf{D}_{st} , and the track, \mathbf{D}_t can now be assembled in a standard manner leading to a global dynamic stiffness matrix for the coupled soil and track system, $\mathbf{D}_g = \mathbf{D}_g(\tilde{k}_1)$. The displacements of the track DoFs, $\check{\mathbf{u}}_t = \check{\mathbf{u}}_t(\tilde{k}_1)$ are solved from

$$\mathbf{D}_g \check{\mathbf{u}}_t = \check{\mathbf{f}}_t, \quad (5.23)$$

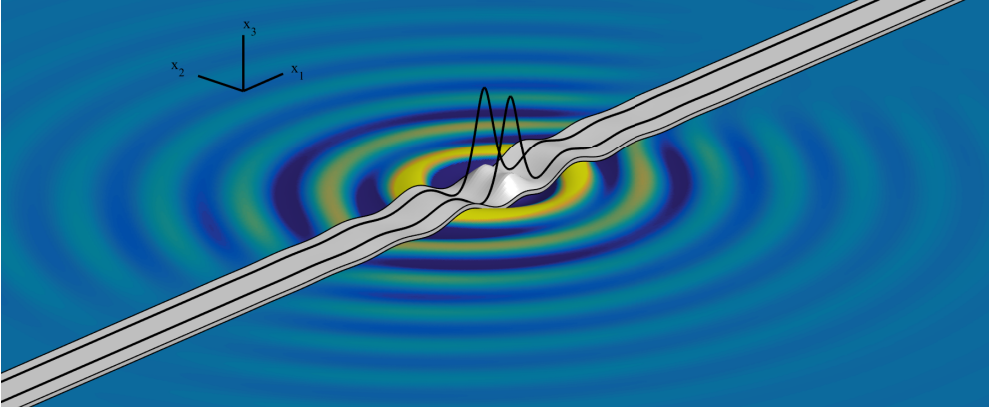


Figure 5.7: Contour plot showing the vertical displacement of the soil surface as obtained with the coupled 2.5D model for the excitation frequency $f = 80$ Hz.

where $\check{\mathbf{f}}_t = \check{\mathbf{f}}_t(\tilde{k}_1)$ is a force vector containing the external loads. The only external loads are the harmonic point loads P_0 on each rail, moving with velocity v in the positive x_1 -direction, i.e. $f(x_1, t) = P_0\delta(x_1 - vt)e^{i\omega t}$. In the moving coordinate system this becomes $\check{f}(\tilde{x}_1, t) = P_0\delta(\tilde{x}_1)e^{i\omega t}$, and after a Fourier transform with respect to \tilde{x}_1 and t the load is described by $\check{f}(\tilde{k}_1, \omega) = P_0$. This means that the same load, P_0 , is applied to the rail DoF for each wavenumber \tilde{k}_1 . The displacements $\check{\mathbf{u}}_s(\tilde{k}_1)$ in the mid-points of the element edges, corresponding to the mid-points of the soil strips, are then obtained from Eq. (5.20), from which the soil strip forces, $\check{\mathbf{f}}_s(\tilde{k}_1)$, can be obtained from Eq. (5.19). When the magnitude of the strip forces are known the total traction on the soil surface for the current wavenumber, \tilde{k}_1 , is obtained by superposition of the contributions from each individual strip. The traction in $(\tilde{k}_1, \tilde{k}_2)$ -domain due to a single strip centered around the \tilde{x}_2 -axis was given in Eq. (5.16). The traction due to a strip centered around the coordinate $\tilde{x}_2 = d$ is then given by the translation operation, i.e.

$$\check{p}_j(\tilde{k}_1, \tilde{k}_2) = \frac{\sin(\tilde{k}_2\Delta/2)}{\tilde{k}_2\Delta/2} e^{id\tilde{k}_2}. \quad (5.24)$$

Each such (unit force) strip traction is scaled by the corresponding strip force in the vector $\check{\mathbf{f}}_s(\tilde{k}_1)$.

The calculations described here are carried out for N discrete wavenumbers \tilde{k}_1 corresponding to the \tilde{x}_1 -direction. That is, for each wavenumber \tilde{k}_1 , the dynamic stiffness matrix of the 2D FE mesh is established, and coupled to a dynamic stiffness matrix for the soil. The establishment of the Green's function and the soil dynamic stiffness matrix, for each wavenumber \tilde{k}_1 , requires a loop over M discrete wavenumbers \tilde{k}_2 corresponding to the \tilde{x}_2 -direction. In the current example, $N = M = 4096$ was chosen, with $\max(\tilde{k}_1) = \max(\tilde{k}_2) = 2\pi/0.15$ rad/m, i.e. the same wavenumber discretization that was used in the 3D model.

The global displacements of the soil surface are calculated in $(\tilde{k}_1, \tilde{k}_2)$ -domain using Eq. (4.64). These displacements are obtained in $(\tilde{x}_1, \tilde{x}_2)$ -space by a double inverse Fourier transform. The

complex nodal displacements of the track structure, $\hat{\mathbf{u}}_t(\tilde{x}_1)$, are obtained in N points along the (\tilde{x}_1) -axis after an inverse Fourier transform of $\check{\mathbf{u}}_t(\tilde{k}_1)$, see Figure 5.7.

5.4.3 A 2.5D FE–PML model

In this model, both the track slab and the soil is represented by 2.5D solid elements in the (x_2, x_3) -plane. The governing FE equations for such elements were presented in Section 4.1.4. Here, fully integrated isoparametric 8-node elements with quadratic shape functions are used. The modeling of the rails and rail pads is identical to the description in Section 5.4.2, i.e. by a one-dimensional element the rail and rail pad in k_1 -domain governed by Eq. (5.12). The only difference is that the coupling of the rail to the slab now accounts for the fact that the slab is described by quadratic elements.

FE model of track and soil

Six elements are used in the thickness direction of the slab, and an element length of 0.3 m is used in the x_2 -direction. For the soil, the element length is approximately 0.3 m in both directions. Only half of the track and the surrounding soil is modeled, with symmetry conditions applied to the boundary in $x_2 = 0$. PMLs, as described in Section 4.1.5, are used to artificially attenuate the waves at the truncated sides of the model. The attenuation function for evanescent waves, $f_j^e(x_j)$ is set to zero. A linear attenuation function for propagating waves is used, as $f_j^p(x_j) = 20(x_j - x_{j0})/L_{\text{PML}}$ [20] where x_{j0} is the x_j -coordinate at the interface between the regular and the PML domain. Material damping is introduced into the

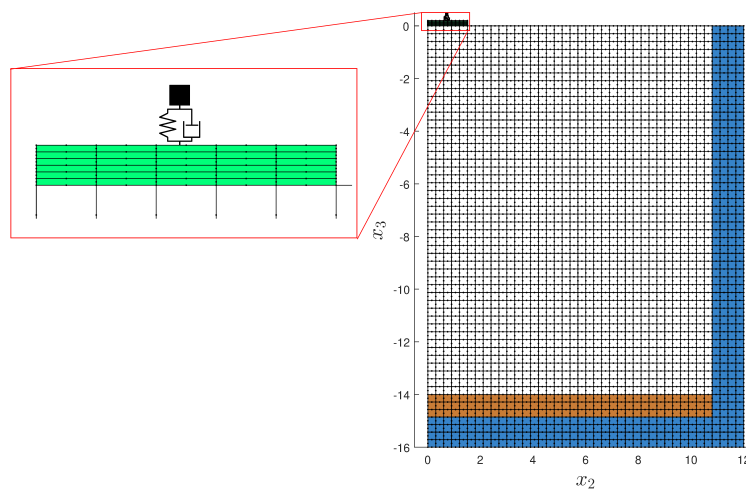


Figure 5.8: Mesh used in 2.5D FE–PML model. Blue colored elements are PML elements. Brown colored elements belong to the half-space material. A magnification of the slab (green colored elements) is shown inside the red box.

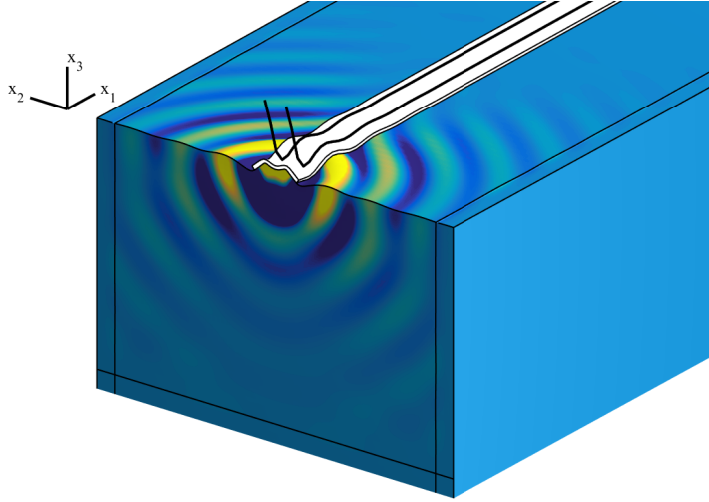


Figure 5.9: Contour plot showing the vertical displacement of the soil for the excitation frequency $f = 80$ Hz. The waves are effectively attenuated inside the PML.

whole model by the use of complex Young's moduli, $E^* = E(1 + i \operatorname{sgn}(\tilde{\omega})\eta)$, where η is the loss factor and sgn is the sign function. The FE mesh is shown in Figure 5.8.

Solution of global equations

As described in Section 4.1.4, the calculations are performed in the moving frame of reference following the load at velocity v , by evaluating the stiffness matrices for the frequency $\tilde{\omega} = \omega - \tilde{k}_1 v$, where ω is the actual frequency of excitation by the moving harmonic load. A global dynamic stiffness matrix for the entire computational domain, $\mathbf{D}_g(\tilde{k}_1)$, is established for each of the N discrete wavenumbers \tilde{k}_1 in the \tilde{x}_1 -direction. The nodal displacement vector $\tilde{\mathbf{u}}(\tilde{k}_1)$ is solved from $\mathbf{D}_g \tilde{\mathbf{u}} = \tilde{\mathbf{f}}$. The only external load is the point load (P_0) on the rail, which are constant for all wavenumbers as discussed in Section 5.4.2. In the current example $N = 4096$ with $\max(\tilde{k}_1) = 5$ rad/m. The complex nodal displacements $\hat{\mathbf{u}}(\tilde{x}_1)$ are obtained in N points along the (\tilde{x}_1) -axis after an inverse Fourier transform of $\tilde{\mathbf{u}}(\tilde{k}_1)$, see Figure 5.9.

5.4.4 Discussion

All three models described above are formulated in a moving frame of reference, following the load at the velocity $v = 30$ m/s. The results are therefore obtained in this moving reference frame. Since the loading is harmonic with frequency ω , the response is also harmonic with the same frequency. To compare the response from the three models, the absolute value of the vertical displacement is extracted along a line located 10 m from the track center line, see Figure 5.10, as well as along the rail, see Figure 5.11. The displacements are plotted against

the track direction coordinate \tilde{x}_1 , where $\tilde{x}_1 = 0$ corresponds to a point perpendicular to the moving load, and positive values of \tilde{x}_1 correspond to points in front of the load.

All three models yield very similar response, both regarding the rail displacements and the free-field displacements. The maximum difference of the peak values is obtained for the higher frequency, where it is still less than 3%. The small differences that do exist are believed to be caused mainly by the different track–soil interface stress conditions. The traction on the soil surface from the two models employing a soil dynamic stiffness based on the semi-analytic approach, is composed of patches or strips of uniform stress. In the 3D model, these patches are applied centered around each SSI node, whereas in the 2.5D case the strips of uniform stress are applied centered around the element edge mid-point. In the 3D model, the contact pressure therefore extends slightly (by half an element width) outside the slab width. However, as seen from the response, these effects are negligible for the free-field response in the case studied here.

In terms of computational cost, it is difficult to make a completely fair comparison. For the two models using the LTM method to establish the soil impedance and response, the Green's function evaluation requires a loop over $N \times M$ wavenumbers in (k_1, k_2) -domain. In the 3D model, a large system of equations is established that is solved once for each excitation frequency. The dynamic stiffness matrix of the soil becomes fully populated. In the coupled 2.5D model a very small system of equations (corresponding to the DoFs of the 2D mesh) is solved, but on the other hand it is solved N times (once for every wavenumber k_1 in the x_1 -direction). In the 2.5D FE–PML model, the system of equations is also solved N times, once for every wavenumber k_1 . Here, the system of equations is considerably larger due to the discretization of the soil, and the computational time depends heavily on the size of the computational domain. To evaluate the response at large distances becomes costly because of the large soil domain requiring discretization. In all models, large savings in computational time can be gained by utilizing that the calculations are independent for each wavenumber k_1 , i.e. parallelization can be employed.

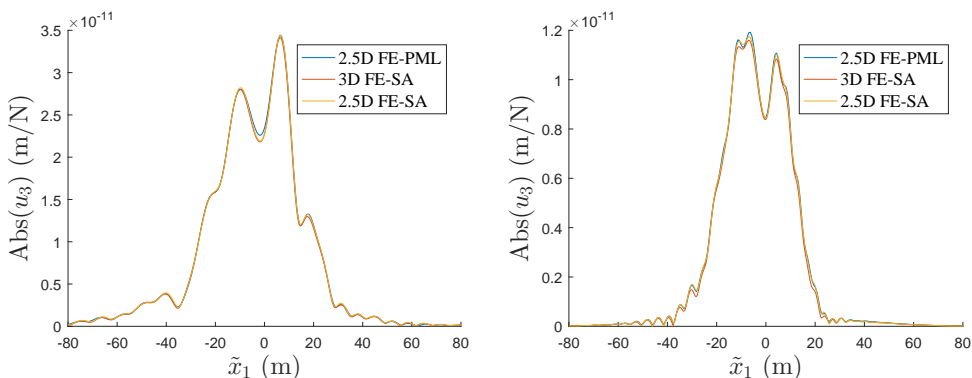


Figure 5.10: Maximum vertical displacement along a line 10 m from the track for the excitation frequencies $f = 40$ Hz (left) and $f = 80$ Hz (right).

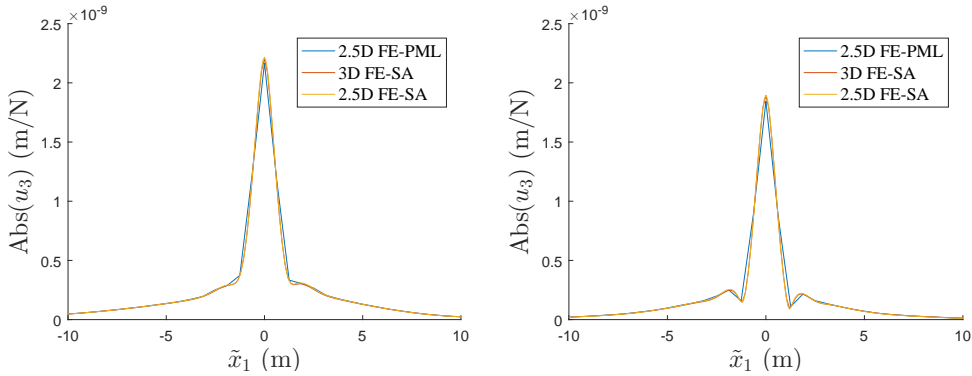


Figure 5.11: Maximum vertical displacement along the rail for a unit harmonic load with the excitation frequencies $f = 40$ Hz (left) and $f = 80$ Hz (right).

It can be argued that the 3D model does not have any advantages over the other two models in the case studied here, i.e. when considering a moving load. However, the model can of course also be used in a fixed frame of reference by setting the velocity $v = 0$. Then it is possible to introduce additional structures (e.g. a building with a surface footing) next to the track, e.g. to numerically predict transfer functions from the track to the building. This would not be possible in the two other models utilizing the 2.5D approach, where only long-stretched invariant structures could be included. In a 2.5D FE–PML model, as opposed to the other two models, it is straightforward to model e.g. a long-stretched trench parallel with the track, or other discontinuities of the soil.

In the present example, the analysis of a unit harmonic load on the track was described. However, the results from such analyses can be utilized for studying the effect of a vehicle running over an uneven rail. For a given unevenness wavelength λ , the frequency of excitation by a wheel running at v is $f = v/\lambda$. The rail receptance (displacement per unit force) for a given frequency f and velocity v , can be used for establishing a sub-model where the vehicle response and the wheel–rail contact forces are calculated. The free-field response due to these contact forces are then obtained by scaling, phase-shifting and translating the free-field response calculated for the unit harmonic load. This is further detailed in appended Paper E. The total response from the dynamic excitation by a vehicle running over an uneven rail is obtained as the sum of contributions from discrete unevenness wavelengths. If measurements of the rail unevenness for a certain stretch are not available, rail unevenness defined in a statistical sense by a power spectral density (PSD) function can be used. Such a PSD function was used in appended Papers B and E for calculating the free-field response due to a train running on an uneven rail.

6 Summary of Appended Papers

6.1 PAPER A

Modeling train-induced ground-borne vibrations using FEM in a moving frame of reference

J. Malmberg, K. Persson, P. Persson.

In proceedings of COMPDYN 2019, 7th International Conference on Computational Methods in Structural Dynamics and Earthquake Engineering, Crete, Greece, June 2019.

Summary

A numerical model for calculating the free-field ground vibrations from surface trains is presented in the paper. A finite element formulation in a frame of reference following the moving load at a fixed velocity, was used for modeling a railway slab track. The underlying soil was represented through a dynamic stiffness matrix, obtained from the Green's function for a horizontally layered visco-elastic half-space, in a moving frame of reference. Three different track models were established and compared. In two of the track models, the slab was represented by beam elements with different assumptions regarding the pressure distribution of the slab–soil interface. The third track model utilized plate elements for representing the slab, accounting for the cross-section flexibility and hence a more general slab–soil pressure distribution. The three track models were used for evaluating the free-field response due to a harmonic load in the frequency range 0–80 Hz moving along the track. One of the beam models, assuming a constant vertical displacement of the soil under the slab cross-section, showed good agreement with the plate model. The response obtained with the simplest beam model, assuming a constant contact pressure under the slab cross-section, was significantly underestimated.

Contributions by Jens Malmberg

Jens Malmberg was the main author of the paper, planned the research tasks, implemented the methods, carried out the investigations and drew conclusions that were presented.

6.2 PAPER B

Evaluating the effect of vibration isolation mats on train-induced ground vibrations

J. Malmberg, K. Persson, P. Persson.

In proceedings of SEMC 2019, 7th International Conference on Structural Engineering, Mechanics and Computation, Cape Town, South Africa, September 2019.

Summary

The numerical modeling technique established in Paper A was applied to evaluate the effect of a vibration isolation mat, placed under a railway slab track, on the free-field ground vibrations. The slab and the underlying supporting plate were modeled using Kirchhoff plate elements, and the vibration isolation mat was modeled as a continuous visco-elastic layer between the two plates. First, the free-field response and the insertion loss obtained with the vibration isolation mat was calculated for a harmonic point load moving along the track. Secondly, band-averaged vibration levels and the insertion loss for a fixed point next to the track were calculated for a train cart, represented by a 10-DoF multi-body system, running at different speeds on an uneven track. The rail unevenness was described by a PSD function. It was found that the isolation mat changes the vibration response significantly in two ways. The introduction of a resilient element changes the transmissibility of the system, hence changing the vibration response due to a specific load acting on the track. Further, the resilient element modifies the track receptance, implying different dynamic wheel–rail interaction forces as the vehicle runs over the uneven rail. Negative insertion loss, i.e. a higher vibration response, were obtained for frequencies near the resonance frequency of the isolated slab, whereas a significant reduction of the response was obtained for higher frequencies.

Contributions by Jens Malmberg

Jens Malmberg was the main author of the paper, planned the research tasks, implemented the methods, carried out the investigations and drew conclusions that were presented.

6.3 PAPER C

Effects of modeling strategies for a slab track on predicted ground vibrations

J. Malmborg, P. Persson, K. Persson.

Soil Dynamics and Earthquake Engineering 136: 106254, 2020.

Summary

In the paper, the effect of modeling strategies regarding the dynamic behavior of a railway slab track on a layered half-space is studied. If the track is modeled as a layered beam, the free-field vibration response due to a moving harmonic load on the track can be evaluated efficiently using a semi-analytical procedure in frequency–wavenumber domain. However, such a beam representation of the track does not account for the cross-section flexibility, and some assumptions regarding the displacements or the stress-distribution in the track–soil interface have to be made. In the paper, a constant displacement and a constant stress-distribution, respectively, were tested. The free-field response obtained with the beam models were compared to that obtained using a solid finite element and a shell finite element representation of the slab, using the technique established in Paper A. First, only the vertical displacements of the slab–soil interface were coupled. Secondly, the effect of coupling the in-plane displacements on the free-field vibrations were studied. Furthermore, a sub-structuring technique was employed to calculate and compare the wheel–rail interaction forces with the different models, for a single-axle vehicle. It was found that for a thin slab, the vertical pressure distribution under the slab is highly influenced by the cross-section flexibility, which in turn significantly affects the predicted free-field vibrations. The two beam models yielded an underestimated response for the studied cases. For a thick slab, however, the beam model with a constant displacement under the slab yielded accurate free-field response, compared to the solid and shell models. It was also found that when the in-plane shear forces of the slab–soil interface was accounted for, increased vibration response levels in the free-field were generally obtained. A beam model, enforcing zero in-plane displacements in the lateral direction of the slab–soil interface, provided good accuracy for a thick slab. All models provided similar rail receptances and subsequently wheel–rail interaction forces.

Contributions by Jens Malmborg

Jens Malmborg was the main author of the paper, planned the research tasks, implemented the methods, carried out the investigations and drew conclusions that were presented.

6.4 PAPER D

Numerical investigation of railway subgrade stiffening: Critical speed and free-field vibrations

J. Malmborg, P. Persson, K. Persson.

Transportation Geotechnics 34: 100748, 2022.

Summary

For a train speed close to the speed of elastic waves in the soil, often referred to as “critical speed”, largely elevated vibration responses occur. This can be a practical problem for soft soil sites, where the phenomenon may cause excessive vibrations in the track and also at distances far from the track. To ensure the running safety of the train, the long-term quality of the track and to reduce the vibrations in the surroundings, such effects must be avoided. An effective counter-measure is to increase the stiffness of the soil underneath the track, thereby increasing the critical velocity.

In this paper, a 2.5D finite element model is used for studying the critical velocity phenomenon and its mitigation through soil stiffening, for a ballasted track on a layered half-space with very soft soil. Soil improvement under the track, in the shape of a solid block or as various number of panels, with varying depth and stiffness is considered. The effect of the soil improvement is evaluated both in terms of the maximum rail and free-field displacements. It is shown that a shallow soil stiffening increases the critical velocity and reduces the rail and free-field response for load speeds near the shear wave velocity of the soft top soil layer. It is also demonstrated that a deep soil stiffening, by use of panels along the track direction, increases the critical velocity further, and may also be efficient in reducing the response for load speeds near the shear wave speed of the underlying half-space.

Contributions by Jens Malmborg

Jens Malmborg was the main author of the paper, planned the research tasks, implemented the methods, carried out the investigations and drew conclusions that were presented.

6.5 PAPER E

A numerical study of train-induced vibrations in light and heavy building systems

J. Malmborg, O. Flodén, P. Persson, K. Persson.

Submitted for publication.

Summary

This paper deals with the numerical prediction of building vibrations induced by a passing train on an adjacent railway track. The calculations are based on a sub-structure approach, where a sequence of different models are used to predict the train–track interaction forces, the free-field ground vibrations due to these forces, and the building-on-soil response when subjected to the incident wave field. The free-field ground vibrations and the track receptance are calculated using a so called 2.5D technique where the railway track is represented by finite elements that couple to a dynamic stiffness of the underlying soil which in turn is obtained from the Green's function of a horizontally layered half-space using a layer transfer matrix approach. A planar multi-body model of the train, coupled to the track receptance, is used for calculating the train–track interaction forces as the train runs over an uneven rail. Finally, the building response to the incident wavefield is calculated using a 3D finite element model, accounting for the soil–structure interaction. This sequence of models and calculations are applied to evaluate the vibrations in two buildings with identical layout, one lightweight timber building and one heavyweight concrete building, due to a passenger train passing by at two different speeds. It was found that the difference in response between the two buildings was small, with only slightly higher response in terms of RMS velocity in the lightweight building. An amplification of the response inside the building, compared to the incident wavefield, was found in frequency bands around the fundamental frequencies of the slab; however in terms of the running RMS velocity, the building response was reduced. Further, it was found that accounting for soil-structure-interaction, as opposed to simply enforcing the free-field displacements at the building foundations, significantly reduced the building response in terms of RMS velocity.

Contributions by Jens Malmborg

Jens Malmborg was the main author of the paper, planned the research tasks, implemented the methods, carried out the investigations and drew conclusions that were presented

6.6 PAPER F

Numerical modelling applied to wave-propagation analysis for arbitrary frequency and layer depths within infinite elastic media

A. Peplow, J. Malmberg, P. Persson

Submitted for publication.

Summary

An efficient computational procedure for harmonic wave-propagation analysis of layered elastic media is presented. The main advantages of the procedure include arbitrary frequency, depth and number of layer strata over an elastic half-space. For a general study of free or forced vibration the methodology is straightforward to implement for computing relevant response output. Computation of wavenumber dispersion diagrams, phase velocity plots and response data in the frequency and time domains are presented to highlight the methodology for two example cases for plane strain and axisymmetry, respectively. The methodology is based upon a well-conditioned dynamic stiffness approach that is especially developed for this purpose; this allows a deep-layered strata to be studied. Since the size of the system of equations remains low the computations are fast on a regular desktop/laptop computer, being of the order of tenths of a second for a forced response analysis. Numerical evidence of a layer resonance due to the presence of a ZGV (zero group velocity) mode-phenomena via a case-study for a ground profile where layers are hundreds of meters in depth, with solutions both in the frequency and time-domains illuminating this special case.

Contributions by Jens Malmberg

Jens Malmberg performed parts of the data collection, implemented the 3D numerical method used for verification, and wrote the corresponding parts of the paper.

7 Concluding Remarks

7.1 CONCLUSIONS AND CONTRIBUTIONS

In the thesis, numerical modeling strategies for predicting ground-borne vibrations from a surface railway track have been studied and developed. Such strategies are highly relevant in a practical civil engineering context to enable accurate predictions and informed design decisions. Focus have been on the vibration transmission from the track to the free-field, but the work also include the actual load generation due to a train running over an uneven rail as well as the vibration propagation into an adjacent building, and a study regarding critical velocity effects for a high-speed trains running on soft soil. An efficient semi-analytical approach for modeling the soil behavior, based on the Green's function for a horizontally layered half-space, has been combined with finite element modeling of the railway track, both in 3D and 2.5D. All computational code for the models was written in FORTRAN by the author. The main contributions of the work presented in the thesis and the appended papers include:

- A novel combination of the Green's function for a layered visco-elastic half-space with a 3D FE representation of a railway track, in the moving frame of reference (Papers A–C).
- A study of insertion loss by the introduction of a resilient mat under the track slab, obtained in a fixed point next to the track due to a passing train on an uneven track (Paper B).
- A study of the importance of the track modeling strategy, regarding the cross-section flexibility and the track–soil in-plane shear forces, on the free-field vibrations (Paper C).
- A novel study of critical velocity effects and their mitigation through stiffening of the soil under the track, using a 2.5D FE model with PML (Paper D).
- An efficient combination of a 2.5D FE representation of a railway track with a semi-analytical soil impedance for predicting the free-field ground vibrations (Paper E).
- A novel comparison of the performance of a lightweight timber building vs a heavy-weight concrete building when subjected to train-induced ground-borne vibrations (Paper E).

The numerical modeling capabilities developed and presented in the thesis can be used for studying a large range of vibration problems in an efficient manner. Many parameters, ranging from material parameters of the track and the surrounding soil to the smoothness of the rail and train wheels, are involved in the prediction of train-induced ground vibrations. Careful estimations of all such parameters are needed for a prediction model to yield accurate results, and it may not always be feasible to perform the measurements required to establish reliable estimates of all the relevant parameters. However, the developed models may also be used for studying how varying an input parameter influences the vibration response, for comparing the performance of different design options, and for evaluating the efficacy of various vibration mitigation measures, both regarding the railway track, the ground or a nearby building.

7.2 SUGGESTIONS FOR FUTURE WORK

In the thesis, only the unevenness of the rail has been considered as the dynamic excitation mechanism. For some dynamic excitation mechanisms, such as rail switches, a non-linear contact algorithm capable of simulating the loss of contact between the wheel and the rail must be adopted to provide accurate contact forces. Such non-linear analyses must be carried out in time-domain. The models presented herein operate in frequency domain and can therefore not be used directly in such a case. However, if non-linear wheel-rail contact forces have been obtained in some other way, e.g. using a planar track model in time-domain, these forces can be applied in the linear 2.5D models to provide the free-field response. It would be interesting to investigate the possibilities of using the frequency dependent rail receptance calculated from the 2.5D model to establish a lumped parameter model (LPM), containing all wheel-rail contact points in the moving frame of reference, that could be used in time-domain with a non-linear contact algorithm.

An interesting subject of research is the quantification of uncertainties of model output that are afflicting numerical predictions due to limited knowledge or natural variations regarding the governing input parameters. It would be useful if the statistical variations regarding some input parameter could be specified and propagated through the prediction models, to establish predictions in a statistical sense, e.g. by means of confidence intervals.

For high-speed trains on poor soils, i.e. for trains running close to “critical velocity”, the strains that develop in the track and/or the subsoil due to the moving dead load of the train may be large and the assumption of a linear-elastic material behavior may be inappropriate. Other researchers have proven that using an “equivalent linear elastic” approach can provide accurate predictions of the track and soil vibrations in such cases. In such an approach, the linearized soil stiffness and damping properties are related to the maximum strain level, and an iterative scheme is followed where these properties are updated in the model until the calculated maximum strain matches the strain on which the stiffness and damping values were based. Adding such an iterative scheme, e.g. to the 2.5D FE model presented in appended Paper D, would only require a small programming effort but would increase the reliability of calculated

critical velocities and mitigation effects from various soil stiffening designs.

Furthermore, it would be interesting to evaluate the use of optimization algorithms for establishing effective and cost efficient soil stiffening designs, e.g. to find an optimal number, depth and position of lime–cement panels underneath the track to increase the critical velocity and to reduce the vibrations in the track and in the free-field.

References

- [1] Central Intelligence Agency (2022), *The World Factbook 2022*, <https://www.cia.gov/library/publications/resources/the-world-factbook/index.html>, [Online; accessed 23-August-2022].
- [2] Hanson, C., Towers, D., Meister, L. (2006), *Transit Noise and Vibration Impact Assessment*, Tech. Rep. FTA-VA-90-1003-06, U.S. Department of Transportation, Federal Transit Administration, Office of Planning and Environment.
- [3] Thompson, D., Kouroussis, G., Ntotsios, E. (2019), *Modelling, simulation and evaluation of ground vibration caused by rail vehicles*, *Vehicle System Dynamics* 57(7), 936–983.
- [4] Münzel, T., Schmidt, F., Steven, S., Herzog, J., Daiber, A., Sørensen, M. (2018), *Environmental noise and the cardiovascular system*, *Journal of the American College of Cardiology* 71(6), 688–697.
- [5] International Organization for Standardization, *Mechanical vibration and shock - Evaluation of human exposure to whole-body vibration - Part 1: General requirements*, Tech. Rep. ISO 2631-1:1997.
- [6] Richart Jr, F., Hall Jr, J., Woods, R. (1970), *Vibrations of Soils and Foundations*, Prentice Hall, Englewood Cliffs, N.J.
- [7] Kungl. Ingenjörsvetenskapsakademien (1979), *Jord- och bergmekanik. Information från IVA:s kommitte för vibrationsfrågor*, Tech. Rep. Meddelande 225.
- [8] Kaynia, A., Madshus, P., Zackrisson, P. (2000), *Ground vibration from high-speed trains: prediction and countermeasure*, *Journal of Geotechnical and Geoenvironmental Engineering* 126(6), 531–537.
- [9] Chopra, A. (1995), *Dynamics of structures*, Prentice Hall, Upper Saddle River.
- [10] Lombaert, G., Degrande, G., François, S., Thompson, D. (2013), *Ground-borne vibration due to railway traffic: a review of excitation mechanisms, prediction methods and mitigation measures*, in: *Proceedings of the 11th International Workshop on Railway Noise, Uddevalla, Sweden*.

- [11] Clough, R., Penzien, J. (1993), *Dynamics of Structures*, McGraw-Hill College.
- [12] Kramer, S. (1996), *Geotechnical Earthquake Engineering*, Prentice Hall.
- [13] Sparr, G., Sparr, A. (1999), *Kontinuerliga system*, Studentlitteratur.
- [14] Andersen, L. (2006), *Linear Elastodynamic Analysis*, Department of Civil Engineering, Aalborg University.
- [15] Kausel, E., Whitman, R., Morray, J., Elsabee, F. (1978), *The spring method for embedded foundations*, Nuclear Engineering and Design **48**(2-3), 377–392.
- [16] Kausel, E. (2017), *Advanced structural dynamics*, Cambridge University Press.
- [17] Ottosen, N., Petersson, H. (1992), *Introduction to the finite element method*, Prentice Hall.
- [18] Yang, Y., Hung, H. (2001), *A 2.5D finite-infinite element approach for modelling visco-elastic bodies subjected to moving loads*, International Journal for Numerical Methods in Engineering **51**, 1317–1336.
- [19] Sheng, X., Jones, C., Thompson, D. (2006), *Prediction of ground vibration from trains using the wavenumber finite and boundary element methods*, Journal of Sound and Vibration **293**, 575–586.
- [20] François, S., Schevenels, M., Lombaert, G., Degrande, G. (2012), *A two-and-a-half dimensional displacement-based PML for elastodynamic wave propagation*, International Journal for Numerical Methods in Engineering **90**, 819–837.
- [21] Basu, U., Chopra, A. (2003), *Perfectly matched layers for time-harmonic elastodynamics of unbounded domains: theory and finite-element implementation*, Computer Methods in Applied Mechanics and Engineering **192**(11-12), 1337–1375.
- [22] Sheng, X., Jones, C., Petyt, M. (1999), *Ground vibration generated by a harmonic load acting on a railway track*, Journal of Sound and Vibration **225**(1), 3–28.
- [23] Sheng, X., Jones, C., Petyt, M. (1999), *Ground vibration generated by a load moving along a railway track*, Journal of Sound and Vibration **228**(1), 129–156.
- [24] Andersen, L., Clausen, J. (2008), *Impedance of surface footings on layered ground*, Computers and Structures **86**, 72–87.
- [25] Thomson, W. (1950), *Transmission of elastic waves through a stratified solid medium*, Journal of Applied Physics **21**, 89–93.
- [26] Haskell, N. (1953), *The dispersion of surface waves on multilayered medium*, Bulletin of the Seismological Society of America **73**, 17–43.
- [27] Wang, R. (1999), *A simple orthonormalization method for stable and efficient computation of Green's functions*, Bulletin of the Seismological Society of America **89**(3), 733–741.

- [28] Kausel, E., Roesset, J. (1981), *Stiffness matrices for layered soils*, Bulletin of the Seismological Society of America 71(6), 1743–1761.
- [29] Kausel, E. (2018), *Generalized stiffness matrix method for layered soils*, Soil Dynamics and Earthquake Engineering 115, 663–672.
- [30] Lysmer, J., Waas, G. (1972), *Shear waves in plane infinite structures*, Journal of the Engineering Mechanics Division 98(1), 85–105.
- [31] Sheng, X., Jones, C., Thompson, D. (2004), *A theoretical model for ground vibration from trains generated by vertical track irregularities*, Journal of Sound and Vibration 272, 937–965.
- [32] Nielsen, J., Igeland, A. (1995), *Vertical dynamic interaction between train and track - influence of wheel and track imperfections*, Journal of Sound and Vibration 187(5), 825–839.
- [33] Lei, X., Noda, N. (2002), *Analyses of dynamic response of vehicle and track coupling system with random irregularity of track vertical profile*, Journal of Sound and Vibration 258(1), 147–165.
- [34] Cantero, D., Arvidsson, T., O'Brien, E., Karoumi, R. (2016), *Train-track-bridge modelling and review of parameters*, Structure and Infrastructure Engineering 12(9), 1051–1064.
- [35] Triepaischajonsak, N., Thompson, D. (2015), *A hybrid modelling approach for predicting ground vibration from trains*, Journal of Sound and Vibration 335, 147–173.
- [36] Lei, X., Wang, J. (2014), *Dynamic analysis of the train and slab track coupling system with finite elements in a moving frame of reference*, Journal of Vibration and Control 20(9), 1301–1317.
- [37] Aggestam, E., Nielsen, J., Bolmsvik, R. (2018), *Simulation of vertical dynamic vehicle-track interaction using a two-dimensional slab track model*, Vehicle System Dynamics 56(11), 1633–1657.
- [38] Aggestam, E., Nielsen, J. (2019), *Multi-objective optimisation of transition zones between slab track and ballasted track using a genetic algorithm*, Journal of Sound and Vibration 446, 91–112.
- [39] Nielsen, J., Lombaert, G., François, S. (2015), *A hybrid model for prediction of ground-borne vibration due to discrete wheel/rail irregularities*, Journal of Sound and Vibration 345, 103–120.
- [40] Koroma, S., Thompson, D., Hussein, M., Ntotsios, E. (2017), *A mixed space-time and wavenumber-frequency domain procedure for modelling ground vibration from surface railway tracks*, Journal of Sound and Vibration 400, 508–532.
- [41] Andersen, L., Nielsen, S., Kirkegaard, P. (2001), *Finite element modelling of infinite Euler beams on Kelvin foundations exposed to moving loads in convected co-ordinates*, Journal of Sound and Vibration 241(4), 587–604.

- [42] Andersen, L., Nielsen, S. (2003), *Vibrations of track caused by variation of the foundation stiffness*, Probabilistic Engineering Mechanics **18**(2), 171–184.
- [43] Koh, C., Ong, J., Chua, D., Feng, J. (2003), *Moving element method for train-track dynamics*, Numerical Methods in Engineering **56**(11), 1549–1567.
- [44] Germonpré, M., Nielsen, J., Degrande, G., Lombaert, G. (2018), *Contributions of longitudinal track unevenness and track stiffness variation to railway induced vibration*, Journal of Sound and Vibration **437**, 292–307.
- [45] Lysmer, J., Kuhlemeyer, R. (1969), *Finite dynamic model for infinite media*, Journal of Engineering Mechanics (ASCE) **859**–877.
- [46] Connolly, D., Giannopoulos, A., Forde, M. (2013), *Numerical modelling of ground borne vibrations from high speed rail lines on embankments*, Soil Dynamics and Earthquake Engineering **46**, 13–19.
- [47] Kouroussis, G., Connolly, D., Alexandrou, G., Vogiatzis, K. (2015), *The effect of railway local irregularities on ground vibration*, Transportation Research Part D: Transport and Environment **39**, 17–30.
- [48] Andersen, L., Nielsen, S. (2005), *Reduction of ground vibration by means of barriers or soil improvement along a railway track*, Soil Dynamics and Earthquake Engineering **25**, 701–716.
- [49] Galvín, P., Romero, A., Domínguez, J. (2010), *Fully three-dimensional analysis of high-speed train-track-soil-structure dynamic interaction*, Journal of Sound and Vibration **329**(24), 5147–5163.
- [50] Alves Costa, P., Caçada, R., Silva Cardoso, A., Bodare, A. (2010), *Influence of soil non-linearity on the dynamic response of high-speed railway tracks*, Soil Dynamics and Earthquake Engineering **30**(4), 221–235.
- [51] Alves Costa, P., Caçada, R., Silva Cardoso, A. (2012), *Track-ground vibrations induced by railway traffic: In-situ measurements and validation of a 2.5D FEM-BEM model*, Soil Dynamics and Earthquake Engineering **32**(1), 111–128.
- [52] Galvín, P., François, S., Schevenels, M., Bongini, E., Degrande, G., Lombaert, G. (2010), *A 2.5D coupled FE-BE model for the prediction of railway induced vibrations*, Soil Dynamics and Earthquake Engineering **30**, 1500–1512.
- [53] François, S., Schevenels, M., Galvín, P., Lombaert, G., Degrande, G. (2010), *A 2.5D coupled FE-BE methodology for the dynamic interaction between longitudinally invariant structures and a layered halfspace*, Computer Methods in Applied Mechanics and Engineering **199**(23–24), 1536–1548.
- [54] Chahour, K., Lefeuvre-Mesgouez, G., Mesgouez, A. (2014), *Spectral analysis of a railway track in contact with a multilayered poroviscoelastic soil subjected to a harmonic moving load*, Soil Dynamics and Earthquake Engineering **64**, 24–37.

- [55] Pyl, L., Degrande, G., Clouteau, D. (2004), *Validation of a source-receiver model for road traffic induced vibrations in buildings. ii: receiver model*, Journal of Engineering Mechanics **130**(12), 1394–1406.
- [56] Fiala, P., Degrande, G., Augusztinovicz, F. (2007), *Numerical modelling of ground-borne noise and vibration in buildings due to surface rail traffic*, Journal of Sound and Vibration **301**, 718–738.
- [57] Lopes, P., Alves Costa, P., Ferraz, R., Calçada, R., Silva Cardoso, A. (2014), *Numerical modeling of vibrations induced by railway traffic in tunnels: From the source to the nearby buildings*, Soil Dynamics and Earthquake Engineering **61**, 269–285.
- [58] Lopes, P., Alves Costa, P., Calçada, R., Silva Cardoso, A. (2014), *Influence of soil stiffness on building vibrations due to railway traffic in tunnels: Numerical study*, Computers and Geotechnics **61**, 277–291.
- [59] Connolly, D., Galvín, P., Olivier, B., Romero, A., Kouroussis, G. (2019), *A 2.5D time-frequency domain model for railway induced soil-building vibration due to railway defects*, Soil Dynamics and Earthquake Engineering **120**, 332–344.
- [60] López-Mendoza, D., Romero, A., Connolly, D., Galvín, P. (2017), *Scoping assessment of building vibration induced by railway traffic*, Soil Dynamics and Earthquake Engineering **93**, 147–161.
- [61] Colaço, A., Alves Costa, P., Amado-Mendes, P., Calçada, R. (2021), *Vibrations induced by railway traffic in buildings: Experimental validation of a sub-structuring methodology based on 2.5D FEM-MFS and 3D FEM*, Engineering Structures **240**, 112381.
- [62] Intel (2016), *Intel Math Kernel Library 11.3, Reference Manual*.

Part II

Appended Publications

Paper A



MODELING TRAIN-INDUCED GROUND-BORNE VIBRATIONS USING FEM IN A MOVING FRAME OF REFERENCE

J. Malmberg¹, K. Persson¹ and P. Persson¹

¹Lund University, Department of Construction Sciences
P.O. Box 118 SE-221 00 Lund, Sweden
e-mail: {jens.malmberg,kent.persson,peter.persson}@construction.lth.se

Keywords: Train-induced ground-vibration, moving frame of reference, Kirchhoff plate slab track.

Abstract. *To predict ground-borne vibration levels caused by railway traffic, models for estimating the load from the vibration source, as well as the vibration transmission through the ground, are needed. In the present paper, a finite element formulation in a frame of reference following the moving load, is used for modeling a railway slab track. The response of the underlying soil is represented through a dynamic stiffness matrix, obtained via the Green's function for a horizontally layered visco-elastic half-space in a moving frame of reference in the frequency–wavenumber domain. The track can be modeled as continuously connected beams, but the use of plate elements allows for more general stress and displacement distributions in the transverse direction of the slab to be resolved. Here, the free-field response due to a harmonic load moving along a slab track, is evaluated and compared using different modeling strategies for the slab.*

1 INTRODUCTION

To predict the level of ground-borne vibration caused by railway traffic, models are needed to estimate the load from the vibration source as well as the vibration transmission through the ground. A number of techniques have been developed in the past decades to study ground vibrations caused by a passing train, ranging from empirical methods to analytical and numerical schemes.

Numerical schemes are often based on either the finite element (FE) or the boundary element (BE) method or a combination thereof. The strength of these methods lies in their ability to model arbitrary geometries and discontinuities. The downside is the high computational cost. The computational cost can be reduced if the soil and track system is assumed to be invariant in the track direction, leading to so called 2.5D models [1, 2, 3, 4]. Further, if the soil stratification is assumed to consist of horizontally layered visco-elastic layers, a fundamental solution (Green's function) for the soil response can be found efficiently in frequency–wavenumber domain. Sheng et al [5, 6] proposed a semi-analytical model, with the track represented by an infinite layered beam resting on a layered ground, where both the ground and the beam is described in the frequency–wavenumber domain. Kaynia et al [7] coupled a series of FE beams, representing the railway track, to a dynamic stiffness matrix of the ground calculated from the Green's function of a layered half-space.

Modeling the track as a beam on a layered half-space is a common approach in the field of ground-borne vibrations due to railway traffic. This approach, however, constricts the track–soil interface stress distribution. Steenbergen et al [8] studied the influence of different interface conditions between a beam on a half-space, subjected to a dynamic moving load, on the free-field response, using a semi-analytical model in the frequency–wavenumber domain. Galvin et al [4] compared the free-field response of a high-speed train passage on a ballasted track on an embankment, calculated using a 2.5D continuum model, to a model with a beam representation of the track, finding large differences attributed to the rigid cross-section of the embankment in the beam model.

In the present paper, a FE model is used for representing a railway slab track. The response of the underlying soil is represented by a dynamic stiffness matrix obtained via the Green's function for a horizontally layered visco-elastic half-space. The model is formulated in a frame of reference following the moving load. The slab and rails can either be modeled as continuously connected beams or by using Kirchhoff plate elements for representing the track slab. Plate elements allow for more general stress and displacement distributions in the track transversal direction to be resolved. Here, the free-field response due to a harmonic load moving along the track at constant velocity, is calculated and compared using different modeling strategies for the track.

In Section 2 an overview of the model is given and the studied case is presented in Section 3. Finally, conclusions are given in Section 4.

2 CALCULATION MODEL

2.1 Overview

The slab track is shown principally in Figure 1. It consists of a supporting layer, a concrete slab, rails and rail pads. Full interaction is assumed between the slab and the supporting layer, so that a homogeneous section with equivalent mass and bending stiffness may be utilized in the calculations. This homogeneous section is simply referred to as the slab in the following.

Three models, model a)–c), with different assumptions regarding the slab and the slab–soil

interface conditions, are established:

- a) The slab is modeled with Bernoulli-Euler beam elements. Displacement continuity of the beam and the soil is enforced only along the beam center line. A uniform stress distribution between the beam and the soil is assumed in the transverse direction of the slab.
- b) The slab is modeled with Bernoulli-Euler beam elements. The slab–soil interface is assumed rigid in the transverse direction. This is enforced by coupling the beam kinematically to a number of soil DoFs in the transverse direction over the width of the slab.
- c) The slab is modeled with Kirchhoff plate elements, allowing for a more general slab–soil interface stress and displacement distribution in the transverse direction of the slab than by the two other models.

In all three models, the rails are modeled as Bernoulli-Euler beams, connected to the slab via a continuous visco-elastic interface layer representing the rail pads. The loading is assumed identical on both rails, hence in model a) and b) the two rails are modeled as one. In model c) symmetry around the track center line is utilized so that only half the track is modeled. The track is coupled to a ground model, represented by a dynamic stiffness matrix. The dynamic stiffness matrix of the ground is derived from the Green’s function for a horizontally layered visco-elastic half-space. Both the ground model and the FE model are expressed in a moving frame of reference, following the vehicle at a given speed v . The models a)–c) are shown schematically in Figure 2.

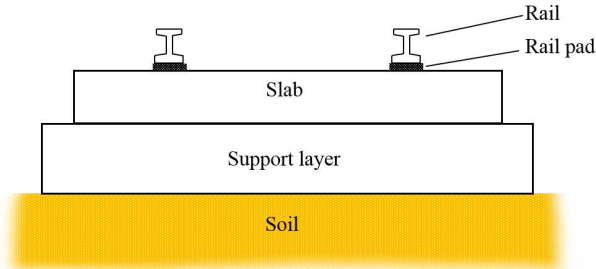


Figure 1: Section of slab track.

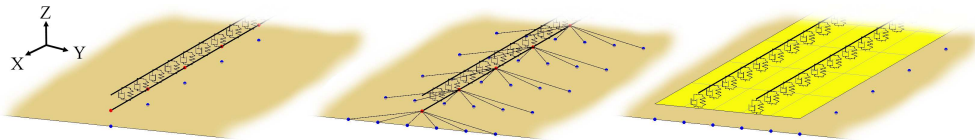


Figure 2: Finite element models of the slab track. From the left: Models a), b) and c). Blue points represent soil nodes at the slab–soil interface.

The soil model is described in Section 2.2. In Section 2.3 the governing equations for the beam, plate and interface finite elements are derived. The coupling between the finite elements and the soil is described in Section 2.4.

2.2 Soil model

The ground is assumed to be composed of horizontal visco-elastic layers. Neglecting body forces, the Navier equations for a single soil layer can be written as

$$(\lambda + \mu) \frac{\partial^2 u_j}{\partial x_i \partial x_j} + \mu \frac{\partial^2 u_i}{\partial x_j \partial x_j} = \rho \frac{\partial^2 u_i}{\partial t^2} \quad (1)$$

where $u_i = u_i(x_1, x_2, x_3, t)$ is the displacement in direction i . λ and μ are the Lamé' parameters. Introducing a coordinate transformation as

$$(\tilde{x}_1, \tilde{x}_2, \tilde{x}_3) = (x_1 - vt, x_2, x_3), \quad (2)$$

where $\tilde{x}_1, \tilde{x}_2, \tilde{x}_3$ denotes the coordinates in the moving frame of reference, and v is the vehicle speed, transforms the Navier equations to

$$(\lambda + \mu) \frac{\partial^2 \tilde{u}_j}{\partial \tilde{x}_i \partial \tilde{x}_j} + \mu \frac{\partial^2 \tilde{u}_i}{\partial \tilde{x}_j \partial \tilde{x}_j} = \rho \left(\frac{\partial^2 \tilde{u}_i}{\partial t^2} - 2v \frac{\partial^2 \tilde{u}_i}{\partial t \partial \tilde{x}_1} + v^2 \frac{\partial^2 \tilde{u}_i}{\partial \tilde{x}_1^2} \right), \quad (3)$$

where $\tilde{u}_i = \tilde{u}_i(\tilde{x}, \tilde{y}, \tilde{z}, t)$ is the displacement in the moving frame of reference [9].

Fourier transforming the Navier equations with respect to the horizontal coordinates and time, $(\tilde{x}_1, \tilde{x}_2, t)$, yields the Navier equations in frequency–wavenumber domain as

$$(\lambda + \mu) \tilde{\Delta} i \tilde{k}_1 + \mu \left(\frac{d^2}{d\tilde{x}_3^2} - \tilde{k}_1^2 - \tilde{k}_2^2 \right) \tilde{U}_1 = -\rho \tilde{\omega}^2 \tilde{U}_1 \quad (4a)$$

$$(\lambda + \mu) \tilde{\Delta} i \tilde{k}_2 + \mu \left(\frac{d^2}{d\tilde{x}_3^2} - \tilde{k}_1^2 - \tilde{k}_2^2 \right) \tilde{U}_2 = -\rho \tilde{\omega}^2 \tilde{U}_2 \quad (4b)$$

$$(\lambda + \mu) \frac{d\tilde{\Delta}}{d\tilde{x}_3} + \mu \left(\frac{d^2}{d\tilde{x}_3^2} - \tilde{k}_1^2 - \tilde{k}_2^2 \right) \tilde{U}_3 = -\rho \tilde{\omega}^2 \tilde{U}_3 \quad (4c)$$

where $\tilde{\Delta} = \tilde{\Delta}(\tilde{k}_1, \tilde{k}_2, \tilde{x}_3, \omega)$ is the Fourier transform, with respect to the horizontal coordinates and time, of the dilation $\Delta(\tilde{x}_1, \tilde{x}_2, \tilde{x}_3, t)$. The vibration frequency of a material point is $\tilde{\omega} = \omega - \tilde{k}_1 v$ and ω is the frequency of the moving load. The horizontal wavenumbers in the direction of \tilde{x}_1 and \tilde{x}_2 are \tilde{k}_1 and \tilde{k}_2 , respectively.

As showed by Sheng [5, 6], the solution to Eq. 4 for an individual layer can be found analytically, and due to continuity of displacements and tractions over interfaces between layers, several layers can be assembled using the Thomson [10] and Haskell [11] layer transfer matrix approach, forming a relationship between the displacement and stresses at the top of the stratum and at the bottom of the stratum. With known boundary conditions at the lowest interface, a relationship between the traction and the displacement at the surface can be obtained as

$$\hat{\mathbf{u}} = \hat{\mathbf{G}} \hat{\mathbf{p}}, \quad (5)$$

where $\hat{\mathbf{u}} = \hat{\mathbf{u}}(\tilde{k}_1, \tilde{k}_2, \omega)$ and $\hat{\mathbf{p}} = \hat{\mathbf{p}}(\tilde{k}_1, \tilde{k}_2, \omega)$ are vectors containing the displacements and tractions respectively on the soil surface, $\hat{\mathbf{G}} = \hat{\mathbf{G}}(\tilde{k}_1, \tilde{k}_2, \omega)$ is the Green's function tensor, \tilde{k}_1 and \tilde{k}_2 are the horizontal wavenumbers. For certain frequencies and stratifications, the original Thomson and Haskell method suffers from loss-of-precision. To avoid these problems in the present work, the different soil layers are assembled in an orthonormalization procedure as proposed by Wang [12].

Equation 5 is evaluated for a set of discrete values of \tilde{k}_1 and \tilde{k}_2 , and the displacement vector $\tilde{\mathbf{u}}(\tilde{x}_1, \tilde{x}_2, \omega)$ is obtained in Cartesian space through a double inverse Fourier transform of $\tilde{\mathbf{u}}(\tilde{k}_1, \tilde{k}_2, \omega)$.

The procedure described above is used for calculating the response on the soil surface, due to a unit load with a rectangular spatial distribution, the size of which is determined by the element size in the connecting superstructure. From this single load case, a dynamic flexibility matrix $\mathbf{F}_g(\omega, v)$ is established for a set of DoFs where the superstructure interacts with the soil surface. These DoFs will be referred to as soil–structure interaction (SSI) DoFs. \mathbf{F}_g is formed, column by column, by interpolating from $\tilde{\mathbf{u}}$. The flexibility matrix is then inverted to form the dynamic stiffness matrix of the soil, $\mathbf{D}_g(\omega, v) = \mathbf{F}_g^{-1}(\omega, v)$, which gives a relation between the steady-state displacements $\tilde{\mathbf{u}}_g$ and forces $\tilde{\mathbf{f}}_g$ for the SSI DoFs, at a certain load circular frequency ω and velocity v , as

$$\mathbf{D}_g \tilde{\mathbf{u}}_g = \tilde{\mathbf{f}}_g. \quad (6)$$

2.3 Finite element model of railway structure

The coordinate transformation used for expressing the governing FE equations in a moving frame of reference introduces convective terms in the damping and stiffness matrices. In Sections 2.3.1–2.3.3 below, the FE equations are derived for the beams, plates and visco-elastic interface elements, respectively.

2.3.1 Beam elements

The equilibrium equation for a Bernoulli-Euler beam reads

$$\frac{\partial^2 M}{\partial x^2} + q - m_b \frac{\partial^2 w}{\partial t^2} = 0, \quad (7)$$

where $M = M(x, t)$ is the bending moment. $q(x, t)$ is a loading force per unit length. m_b is the mass per unit length of the beam. $w = w(x, t)$ is the deflection. With the coordinate transformation described by Eq. 2, Eq. 7 can be written as

$$\frac{\partial^2 \tilde{M}}{\partial \tilde{x}^2} + \tilde{q} - m_b \left(\frac{\partial^2 \tilde{w}}{\partial t^2} - 2v \frac{\partial^2 \tilde{w}}{\partial \tilde{x} \partial t} + v^2 \frac{\partial^2 \tilde{w}}{\partial \tilde{x}^2} \right) = 0, \quad (8)$$

where $\tilde{\cdot}$ denotes that a variable is expressed in the moving frame of reference. The weak form is obtained by multiplying Eq. 8 by an arbitrary weight function $g = g(\tilde{x})$ and integrating it over the region. It can be shown that the resulting weak form for the Bernoulli-Euler beam in a moving frame of reference is

$$\int_a^b \frac{\partial^2 g}{\partial \tilde{x}^2} \tilde{M} dx - \left[\frac{\partial g}{\partial \tilde{x}} \tilde{M} \right]_a^b + [g \tilde{V}]_a^b + \int_a^b g \tilde{q} dx - m_b \int_a^b g \left(\frac{\partial^2 \tilde{w}}{\partial t^2} - 2v \frac{\partial^2 \tilde{w}}{\partial \tilde{x} \partial t} + v^2 \frac{\partial^2 \tilde{w}}{\partial \tilde{x}^2} \right) dx = 0. \quad (9)$$

With the kinematic and constitutive assumptions for a Bernoulli-Euler beam, \tilde{M} can be written as

$$\tilde{M} = -EI \frac{\partial^2 \tilde{w}}{\partial \tilde{x}^2}, \quad (10)$$

where EI is the bending stiffness. To obtain the FE formulation, the deflection $\tilde{w}(\tilde{x}, t)$ is approximated using the element nodal values $\mathbf{a}(t)$ and the shape functions $\mathbf{N}(\tilde{x})$, as $\tilde{w} = \mathbf{N}\mathbf{a}$.

Adopting the Galerking method, the mass, damping and stiffness matrices, as well as the load and boundary vectors, are identified as

$$\mathbf{K} = EI \int_a^b \left(\frac{d^2 \mathbf{N}(\tilde{x})}{d\tilde{x}^2} \right)^T \frac{d^2 \mathbf{N}(\tilde{x})}{d\tilde{x}^2} dx + m_b v^2 \int_a^b \mathbf{N}^T \frac{d^2 \mathbf{N}}{d\tilde{x}^2} dx, \quad (11)$$

$$\mathbf{C} = -2m_b v \int_a^b \mathbf{N}^T \frac{d\mathbf{N}}{d\tilde{x}} dx, \quad (12)$$

$$\mathbf{M} = m_b \int_a^b \mathbf{N}^T \mathbf{N} dx, \quad (13)$$

$$\mathbf{f}_l = \int_a^b \mathbf{N}^T \tilde{q} dx, \quad (14)$$

$$\mathbf{f}_b = [\mathbf{N}^T \tilde{V}]_a^b - \left[\frac{\partial \mathbf{N}^T}{\partial \tilde{x}} \tilde{M} \right]_a^b. \quad (15)$$

A 2-node beam element with two DoFs per node (vertical displacement and one rotation), based on the above formulation, is implemented and used in the present work. Similar derivations for the convective Bernoulli-Euler beams can be found in e.g. [13, 14].

2.3.2 Plate elements

The equilibrium equation for a Kirchhoff plate reads, see e.g. [15],

$$\frac{\partial^2 M_{xx}}{\partial x^2} + 2 \frac{\partial^2 M_{xy}}{\partial x \partial y} + \frac{\partial^2 M_{yy}}{\partial y^2} + q - \rho h \frac{\partial^2 w}{\partial t^2} = 0, \quad (16)$$

where $M_{xx} = M_{xx}(x, y, t)$, $M_{yy} = M_{yy}(x, y, t)$ and $M_{xy} = M_{xy}(x, y, t)$ are the bending moments in the x - and y -directions. $q(x, y, t)$ is a loading force per unit area. h and ρ is the plate thickness and the mass density respectively. $w = w(x, y, t)$ is the deflection of the mid-section. With the coordinate transformation described by Eq. 2, Eq. 16 can be written as

$$\frac{\partial^2 \tilde{M}_{xx}}{\partial \tilde{x}^2} + 2 \frac{\partial^2 \tilde{M}_{xy}}{\partial \tilde{x} \partial \tilde{y}} + \frac{\partial^2 \tilde{M}_{yy}}{\partial \tilde{y}^2} + \tilde{q} - \rho h \left(\frac{\partial^2 \tilde{w}}{\partial t^2} - 2v \frac{\partial^2 \tilde{w}}{\partial \tilde{x} \partial t} + v^2 \frac{\partial^2 \tilde{w}}{\partial \tilde{x}^2} \right) = 0. \quad (17)$$

The weak form is obtained by multiplying Eq. 17 by an arbitrary weight function $g = g(\tilde{x}, \tilde{y})$ and integrating it over the region. It can be shown that the resulting weak form for the Kirchhoff plate in a moving frame of reference is

$$\int_A (\tilde{\nabla} g)^T \tilde{\mathbf{M}} dA - \oint_{\mathcal{L}} \frac{dg}{dn} \tilde{M}_{nn} d\mathcal{L} + \oint_{\mathcal{L}} g (\tilde{V}_{nz} + \frac{d\tilde{M}_{nm}}{dm}) d\mathcal{L} + \int_A g \tilde{q} dA - \rho h \int_A \left(g \frac{\partial^2 \tilde{w}}{\partial t^2} - 2vg \frac{\partial^2 \tilde{w}}{\partial \tilde{x} \partial t} + v^2 g \frac{\partial^2 \tilde{w}}{\partial \tilde{x}^2} \right) dA = 0, \quad (18)$$

where the matrix differential operator $\tilde{\nabla}$ is defined as

$$\tilde{\nabla} = \left[\frac{\partial^2}{d\tilde{x}^2} \quad \frac{\partial^2}{d\tilde{y}^2} \quad 2 \frac{\partial^2}{d\tilde{x} d\tilde{y}} \right]^T, \quad (19)$$

and the moment vector $\tilde{\mathbf{M}}$ as

$$\tilde{\mathbf{M}} = \tilde{\mathbf{M}}(\tilde{x}, \tilde{y}, t) = [\tilde{M}_{xx}(x, y, t) \quad \tilde{M}_{yy}(x, y, t) \quad \tilde{M}_{xy}(x, y, t)]^T. \quad (20)$$

The constitutive equation for the cross-section of a Kirchhoff plate can be written as $\tilde{\mathbf{M}} = -(h^3/12)\mathbf{D}\tilde{\nabla}\tilde{w}$ where \mathbf{D} is the plane stress constitutive matrix for isotropic elasticity. To obtain the FE formulation, the deflection $\tilde{w}(\tilde{x}, \tilde{y}, t)$ is approximated using the element nodal values $\mathbf{a}(t)$ and the shape functions $\mathbf{N}(\tilde{x}, \tilde{y})$, as $\tilde{w} = \mathbf{N}\mathbf{a}$.

Adopting the Galerking method, the mass, damping and stiffness matrices, as well as the load and boundary vectors, are identified as

$$\mathbf{K} = \frac{h^3}{12} \int_A (\tilde{\nabla}\mathbf{N})^T \mathbf{D} (\tilde{\nabla}\mathbf{N}) dA + \rho h v^2 \int_A \mathbf{N}^T \frac{\partial^2 \mathbf{N}}{\partial \tilde{x}^2} dA, \quad (21)$$

$$\mathbf{C} = -2\rho h v \int_A \mathbf{N}^T \frac{\partial \mathbf{N}}{\partial \tilde{x}} dA, \quad (22)$$

$$\mathbf{M} = \rho h \int_A \mathbf{N}^T \mathbf{N} dA, \quad (23)$$

$$\mathbf{f}_l = \int_A \mathbf{N}^T \tilde{q} dA, \quad (24)$$

$$\mathbf{f}_b = \oint_{\mathcal{L}} \mathbf{N}^T (\tilde{V}_{nz} + \frac{d\tilde{M}_{nm}}{dm}) d\mathcal{L} - \oint_{\mathcal{L}} (\nabla\mathbf{N})^T \mathbf{n} \tilde{M}_{nm} d\mathcal{L}. \quad (25)$$

A 4-node rectangular element with three DoFs per node (vertical displacement and two rotations), based on the above formulation, is implemented and used in the present work.

2.3.3 Visco-elastic interface elements

The rail pads are modeled by visco-elastic interface elements, representing continuous springs and dashpots. In the following derivation of the equations for the interface elements, an interface element is assumed to be located between two beam elements parallel with the x -axis. The loads on the upper and lower beams due to the visco-elastic interface are written

$$q_u(x, y, t) = -k(w_u - w_l) - c\left(\frac{\partial w_u}{\partial t} - \frac{\partial w_l}{\partial t}\right) = 0, \quad (26)$$

$$q_l(x, y, t) = -k(w_l - w_u) - c\left(\frac{\partial w_l}{\partial t} - \frac{\partial w_u}{\partial t}\right) = 0, \quad (27)$$

where $w_u = w_u(x, t)$ and $w_l = w_l(x, t)$ is the deflection in the upper and lower beam respectively, k is the spring stiffness and c is the damping coefficient. With the coordinate transformation described by Eq. 2,

$$\tilde{q}_u(\tilde{x}, t) = -k(\tilde{w}_u - \tilde{w}_l) - c\left\{\left(\frac{\partial \tilde{w}_u}{\partial t} - \frac{\partial \tilde{w}_l}{\partial t}\right) - v\left(\frac{\partial \tilde{w}_u}{\partial \tilde{x}} - \frac{\partial \tilde{w}_l}{\partial \tilde{x}}\right)\right\}, \quad (28)$$

$$\tilde{q}_l(\tilde{x}, t) = -k(\tilde{w}_l - \tilde{w}_u) - c\left\{\left(\frac{\partial \tilde{w}_l}{\partial t} - \frac{\partial \tilde{w}_u}{\partial t}\right) - v\left(\frac{\partial \tilde{w}_l}{\partial \tilde{x}} - \frac{\partial \tilde{w}_u}{\partial \tilde{x}}\right)\right\}. \quad (29)$$

The displacements of the upper and lower beam, w_u and w_l , are approximated using the shape functions \mathbf{N}_u and \mathbf{N}_l and element nodal displacements $\mathbf{a}_u(t)$ and $\mathbf{a}_l(t)$ for the upper and lower beams, respectively. With Eq. 14 the load vectors for the respective beams can be written

$$\begin{aligned} \mathbf{f}_{l_u} = & \int_a^b \mathbf{N}_u^T \tilde{q}_u dx = -k \left\{ \int_a^b \mathbf{N}_u^T \mathbf{N}_u dx \mathbf{a}_u - \int_a^b \mathbf{N}_u^T \mathbf{N}_l dx \mathbf{a}_l \right\} - \\ & c \left\{ \int_a^b \mathbf{N}_u^T \mathbf{N}_u dx \dot{\mathbf{a}}_u + \int_a^b \mathbf{N}_u^T \mathbf{N}_l dx \dot{\mathbf{a}}_l \right\} + c v \left\{ \int_a^b \mathbf{N}_u^T \frac{\partial \mathbf{N}_u}{\partial \tilde{x}} dx \mathbf{a}_u - \int_a^b \mathbf{N}_u^T \frac{\partial \mathbf{N}_l}{\partial \tilde{x}} dx \mathbf{a}_l \right\}, \end{aligned} \quad (30)$$

$$\begin{aligned} \mathbf{f}_{l_i} = & \int_a^b \mathbf{N}_l^T \tilde{q}_l dx = -k \left\{ \int_a^b \mathbf{N}_l^T \mathbf{N}_l dx \mathbf{a}_l - \int_a^b \mathbf{N}_l^T \mathbf{N}_u dx \mathbf{a}_u \right\} - \\ & c \left\{ \int_a^b \mathbf{N}_l^T \mathbf{N}_l dx \dot{\mathbf{a}}_l + \int_a^b \mathbf{N}_l^T \mathbf{N}_u dx \dot{\mathbf{a}}_u \right\} + cv \left\{ \int_a^b \mathbf{N}_l^T \frac{\partial \mathbf{N}_l}{\partial \tilde{x}} dx \mathbf{a}_l - \int_a^b \mathbf{N}_l^T \frac{\partial \mathbf{N}_u}{\partial \tilde{x}} dx \mathbf{a}_u \right\}. \end{aligned} \quad (31)$$

With the shape function vectors $\tilde{\mathbf{N}}_u$ and $\tilde{\mathbf{N}}_l$ and the displacement vector \mathbf{a} defined as

$$\begin{aligned} \tilde{\mathbf{N}}_u(\tilde{x}, \tilde{y}) &= [\mathbf{N}_u \quad 0\mathbf{N}_l], \quad \tilde{\mathbf{N}}_l(\tilde{x}, \tilde{y}) = [0\mathbf{N}_u \quad \mathbf{N}_l] \\ \tilde{\mathbf{f}}_{l_u}(t) &= [\mathbf{f}_{l_u} \quad 0\mathbf{f}_{l_l}], \quad \tilde{\mathbf{f}}_{l_l}(t) = [0\mathbf{f}_{l_u} \quad \mathbf{f}_{l_l}], \quad \mathbf{f}_L(t) = [\mathbf{f}_{l_u} \quad \mathbf{f}_{l_l}]^T \\ \tilde{\mathbf{a}}_u(t) &= [\mathbf{a}_u \quad 0\mathbf{a}_l], \quad \tilde{\mathbf{a}}_l(t) = [0\mathbf{a}_u \quad \mathbf{a}_l], \quad \mathbf{a}(t) = [\mathbf{a}_u \quad \mathbf{a}_l]^T \end{aligned} \quad (32)$$

it is possible to write the load vector as

$$\begin{aligned} \mathbf{f}_L(t) &= \tilde{\mathbf{f}}_{l_u}(t) + \tilde{\mathbf{f}}_{l_l}(t) = \\ & -k \left\{ \int_a^b \tilde{\mathbf{N}}_u^T \tilde{\mathbf{N}}_u dx + \int_a^b \tilde{\mathbf{N}}_l^T \tilde{\mathbf{N}}_l dx - \int_a^b \tilde{\mathbf{N}}_u^T \tilde{\mathbf{N}}_l dx - \int_a^b \tilde{\mathbf{N}}_l^T \tilde{\mathbf{N}}_u dx \right\} \mathbf{a} \\ & -c \left\{ \int_a^b \tilde{\mathbf{N}}_u^T \tilde{\mathbf{N}}_u dx + \int_a^b \tilde{\mathbf{N}}_l^T \tilde{\mathbf{N}}_l dx + \int_a^b \tilde{\mathbf{N}}_u^T \tilde{\mathbf{N}}_l dx + \int_a^b \tilde{\mathbf{N}}_l^T \tilde{\mathbf{N}}_u dx \right\} \dot{\mathbf{a}} \\ & +cv \left\{ \int_a^b \tilde{\mathbf{N}}_u^T \frac{\partial \tilde{\mathbf{N}}_u}{\partial \tilde{x}} dx + \int_a^b \tilde{\mathbf{N}}_l^T \frac{\partial \tilde{\mathbf{N}}_l}{\partial \tilde{x}} dx - \int_a^b \tilde{\mathbf{N}}_u^T \frac{\partial \tilde{\mathbf{N}}_l}{\partial \tilde{x}} dx - \int_a^b \tilde{\mathbf{N}}_l^T \frac{\partial \tilde{\mathbf{N}}_u}{\partial \tilde{x}} dx \right\} \mathbf{a}. \end{aligned} \quad (33)$$

The vector $\mathbf{f}_L(t)$ collects the forces on the upper and lower beam, caused by the interface element. The forces on the interface element are therefore $\mathbf{f}_i(t) = -\mathbf{f}_L(t)$, and the stiffness and damping matrices of the interface element can be identified from Eq. 33 as

$$\begin{aligned} \mathbf{K} &= k \left\{ \int_a^b \tilde{\mathbf{N}}_u^T \tilde{\mathbf{N}}_u dx + \int_a^b \tilde{\mathbf{N}}_l^T \tilde{\mathbf{N}}_l dx - \int_a^b \tilde{\mathbf{N}}_u^T \tilde{\mathbf{N}}_l dx - \int_a^b \tilde{\mathbf{N}}_l^T \tilde{\mathbf{N}}_u dx \right\} \\ & -cv \left\{ \int_a^b \tilde{\mathbf{N}}_u^T \frac{\partial \tilde{\mathbf{N}}_u}{\partial \tilde{x}} dx + \int_a^b \tilde{\mathbf{N}}_l^T \frac{\partial \tilde{\mathbf{N}}_l}{\partial \tilde{x}} dx - \int_a^b \tilde{\mathbf{N}}_u^T \frac{\partial \tilde{\mathbf{N}}_l}{\partial \tilde{x}} dx - \int_a^b \tilde{\mathbf{N}}_l^T \frac{\partial \tilde{\mathbf{N}}_u}{\partial \tilde{x}} dx \right\}, \end{aligned} \quad (34)$$

$$\mathbf{C} = c \left\{ \int_a^b \tilde{\mathbf{N}}_u^T \tilde{\mathbf{N}}_u dx + \int_a^b \tilde{\mathbf{N}}_l^T \tilde{\mathbf{N}}_l dx - \int_a^b \tilde{\mathbf{N}}_u^T \tilde{\mathbf{N}}_l dx - \int_a^b \tilde{\mathbf{N}}_l^T \tilde{\mathbf{N}}_u dx \right\}. \quad (35)$$

The above expressions are also valid for an interface element between a beam element overlying a plate element in the xy -plane, such as in model c), with the shape functions for the plate evaluated at the y -coordinate of the beam.

2.4 Coupling to soil

Assuming steady-state conditions, the governing equation for the railway track structure can be written as

$$(-\omega^2 \mathbf{M}_r + i\omega \mathbf{C}_r + \mathbf{K}_r) \tilde{\mathbf{u}}_r = \tilde{\mathbf{f}}_r, \quad (36)$$

or

$$\mathbf{D}_r \tilde{\mathbf{u}}_r = \tilde{\mathbf{f}}_r, \quad (37)$$

where \mathbf{M}_r , \mathbf{C}_r and \mathbf{K}_r is the mass, damping and stiffness matrix respectively. $\mathbf{D}_r = (-\omega^2 \mathbf{M}_r + i\omega \mathbf{C}_r + \mathbf{K}_r)$ is the dynamic stiffness matrix, and $\tilde{\mathbf{u}}_r$ and $\tilde{\mathbf{f}}_r$ is the displacement and force vector for the track structure, respectively.

The track and soil is coupled in a standard FE manner. Only the vertical DoFs of the track structure and the soil are coupled. A global system of equations for the soil and the railway structure is formed by combining Eqs. 6 and 37, yielding

$$\mathbf{D}_t \tilde{\mathbf{u}}_r = \tilde{\mathbf{f}}_r, \quad (38)$$

where \mathbf{D}_t represents the total dynamic stiffness matrix for the track structure and soil.

Once the track displacements $\tilde{\mathbf{u}}_r$, and thereby also the displacement in the soil DoFs $\tilde{\mathbf{u}}_g$, have been obtained by solving Eq. 38, the corresponding forces on the soil surface, $\tilde{\mathbf{f}}_g$ are calculated by Eq. 6. A second flexibility matrix $\mathbf{F}_{gf}(\omega, v)$ is established, in the same manner as $\mathbf{F}_g(\omega, v)$ as described in Section 2.2, expressing the displacements in free-field due to forces on the soil–structure interface. The free-field displacements, $\tilde{\mathbf{u}}_f$, are then calculated as

$$\tilde{\mathbf{u}}_f = \mathbf{F}_{gf} \tilde{\mathbf{f}}_g. \quad (39)$$

3 MODEL COMPARISON

To compare the effect of the three different modeling strategies for the track on the free-field response, each model is used for evaluating the response to a moving unit harmonic point load acting on the rail. The track properties are given in Table 1. The track rests on a 14 m deep layer of clay overlaying a half-space, with properties according to Table 2. An element length of 0.3 m is used, meaning that 12 elements are used in the transverse direction of the slab in model c). For model b) the slab is rigidly connected to 13 soil DoFs in the transverse direction. In all three models, the number of elements in the track direction is 500, yielding a total track length of 150 meters, which has been found to be sufficient to avoid problems with reflecting waves at the boundaries of the FE model in the studied case. The track gauge is 1.435 m.

Figure 3 shows the wavefield and the track deformation due to a harmonic point load with frequency $f = 50$ Hz traveling at $v = 60$ m/s, as obtained with the three different models. The difference in the slab deformation in the transverse direction due to the different modeling approaches is clearly visible. The displacements shown in Figure 3 are in the moving frame of reference, following the load at speed $v = 60$ m/s. In this frame of reference, the displacements are in steady state with the loading frequency $f = 50$ Hz. For a fixed point in the free-field, however, the response is transient and contains a broad band of frequencies due to the Doppler effect. A higher load speed results in a broader frequency content of the response in a fixed point. This can be seen in Figure 4 that shows the displacement spectrum for a fixed point 10 m and 25 m from the track, due to a harmonic 50 Hz load travelling at $v = 30$ m/s and $v = 60$ m/s. All three models yield similar results, however, the response obtained with model c) using plate elements is slightly higher than obtained with the other two models, for this particular load frequency.

To compare the three models for a range of excitation frequencies, a moving rms-value of the vibration velocity in a fixed point is calculated for each excitation frequency f , as

$$v_{rms}(t) = \sqrt{\frac{1}{T} \int_t^{t+T} \dot{u}(t)^2 dt}, \quad (40)$$

where $\dot{u}(t)$ is the velocity time history response for a fixed point. T is the window length and is here set to $T = 1$ s. In Figure 5 the maximum of $v_{rms}(t)$ is shown for each excitation frequency for the three models, for a fixed point located 10 and 25 m from the track respectively and the load speeds $v = 30$ and $v = 60$ m/s. For both load speeds, and both distances, the free-field response is very similar for all three models up to about $f = 50$ Hz. At higher frequencies, both models a) and b) underestimate the response. However, the underestimation with model b) is modest. For model a) the maximum underestimation is almost 10 dB at 70 Hz.

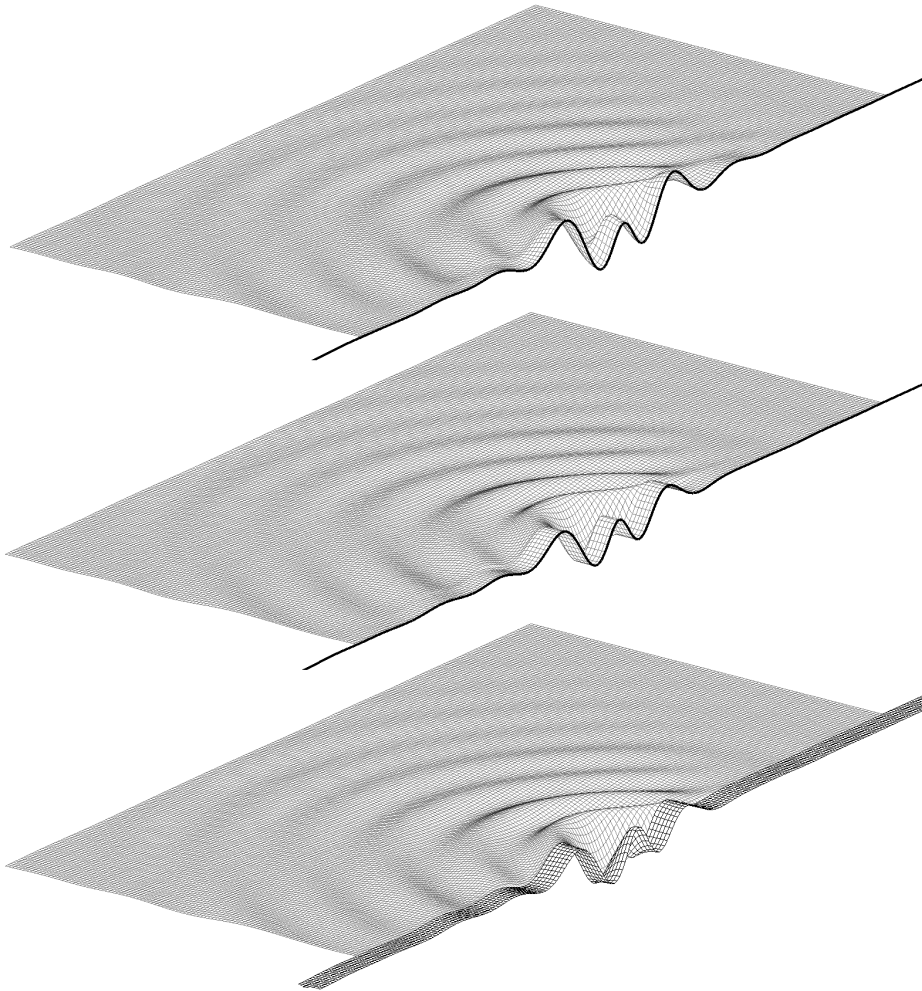


Figure 3: Soil and slab displacements in models a)–c), from top to bottom, when subjected to a harmonic load with frequency $f = 50$ Hz moving along the track at speed $v = 60$ m/s. The size of the displayed area is $60 \text{ m} \times 30 \text{ m}$.

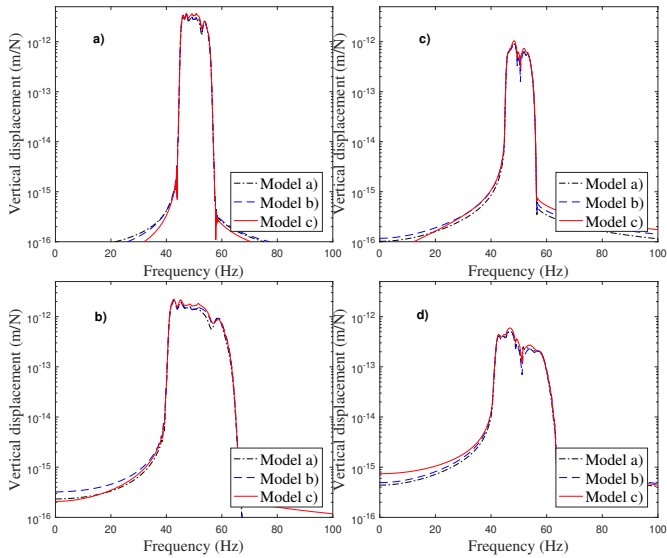


Figure 4: Response of a fixed point in the free-field due to a 50 Hz load traveling on the track. a) and b) show the results for a fixed point 10 meters from the track, with a load speed of $v = 30$ and $v = 60$ m/s, respectively. c) and d) are for a point 25 meters from the track.

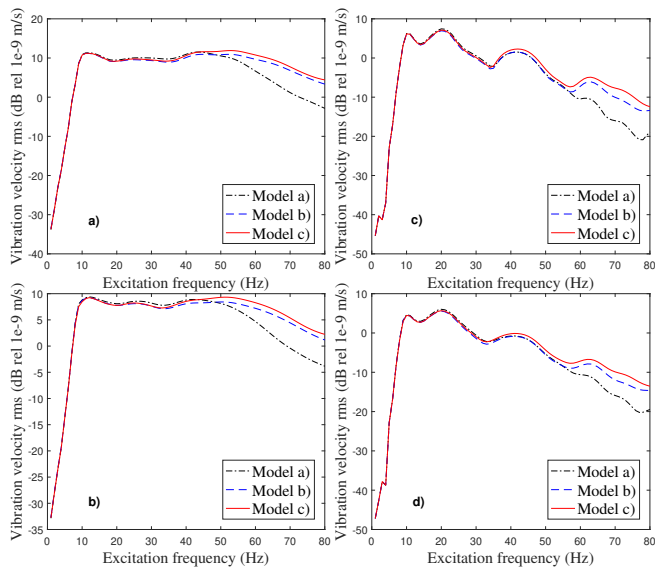


Figure 5: Velocity rms-value of a fixed point in the free-field due to a harmonic load traveling on the track. a) and b) show the results for a fixed point 10 meters from the track, with a load speed of $v = 30$ and $v = 60$ m/s, respectively. c) and d) are for a point 25 meters from the track.

	Parameter	Value
Rail	Mass (kg/m)	60
	Young's modulus (GPa)	210
	Second moment of inertia (m ⁴)	3.217×10^{-5}
	Loss factor (-)	0.01
Rail	Stiffness (MN/m ²)	92
pads	Damping (kNs/m ²)	73
Slab + support layer	Density (kg/m ³)	2310
	Young's modulus (GPa)	26.7
	Poisson's ratio	0.2
	Width (m)	3.6
	Thickness (m)	0.55
	Loss factor (-)	0.04

Table 1: Track properties.

4 CONCLUSIONS

In the paper a numerical prediction model for train-induced ground-vibration has been presented. The model is formulated in a frame of reference following the moving load, which offers some advantages over conventional FE models using a fixed frame of reference. Using a fixed frame of reference, the computational domain must be large for the moving load to stay within the model during the time of analysis. In the moving frame of reference following the load, on the other hand, the load stays at the same location in the model throughout the analysis, allowing a smaller model. Furthermore, frequency domain methods can be used for analyzing the moving load. A drawback of the model is that it is not suitable for analyzing load cases where the resulting wavelengths are very short, such as moving loads approaching the soil shear wave velocity. Short wavelengths, making the current approach inappropriate, may also result from non-moving loads, depending on the soil and track stiffness and the frequency of the load.

Three different models of a railway slab track have been established and compared. In the first two models, the railway track is modeled as a Bernoulli-Euler beam on a layered half-space, with different assumptions regarding the displacement and stress distribution at the track-soil interface. In the third model, the track slab is modeled using Kirchhoff plate elements, enabling a more general displacement and stress distribution in the track transverse direction to be resolved. It is shown that in the case studied here, the beam model where the track-soil interface is considered rigid over the width of the slab, only slightly underestimates the response, at higher frequencies. The beam model where a uniform traction is assumed at the track-soil interface, on the other hand, underestimates the response significantly at frequencies above 50 Hz.

5 Acknowledgments

Part of the project was funded by the City of Helsingborg through the call Plattformen. The authors of this work gratefully acknowledge the financial support.

Layer	Parameter	Value
Soil	Depth (m)	14.0
	Young's modulus (MPa)	475
	Poisson's ratio	0.48
	Density (kg/m ³)	2125
	Loss factor (-)	0.14
Bedrock (half-space)	Depth (m)	∞
	Young's modulus (MPa)	8800
	Poisson's ratio	0.40
	Density (kg/m ³)	2600
	Loss factor (-)	0.04

Table 2: Soil properties.

REFERENCES

- [1] Y. Yang, H. Hung, A 2.5D finite-infinite element approach for modelling visco-elastic bodies subjected to moving loads. *International Journal for Numerical Methods in Engineering*, **51**. 1317–1336, 2008.
- [2] X. Sheng, C.J.C. Jones, D.J. Thompson, Prediction of ground vibration from trains using the wavenumber finite and boundary element methods. *Journal of Sound and Vibration*, **293**. 575–586, 2006.
- [3] G. Lombaert, G. Degrande, J. Kogut, S. Francois, The experimental validation of a numerical model for the prediction of railway induced vibrations. *Journal of Sound and Vibration*, **297**. 512–535, 2006.
- [4] P. Galvin, S. Francois, M. Schevenels, E. Bongini, G. Degrande, G. Lombaert, A 2.5D coupled FE-BE model for the prediction of railway induced vibrations. *Soil Dynamics and Earthquake Engineering*, **30**. 1500–1512, 2010.
- [5] X. Sheng, C.J.C. Jones, M. Petyt, Ground vibration generated by a harmonic load acting on a railway track. *Journal of Sound and Vibration* **225(1)**.3–28, 1999.
- [6] X. Sheng, C.J.C. Jones, M. Petyt, Ground vibration generated by a load moving along a railway track. *Journal of Sound and Vibration*, **228(1)**. 129–156, 1999.
- [7] A.M. Kaynia, C. Madshus, P. Zackrisson, Ground vibration from high-speed trains: prediction and countermeasure. *Journal of Geotechnical and Geoenvironmental Engineering*, **126(6)**. 531–537, 2000.
- [8] M.J.M.M. Steenbergen, A.V. Metrikine, The effect of the interface conditions on the dynamic response of a beam on a half-space to a moving load. *European Journal of Mechanics A/Solids*, **26**. 33–54, 2007.
- [9] L.V. Andersen, *Linear Elastodynamic Analysis*, Department of Civil Engineering, Aalborg University. DCE Lecture Notes, No. 3, 2006.
- [10] W. Thomson, Transmission of elastic waves through a stratified solid medium. *Journal of Applied Physics*, **21**. 89–93, 1950.

- [11] N. Haskell, The dispersion of surface waves on multilayered medium. *Bulletin of the Seismological Society of America*, **73**. 17–43, 1953.
- [12] R. Wang, A simple orthonormalization method for stable and efficient computation of Green's functions. *Bulletin of the Seismological Society of America*, **89(3)**. 733–741, 1999.
- [13] L. Andersen, S.R.K. Nielsen, P.H. Kirkegaard, Finite element modelling of infinite Euler beams on Kelvin foundations exposed to moving loads in convected co-ordinates. *Journal of Sound and Vibration*, **241(4)**. 587–604, 2001.
- [14] X. Lei, J. Wang, Dynamic analysis of the train and slab track coupling system with finite elements in a moving frame of reference. *Journal of Vibration and Control*, **20(9)**. 1301–1317, 2014.
- [15] N. Ottosen, H. Petersson, *Introduction to the finite element method*, Prentice Hall, 1992.

Paper B



Evaluating the effect of vibration isolation mats on train-induced ground vibrations

J. Malmberg, K. Persson, P. Persson
Department of Construction Sciences, Lund University
P.O. Box 118, SE-22100 Lund, Sweden

Abstract

In the present paper, the effectiveness of a vibration isolation mat for a railway slab track system is studied using a finite element model of the railway track. The finite elements are formulated in a moving frame of reference following the moving load at a particular speed. The rails are modeled using Bernoulli beams, whereas the track slab and an underlying supporting plate are modeled using Kirchhoff plate elements. The vibration isolation mat is modeled as a continuous visco-elastic layer between the track slab and the supporting plate. The response of the underlying soil is represented through a dynamic stiffness matrix, obtained via the Green's function for a horizontally layered visco-elastic strata in a moving frame of reference in the frequency–wavenumber domain. The model accounts for the quasi-static excitation caused by the static axle loads of a vehicle, as well as the dynamic excitation caused by the vehicle running over an uneven rail. The free-field response and the insertion loss obtained with the vibration isolation mat is first evaluated for a harmonic load moving along the track. Band-averaged vibration levels and the insertion loss for a fixed point next to the track are then calculated for a train cart, represented by a 10 degree-of-freedom multi-body system, running at different speeds.

1. INTRODUCTION

Due to an increasing population, many cities experience urban densification where previously unexploited land areas close to railways are now being used for new residential and office buildings. Furthermore, increasing demands on infrastructure results in heavily trafficked roads and railways close to residential areas. Annoyance from traffic-induced vibrations and noise is therefore a growing problem. To predict vibration levels arising from traffic, and to evaluate vibration mitigation measures, models are needed for estimating the load from the vibration source as well as the vibration transmission through the ground.

One technique for reducing the vibrations from railways is to introduce an elastic mat underneath the ballast, or underneath the slab in the case of ballastless slab tracks. The performance of such elastic mats have been studied by other authors using various 2.5D and 3D models, e.g. [1–3] where boundary elements are used to account for the soil response.

In the present paper, the effectiveness of a vibration isolation mat for a railway slab track system is studied. A 3D finite element (FE) formulation in a moving frame of reference following the load is used for describing the railway track. The underlying soil response is included through a dynamic stiffness matrix obtained via the Green's function for a horizontally layered visco-elastic strata in a moving frame of reference, in the frequency–wavenumber domain. The free-field response and the insertion loss obtained with the vibration isolation mat is first evaluated for a harmonic load moving along the track. Band-averaged vibration levels and insertion loss for a fixed point next to the track are then calculated for a train cart, represented by a 10 degree-of-freedom multi-body system, running on an uneven track.

In Section 2 an overview of the model is given and the studied case is presented in Section 3. Finally, conclusions are given in Section 4.

2. MODEL OVERVIEW

In the present work the Green's function of a horizontally layered stratum, in a moving frame of reference, is calculated in the frequency–wavenumber domain and transformed to frequency–spatial domain through a double

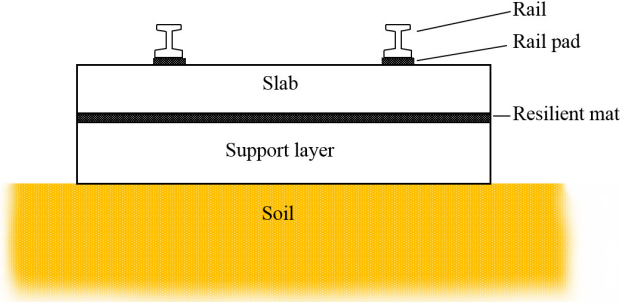


Figure 1: Section of slab track with resilient mat between the slab and the support layer.

inverse Fourier transform. It is then used to derive a dynamic stiffness matrix of the ground. The ground model is coupled to an FE representation of the railway structure, including the supporting layer, slab and rails. The supporting layer and the slab are modeled as two overlaying Kirchhoff plates. A continuous visco-elastic interface layer is introduced between the supporting layer and the slab to represent mortar or, in the case of a floating slab track, a vibration isolation mat. The rails are modeled as Bernoulli-Euler beams, connected to the slab via a continuous visco-elastic interface layer representing the rail pads. Both the ground model and the FE model are expressed in a moving frame of reference, following the vehicle at a given speed v , by introducing a coordinate transformation as

$$(\tilde{x}, \tilde{y}, \tilde{z}) = (x - vt, y, z), \quad (1)$$

where $\tilde{x}, \tilde{y}, \tilde{z}$ denotes the coordinates in the moving frame of reference.

2.1. Soil model

Introducing the coordinate transformation into the Navier's equations yields

$$\begin{aligned} (\lambda + \mu) \frac{\partial^2 \tilde{u}_j}{\partial \tilde{x}_i \partial \tilde{x}_j} + \mu \frac{\partial^2 \tilde{u}_i}{\partial \tilde{x}_j \partial \tilde{x}_j} &= \\ = \rho \left(\frac{\partial^2 \tilde{u}_i}{\partial t^2} - 2v \frac{\partial^2 \tilde{u}_i}{\partial t \partial \tilde{x}_1} + v^2 \frac{\partial^2 \tilde{u}_i}{\partial \tilde{x}_1^2} \right), \end{aligned} \quad (2)$$

where $\tilde{u}_i = \tilde{u}_i(\tilde{x}, \tilde{y}, \tilde{z}, t)$ is the displacement in the moving frame of reference. Fourier transforming Eq. 2 with respect to the horizontal coordinates and time, $(\tilde{x}, \tilde{y}, t)$, yields the convective Navier equations in frequency-wavenumber domain. As showed by Sheng [4], the solution for an individual layer can be found analytically, and due to continuity of displacements and tractions over interfaces between layers, several layers can be assembled using the Thomson [5] and Haskell [6] layer transfer matrix approach, forming a relationship between the displacement and stresses at the top of the stratum and at the bottom of the stratum. With known boundary conditions at the lowest interface, a relationship between the traction and the displacement at the surface can be obtained as

$$\hat{\mathbf{u}} = \hat{\mathbf{G}} \hat{\mathbf{p}}, \quad (3)$$

where $\hat{\mathbf{u}} = \hat{\mathbf{u}}(\tilde{k}_x, \tilde{k}_y, \omega)$ and $\hat{\mathbf{p}} = \hat{\mathbf{p}}(\tilde{k}_x, \tilde{k}_y, \omega)$ are vectors containing the displacements and tractions respectively on the soil surface, $\hat{\mathbf{G}} = \hat{\mathbf{G}}(\tilde{k}_x, \tilde{k}_y, \omega)$ is the Green's function tensor, \tilde{k}_x and \tilde{k}_y are the horizontal wavenumbers, and ω is the circular frequency of the moving harmonic load. For certain frequencies and stratifications, the original Thomson and Haskell method suffers from loss-of-precision. To avoid these problems in the present work, the different soil layers are assembled in an orthonormalisation procedure as proposed by Wang [7].

Equation 3 is evaluated for a set of discrete values of \tilde{k}_x and \tilde{k}_y , and the displacement vector $\hat{\mathbf{u}}(\tilde{x}, \tilde{y}, \omega)$ is obtained in Cartesian space through a double inverse Fourier transform of $\hat{\mathbf{u}}(\tilde{k}_x, \tilde{k}_y, \omega)$.

The procedure described above is used for calculating the response on the soil surface, due to a unit load with a rectangular spatial distribution. From this single load case, a dynamic flexibility matrix $\mathbf{F}_g(\omega, v)$ is established

for a set of DoFs where the superstructure interacts with the soil surface. These DoFs will be referred to as soil-structure interaction (SSI) DoFs. \mathbf{F}_g is formed, column by column, by interpolating from $\tilde{\mathbf{u}}$. The flexibility matrix is then inverted to form the dynamic stiffness matrix of the soil, $\mathbf{D}_g(\omega, v) = \mathbf{F}_g^{-1}(\omega, v)$, which gives a relation between the steady-state displacements $\tilde{\mathbf{u}}_g$ and forces $\tilde{\mathbf{f}}_g$ for the SSI DoFs, at a certain circular frequency ω and velocity v , as

$$\mathbf{D}_g \tilde{\mathbf{u}}_g = \tilde{\mathbf{f}}_g. \quad (4)$$

2.2. Railway structure

Assuming steady-state conditions, the governing equation for the railway structure can be written as

$$(-\omega^2 \mathbf{M}_s + i\omega \mathbf{C}_s + \mathbf{K}_s) \tilde{\mathbf{u}}_s = \tilde{\mathbf{f}}_s, \quad (5)$$

or

$$\mathbf{D}_s \tilde{\mathbf{u}}_s = \tilde{\mathbf{f}}_s, \quad (6)$$

where \mathbf{M}_s , \mathbf{C}_s and \mathbf{K}_s is the mass, damping and stiffness matrix respectively. $\mathbf{D}_s = (-\omega^2 \mathbf{M}_s + i\omega \mathbf{C}_s + \mathbf{K}_s)$ is the dynamic stiffness matrix, and $\tilde{\mathbf{u}}_s$ and $\tilde{\mathbf{f}}_s$ is the displacement and force vector respectively. The coordinate transformation used to express the governing FE equations in a moving frame of reference introduces convective terms in the damping and stiffness matrices, see e.g. [8–10]. The track slab and the supporting layer are described using four-node rectangular Kirchhoff plate elements with three DoFs per node (vertical displacement + two rotations). The rail is described by two-node Bernoulli-Euler beam elements. The visco-elastic layer between the slab and the supporting layer, as well as the rail pads, are described by continuously distributed springs and dashpots. In both cases, the shear transfer between the two plates is disregarded.

2.3. Coupling between soil and FE

The track is coupled to the SSI DoFs in a standard FE manner. Here, only the vertical DoFs of the supporting plate are coupled to the soil. For the finite elements, displacements and stress distributions are governed by the element shape functions. However, for the soil, the displacements and interface tractions are governed by the load distribution chosen for calculating the soil response fundamental solution. Thus, continuity of displacements and stresses is not guaranteed along the superstructure–soil surfaces, but force and displacement continuity is enforced at the exact location of the nodes.

A global system of equations for the ground and the railway structure is formed by combining Eqs. 4 and 5, yielding

$$\mathbf{D}_t \tilde{\mathbf{u}}_s = \tilde{\mathbf{f}}_s, \quad (7)$$

where \mathbf{D}_t represents the total dynamic stiffness matrix for the structure assembled onto the ground DoFs.

2.4. Free-field response

Once the displacements $\tilde{\mathbf{u}}_s$, and thereby also the subset $\tilde{\mathbf{u}}_g$, have been obtained by solving Eq. 7, the corresponding forces on the soil surface, $\tilde{\mathbf{f}}_g$ are calculated by Eq. 4. A second flexibility matrix $\mathbf{F}_{gf}(\omega, v)$ is established, in the same manner as $\mathbf{F}_g(\omega, v)$, as described in Section 2.1. The free-field displacements, $\tilde{\mathbf{u}}_f$, are then calculated as

$$\tilde{\mathbf{u}}_f = \mathbf{F}_{gf} \tilde{\mathbf{f}}_g. \quad (8)$$

These displacements are in the moving frame of reference, following the load at speed v . In this frame of reference, the displacements are in steady state with the loading frequency f . For a fixed point in the free-field, however, the response is transient. Due to the Doppler effect, the response will contain frequencies other than the excitation frequency. The fixed point response time history, $u(t)$, is obtained by moving with the train speed, along a line parallel with the track, in the opposite travel direction of the train.

3. STUDIED CASE

The model described above is used for evaluating the effect of a resilient mat placed under the track slab. The track rests on a 14 m deep layer of clay overlaying a half-space. The properties of the track and the soil layers are shown in Table 1 and Table 2, respectively. Due to symmetry, only half the track is modeled. The element length is 0.3 m in both the plates and the beams.

Table 1: Track properties.

	Parameter	Value
Rail	Mass (kg/m)	60
	Youngs modulus (GPa)	210
	Second moment of inertia (m ⁴)	3.217×10^{-5}
	Loss factor (-)	0.01
Rail pads	Stiffness (MN/m ²)	92.3
	Damping (kNs/m ²)	73.4
Concrete slab	Density (kg/m ³)	2500
	Youngs modulus (GPa)	34
	Poisson's ratio	0.2
	Width (m)	3.0
	Thickness (m)	0.3
	Loss factor (-)	0.04
HSL	Density (kg/m ³)	2200
	Youngs modulus (GPa)	25
	Poisson's ratio	0.2
	Width (m)	3.0
	Thickness (m)	0.4
	Loss factor (-)	0.04
Slab mat	Stiffness (MN/m ³)	10
	Damping (kNs/m ³)	20
Mortar	Stiffness (MN/m ³)	1000
	Damping (kNs/m ³)	250

Table 2: Soil properties.

Layer	Parameter	Value
Soil	Depth (m)	14.0
	Youngs modulus (MPa)	475
	Poisson's ratio	0.48
	Density (kg/m ³)	2125
	Loss factor (-)	0.14
Bedrock (half-space)	Depth (m)	∞
	Youngs modulus (MPa)	8800
	Poisson's ratio	0.40
	Density (kg/m ³)	2600
	Loss factor (-)	0.04

First, the track receptance and the free-field response is calculated for a simple harmonic unit load moving along the track at speeds $v = 30$ m/s and $v = 60$ m/s, for both the unisolated and the isolated track. Then, the free-field response due to a train cart running over an uneven track at those same velocities is calculated for both models.

3.1. Track receptance

The receptance, i.e. the displacement of the loading point, when subjecting the track to a moving harmonic unit load, is calculated for the velocities $v = 0$ m/s, $v = 30$ m/s and $v = 60$ m/s. The load is applied symmetrically on both rails, i.e. half a unit load is applied on each rail. For the floating slab, the receptance decreases noticeably with increasing load velocity and the resonance peak is shifted to a lower frequency, as shown in Figure 2. Figure 3 shows the free-field displacements for $v = 60$ m/s and $f = 40$ Hz, for the floating slab.

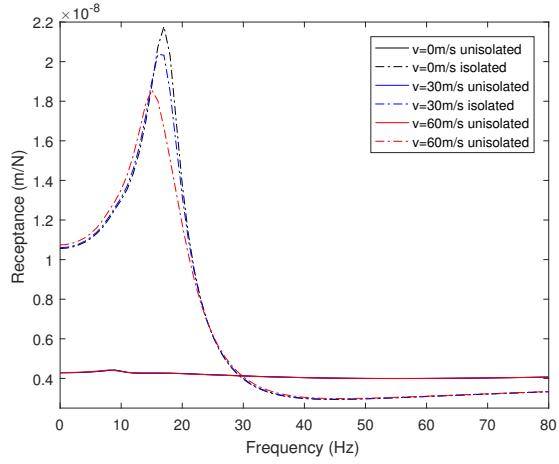


Figure 2: Track receptance.

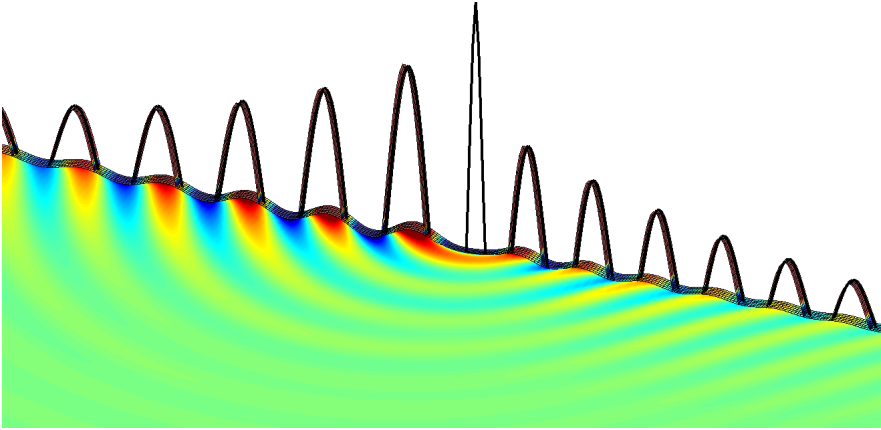


Figure 3: Free-field displacements due a harmonic point load at $f = 40$ Hz moving at a speed $v = 60$ m/s on the floating slab. The Doppler effect is clearly visible.

3.2. Insertion loss

The insertion loss quantifies the change in response due to a modification of the system. Here, it relates the displacement in the free-field obtained with the resilient mat, to the displacement obtained without the resilient mat. The insertion loss is defined as

$$IL = 20 \log_{10} \frac{u_o}{u_r}, \quad (9)$$

where u_o and u_r is the displacement in the original (unisolated) configuration and the modified (isolated) configuration, respectively.

As described in Section 2.4, the response in a fixed point in the free-field $u(t)$, due to harmonic load moving along the track, is transient. The root-mean-square (rms) value of $u(t)$ is

$$u_{rms} = \sqrt{\frac{1}{T} \int_0^T u(t)^2 dt}. \quad (10)$$

The rms-value of the displacement is used for calculating an insertion loss for a fixed point, due to the moving load.

Figures 4a–b show the insertion loss for points in the free-field 5 m and 25 m from the track, respectively, when the load velocity is $v = 30$ m/s. The insertion loss is shown for three points following the moving load. These points are located perpendicular to (0 m), ahead of (+10/+25 m) and behind (–10/–25 m) the moving load. Furthermore, the insertion loss calculated from the rms-value of the displacement in a fixed point is also shown. Figures 4c–d show the corresponding results for the load velocity $v = 60$ m/s.

The insertion loss is considerably higher for the point perpendicular to the moving load, than for the other two points following the load. Naturally, the insertion loss is therefore also lower for a fixed point as the load passes. The insertion loss is slightly lower for the higher load velocity, and slightly higher further from the track. Negative insertion loss is observed near the resonance frequency of the floating slab.

3.3. Train passage

Here, a 10 DoF vehicle, modeled as a multi-body system, is introduced into the model. The contact between the vehicle wheels and the rail is accounted for by means of a linearized Hertzian contact spring, i.e. the wheel is assumed to be in contact with the rail at all times. Since the track is described in a moving frame of reference following the vehicle, each wheel is connected to the same rail element throughout the analysis.

The rail unevenness is often described by a power spectral density (PSD) function, allowing the rail irregularities to be decomposed into spectral components of different wavelengths. For a single harmonic component of the track irregularity, with wavelength λ , the frequency of excitation is $f = v/\lambda$ where v is the vehicle speed. Here, the German track PSD is used to describe the rail irregularities,

$$P_z(\beta) = \frac{A_p \beta_c^2}{(\beta^2 + \beta_r^2)(\beta^2 + \beta_c^2)} \left[\frac{\text{m}^2}{\text{rad/m}} \right], \quad (11)$$

where $\beta = 2\pi/\lambda$, the constants $\beta_r = 0.0206$ rad/m and $\beta_c = 0.8246$ rad/m. A_p is a parameter defining the track quality, ranging from $A_p = 4.032 \times 10^{-7}$ m²/(rad/m) to $A_p = 10.8 \times 10^{-7}$ m²/(rad/m). Here, a poor track quality is assumed and hence the higher value is used in this example.

An expression for the total response power spectrum in a fixed point, when the rail irregularities are described by a PSD, was derived by Sheng [11]. The total response from the dynamic excitation of the rail irregularities, is obtained by combining the contributions from a number of discrete irregularity wavelengths. The vertical velocity levels, as well as the insertion loss based on these velocity levels, are calculated for points located 5 m and 25 m from the track, for the train speeds $v = 30$ m/s and $v = 60$ m/s. The results are presented in 1/3 octave bands, see Figure 5. As for the harmonic point load, the response in the free-field generally increases with increasing velocity.

The insertion loss is slightly higher for points further from the track, in the frequency bands above 20 Hz. The response in low frequency bands are dominated by the quasi-static load, which is significant for the free-field response close to the track. Again, negative insertion loss is obtained close to the resonance frequency of the floating slab. Close to the track, positive insertion loss is observed for the low frequencies where the response is dominated by the quasi-static response.

Table 3: Vehicle properties (from [10]).

Parameter	Value
Primary suspension stiffness k_p (MN/m)	1.18
Primary suspension damping c_p (kNs/m)	39.2
Secondary suspension stiffness k_s (MN/m)	0.53
Secondary suspension damping c_s (kNs/m)	90.2
Wheel mass m_w (kg)	1.78×10^3
Bogie mass m_b (kg)	3.04×10^3
Bogie inertia I_b (kgm ²)	3.93×10^3
Body mass m_c (kg)	41.75×10^3
Body inertia I_c (kgm ²)	2.08×10^6

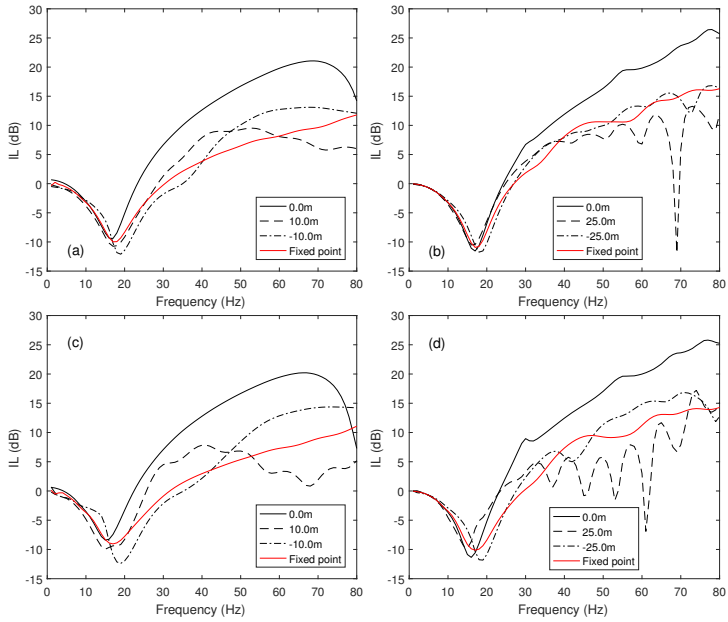


Figure 4: (a) and (b): Insertion loss in free-field points 5 m and 25 m from the track, respectively, for a moving point load at $v=30$ m/s. (c) and (d): Insertion loss in free-field points 5 m and 25 m from the track, respectively, for a moving point load at $v=60$ m/s.

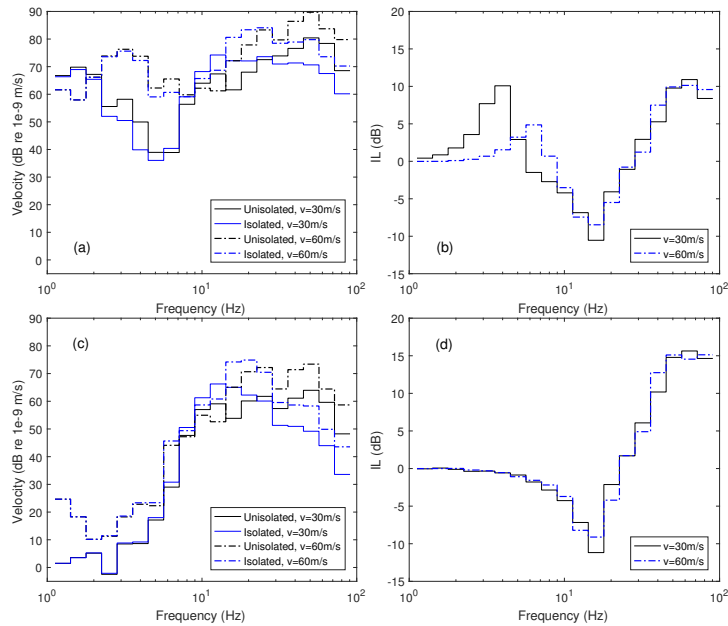


Figure 5: (a) Free-field vibration velocity levels in 1/3 octave bands for a point located 5 m from the track. (b) Corresponding insertion loss. (c) Free-field vibration velocity levels in 1/3 octave bands for a point located 25 m from the track. (d) Corresponding insertion loss.

4. Conclusions

In this paper a numerical model of a railway track has been applied to study the effect of a vibration isolation mat. The model is formulated in a frame of reference following the load moving along the track at a fixed velocity. This formulation is efficient, allowing smaller models compared to traditional 3D FE formulations. Furthermore, the moving load can be analyzed in frequency domain.

It is shown that, when a simple harmonic load moves along the track, the effect of the resilient mat on the free-field response is reduced with increasing velocity of the load. For points that are following the moving load, the insertion loss is considerably higher for a point perpendicular to the load than for other points equidistant from the track. A fixed point experiences the wave field from the moving load from all different angles as the load approaches and departs, and naturally the insertion loss is therefore lower than the maximum. Furthermore, the insertion loss is slightly higher 25 m from the track than 5 m from the track.

Introducing a resilient mat under the track slab modifies the free-field response arising from a specific load on the track, and furthermore, the modified track stiffness changes the dynamic wheel-rail interaction forces due to track unevenness. Here, the vehicle is modeled as a multi-body system, and the track unevenness is treated as a stationary stochastic process described by a PSD function. The response in the free-field generally increases with increasing velocity of the train. The insertion loss is slightly higher in the frequency bands above 20 Hz, for points further from the track. The response in low frequency bands are dominated by the quasi-static load, which is significant for the free-field response close to the track. Here, a positive insertion loss is observed, whereas again, as in the case with the moving point load, a negative insertion loss is obtained close to the resonance frequency of the floating slab.

5. Acknowledgments

The research was carried out in the framework of the project “Urban Tranquility” under the Interreg V programme. The authors of this work gratefully acknowledge the European Regional Development Fund for the financial support. Gratitude is also expressed to the City of Helsingborg for the research funding through the call “Plattformen”.

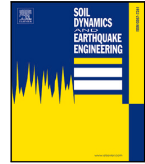
References

- [1] Alves Costa P, Calcada A, Silva Cardoso A. Ballast mats for the reduction of railway traffic vibrations. Numerical study. *Soil Dynamics and Earthquake Engineering* 2012;42, 137–150.
- [2] Lombaert G, Degrande G, Vanhauwere B, Vandeborghht B, Francois S. The control of ground-borne vibrations from railway traffic by means of continuous floating slabs. *Journal of Sound and Vibration* 2006;297, 946–961.
- [3] Galvin P, Romero A, Domingues J. Vibrations induced by HST passage on ballast and non-ballast tracks. *Soil Dynamics and Earthquake Engineering* 2010;30, 862–873.
- [4] Sheng X, Jones CJC, Petyt M. Ground vibration generated by a load moving along a railway track. *Journal of Sound and Vibration* 1999;228(1), 129–156.
- [5] Thomson W. Transmission of elastic waves through a stratified solid medium. *Journal of Applied Physics* 1950;21, 89–93.
- [6] Haskell N. The dispersion of surface waves on multilayered medium. *Bulletin of the Seismological Society of America* 1953;73, 17–43.
- [7] Wang R. A simple orthonormalization method for stable and efficient computation of Green’s functions. *Bulletin of the Seismological Society of America* 1999;89(3), 733–741.
- [8] Andersen, LV. Linear Elastodynamic Analysis, Department of Civil Engineering, Aalborg University. DCE Lecture Notes, No. 3, 2006.

- [9] Andersen L, Nielsen SRK, Kirkegaard PH. Finite element modelling of infinite Euler beams on Kelvin foundations exposed to moving loads in convected co-ordinates. *Journal of Sound and Vibration* 2001;241(4), 587–604.
- [10] Lei X, Wang J. Dynamic analysis of the train and slab track coupling system with finite elements in a moving frame of reference. *Journal of Vibration and Control* 2014;20(9), 1301–1317.
- [11] Sheng X, Jones CJC, Thompson DJ. A theoretical model for ground vibration from trains generated by vertical track irregularities. *Journal of Sound and Vibration* 2004;272, 937–965.

Paper C





Effects of modeling strategies for a slab track on predicted ground vibrations

J. Malmberg*, P. Persson, K. Persson

Department of Construction Sciences, Lund University, P.O. Box 118, SE-22100 Lund, Sweden

ARTICLE INFO

Keywords:

Train-induced ground vibration
Moving frame of reference
Slab track
Finite element
Green's function

ABSTRACT

In the paper, the effect of modeling strategies regarding the dynamic behavior of a railway slab track on a layered half-space is studied. The track is modeled with various degrees of accuracy through the use of either beam theory, shell finite elements or solid finite elements. The underlying soil response is included through a dynamic stiffness, obtained via the Green's function for a horizontally layered visco-elastic half-space in the frequency–wavenumber domain. The effect of different assumptions regarding the track cross-section behavior and the track–soil interface conditions on the resulting free-field vibrations are studied for a harmonic load moving along the track. First, only the out-of-plane displacements of the slab–soil interface are coupled, i.e. only the vertical contact pressure is accounted for. Secondly, the effect of coupling the slab–soil in-plane displacements on the free-field vibrations is studied. It is found that the in-plane slab–soil coupling significantly affects the vertical vibration in the free-field. It is also found that a beam model of the track yields accurate response levels compared to a solid continuum model in the case of a thick slab, whereas considerable differences are obtained for a thin slab.

1. Introduction

Due to an increasing population, many cities experience urban densification. Previously unexploited areas, close to railways and heavily trafficked roads, are now being developed for residential and office buildings. Annoyance from traffic-induced vibrations and noise is therefore a growing problem.

To estimate the load from the vibration source and to predict the vibration transmission through the ground, models are needed. Ground vibrations caused by passing trains have been studied using a wide range of different techniques in the past decades, ranging from empirical methods to analytical and numerical calculation models. Numerical prediction models often employ either the finite element (FE) method or the boundary element (BE) method, or a combination thereof. The FE method enables arbitrary geometries and discontinuities to be modeled, but the need to discretize a large computational domain may lead to long computation times. Furthermore, when modeling wave propagation, the truncation of the model geometry may lead to spurious reflections of elastic waves unless the artificial boundaries are properly modeled. The BE method inherently includes non-reflecting boundaries, but depending on the model size, the computational cost may still be high. If the soil and track are assumed to be invariant in the track direction, the computational cost may be reduced through the use of so called 2.5D models [1–6], where a Fourier transform with respect to the coordinates in the track direction is performed and a 2D problem

is solved for a sequence of wavenumbers, using either the FE method, the BE method, analytical methods, or a combination of these.

Apart from the FE and BE methods, some models utilize that a fundamental solution (Green's function) for the soil response can be found analytically in frequency–wavenumber domain for a horizontally layered visco-elastic half-space. Several authors have used such a soil model coupled to a railway track. *Sheng et al.* [7,8] derived a semi-analytical model, with the track represented by an infinite layered beam resting on a layered ground, where both the ground and the beam are described in the frequency–wavenumber domain, in the reference frame of the moving load. *Kaynia et al.* [9] coupled a series of FE beams, representing the railway track, to a dynamic stiffness matrix of the ground calculated from the Green's function of a layered half-space. *Triepaischajonsak et al.* [10] calculated the track/ground interaction forces in time domain using a beam on elastic foundation, and introduced the calculated forces into a ground model in frequency–wavenumber domain to predict the free-field vibrations. *Koroma et al.* [11] used a time-domain FE model of the track, with the soil stiffness described by lumped parameter models, to calculate the track–soil interaction forces that were subsequently used for calculating the free-field vibrations in frequency–wavenumber domain using a layered half-space model.

Modeling the track as a beam is a common approach in both track/vehicle dynamics analyses and predictions of ground-borne

* Corresponding author.

E-mail address: jens.malmberg@construction.lth.se (J. Malmberg).

<https://doi.org/10.1016/j.soildyn.2020.106254>

Received 8 January 2020; Received in revised form 18 April 2020; Accepted 5 June 2020

Available online 11 June 2020

0267-7261/© 2020 The Authors. Published by Elsevier Ltd. This is an open access article under the CC BY license (<http://creativecommons.org/licenses/by/4.0/>).

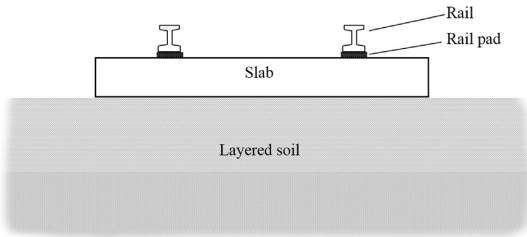


Fig. 1. Schematic cross-section of slab track on a layered soil.

vibrations. However, when the track is modeled as a beam, some assumptions regarding the displacements or the stress distribution in the track–soil interface have to be made, which may affect the resulting ground vibrations. *Steenbergen et al. [12]* used a semi-analytical model for studying the influence of different vertical interface conditions between a beam on a half-space, on the free-field response. *Galvín et al. [4]* compared the free-field response of a high-speed train passage on a ballasted track on an embankment, obtained with different modeling approaches. The results obtained with a beam model of the track showed large differences when compared to those obtained with a continuum model. The differences were attributed to the rigid cross-section of the embankment in the beam model.

State-of-the-art models for train-induced ground vibrations, utilizing continuum representations of the railway track, account for both the track cross-section flexibility and the in-plane shear forces of the track–soil interface. To the authors knowledge, it has previously not been demonstrated what the implications are of using a simplified approach concerning the track and track–soil coupling, when predicting the ground vibrations caused by a load moving over a slab track. The subject was touched upon in a conference paper by the authors [13]. For use in early design stages, prediction tools need to be fast to enable swift evaluation of different design alternatives or response sensitivity to model parameters, while maintaining sufficient accuracy to provide meaningful results. In the present paper, the free-field ground vibrations due to a harmonic load moving at constant velocity along a railway slab track are calculated using different assumptions of the slab cross-section behavior and the track–soil interface conditions.

2. Study overview

The influence of various modeling strategies on the predicted ground vibrations was studied for a slab track that is shown principally in Fig. 1. It consists of a concrete slab, rails and rail pads. The track cross-section flexibility affects the distribution of the resulting track–soil contact forces in both the longitudinal and the lateral directions. The deformation of the slab cross-section is expected to be very small for a thick slab, justifying a beam representation of the slab. For a thin slab however, the deformation of the slab cross-section may become significant, making a beam representation of the slab less appropriate. To reveal these differences relating to the cross-section flexibility, the study was performed for two different slab thicknesses, $t = 0.2$ m and $t = 0.5$ m. The slab width is 3.0 m for both thicknesses. The track properties used are given in Table 1.

The track is assumed to rest on a 14 m deep layer of clay overlaying a half-space. The analyses are performed for two different values of the clay layer’s Young’s modulus, presented in Table 2. The stiffer soil properties are that of a stiff clay till, where the parameters were obtained through geotechnical and geophysical measurements at a site in the city of Lund, Sweden, close to a research facility housing highly vibration-sensitive equipment. The Rayleigh wave speed for this soil is $c_R = 261$ m/s. The Young’s modulus for the softer soil is chosen to give

a Rayleigh wave speed approximately equal to half of that for the stiffer soil, $c_R = 131$ m/s.

Four computational models, Models (a)–(d), with different assumptions regarding the slab and the slab–soil interface conditions, are established as:

- (a) The slab is modeled as a Bernoulli–Euler beam. Vertical displacement continuity of the beam and the soil is enforced along the beam center line. A uniform normal stress distribution between the beam and the soil is assumed in the lateral direction of the slab. In-plane coupling of the slab–soil is disregarded.
- (b) The slab is modeled as a Bernoulli–Euler beam. The slab–soil interface is assumed rigid vertically and laterally, enforcing displacement continuity of the beam and the soil under the full width of the slab. The axial rigidity of the slab is modeled using the bar equation.
- (c) The slab is modeled with Kirchhoff shell elements, allowing a more general slab–soil interface stress and displacement distribution in the lateral direction of the slab than by the aforementioned models. Displacement and force continuity is enforced in the nodes of the slab–soil interface.
- (d) The slab is modeled with 3D solid elements, allowing the most general stress and displacement field of the four models. Displacement and force continuity is enforced in the nodes of the slab–soil interface.

Models (a)–(b) are semi-analytical, not requiring the introduction of finite elements as for Models (c)–(d). The rails are modeled as Bernoulli–Euler beams in all four models. The loading is assumed identical on both rails and in Models (a) and (b) the two rails are accordingly modeled as one single rail with properties equivalent to two rails. In Models (c) and (d), only half of the track is modeled, due to assumed symmetry around the track center line. The models are formulated in a moving frame of reference following the load at a specific speed, requiring that the track is assumed invariant in the load travel direction. Hence, the discrete rail supports are modeled as a continuous visco-elastic interface layer between the rail and the slab. The underlying soil response is included through a dynamic stiffness, obtained via the Green’s function for a horizontally layered visco-elastic stratum in the frequency–wavenumber domain, as further described in Section 3. The track models and their coupling to the soil is further detailed in Section 4. The Models (a)–(d) are shown schematically in Fig. 2.

Fig. 3 shows a contour plot of the soil surface vertical response amplitude due to a vertical harmonic point load excitation of the soil surface, against frequency and radial wavenumber. The right subplot is for the stiffer soil. Also indicated in the subfigures are the dispersion curves of the Rayleigh wave for the upper layer and half-space materials. For low frequencies, the response is low and dominated by the characteristics of the half-space material. For increasing frequencies the wave that dominates the response propagates in the upper layer with decreasing influence of the half-space material. This effect is seen in the contour plots at around 5 Hz (left) and 10 Hz (right), where the yellow colored area (high response), tends to the dispersion curve of the Rayleigh wave of the upper layer material for increasing frequencies.

To compare the effect of the various modeling strategies for the track, each of Model (a)–(d) was used for evaluating the vertical free-field response to a moving unit harmonic point load acting on the rail. Humans are sensitive to whole-body vibrations for frequencies below 80 Hz. As seen from Fig. 3, the response for the studied ground conditions is low below 5 Hz. The current study is therefore limited to the frequency range 5 to 80 Hz. The velocity of the moving load, set to $v = 30$ m/s, was chosen since it is a common train velocity in urban areas. First, only vertical coupling of the slab to the soil was accounted for, i.e. the shear transfer between the track and soil was disregarded. Then, the in-plane slab–soil displacements were also coupled, assuming a full transfer of shear stresses between the track and soil.

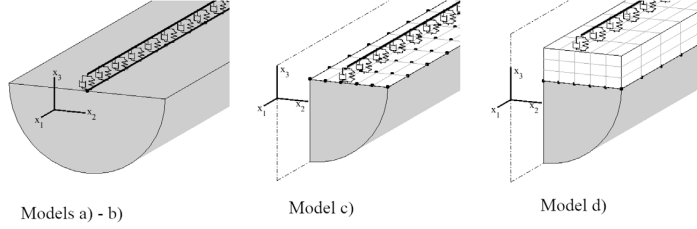


Fig. 2. Schematic view of computational models. In Models (a) and (b) the slab is modeled as Bernoulli–Euler beams with different slab–soil interface conditions. In Models (c) and (d) the slab is modeled by Kirchhoff shell and 3D solid continuum finite elements, respectively.

Table 1
Track properties.

	Parameter	Value
Rail	Mass (kg/m)	60
	Young's modulus (GPa)	210
	Second moment of inertia (m ⁴)	3.217 × 10 ⁻⁵
	Loss factor (-)	0.01
	Track gauge (m)	1.435
Rail pads	Stiffness (MN/m ²)	250
	Damping (kNs/m ²)	22.5
Slab	Density (kg/m ³)	2500
	Young's modulus (GPa)	30
	Poisson's ratio	0.2
	Width (m)	3.0
	Thickness (m)	0.2 / 0.5
	Loss factor (-)	0.04

Table 2
Ground properties.

Layer	Parameter	Value
Soil	Depth (m)	14
	Young's modulus (MPa)	475 / 120
	Poisson's ratio	0.48
	Density (kg/m ³)	2125
	Loss factor (-)	0.14
Bedrock (half-space)	Depth (m)	∞
	Young's modulus (MPa)	8800
	Poisson's ratio	0.40
	Density (kg/m ³)	2600
	Loss factor (-)	0.04

In the semi-analytical models, i.e. Models (a)–(b), the track has infinite length. These models are formulated in frequency–wavenumber domain with a maximum wavenumber of 42 rad/m in each direction, normal and parallel to the track. The number of wavenumber points is set to 4096 × 4096. In Model (b) the slab–soil interface is laterally discretized into 21 strips.

In the FE models, i.e. Models (c)–(d), the total track length is 90 m. The displacement boundary conditions are free at the truncated ends of the track. The length 90 m has been found to be sufficient to avoid problems with reflecting waves at the free boundaries. An element length of 0.15 m is used in both x_1 - and x_2 -directions. In Model (d), six elements are used in the thickness direction of the slab.

Damping is introduced in all models through the use of complex Young's moduli for the ground, the slab and the rails. All calculations presented herein are carried out using an in-house code. The numerical implementations have been validated by running and comparing the results obtained for various cases presented in the literature (e.g. [14–16]), as well as by comparative calculations using the commercial FE software Abaqus.

3. Soil model

The ground is assumed to be composed of horizontal visco-elastic layers. Neglecting body forces, the Navier equations for a single soil layer can be written as

$$(\lambda + \mu) \frac{\partial^2 u_j}{\partial x_i \partial x_j} + \mu \frac{\partial^2 u_i}{\partial x_j \partial x_j} = \rho \frac{\partial^2 u_i}{\partial t^2}, \quad (1)$$

where $u_i = u_i(x_1, x_2, x_3, t)$ is the displacement in direction i . The Lamé parameters are λ and μ .

The equations are obtained in the frame of reference following the load moving at a fixed speed v along the x_1 -axis by applying the coordinate transformation,

$$(\bar{x}_1, \bar{x}_2, \bar{x}_3) = (x_1 - vt, x_2, x_3), \quad (2)$$

where $\bar{x}_1, \bar{x}_2, \bar{x}_3$ denotes the coordinates in the moving frame of reference. Partial derivatives in the two reference frames are related as [17]

$$\frac{\partial}{\partial x_1} = \frac{\partial}{\partial \bar{x}_1}, \quad \frac{\partial}{\partial t} \Big|_{x_1} = \frac{\partial}{\partial t} \Big|_{\bar{x}_1} - v \frac{\partial}{\partial \bar{x}_1}, \quad (3)$$

which applied to Eq. (1) yields

$$(\lambda + \mu) \frac{\partial^2 \bar{u}_j}{\partial \bar{x}_i \partial \bar{x}_j} + \mu \frac{\partial^2 \bar{u}_i}{\partial \bar{x}_j \partial \bar{x}_j} = \rho \left(\frac{\partial^2 \bar{u}_i}{\partial t^2} - 2v \frac{\partial^2 \bar{u}_i}{\partial t \partial \bar{x}_1} + v^2 \frac{\partial^2 \bar{u}_i}{\partial \bar{x}_1^2} \right), \quad (4)$$

where $\bar{u}_i = \bar{u}_i(\bar{x}_1, \bar{x}_2, \bar{x}_3, t)$ is the displacement in the moving frame of reference.

Fourier transforming the Navier equations with respect to the horizontal coordinates and time, $(\bar{x}_1, \bar{x}_2, t)$, yields the Navier equations in frequency–wavenumber domain as

$$(\lambda + \mu) \bar{\Delta} i \bar{k}_1 + \mu \left(\frac{d^2}{d\bar{x}_2^2} - \bar{k}_1^2 - \bar{k}_2^2 \right) \bar{U}_1 = -\rho \bar{\omega}^2 \bar{U}_1, \quad (5a)$$

$$(\lambda + \mu) \bar{\Delta} i \bar{k}_2 + \mu \left(\frac{d^2}{d\bar{x}_3^2} - \bar{k}_1^2 - \bar{k}_2^2 \right) \bar{U}_2 = -\rho \bar{\omega}^2 \bar{U}_2, \quad (5b)$$

$$(\lambda + \mu) \frac{d\bar{\Delta}}{d\bar{x}_3} + \mu \left(\frac{d^2}{d\bar{x}_3^2} - \bar{k}_1^2 - \bar{k}_2^2 \right) \bar{U}_3 = -\rho \bar{\omega}^2 \bar{U}_3, \quad (5c)$$

where $\bar{\Delta} = \bar{\Delta}(\bar{k}_1, \bar{k}_2, \bar{x}_3, \omega)$ and $\bar{U}_i = \bar{U}_i(\bar{k}_1, \bar{k}_2, \bar{x}_3, \omega)$ are the Fourier transforms, with respect to the horizontal coordinates and time, of the dilation $\Delta(\bar{x}_1, \bar{x}_2, \bar{x}_3, t)$ and the displacement $\bar{u}_i(\bar{x}_1, \bar{x}_2, \bar{x}_3, t)$, respectively. The imaginary unit is denoted i . The vibration frequency of a material point is $\bar{\omega} = \omega - \bar{k}_1 v$ and ω is the circular frequency of the moving load. The horizontal wavenumbers in the direction of \bar{x}_1 and \bar{x}_2 are \bar{k}_1 and \bar{k}_2 , respectively.

The solution to Eq. (5) for an individual layer can be found analytically, as showed by Sheng *et al.* [7,8]. Due to continuity of displacements and tractions over interfaces between layers, the Thomson [18] and Haskell [19] layer transfer matrix approach can be used to assemble several layers, forming a relationship between the displacement and stresses at the top of the stratum and at the bottom of the stratum. A relationship between the traction and the displacements at the soil surface can be obtained as

$$\hat{\mathbf{u}} = \hat{\mathbf{G}} \hat{\mathbf{p}}, \quad (6)$$

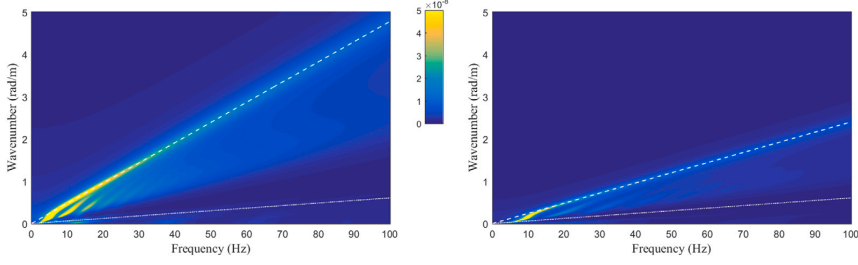


Fig. 3. Contour plot of the soil surface vertical displacement, due to a point load on the soil surface, in frequency-wavenumber domain. Dashed and dotted lines represent the dispersion curves of the Rayleigh wave for the soil and half-space material, respectively. Left: Softer soil. Right: Stiffer soil. (For interpretation of the references to color in this figure legend, the reader is referred to the web version of this article.)

where

$$\hat{\mathbf{u}} = \hat{\mathbf{u}}(\bar{k}_1, \bar{k}_2, \omega) = \begin{bmatrix} \hat{u}_1 \\ \hat{u}_2 \\ \hat{u}_3 \end{bmatrix}, \quad \hat{\mathbf{p}} = \hat{\mathbf{p}}(\bar{k}_1, \bar{k}_2, \omega) = \begin{bmatrix} \hat{p}_1 \\ \hat{p}_2 \\ \hat{p}_3 \end{bmatrix}, \quad (7)$$

are vectors containing the displacements and tractions, respectively, on the soil surface, and

$$\hat{\mathbf{G}} = \hat{\mathbf{G}}(\bar{k}_1, \bar{k}_2, \omega) = \begin{bmatrix} \hat{G}_{11} & \hat{G}_{12} & \hat{G}_{13} \\ \hat{G}_{21} & \hat{G}_{22} & \hat{G}_{23} \\ \hat{G}_{31} & \hat{G}_{32} & \hat{G}_{33} \end{bmatrix}, \quad (8)$$

is the Green's function tensor for the layered half-space.

For certain frequencies and stratifications, the original Thomson and Haskell method suffers from loss-of-precision. To avoid these problems in the present work, the different soil layers are assembled in an orthonormalization procedure as proposed by Wang [20].

Eq. (6) is evaluated for a set of discrete values of \bar{k}_1 and \bar{k}_2 , and the displacement vector $\hat{\mathbf{u}}(\bar{x}_1, \bar{x}_2, \omega)$ in Cartesian space is obtained through a double inverse Fourier transform of $\hat{\mathbf{u}}(\bar{k}_1, \bar{k}_2, \omega)$.

4. Track models

4.1. Semi-analytical beam models: Models (a) and (b)

Here, due to the assumed symmetry, both rails are represented as one infinite beam with the total bending stiffness $(EI)_r$ and mass m_r . The rail is supported by continuously distributed springs and dashpots representing the rail pads, with stiffness k_p and damping c_p . The rail pads are connected to the slab, represented by an infinite beam with bending stiffness $(EI)_s$ and mass m_s . To account for the shear force in the axial direction of the soil-slab interface, an infinite bar with axial stiffness $(EA)_s$ represents the axial rigidity of the slab. The rail is subjected to a harmonic load P_0 with circular frequency Ω , moving in the positive x_1 -direction with the velocity v . The system is described by three equations:

$$\begin{aligned} (EI)_r \frac{\partial^4 u_r}{\partial x_1^4} + m_r \frac{\partial^2 u_r}{\partial t^2} + k_p (u_r - u_s) + c_p \left(\frac{\partial u_r}{\partial t} - \frac{\partial u_s}{\partial t} \right) &= \delta(x_1 - vt) P_0 e^{i\Omega t}, \\ (EI)_s \frac{\partial^4 u_s}{\partial x_1^4} + m_s \frac{\partial^2 u_s}{\partial t^2} + k_p (u_s - u_r) + c_p \left(\frac{\partial u_s}{\partial t} - \frac{\partial u_r}{\partial t} \right) &= -F_3, \\ (EA)_s \frac{\partial^2 w_s}{\partial x_1^2} - m_s \frac{\partial^2 w_s}{\partial t^2} &= F_1, \end{aligned} \quad (9)$$

where $u_r = u_r(x_1, t)$ and $u_s = u_s(x_1, t)$ is the vertical displacement of the rail and slab, respectively and $w_s = w_s(x_1, t)$ is the axial displacement of the slab. Further, $F_3 = F_3(x_1, t)$ is the vertical force in the slab-soil interface and $F_1 = F_1(x_1, t)$ is the shear force in the axial direction of the slab-soil interface. The interface force terms couple the third equation to the first two in Eq. (9), through the soil dynamic stiffness as shown

below in Eq. (17). The equations are obtained in the frame of reference following the load by applying the coordinate transformation in Eq. (2),

$$\begin{aligned} (EI)_r \frac{\partial^4 \bar{u}_r}{\partial \bar{x}_1^4} + m_r \left(\frac{\partial^2 \bar{u}_r}{\partial t^2} - 2v \frac{\partial^2 \bar{u}_r}{\partial \bar{x}_1 \partial t} + v^2 \frac{\partial^2 \bar{u}_r}{\partial \bar{x}_1^2} \right) + k_p (\bar{u}_r - \bar{u}_s) &+ c_p \left(\left(\frac{\partial \bar{u}_r}{\partial t} - v \frac{\partial \bar{u}_r}{\partial \bar{x}_1} \right) - \left(\frac{\partial \bar{u}_s}{\partial t} - v \frac{\partial \bar{u}_s}{\partial \bar{x}_1} \right) \right) \\ &= \delta(\bar{x}_1) P_0 e^{i\Omega t}, \\ (EI)_s \frac{\partial^4 \bar{u}_s}{\partial \bar{x}_1^4} + m_s \left(\frac{\partial^2 \bar{u}_s}{\partial t^2} - 2v \frac{\partial^2 \bar{u}_s}{\partial \bar{x}_1 \partial t} + v^2 \frac{\partial^2 \bar{u}_s}{\partial \bar{x}_1^2} \right) + k_p (\bar{u}_s - \bar{u}_r) &+ c_p \left(\left(\frac{\partial \bar{u}_s}{\partial t} - v \frac{\partial \bar{u}_s}{\partial \bar{x}_1} \right) - \left(\frac{\partial \bar{u}_r}{\partial t} - v \frac{\partial \bar{u}_r}{\partial \bar{x}_1} \right) \right) = -\bar{F}_3, \\ (EA)_s \frac{\partial^2 \bar{w}_s}{\partial \bar{x}_1^2} - m_s \left(\frac{\partial^2 \bar{w}_s}{\partial t^2} - 2v \frac{\partial^2 \bar{w}_s}{\partial \bar{x}_1 \partial t} + v^2 \frac{\partial^2 \bar{w}_s}{\partial \bar{x}_1^2} \right) &= \bar{F}_1, \end{aligned} \quad (10)$$

where, again, $\bar{\cdot}$ denotes that a variable is expressed in the moving frame of reference. Fourier transforming Eq. (10) with respect to \bar{x} yields

$$\begin{aligned} (EI)_r \bar{k}_1^4 \bar{u}_r + m_r \left(\frac{\partial^2 \bar{u}_r}{\partial t^2} - 2iv \bar{k}_1 \frac{\partial \bar{u}_r}{\partial t} - v^2 \bar{k}_1^2 \bar{u}_r \right) + k_p (\bar{u}_r - \bar{u}_s) &+ c_p \left(\left(\frac{\partial \bar{u}_r}{\partial t} - iv \bar{u}_r \right) - \left(\frac{\partial \bar{u}_s}{\partial t} - iv \bar{u}_s \right) \right) = P_0 e^{i\Omega t}, \\ (EI)_s \bar{k}_1^4 \bar{u}_s + m_s \left(\frac{\partial^2 \bar{u}_s}{\partial t^2} - 2iv \bar{k}_1 \frac{\partial \bar{u}_s}{\partial t} - v^2 \bar{k}_1^2 \bar{u}_s \right) + k_p (\bar{u}_s - \bar{u}_r) &+ c_p \left(\left(\frac{\partial \bar{u}_s}{\partial t} - iv \bar{u}_s \right) - \left(\frac{\partial \bar{u}_r}{\partial t} - iv \bar{u}_r \right) \right) = -\bar{F}_3, \\ (EA)_s \bar{k}_1^2 \bar{w}_s + m_s \left(\frac{\partial^2 \bar{w}_s}{\partial t^2} - 2iv \bar{k}_1 \frac{\partial \bar{w}_s}{\partial t} - v^2 \bar{k}_1^2 \bar{w}_s \right) &= \bar{F}_1, \end{aligned} \quad (11)$$

with $\bar{u} = \bar{u}(\bar{k}_1, t) = \int_{-\infty}^{\infty} \bar{u}(\bar{x}_1, t) e^{-i\bar{k}_1 \bar{x}_1} d\bar{x}_1$, $\bar{w} = \bar{w}(\bar{k}_1, t) = \int_{-\infty}^{\infty} \bar{w}(\bar{x}_1, t) e^{-i\bar{k}_1 \bar{x}_1} d\bar{x}_1$, $\bar{F}_i = \bar{F}_i(\bar{k}_1, t) = \int_{-\infty}^{\infty} \bar{F}_i(\bar{x}_1, t) e^{-i\bar{k}_1 \bar{x}_1} d\bar{x}_1$, and \bar{k}_1 denotes the wavenumber in the direction of \bar{x}_1 .

Further, assuming steady-state vibration with circular frequency Ω , i.e. $\bar{u}(\bar{k}_1, t) = \bar{u}(\bar{k}_1) e^{i\Omega t}$ and $\bar{w}(\bar{k}_1, t) = \bar{w}(\bar{k}_1) e^{i\Omega t}$, and setting $\omega = \Omega - \bar{k}_1 v$ yields

$$\begin{aligned} (EI)_r \bar{k}_1^4 \bar{u}_r - \omega^2 m_r \bar{u}_r + k_p (\bar{u}_r - \bar{u}_s) + i\omega c_p (\bar{u}_r - \bar{u}_s) &= P_0, \\ (EI)_s \bar{k}_1^4 \bar{u}_s - \omega^2 m_s \bar{u}_s + k_p (\bar{u}_s - \bar{u}_r) + i\omega c_p (\bar{u}_s - \bar{u}_r) &= -\bar{F}_3, \\ (EA)_s \bar{k}_1^2 \bar{w}_s - \omega^2 m_s \bar{w}_s &= \bar{F}_1. \end{aligned} \quad (12)$$

Sheng et al. [7, 8] assumed a uniform contact pressure in the lateral direction of the track-soil interface and disregarded any horizontal coupling. This is also the assumption made here for Model (a). Steenbergen et al. [12] and Ntostios et al. [15] accounted for a varying contact pressure in the track-soil interface by discretizing the interface laterally into a number of strips, assuming a constant pressure within each strip. The same principle is adopted here for Model (b), not only the vertical contact pressure, but also for the interface shear stress in the

longitudinal and lateral directions. The interface is discretized into N strips with a uniform width, i.e. the width of a single strip is $\Delta = b/N$, where b is the slab width.

A strip centered around the \bar{x}_2 -axis, with a force $f_j(\bar{x}_1)$ per unit length in the \bar{x}_1 -direction is considered. The force acts in direction j . The strip stress is

$$p_j(\bar{x}_1, \bar{x}_2) = \begin{cases} \frac{f_j(\bar{x}_1)}{\Delta}, & -\Delta/2 < \bar{x}_2 < \Delta/2 \\ 0, & \text{otherwise} \end{cases} \quad (13)$$

In wavenumber domain the interface stress becomes

$$\hat{p}_j(\bar{k}_1, \bar{k}_2) = \hat{f}_j(\bar{k}_1) \frac{\sin(\bar{k}_2 \Delta/2)}{\bar{k}_2 \Delta/2}, \quad (14)$$

where $\hat{f}_j(\bar{k}_1)$ denotes the Fourier transform of $f_j(\bar{x}_1)$. Denote the soil displacement in direction i due to the soil surface stress in direction j by \hat{u}_{ij} . From Eq. (6) this displacement is obtained as $\hat{u}_{ij}(\bar{k}_1, \bar{k}_2) = \hat{G}_{ij}(\bar{k}_1, \bar{k}_2) \hat{p}_j(\bar{k}_1, \bar{k}_2)$ (no summation on repeated indices).

Letting $\hat{f}_j(\bar{k}_1) = 1$, the soil displacement at an arbitrary \bar{x}_2 -coordinate, due to the loaded strip becomes

$$\begin{aligned} \hat{u}_{ij}(\bar{k}_1, \bar{x}_2) &= \frac{1}{2\pi} \int_{-\infty}^{\infty} \hat{u}_{ij}(\bar{k}_1, \bar{k}_2) e^{i\bar{k}_2 \bar{x}_2} d\bar{k}_2 \\ &= \frac{1}{2\pi} \int_{-\infty}^{\infty} \hat{G}_{ij}(\bar{k}_1, \bar{k}_2) \hat{p}_j(\bar{k}_1, \bar{k}_2) e^{i\bar{k}_2 \bar{x}_2} d\bar{k}_2 = \\ &\quad \frac{1}{2\pi} \int_{-\infty}^{\infty} \hat{G}_{ij}(\bar{k}_1, \bar{k}_2) \frac{\sin(\bar{k}_2 \Delta/2)}{\bar{k}_2 \Delta/2} e^{i\bar{k}_2 \bar{x}_2} d\bar{k}_2 = \hat{H}_{ij}(\bar{k}_1, \bar{x}_2). \end{aligned} \quad (15)$$

$\hat{H}_{ij}(\bar{k}_1, \bar{x}_2)$ is a transfer function, expressing the displacements at \bar{x}_2 due to a unit load $\hat{f}_j(\bar{k}_1) = 1$ uniformly distributed over the strip centered around $\bar{x}_2 = 0$. Due to the translational invariability of the soil, $\hat{H}_{ij}(\bar{k}_1, \bar{x}_2)$ can be used for calculating the soil displacement at any distance along the \bar{x}_2 -axis from any loaded strip, by replacing the coordinate \bar{x}_2 with the distance. Hence, for each wavenumber \bar{k}_1 , a matrix expression can be established linking the displacements and forces in all the strips,

$$\begin{bmatrix} \hat{H}_{11}(0) & \hat{H}_{12}(0) & \dots & \hat{H}_{13}(-(N-1)\Delta) \\ \hat{H}_{21}(0) & \hat{H}_{22}(0) & \dots & \hat{H}_{23}(-(N-1)\Delta) \\ \hat{H}_{31}(0) & \hat{H}_{32}(0) & \dots & \hat{H}_{33}(-(N-1)\Delta) \\ \hat{H}_{11}(\Delta) & \hat{H}_{12}(\Delta) & \dots & \hat{H}_{13}(-(N-2)\Delta) \\ \vdots & \vdots & \dots & \vdots \\ \hat{H}_{31}((N-1)\Delta) & \hat{H}_{32}((N-1)\Delta) & \dots & \hat{H}_{33}(0) \end{bmatrix} \begin{bmatrix} \hat{f}_1^1 \\ \hat{f}_2^1 \\ \vdots \\ \hat{f}_3^N \end{bmatrix} = \begin{bmatrix} \hat{u}_1^1 \\ \hat{u}_2^1 \\ \vdots \\ \hat{u}_3^N \end{bmatrix}, \quad (16)$$

where the argument \bar{k}_1 has been dropped for brevity. Further, \hat{f}_j^i and \hat{u}_j^i denote the force and displacement, respectively, in direction j of strip i . Eq. (16) can be written as $\hat{\mathbf{H}}\hat{\mathbf{F}} = \hat{\mathbf{u}}$. For known displacements, the strip forces are $\hat{\mathbf{F}} = \hat{\mathbf{H}}^{-1}\hat{\mathbf{u}}$. Enforcing equal displacements in all strips, a (3×3) system is obtained from $\hat{\mathbf{H}}^{-1}$,

$$\begin{bmatrix} k_{11} & k_{12} & k_{13} \\ k_{21} & k_{22} & k_{23} \\ k_{31} & k_{32} & k_{33} \end{bmatrix} \begin{bmatrix} \hat{u}_1 \\ \hat{u}_2 \\ \hat{u}_3 \end{bmatrix} = \begin{bmatrix} \hat{F}_1 \\ \hat{F}_2 \\ \hat{F}_3 \end{bmatrix}, \quad (17)$$

where $\hat{F}_i = \hat{F}_i(\bar{k}_1)$ is the total force in the i -direction from all strips, i.e. the same force acting on the slab in Eq. (12). It is assumed that the slab is rigid in the lateral direction. Further, continuity of vertical and axial displacements between the slab and the soil are assumed. Hence, $\hat{u}_2(\bar{k}_1) = 0$, $\hat{u}_3(\bar{k}_1) = \hat{u}_s(\bar{k}_1)$ and $\hat{u}_1(\bar{k}_1) = \hat{w}_s(\bar{k}_1)$. These relationships are inserted into Eq. (12) that now constitutes a solvable system of equations. When the track displacements have been calculated, the individual strip forces can be obtained from $\hat{\mathbf{F}} = \hat{\mathbf{H}}^{-1}\hat{\mathbf{u}}$ and used for calculating the free-field soil surface response.

4.2. Finite element models: Models (c) and (d)

To account for the deformation of the slab in the lateral, finite elements are used for modeling the track in Models (c) and (d). The coordinate transformation in Eq. (2), when applied to the equations governing the FE formulations, introduces convective terms in the damping and stiffness matrices. The finite elements used for the track are described in Section 4.2.1. In Section 4.2.2, the coupling of the FE track to the soil is described.

4.2.1. Element equations for railway track

With the coordinate transformation in Eq. (2) and the partial derivative relations in Eq. (3), the Cauchy equation of motion can be written as

$$\bar{\nabla}^T \bar{\sigma} = \rho \left(\frac{\partial^2 \bar{\mathbf{u}}}{\partial t^2} - 2v \frac{\partial^2 \bar{\mathbf{u}}}{\partial t \partial \bar{x}_1} + v^2 \frac{\partial^2 \bar{\mathbf{u}}}{\partial \bar{x}_1^2} \right), \quad (18)$$

where the matrix differential operator $\bar{\nabla}$, the stress vector $\bar{\sigma}$ and the displacement vector $\bar{\mathbf{u}}$ are defined as

$$\bar{\nabla}^T = \begin{bmatrix} \frac{\partial}{\partial \bar{x}_1} & 0 & 0 & \frac{\partial}{\partial \bar{x}_2} & \frac{\partial}{\partial \bar{x}_3} & 0 \\ 0 & \frac{\partial}{\partial \bar{x}_2} & 0 & \frac{\partial}{\partial \bar{x}_1} & 0 & \frac{\partial}{\partial \bar{x}_3} \\ 0 & 0 & \frac{\partial}{\partial \bar{x}_3} & 0 & \frac{\partial}{\partial \bar{x}_1} & \frac{\partial}{\partial \bar{x}_2} \end{bmatrix}, \quad (19)$$

$$\bar{\sigma}^T = [\bar{\sigma}_{11} \quad \bar{\sigma}_{22} \quad \bar{\sigma}_{33} \quad \bar{\sigma}_{12} \quad \bar{\sigma}_{13} \quad \bar{\sigma}_{23}], \quad (20)$$

$$\bar{\mathbf{u}}^T = [\bar{u}_1 \quad \bar{u}_2 \quad \bar{u}_3], \quad (21)$$

The weak form is obtained by multiplying Eq. (18) by an arbitrary weight function vector $\mathbf{g} = \mathbf{g}(\bar{x}_1, \bar{x}_2, \bar{x}_3)$ and integrating it over the region. The resulting weak form, after partial integration, becomes

$$\begin{aligned} \int_V (\bar{\nabla} \mathbf{g})^T \bar{\sigma} dV + \rho \int_V \mathbf{g}^T \frac{\partial^2 \bar{\mathbf{u}}}{\partial t^2} dV - 2\rho v \int_V \mathbf{g}^T \frac{\partial^2 \bar{\mathbf{u}}}{\partial t \partial \bar{x}_1} dV \\ + \rho v^2 \int_S \mathbf{g}^T \frac{\partial \bar{\mathbf{u}}}{\partial \bar{x}_1} n_x dS - \rho v^2 \int_V \frac{\partial \bar{\mathbf{g}}}{\partial \bar{x}_1} \frac{\partial \bar{\mathbf{u}}}{\partial \bar{x}_1} dV = \int_S \mathbf{g}^T \mathbf{t} dS, \end{aligned} \quad (22)$$

where \mathbf{t} is the traction vector.

To obtain the FE formulation, the displacements $\bar{\mathbf{u}}(\bar{x}_1, \bar{x}_2, \bar{x}_3, t)$ are approximated using the element nodal values $\mathbf{a}(t)$ and the shape functions $\mathbf{N}(\bar{x}_1, \bar{x}_2, \bar{x}_3)$ as $\bar{\mathbf{u}} = \mathbf{N}\mathbf{a}$. Adopting the Galerkin method, the mass, damping and stiffness matrices, and the load vector, are identified as

$$\mathbf{K} = \int_V (\bar{\nabla} \mathbf{N})^T \mathbf{D} (\bar{\nabla} \mathbf{N}) dV - \rho v^2 \int_V \frac{\partial \mathbf{N}}{\partial \bar{x}_1} \frac{\partial \mathbf{N}}{\partial \bar{x}_1} dV + \rho v^2 \int_S \mathbf{N}^T \frac{\partial \mathbf{N}}{\partial \bar{x}_1} n_x dS, \quad (23)$$

$$\mathbf{C} = -2\rho v \int_V \mathbf{N}^T \frac{\partial \mathbf{N}}{\partial \bar{x}_1} dV, \quad (24)$$

$$\mathbf{M} = \rho \int_V \mathbf{N}^T \mathbf{N} dV, \quad (25)$$

$$\mathbf{f}_i = \int_S \mathbf{N}^T \mathbf{t} dS, \quad (26)$$

where \mathbf{D} is the constitutive matrix for isotropic elasticity. Similar derivations for the convective solid finite elements can be found in e.g. [17]. Analogously, convective terms in the stiffness and damping matrices are also obtained for the other element types. When the velocity v is set to zero, the equations reduce to the standard FE equations, whose derivations can be found in for example [21].

In Model (c), the track slab is modeled using 4-node rectangular Kirchhoff shell elements with five degrees-of-freedom (DoFs) per node (three displacements and two rotations). In Model (d), standard 8-node isoparametric brick elements with three displacement DoFs per node are used. In Models (c) and (d), 2-node Bernoulli–Euler beam elements with two DoFs per node (vertical displacement and one rotation), are used for modeling the rails. The rail pads, i.e. the coupling between the rails and the slab, are modeled by visco-elastic interface elements representing continuous springs and dashpots. Here, the equations are

derived for an interface element when the rail is parallel to the x -axis. Denoting the spring stiffness and dashpot coefficient by k and c , respectively, the loads on the rail and slab from the visco-elastic interface are written

$$q_r(x_1, t) = -k(w_r - w_s) - c \left(\frac{\partial w_r}{\partial t} - \frac{\partial w_s}{\partial t} \right), \quad (27)$$

$$q_s(x_1, x_{2r}, t) = -k(w_s - w_r) - c \left(\frac{\partial w_s}{\partial t} - \frac{\partial w_r}{\partial t} \right), \quad (28)$$

where $w_r = w_r(x_1, t)$ is the deflection in the rail, and $w_s = w_s(x_1, x_{2r}, t)$ is the deflection of the slab at the x_2 -coordinate of the rail $x_2 = x_{2r}$. With the coordinate transformation in Eq. (2) and the partial derivative relations in Eq. (3), these loads are obtained in the moving frame of reference as

$$\bar{q}_r(\bar{x}_1, t) = -k(\bar{w}_r - \bar{w}_s) - c \left\{ \left(\frac{\partial \bar{w}_r}{\partial t} - \frac{\partial \bar{w}_s}{\partial t} \right) - v \left(\frac{\partial \bar{w}_r}{\partial \bar{x}_1} - \frac{\partial \bar{w}_s}{\partial \bar{x}_1} \right) \right\}, \quad (29)$$

$$\bar{q}_s(\bar{x}_1, t) = -k(\bar{w}_s - \bar{w}_r) - c \left\{ \left(\frac{\partial \bar{w}_s}{\partial t} - \frac{\partial \bar{w}_r}{\partial t} \right) - v \left(\frac{\partial \bar{w}_s}{\partial \bar{x}_1} - \frac{\partial \bar{w}_r}{\partial \bar{x}_1} \right) \right\}. \quad (30)$$

The displacements of the rail, $w_r(\bar{x}_1)$ are approximated using the beam element shape functions $\mathbf{N}_r(\bar{x}_1)$ and the element nodal displacements $\mathbf{a}_r(t)$. Likewise, the slab displacements $w_s(\bar{x}_1, \bar{x}_{2r})$ are approximated using the shell or solid element shape functions $\mathbf{N}_s(\bar{x}_1, \bar{x}_2)$ evaluated at $\bar{x}_2 = \bar{x}_{2r}$, and the element nodal displacements $\mathbf{a}_s(t)$. By equating the forces acting on the rail and slab to the internal forces of the interface element, the following expressions are obtained for the interface element stiffness and damping matrices:

$$\begin{aligned} \mathbf{K} = k & \left\{ \int_{-L/2}^{L/2} \bar{\mathbf{N}}_u^T \bar{\mathbf{N}}_u d\bar{x}_1 + \int_{-L/2}^{L/2} \bar{\mathbf{N}}_l^T \bar{\mathbf{N}}_l d\bar{x}_1 \right. \\ & \left. - \int_{-L/2}^{L/2} \bar{\mathbf{N}}_u^T \bar{\mathbf{N}}_l d\bar{x}_1 - \int_{-L/2}^{L/2} \bar{\mathbf{N}}_l^T \bar{\mathbf{N}}_u d\bar{x}_1 \right\} \\ -c v & \left\{ \int_{-L/2}^{L/2} \bar{\mathbf{N}}_u^T \frac{d\bar{\mathbf{N}}_u}{d\bar{x}_1} d\bar{x}_1 + \int_{-L/2}^{L/2} \bar{\mathbf{N}}_l^T \frac{d\bar{\mathbf{N}}_l}{d\bar{x}_1} d\bar{x}_1 \right. \\ & \left. - \int_{-L/2}^{L/2} \bar{\mathbf{N}}_u^T \frac{d\bar{\mathbf{N}}_l}{d\bar{x}_1} d\bar{x}_1 - \int_{-L/2}^{L/2} \bar{\mathbf{N}}_l^T \frac{d\bar{\mathbf{N}}_u}{d\bar{x}_1} d\bar{x}_1 \right\}, \end{aligned} \quad (31)$$

$$\begin{aligned} \mathbf{C} = c & \left\{ \int_{-L/2}^{L/2} \bar{\mathbf{N}}_u^T \bar{\mathbf{N}}_u d\bar{x}_1 + \int_{-L/2}^{L/2} \bar{\mathbf{N}}_l^T \bar{\mathbf{N}}_l d\bar{x}_1 \right. \\ & \left. - \int_{-L/2}^{L/2} \bar{\mathbf{N}}_u^T \bar{\mathbf{N}}_l d\bar{x}_1 - \int_{-L/2}^{L/2} \bar{\mathbf{N}}_l^T \bar{\mathbf{N}}_u d\bar{x}_1 \right\}, \end{aligned} \quad (32)$$

where L is the element length and the vectors $\bar{\mathbf{N}}_u$ and $\bar{\mathbf{N}}_l$ collect the shape functions for both the rail and the slab as

$$\begin{aligned} \bar{\mathbf{N}}_u(\bar{x}_1) &= [\mathbf{N}_r(\bar{x}_1) \quad 0 \times \mathbf{N}_s(\bar{x}_1, \bar{x}_2 = \bar{x}_{2r})], \\ \bar{\mathbf{N}}_l(\bar{x}_1) &= [0 \times \mathbf{N}_r(\bar{x}_1) \quad \mathbf{N}_s(\bar{x}_1, \bar{x}_2 = \bar{x}_{2r})] \end{aligned} \quad (33)$$

Following standard FE assembly, the equations of motion for the track structure can be written as

$$\mathbf{M}_t \ddot{\mathbf{u}}_t + \mathbf{C}_t \dot{\mathbf{u}}_t + \mathbf{K}_t \mathbf{u}_t = \bar{\mathbf{f}}_t, \quad (34)$$

where \mathbf{M}_t , \mathbf{C}_t and \mathbf{K}_t is the total mass, damping and stiffness matrix, respectively, of the complete track structure. Further, \mathbf{u}_t and $\bar{\mathbf{f}}_t$ is the displacement and force vector for the complete track structure, respectively, in the moving frame of reference.

4.2.2. Coupling of finite element track to soil

Assuming steady-state conditions, the governing equation for the railway track structure can be written as

$$(-\omega^2 \mathbf{M}_t + i\omega \mathbf{C}_t + \mathbf{K}_t) \mathbf{u}_t = \mathbf{D}_t \mathbf{u}_t = \bar{\mathbf{f}}_t, \quad (35)$$

where ω is the circular frequency of vibration in the moving frame of reference and the dynamic stiffness matrix of the track is $\mathbf{D}_t = (-\omega^2 \mathbf{M}_t + i\omega \mathbf{C}_t + \mathbf{K}_t)$.

The track is coupled to a dynamic stiffness matrix representing the soil. This dynamic stiffness matrix is derived from the previously described Green's function for a horizontally layered visco-elastic half-space. The soil response is calculated for a unit load on the soil surface. The unit load is applied with uniform traction over a rectangular

area, the size of which equals the element size in the connecting superstructure. Considering an element size of $2a \times 2b$, in the \bar{x}_1 - and \bar{x}_2 -direction, respectively, the traction p_j for a load in direction j is

$$p_j(\bar{x}_1, \bar{x}_2, \omega) = \begin{cases} 1/(4ab), & -a < \bar{x}_1 < a, -b < \bar{x}_2 < b \\ 0, & \text{otherwise} \end{cases}. \quad (36)$$

In wavenumber domain the traction becomes

$$\bar{p}_j(\bar{k}_1, \bar{k}_2, \omega) = \frac{\sin(\bar{k}_1 a)}{\bar{k}_1 a} \frac{\sin(\bar{k}_2 b)}{\bar{k}_2 b}. \quad (37)$$

The soil response is calculated for three load cases, with the unit load acting in the \bar{x}_1 -, \bar{x}_2 - and \bar{x}_3 -directions, respectively. From these three load cases, a dynamic flexibility matrix $\mathbf{C}_s(\omega, v)$ is established for a set of DoFs where the superstructure interacts with the soil surface. These DoFs will be referred to as soil-structure interaction (SSI) DoFs. The flexibility matrix is then inverted to form the dynamic stiffness matrix of the soil, $\mathbf{D}_s(\omega, v) = \mathbf{C}_s^{-1}(\omega, v)$, which gives a relation between the steady-state displacements $\bar{\mathbf{u}}_s$ and forces $\bar{\mathbf{f}}_s$ for the SSI DoFs, at a certain load circular frequency ω and velocity v , as

$$\mathbf{D}_s \bar{\mathbf{u}}_s = \bar{\mathbf{f}}_s, \quad (38)$$

The track and soil are coupled in a standard FE manner, and a global system of equations for the soil and the railway structure is formed by combining Eqs. (35) and (38), yielding

$$\mathbf{D}_g \bar{\mathbf{u}}_t = \bar{\mathbf{f}}_t, \quad (39)$$

where \mathbf{D}_g represents the global dynamic stiffness matrix for the track structure and the soil.

The free-field response is calculated in a two-step procedure. The first step involves calculating the displacements in the slab-soil interface due to the moving load on the track by solving Eq. (39). The corresponding forces on the soil surface, $\bar{\mathbf{f}}_s$, are calculated by Eq. (38). In the second step, the free-field response due to these forces is calculated. A flexibility matrix $\mathbf{C}_{s,f}(\omega, v)$ is established expressing the displacements in free-field due to forces on the soil-structure interface, i.e. the SSI DoFs, again using the previously described unit loadcases. The free-field displacements, $\bar{\mathbf{u}}_f$, are then calculated as

$$\bar{\mathbf{u}}_f = \mathbf{C}_{s,f} \bar{\mathbf{f}}_s. \quad (40)$$

These free-field displacements are obtained in the frame of reference of the moving load. The response is in steady-state with the frequency of the harmonic load.

5. Results from numerical studies

In Section 5.1 the free-field vertical response, due to a moving harmonic unit load on the track, as obtained from the different models when disregarding any in-plane interaction between the slab and the soil is presented. Section 5.2 contains the corresponding results when in-plane slab-soil interaction is accounted for. Finally, in Section 5.3, a vehicle model is introduced to calculate the wheel-rail contact forces as the vehicle runs over an uneven rail.

5.1. Free-field displacements assuming only vertical slab-soil interaction

To compare the free-field response obtained from the different models, the vertical displacement is extracted for points along a line parallel with the track, as illustrated in Fig. 4. The displacements are calculated in the coordinate system following the moving load, meaning that $\bar{x}_1 = 0$ corresponds to a point perpendicular to the moving load. Positive \bar{x}_1 -values correspond to points ahead of the load. In this coordinate system the responses are harmonic with the frequency of the harmonic moving load.

The response magnitude along a line located 10 m from the track center line, as obtained with the different models when only accounting

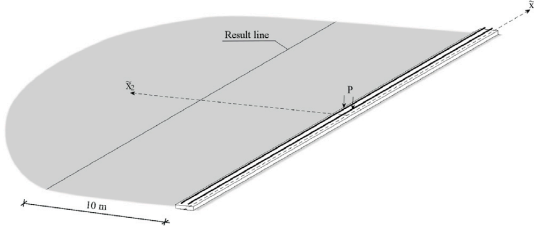


Fig. 4. Illustration of the result line in relation to the moving load. The response is calculated in the moving frame of reference, along a line located 10 m from the track centerline.

for the vertical interaction between the slab and the soil, for a harmonic unit load (0.5 N per rail) moving along the track at $v = 30$ m/s are shown in Figs. 5–7 for the excitation frequencies $f = 40$ Hz, $f = 60$ Hz and $f = 80$ Hz, respectively. For these frequencies, the Rayleigh wavelength for the stiffer soil is $\lambda = 6.5$ m (\sim twice the slab width), $\lambda = 4.3$ m and $\lambda = 3.3$ m (similar to the slab width), respectively. For the softer soil, these frequencies correspond to Rayleigh wavelengths $\lambda = 3.3$ m (similar to the slab width), $\lambda = 2.2$ m and $\lambda = 1.6$ m (\sim half the slab width), respectively. These frequencies are selected to demonstrate the features of the different modeling strategies. Condensed results for the frequency range (5–80 Hz) are shown in the next subsection. Subfigures (a) and (b) show the response of the softer soil for the thin and thick slab, respectively, whereas (c) and (d) show the corresponding results for the stiffer soil. The response along a line located at a greater distance (25 m) from the track has also been studied, but these results are not presented here because they show the same general differences as obtained for the shorter distance.

As expected, Models (c) and (d) yield almost indistinguishable results for both slab thicknesses and both soil types in the entire frequency range. In the following discussion, these responses are considered accurate. For low frequencies, the different vertical contact pressure distributions implied by the different modeling strategies have virtually no effect on the free-field response. This is because, for low frequencies, the wavelength of the fundamental Rayleigh wave that dominates the response is long compared to the width of the slab.

At 40 Hz (see Fig. 5), the response obtained assuming a laterally constant slab–soil pressure, Model (a), is significantly underestimated for both slabs on soft soil, as seen in subfigures (a) and (b). The response is close to zero perpendicular to the load, i.e. at $\bar{x}_1 = 0$. This is because the Rayleigh wavelength is similar to the slab width at this frequency, and a uniform pressure exerted over one wavelength does not excite such a wave. This can be explained by the wavenumber content of a uniform load, $\hat{p} = \sin(\bar{k}_2 a) / (\bar{k}_2 a)$, where $2a$ is the load width. This expression becomes zero for $\bar{k}_2 = \pi/a$, i.e. when $2a = \lambda$. Hence, excitation of the Rayleigh wave perpendicular to the track is very small in Model (a) for frequencies where the wavelength is similar to the slab width.

In the case of a thick slab, the response obtained assuming a laterally constant displacement under the slab, Model (b), is almost indistinguishable from that obtained with Models (c) and (d), see subfigure (b). However, this is not the case for the thinner slab, see subfigure (a), where also Model (b) produces a slightly underestimated response. The absolute value of the slab–soil pressure distributions directly under the load for $f = 40$ Hz are shown in Fig. 8 for the different models. For the thin slab, the presence of the rails is visible as local peaks in the contact pressure obtained using Models (c) and (d). In addition, the high contact pressures around the slab edges, obtained by enforcing rigidity in the \bar{x}_2 -direction using Model (b), are not present for the thin slab when the cross-section flexibility is accounted for, as in Models (c) and (d). For the thick slab, however, the true pressure distribution

approaches that of a rigid slab and hence the free-field response levels are also almost identical. For the stiffer soil, the Rayleigh wavelength is approximately twice the slab width at 40 Hz. For such a wavelength to slab width ratio, the uniform pressure produces higher vibrations than the pressure distribution obtained with a rigid surface, c.f. Fig. 5(c) and (d). The soil is even slightly more responsive to the “true” pressure distribution obtained for the thin slab, with lower edge pressures and instead having a higher overall pressure in the center of the slab, see Figs. 5(c) and 8(c).

At higher frequencies, Model (a) yield an underestimated response for both slab thicknesses and soil types, see Figs. 6–7. For the thin slab and soft soil, the response obtained from Model (b) is overestimated for frequencies with a fundamental Rayleigh wavelength shorter than the slab width. For the stiff soil, the wavelength of the fundamental Rayleigh wave is longer than the slab width in the entire studied frequency range, and assuming a rigid slab in the cross direction yields an underestimated response for the thin slab, but an accurate response for the thick slab. The differences in the slab–soil contact pressures, obtained with the Models (a)–(d), are similar to those discussed above for $f = 40$ Hz, and are therefore not shown here for the higher frequencies.

5.2. Free-field displacements including in-plane slab–soil interaction

When the in-plane slab–soil displacements are coupled, shear forces arise in the interface. These shear forces also affect the vertical vibration levels in the free field. The maximum vertical displacement along a line located 10 m from the track center line, for a unit load moving along the track at $v = 30$ m/s, are shown in Figs. 9–11 for the Models (b)–(d) when in-plane interaction between the slab and soil is enforced. The excitation frequencies for which the response is shown are again $f = 40$ Hz, $f = 60$ Hz and $f = 80$ Hz, respectively.

The effects of in-plane slab–soil interaction on the vertical response levels are most noticeable around the frequencies for which the wavelength of the Rayleigh wave in the soil is similar to the slab width, see Fig. 9(a)–(b) (c.f. Fig. 5) and Fig. 11(c)–(d) (c.f. Fig. 7). The influence of the in-plane slab–soil interaction is complex, as it introduces shear forces on the soil surface that also change the vertical interaction forces, both of which effects influence the free-field response.

As all models are established in the moving frame of reference, following the load at the given velocity $v = 30$ m/s, the results are also obtained in this reference frame. Hence, to obtain the displacement response of a fixed point, the receiver is moved through the model in the opposite travel direction of the load, yielding a transient time–history of the displacement response. This is done by traversing through the steady-state responses along the result line with $v = 30$ m/s, accounting for the phase of the response at each point along the line. The transient response contains a wide range of frequencies due to the Doppler effect. The time derivative of the fixed point displacement time–history yields the fixed point particle velocity. To efficiently compare the free-field responses for a range of excitation frequencies, two measures are used here. The first measure is the fixed point maximum vertical particle velocity. The second measure is the energy of the velocity time–history signal, calculated as

$$E_{\dot{u}_f} = \int_{-\infty}^{\infty} |\dot{u}_f(t)|^2 dt \quad (14)$$

where $\dot{u}_f(t)$ is the vertical velocity time–history response for a fixed point, due to the moving unit load with frequency f .

The maximum vertical particle velocities and the signal energies $E_{\dot{u}_f}$ obtained from the different models are shown in Fig. 12 and Fig. 14, respectively, for a fixed point 10 m from the track. The results in Figs. 12 and 14 are normalized to the response obtained with Model (d), and shown in Fig. 13 and Fig. 15, respectively. In these figures, the response from the different models when the in-plane slab–soil interaction was disregarded, is also shown for reference.

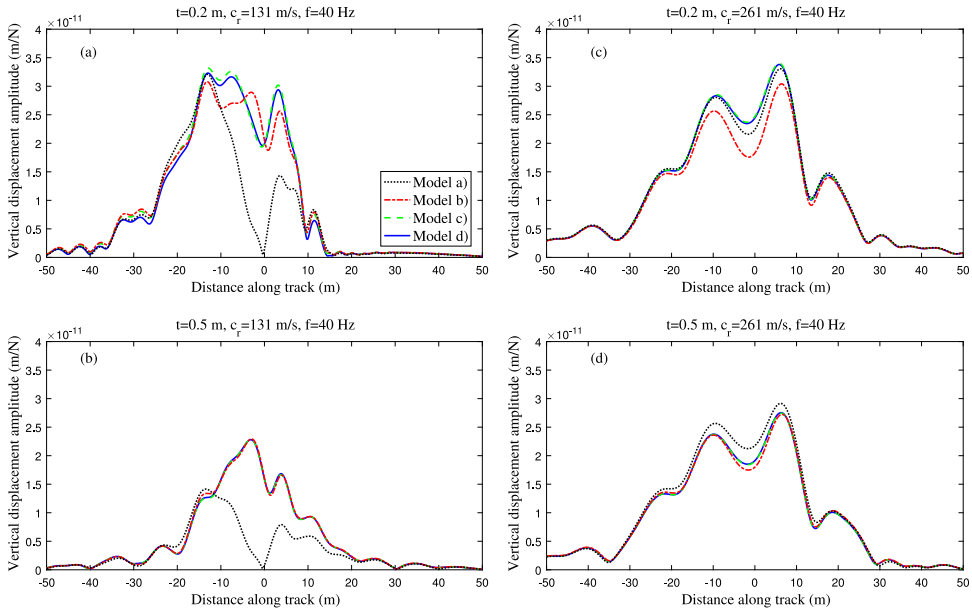


Fig. 5. Maximum free-field displacement 10 m from the track center line, due to a unit harmonic load at $f = 40$ Hz moving along the track at $v = 30$ m/s, as obtained with Models (a)–(d), accounting only for vertical interaction between slab and soil. Figures (a) and (b) are for the thin and thick slab, respectively, on the softer soil. Figures (c) and (d) are the corresponding results for the stiffer soil.

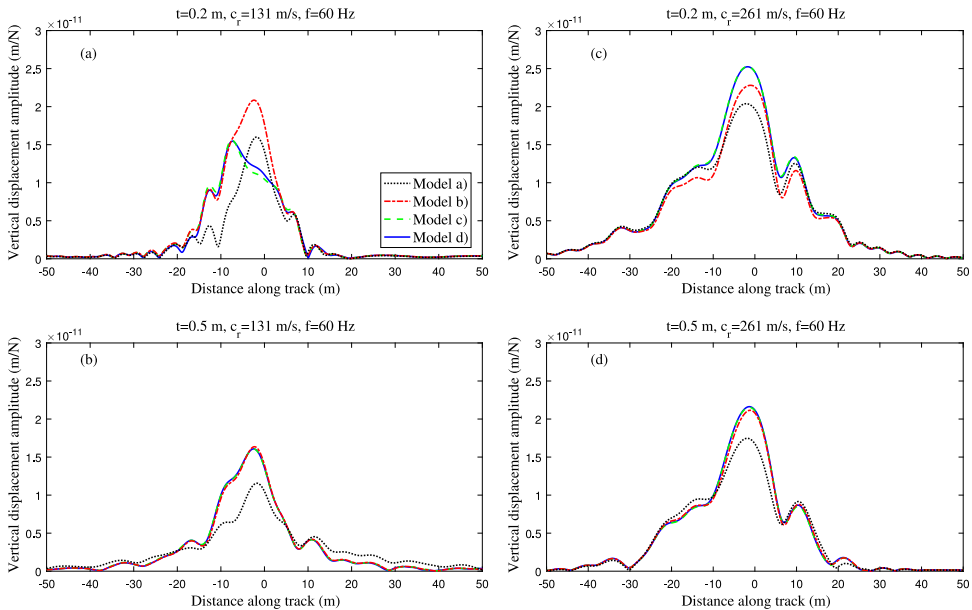


Fig. 6. Maximum free-field displacement 10 m from the track center line, due to a unit harmonic load at $f = 60$ Hz moving along the track at $v = 30$ m/s, as obtained with Models (a)–(d), accounting only for vertical interaction between slab and soil. Figures (a) and (b) are for the thin and thick slab, respectively, on the softer soil. Figures (c) and (d) are the corresponding results for the stiffer soil.

It can be seen in Figs. 13 and 15 that for the cases studied here, the predicted vertical free-field response is in general significantly higher when in-plane slab–soil interaction is accounted for and that its effects are equally significant for both the thick and the thin slab on both

soil types. Disregarding the in-plane slab–soil interaction yields an underestimation of the peak particle vertical velocity and the vertical velocity signal energy, of as much as 30% and 50% respectively, c.f. the gray/blue solid lines in Figs. 13 and 15. Model (c) (shell elements)

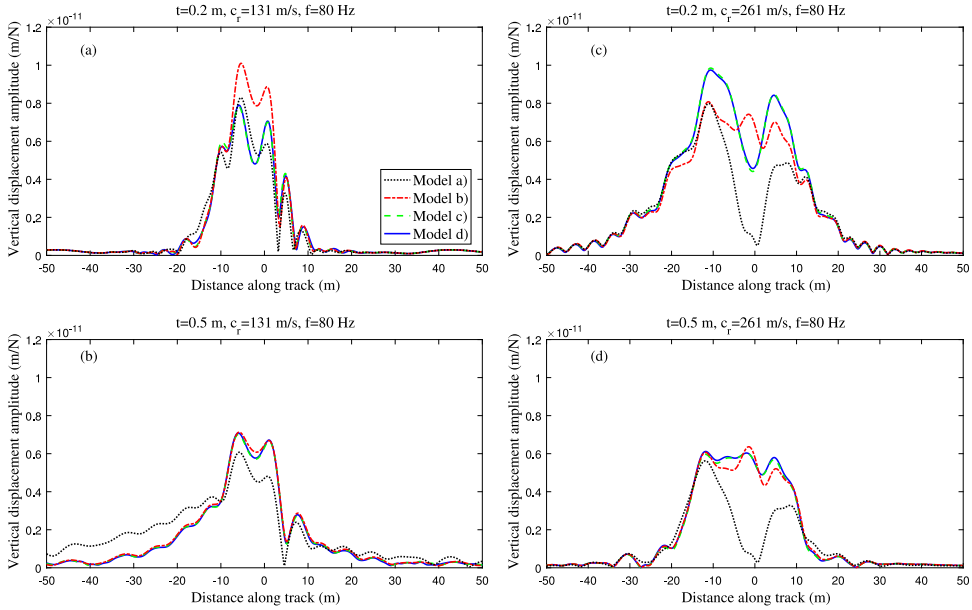


Fig. 7. Maximum free-field displacement 10 m from the track center line, due to a unit harmonic load at $f = 80$ Hz moving along the track at $v = 30$ m/s, as obtained with Models (a)–(d), accounting only for vertical interaction between slab and soil. Figures (a) and (b) are for the thin and thick slab, respectively, on the softer soil. Figures (c) and (d) are the corresponding results for the stiffer soil.

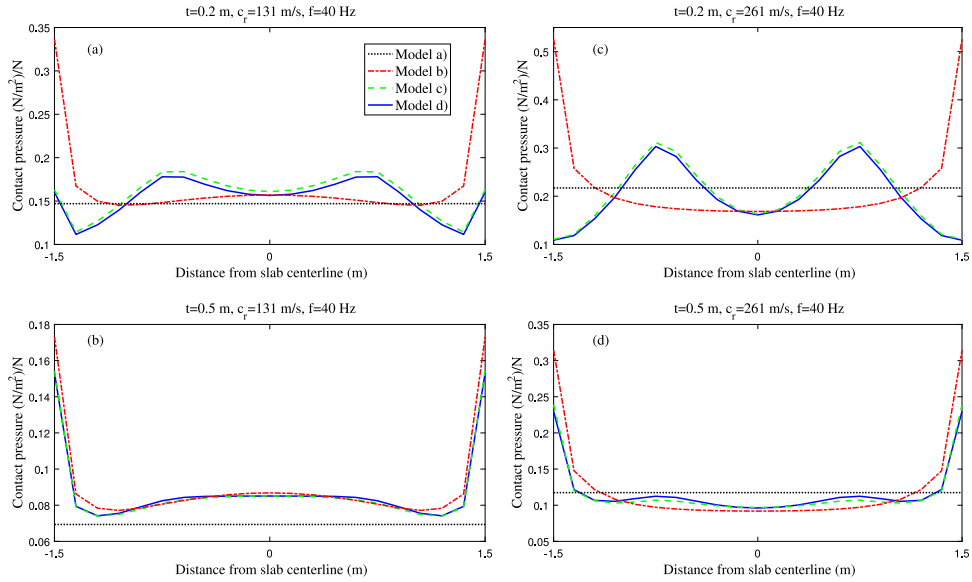


Fig. 8. Vertical slab-soil contact pressure directly under the unit harmonic load at $f = 40$ Hz moving along the track at $v = 30$ m/s, as obtained with Models (a)–(d). Figures (a) and (b) are for the thin and thick slab, respectively, on the softer soil. Figures (c) and (d) are the corresponding results for the stiffer soil.

yields similar vibration levels as Model (d) (solid elements) for both slab thicknesses on both soils, both in terms of maximum particle velocity and velocity signal energy. When in-plane slab–soil interaction was disregarded, the two models provided almost indistinguishable

results. When the in-plane interaction is included, the differences increase. In Model (c) the mid-section is located in the plane of the soil surface, i.e. the membrane and bending behaviors of the shell elements are decoupled. Furthermore, whereas the model with solid elements enables the slab lower surface to deform differently than the

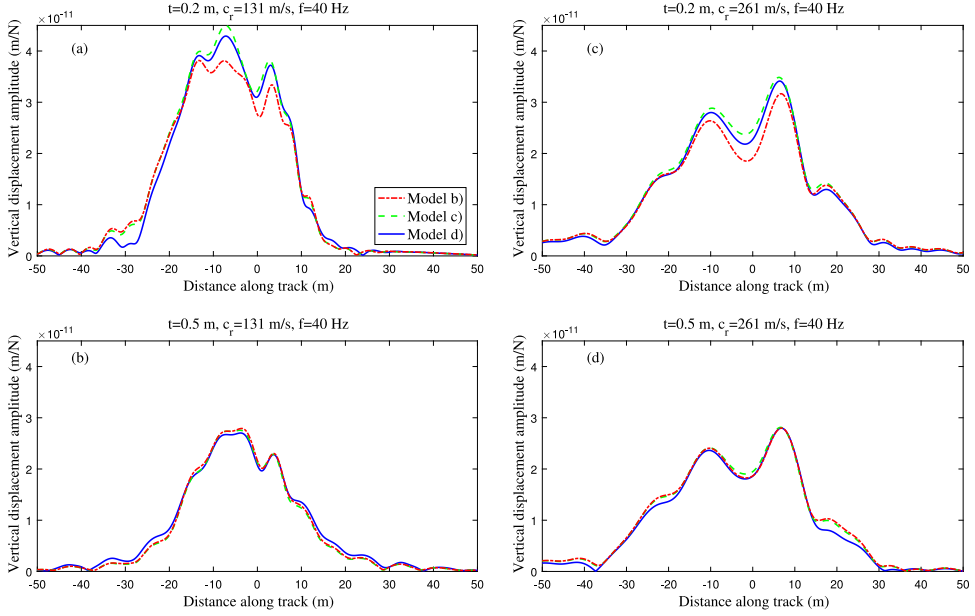


Fig. 9. Maximum free-field displacement 10 m from the track center line, due to a unit harmonic load at $f = 40$ Hz moving along the track at $v = 30$ m/s, as obtained with Models (b)–(d), accounting for in-plane slab–soil interaction. Figures (a) and (b) are for the thin and thick slab, respectively, on the softer soil. Figures (c) and (d) are the corresponding results for the stiffer soil.

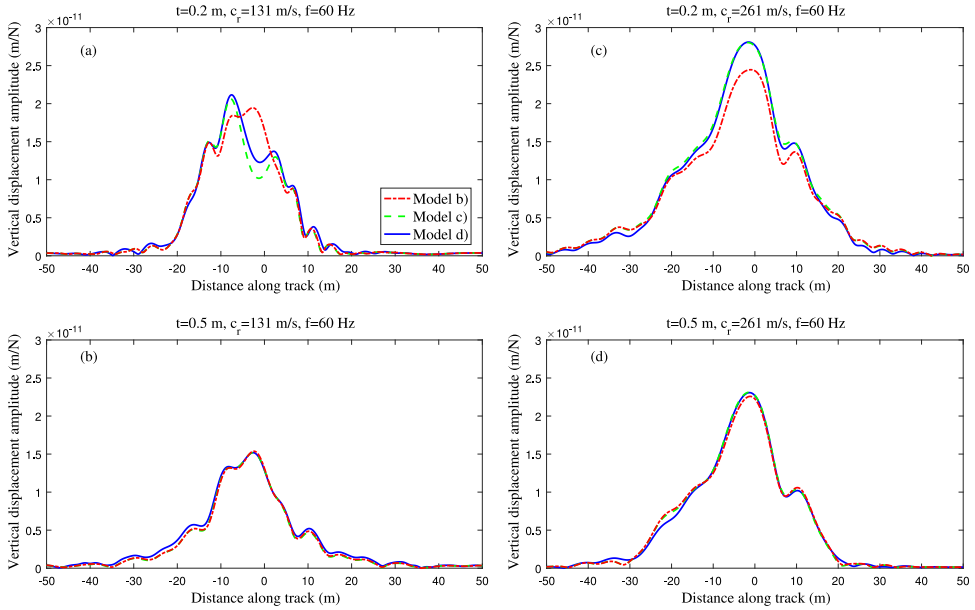


Fig. 10. Maximum free-field displacement 10 m from the track center line, due to a unit harmonic load at $f = 60$ Hz moving along the track at $v = 30$ m/s, as obtained with Models (b)–(d), accounting for in-plane slab–soil interaction. Figures (a) and (b) are for the thin and thick slab, respectively, on the softer soil. Figures (c) and (d) are the corresponding results for the stiffer soil.

upper surface, the shell elements necessarily engage the entire thickness of the slab. Similarly, the axial and bending behaviors of the beam representing the slab in Model (b) are also decoupled. For the thick slab, the response levels obtained with Model (b) are about as accurate

as those from Model (c), and within about $\pm 10\%$ of those obtained with Model (d).

The maximum vibration levels, both in terms of peak vertical particle velocity and velocity signal energy, occur around 25–30 Hz for

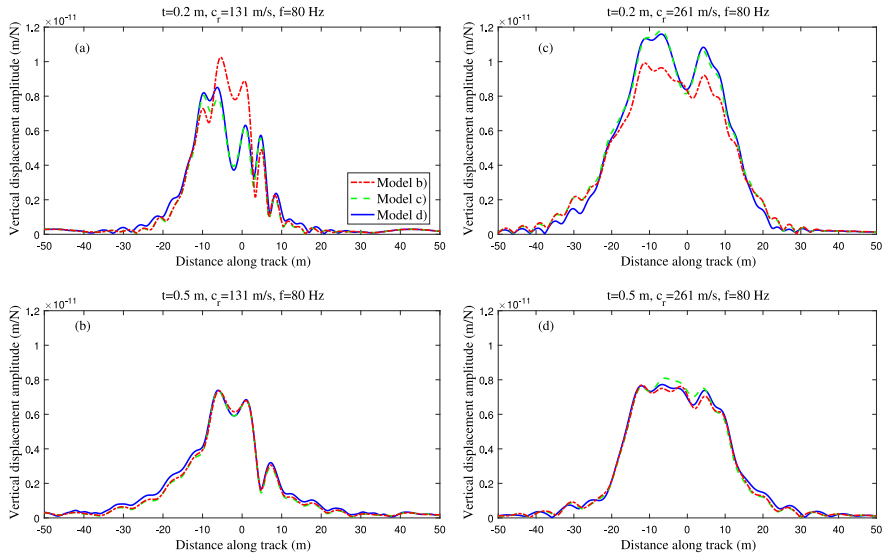


Fig. 11. Maximum free-field displacement 10 m from the track center line, due to a unit harmonic load at $f = 80$ Hz moving along the track at $v = 30$ m/s, as obtained with Models (b)–(d), accounting for in-plane slab–soil interaction. Figures (a) and (b) are for the thin and thick slab, respectively, on the softer soil. Figures (c) and (d) are the corresponding results for the stiffer soil.

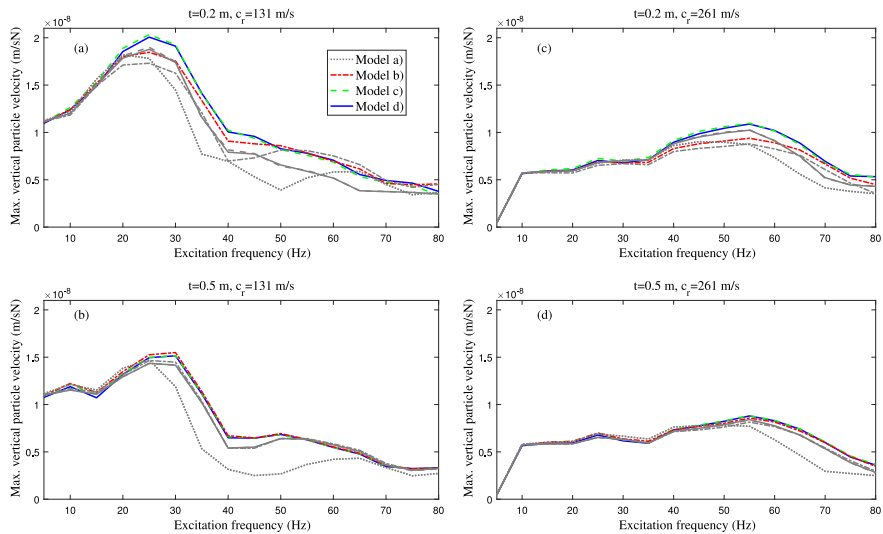


Fig. 12. Maximum particle vertical velocity in a fixed point 10 m from the track center line, due to a unit harmonic load moving along the track at $v = 30$ m/s, as obtained with Models (a)–(d). Figures (a) and (b) are for the thin and thick slab, respectively, on the softer soil. Figures (c) and (d) are the corresponding results for the stiffer soil. Curves in gray are without accounting for in-plane slab–soil interaction.

the softer soil and around 50–55 Hz for the stiffer soil. For these frequencies, the Rayleigh wavelength is slightly shorter than twice the slab width. Further, it can be seen that the thicker slab yields significantly lower vibration levels.

5.3. Rail receptance and wheel–rail interaction force

In the previous subsections the differences between the different modeling strategies, regarding the free-field response due to a moving unit load, have been presented. However, when a vehicle runs over

an uneven rail, the dynamic forces that arise between the wheels and the rail depend on the rail receptance (displacement per unit force), as well as the vehicle and wheel–rail contact receptance. Hence, models providing different rail receptances will also provide different wheel–rail interaction forces. The absolute values of the loading point receptance, as obtained with the different models are shown in Fig. 16, for a load velocity of $v = 30$ m/s. The receptance is slightly higher for the cases with a thin slab than with a thick slab, c.f. subfigures (a) and (b) for the soft soil and subfigures (c) and (d) for the stiff soil. Further, the softer soil provides a higher rail point receptance than

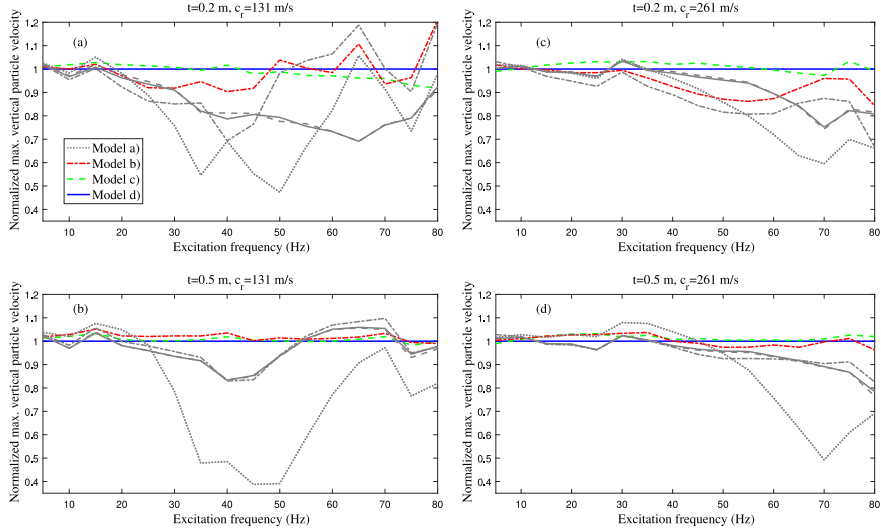


Fig. 13. Normalized maximum particle vertical velocity in a fixed point 10 m from the track center line, due to a unit harmonic load moving along the track at $v = 30$ m/s, as obtained with Models (a)–(d). The curves are normalized against Model (d). Figures (a) and (b) are for the thin and thick slab, respectively, on the softer soil. Figures (c) and (d) are the corresponding results for the stiffer soil. Curves in gray are without accounting for in-plane slab–soil interaction.

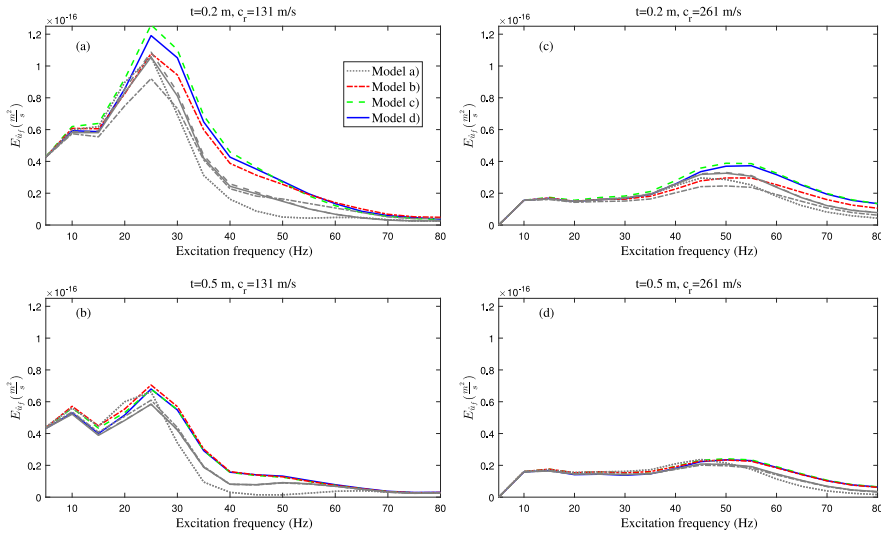


Fig. 14. Vertical velocity signal energy in a fixed point 10 m from the track center line, due to a unit harmonic load moving along the track at $v = 30$ m/s, as obtained with Models (a)–(d). Figures (a) and (b) are for the thin and thick slab, respectively, on the softer soil. Figures (c) and (d) are the corresponding results for the stiffer soil. Curves in gray are without accounting for in-plane slab–soil interaction.

the stiffer soil. The in-plane slab–soil interaction has a negligible effect ($<2\%$) on the rail receptance for the cases studied here. In Fig. 16, the values shown for Models (b)–(d) were calculated with in-plane slab–soil interaction taken into account.

A maximum of the rail receptance occurs around the cut-on frequency of the upper soil layer. For the stiffer soil conditions this can be discerned as the peak value at 10 Hz. For the softer soil conditions, the cut-on frequency is close to 5 Hz which is the lowest frequency included in the current study. For each studied case, the different models yield similar values of the receptance, however some differences can be discerned. Models (c) and (d) provide almost identical rail

receptances, with a maximum difference of less than 2%. Models (a) and (b) do not account for the slab flexibility in the \bar{x}_2 -direction and overestimate the stiffness in that sense, since the entire track cross-section is forced to move uniformly. Model (b) is seen to provide a slight underestimation of the receptance in the entire frequency span, with a maximum underestimation of about 5%, compared to Model (d), in the cases involving the thin slab. The differences between Models (a) and (b) are only due to the different slab–soil interface conditions, and the receptance obtained with Model (a) deviates by approximately $\pm 10\%$ compared to Model (d).

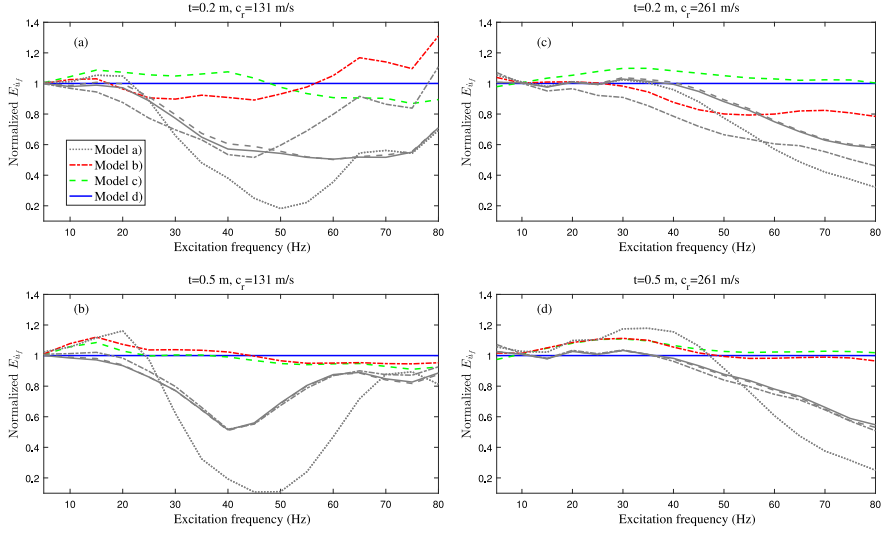


Fig. 15. Normalized vertical velocity energy in a fixed point 10 m from the track center line, due to a unit harmonic load moving along the track at $v = 30$ m/s, as obtained with Models (a)–(d). The curves are normalized against Model (d). Figures (a) and (b) are for the thin and thick slab, respectively, on the softer soil. Figures (c) and (d) are the corresponding results for the stiffer soil. Curves in gray are without accounting for in-plane slab–soil interaction.

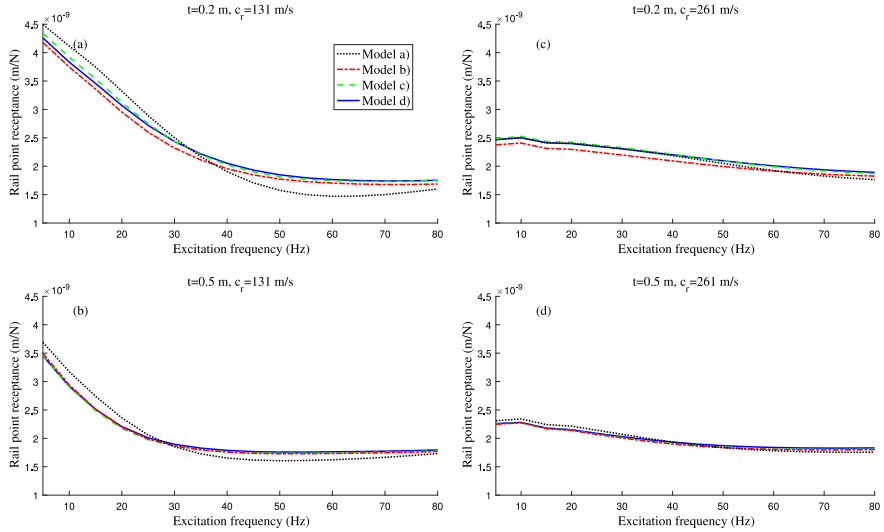


Fig. 16. Rail loading point receptance, due to a unit harmonic load moving along the track at $v = 30$ m/s, as obtained with Models (a)–(d). Figures (a) and (b) are for the thin and thick slab, respectively, on the softer soil. Figures (c) and (d) are the corresponding results for the stiffer soil.

The rail receptances for a given load speed are used for calculating the wheel–rail contact forces due to a vehicle running over an uneven rail. For a real vehicle with multiple axles, the receptances ahead and behind the loading points are required to set up a compliance matrix containing all the wheel–rail contact points. Here, however, a single axle vehicle is considered and thus only the receptance in the loading point is needed. The vehicle model is shown in Fig. 17, and its properties, taken from [14], are shown in Table 3. The vehicle model consists of the sprung/unsprung masses m_s and m_w , and a suspension defined by the spring stiffness k_s and k'_s and the damper c_s .

For a given circular frequency of excitation $\omega = 2\pi f$ the dynamic stiffness of the vehicle can be written as

$$\mathbf{D}_v = \begin{bmatrix} -\omega^2 m_w + i\omega c_s + k_s & -k_s & -i\omega c_s \\ -k_s & -\omega^2 m_s + k_s + k'_s & -k'_s \\ -i\omega c_s & -k'_s & i\omega c_s + k'_s \end{bmatrix}, \quad (42)$$

with the corresponding displacement vector

$$\mathbf{u}_v = \begin{bmatrix} u_w \\ u_s \\ u_d \end{bmatrix}. \quad (43)$$

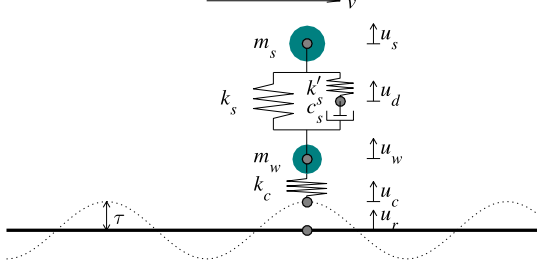


Fig. 17. Single-axle vehicle moving with fixed speed v on rail with unevenness magnitude τ .

In the present study, a unit height of 0.1 mm is used for each studied unevenness wavelength. The excitation frequency and the unevenness wavelength are related through the vehicle speed as $f = v/\lambda$. A linearized Hertzian contact spring, with stiffness k_c , accounts for the wheel-rail contact. The contact spring is assembled between the wheel and a contact point on the rail. For a given frequency of excitation, the displacement of the contact point can be written as $u_c = u_r + \tau$, where u_r is the rail displacement and τ describes the unevenness magnitude. The rail dynamic stiffness d_r at DoF u_r is the inverse of the complex valued point receptance. By eliminating the DoF u_c , the following system of equations is obtained,

$$\begin{bmatrix} -\omega^2 m_w + i\omega c_s + k_s + k_c & -k_s & -i\omega c_s & -k_c \\ -k_s & -\omega^2 m_s + k_s + k'_s & -k'_s & 0 \\ -i\omega c_s & -k'_s & i\omega c_s + k'_s & 0 \\ -k_c & 0 & 0 & d_r + k_c \end{bmatrix} \begin{bmatrix} u_w \\ u_s \\ u_d \\ u_r \end{bmatrix} = \begin{bmatrix} k_c \tau \\ 0 \\ 0 \\ -k_c \tau \end{bmatrix}. \quad (44)$$

The force in the contact spring is then simply $k_c(u_w - u_c) = k_c(u_w - u_r - \tau)$. Fig. 18 shows the absolute value of the wheel-rail contact force, as a

Table 3
Vehicle properties [14].

Parameter	Value
m_s (kg)	19 250
m_w (kg)	1750
k_s (N/m)	2.66×10^6
c_s (Ns/m)	3.5×10^4
k'_s (N/m)	3×10^6
k_c (N/m)	2.7×10^9

function of excitation frequency, for the different models. All models provide similar contact forces, the differences being of the same order of magnitude as the differences in the loading point receptance.

6. Conclusions

In the paper, four different modeling strategies with respect to assumptions about the slab track cross-section behavior and the track-soil interface conditions have been compared by calculating the vertical free-field response to a unit harmonic load moving along the track at a fixed speed. In the most general model used here, the slab is represented by 3D solid elements, and the response from this model is used as a reference to which the other models are compared. Two different slab thicknesses have been studied, on two stratifications with different stiffness of the top soil layer. Although the free-field response has been presented here only for a point 10 m from the track, the response further from the track has also been studied, and the same general conclusions apply also for those cases.

It has been found that for a thin slab, the pressure distribution under the slab due to load on the rails is highly influenced by the slab cross-section flexibility, and this in turn has a large effect on the predicted free-field vibrations. As expected, this pressure distribution and the resulting free-field vibrations, calculated with a solid continuum model (Model d), are predicted equally well with a computationally cheaper shell element model (Model c). However, the two beam models, assuming laterally constant slab-soil contact pressure (Model a) or laterally constant displacement (Model b), yield significantly different responses due to the inadequately assumed slab-soil pressure distributions. For the thicker slab, the cross-section flexibility is very low and the pressure

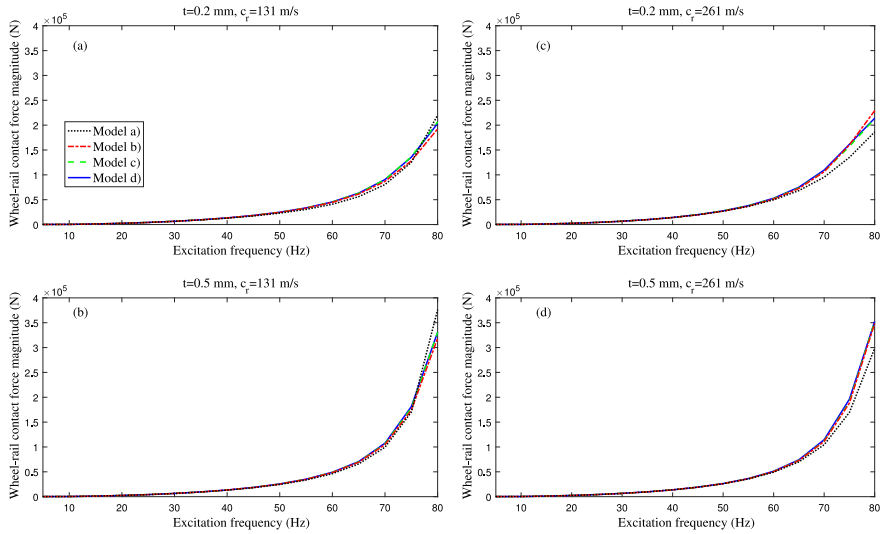


Fig. 18. Absolute value of wheel-rail contact force at different excitation frequencies, $f = v/\lambda$ due to the single-axle vehicle moving along the track at $v = 30$ m/s over a harmonic unevenness of 0.1 mm. Figures (a) and (b) are for the thin and thick slab, respectively, on the softer soil. Figures (c) and (d) are the corresponding results for the stiffer soil.

distribution under the slab due to a load on the rails, approaches that of a rigid slab. In that case, the beam model assuming laterally constant displacement (Model b) yields accurate results. It could be argued that Timoshenko beam theory is generally preferred over Bernoulli–Euler theory for modeling a thick slab, but the close agreement between Models (b) and (d) here indicate that the effects of disregarding the beam shear deformation is negligible in the studied cases.

Further, it has been found that if full shear transfer between the slab and the soil is assumed, increased vibration levels in the free-field are generally obtained, especially around the frequencies where the wavelength of the fundamental Rayleigh wave that dominates the response, is similar to the slab width. For the thick slab, both the shell model (Model c) and the beam model with laterally constant displacement (Model b), yield response levels that are within only a few percents of that obtained with the solid model (Model d). In the cases studied here, the rail point receptances and the wheel–rail interaction forces, as obtained with the different models are very similar, and are only marginally influenced by the in-plane slab–soil interaction.

Hence it can be concluded that for a thick slab, a beam model enforcing constant displacements under the slab width, is sufficient both with regards to the accuracy of the predicted rail receptance and the wheel–rail interaction forces, as well as the free-field vibrations, when compared to a solid continuum approach. However, for a thin slab, the cross-section flexibility has a significant impact on the free-field vibrations, which may be accounted for by using a shell model. In any case, the in-plane shear forces in the slab–soil interface need to be regarded since they significantly affect the predicted free-field vibration levels.

Declaration of competing interest

The authors declare that they have no known competing financial interests or personal relationships that could have appeared to influence the work reported in this paper.

Acknowledgment

The authors gratefully acknowledge financial support from the Swedish Innovation Agency (Vinnova) under grant no. 2018-04159.

References

[1] Yang Y, Hung H. A 2.5D finite-infinite element approach for modelling visco-elastic bodies subjected to moving loads. *Internat J Numer Methods Eng* 2008;51:1317–36.

[2] Sheng X, Jones CJC, Thompson DJ. Prediction of ground vibration from trains using the wavenumber finite and boundary element methods. *J Sound Vib* 2006;293:575–86.

[3] Lombaert G, Degrande G, Kogut J, François S. The experimental validation of a numerical model for the prediction of railway induced vibrations. *J Sound Vib* 2006;297:512–35.

[4] Galvín P, François S, Schevenels M, Bongini E, Degrande G, Lombaert G. A 2.5D coupled FE-BE model for the prediction of railway induced vibrations. *Soil Dyn Earthq Eng* 2010;30:1500–12.

[5] François S, Schevenels M, Galvín P, Lombaert G, Degrande G. A 2.5D coupled FE-BE methodology for the dynamic interaction between longitudinally invariant structures and a layered halfspace. *Comput Methods Appl Mech Engrg* 2010;199(23–24):1536–48.

[6] Alves Costa P, Calçada R, Silva Cardoso A. Track-ground vibrations induced by railway traffic: In-situ measurements and validation of a 2.5D FEM-BEM model. *Soil Dyn Earthq Eng* 2012;32(1):111–28.

[7] Sheng X, Jones CJC, Petyt M. Ground vibration generated by a harmonic load acting on a railway track. *J Sound Vib* 1999;225(1):3–28.

[8] Sheng X, Jones CJC, Petyt M. Ground vibration generated by a load moving along a railway track. *J Sound Vib* 1999;228(1):129–56.

[9] Kaynia AM, Madhus C, Zackrisson P. Ground vibration from high-speed trains: prediction and countermeasure. *J Geotech Geoenvironmental Eng* 2000;126(6):531–7.

[10] Triepaischajonsak N, Thompson DJ. A hybrid modelling approach for predicting ground vibration from trains. *J Sound Vib* 2015;335:147–73.

[11] Koroma SG, Thompson DJ, Hussein MFM, Ntosios E. A mixed space–time and wavenumber-frequency domain procedure for modelling ground vibration from surface railway tracks. *J Sound Vib* 2017;400:508–32.

[12] Steenbergen MJMM, Metrikine AV. The effect of the interface conditions on the dynamic response of a beam on a half-space to a moving load. *Eur J Mech A Solids* 2007;26:33–54.

[13] Malmberg J, Persson K, Persson P. Modeling train-induced ground-borne vibrations using FEM in a moving frame of reference. In: *Proceedings of compdyn 2019: 7th international conference on computational methods in structural dynamics and earthquake engineering*; 2019.

[14] Sheng X, Jones CJC, Thompson DJ. A theoretical model for ground vibration from trains generated by vertical track irregularities. *J Sound Vib* 2004;272:937–65.

[15] Ntosios E, Thompson D, Hussein M. The effect of track load correlation on ground-borne vibration from railways. *J Sound Vib* 2017;402:142–63.

[16] Lombaert G, Degrande G, Vanhauwere B, Vandeborghht B, François S. The control of ground-borne vibrations from railway traffic by means of continuous floating slabs. *J Sound Vib* 2006;297:946–61.

[17] Andersen LV. *Linear elastodynamic analysis*. Department of Civil Engineering, Aalborg University; 2006, DCE Lecture Notes, No. 3.

[18] Thomson W. Transmission of elastic waves through a stratified solid medium. *J Appl Phys* 1950;21:89–93.

[19] Haskell N. The dispersion of surface waves on multilayered medium. *Bull Seismol Soc Am* 1953;73:17–43.

[20] Wang R. A simple orthonormalization method for stable and efficient computation of Green's functions. *Bull Seismol Soc Am* 1999;89(3):733–41.

[21] Ottosen N, Petersson H. *Introduction to the finite element method*. Harlow, United Kingdom: Pearson Education Ltd.; 1992.

Paper D



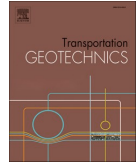


ELSEVIER

Contents lists available at ScienceDirect

Transportation Geotechnics

journal homepage: www.elsevier.com/locate/trgeo



Numerical investigation of railway subgrade stiffening: Critical speed and free-field vibrations

J. Malmborg^{*}, P. Persson, K. Persson

Department of Construction Sciences, Lund University, P.O. Box 118, SE-22100 Lund, Sweden

ARTICLE INFO

Keywords:

Train-induced ground vibration
Soil stabilization
Lime-cement columns
2.5D finite elements
Perfectly matched layers

ABSTRACT

For a train speed close to the speed of elastic waves in the soil, often referred to as “critical speed”, largely elevated vibration responses occur. This can be a practical problem for soft soil sites, where the phenomenon may cause excessive vibrations in the track and also at distances far from the track. To ensure the running safety of the train, the long-term quality of the track and to reduce the vibrations in the surroundings, such effects must be avoided. An effective counter-measure is to increase the stiffness of the soil underneath the track, thereby increasing the critical velocity.

In this paper, a 2.5D finite element model is used for studying the critical velocity phenomenon and its mitigation through soil stiffening, for a ballasted track on a layered half-space with very soft soil. Soil improvement under the track, in the shape of a solid block or as various number of panels, with varying depth and stiffness is considered. The effect of the soil improvement is evaluated both in terms of the maximum rail and free-field displacements. It is shown that a shallow soil stiffening increases the critical velocity and reduces the rail and free-field response for load speeds near the shear wave velocity of the soft top soil layer. It is also demonstrated that a deep soil stiffening, by use of panels along the track direction, increases the critical velocity further, and may also be efficient in reducing the response for load speeds near the shear wave speed of the underlying half-space.

Introduction

When a train moves along a railway track vibrations are generated that propagate to the surrounding soil. The vibration levels are highly dependent on the soil conditions. If a train runs at a speed close to the speed of the elastic waves in the soil, which is possible for soft soils, it may lead to a largely elevated vibration response [1–5]. Such critical velocity effects must be avoided to ensure the running safety of the train, the long-term quality of the track, and to reduce the vibrations in the surroundings.

In order to ensure efficient and accurate design of vibration mitigation measures, prediction models capable of representing the physical behavior and allowing for quantifying the changes to the response given a change in input parameters are needed. The numerical prediction of train-induced vibrations poses great challenges due to several reasons. Many of the governing parameters, such as soil layering and mechanical properties of the different soil layers, the track conditions and the dynamic properties of the train, are often not fully known. Further, the nature of the problem necessitates accounting for a large soil volume

which may become computationally expensive, e.g. in the case of large 3D finite element (FE) or boundary element (BE) models.

Large computational savings can be made if the response is assumed linear-elastic and the ground is assumed to be horizontally layered. A semi-analytical solution to the wave propagation problem can be found in frequency-wavenumber domain, and a railway track model consisting of infinite layered structural elements can be coupled to such a ground model as proposed by Sheng et al. [6,7]. An increased modeling flexibility compared to such semi-analytical models can be obtained by so called 2.5D FE and BE techniques where the assumed geometric invariance in the track direction is utilized when formulating the governing FE/BE equations. Then, only a cross-section of the geometry is considered, and a Fourier transformation with respect to the track coordinate is carried out on the governing equations. The solution is found by performing an analysis on the 2D geometry for a range of wavenumbers, and the 3D response is obtained as an inverse Fourier transformation of the wavenumber domain response. In the field of train-induced vibration the 2.5D FE technique was first proposed by Yang and Hung [8] and has then been used by several researchers to study

^{*} Corresponding author.

E-mail address: jens.malmborg@construction.lth.se (J. Malmborg).

<https://doi.org/10.1016/j.trgeo.2022.100748>

Received 27 September 2021; Received in revised form 24 February 2022; Accepted 25 February 2022

Available online 1 March 2022

2214-3912/© 2022 The Authors. Published by Elsevier Ltd. This is an open access article under the CC BY license (<http://creativecommons.org/licenses/by/4.0/>).

train-induced vibrations. Similarly, 2.5D BE methods have been proposed, in which the need for geometry discretization is reduced even further. A combination of the two methods, 2.5D FE-BE, where the track is modeled using FE and the soil by BE, have been formulated and used by a number of researchers [9–13].

To mitigate the vibrations observed by a receiver next to the track, measures may be directed to the source (i.e. train/track), the propagation path (i.e. the soil) or the receiver. When directed to the propagation path between the railway track and the receiver, the idea is generally to disturb the approaching waves by introducing a barrier, e.g. open or in-filled trenches [14,15], sheet walls [16], local soil improvement [17,19,21,20] or so called wave impeding blocks [26,24,25,27]. Vibration mitigation at the source may be accomplished through the use of resilient elements, i.e. under sleeper-mats [22] and so called floating slab tracks [23], where the upper part of the track structure is dynamically isolated. Furthermore, the geometrical and mechanical properties of the track and the embankment/cutting affect the dynamic behavior and the resulting wave propagation [28,29]. Here, however, focus will be on vibration mitigation by increasing the stiffness of the soil underneath the track. Stiffening the subsoil can be carried out practically through diverse techniques, e.g. mass stabilization, jet-grouting or installation of lime-cement columns. The latter technique enables soil stabilization to large depths as well as allowing for a wide range of column pattern designs. Panels oriented along the track direction, formed by installing over-lapping lime-cement columns, are used in Sweden to increase the critical speed of railway tracks on soft soil [18]. Soil stabilization may be carried out for several reasons; reducing track settlements, avoiding critical velocity effects, and mitigating the environmental vibrations next to the track, and may therefore be beneficial for track owners, train operators as well as residents near the railway track.

Andersen and Nielsen [14] studied the reduction of train-induced ground vibrations obtained with soil improvement and barriers along the track, using a coupled FE-BE model, for trains moving at sub-critical speed. It was concluded that, for vertical excitation on the track, trenches provide more efficient mitigation of the ground surface vibrations than local soil improvement in the embankment. Peplow and Kaynia [30] used a 2D BE model to study the reduction of ground vibrations by lime-cement stabilization underneath the railway track, and compared the obtained results with measurement data. The analyses were performed for a stationary, oscillating load for frequencies in the interval 10 to 100 Hz, and the stabilization proved efficient in mitigating the vibrations in the lower frequency range. Thompson et al. [13] used a 2.5D FE-BE model to study the insertion loss obtained by stiffening the soil underneath a railway track for which the train speed was lower than the wave speeds of the ground materials. Blocks with a thickness up to 3

m with varying stiffness and placement were considered. Such a solution was found to be efficient in reducing the free-field vibrations for frequencies above the “cut-on” frequency of the upper soil layer. It was found that both an increased thickness and stiffness of the block provided a higher insertion loss. Dong et al. [31] used a model based on the thin-layer FE method to assess the effects of soil stiffening under the track. A complete soil replacement, with infinite lateral extent, up to the depth 5 m was considered, and the resulting increase in critical speed and decrease in rail displacements was studied. In [32] the same authors studied the influence of subgrade non-linearity on critical speed and rail deflection, by incorporating a “linear equivalent” approach to adapt the stiffness and damping parameters to the calculated strain levels. It was found that accounting for subgrade non-linearity reduced the critical speed and increased the rail deflections, compared to the strictly linear-elastic model. Connolly et al. [34] used a variety of different numerical modeling approaches to demonstrate effects of subgrade layering, track and train types, soil non-linearity and discrete soil stiffening using stone columns and jet grouting, on the critical velocity. Noren-Cosgriff et al. [19] studied the applicability of 2D models when evaluating the vibration mitigating effects of lime-cement columns under the track and as vibration reducing screen with limited extent next to the track, finding that satisfactory results are obtained by representing the ground with lime-cement columns as an equivalent effective medium, but that the mitigating effects may be overestimated in 2D models. Fernandez-Ruiz et al. [20] investigated numerically the effect of stone columns underneath a railway track on the rail displacements for a load moving at various speeds, using a 3D FE model in time-domain. The stone column “critical length”, with regard to rail displacement, rail dynamic amplification and critical speed, was defined as the column length beyond which no improvement regarding said quantities were obtained. It was shown that critical speed continued to increase for column lengths beyond the length for which no further improvement of rail displacements were obtained.

In this paper, the critical velocity phenomenon and the mitigating effects of soil stiffening, on both rail and free-field displacements, are studied numerically using a 2.5D FE model. The large strains that may develop at critical speed imply a non-linear response [2,32,33]. However, because the purpose of the present work is to study trends and tendencies regarding the mitigating effects of various soil stiffening approaches, rather than to establish absolute vibration levels, a linear-elastic model is deemed sufficient. Deep soil stabilization by a massive block and by various numbers of panels under the track is analyzed and compared. The analysis is carried out with regard to the track and free-field displacements for a moving point load on the rail of a ballasted track on a very soft layer of clay. Such deep soil stabilization is used in practice [18]. However the amount of research papers on the subject is

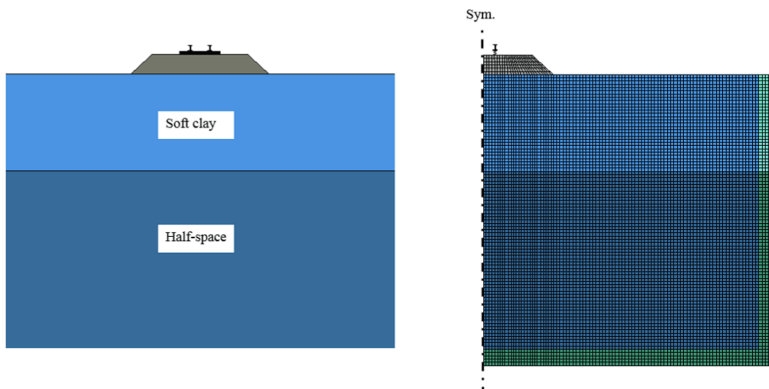


Fig. 1. Left: Schematic cross-section of track on a layered soil. Right: Corresponding 2.5D FE model with PML at the truncated soil domains.

scarce, especially numerical studies regarding the effect of stabilizing panels on the critical velocity.

The paper is structured as follows. The computational model is described in Section 2. In Section 3, the significance of the depth of the soft upper soil layer, with regard to the soil displacements, is studied for a moving load acting directly on the soil as well as for a load acting on a railway track. In Section 4 soil improvement underneath the track is considered and its effect on the rail and free-field displacements is studied. The depth and the lateral extent of the soil improvement is varied. Finally, in Section 5 important findings are discussed.

Computational model

2.5D FE model

In the study, a 2.5D FE model is used for calculating the track and free-field vibrations for a moving load. The FE code, developed by the first author, is written in Fortran [35] and utilizes Intel MKL [36] for mathematical operations such as FFT and solving linear systems of equations. The geometry is assumed invariant in the track direction. Through a double Fourier transformation of the governing equations, with respect to time the track coordinate, the 3D time-domain problem is solved via a sequence of frequency-domain analyses of the 2D cross-section of the longitudinally invariant geometry. Each such 2D analysis corresponds to a specific wavenumber in the track direction. Hence, only a cross-section of the railway track and the surrounding soil is discretized by finite elements. The resulting system of equations can be written as:

$$(-\omega^2 \mathbf{M} + \mathbf{K}_0 + ik_1 \mathbf{K}_1 + k_1^2 \mathbf{K}_2) \mathbf{a}(k_1, \omega) = \mathbf{f}_1(k_1, \omega), \quad (1)$$

where the 2.5D FE stiffness matrices \mathbf{K}_0 , \mathbf{K}_1 , \mathbf{K}_2 and the mass matrix \mathbf{M} are independent of the wavenumber k_1 . Detailed expressions for these matrices can be found in e.g. [9,37,38]. The vector $\mathbf{a}(k_1, \omega)$ represents the nodal displacements and $\mathbf{f}_1(k_1, \omega)$ is the load vector. By an inverse Fourier transformation of $\mathbf{a}(k_1, \omega)$ with respect to the wavenumber k_1 , the nodal displacements are obtained in space $\mathbf{a}(x, \omega)$.

Here, both the soil and the track embankment are modeled by 8-node isoparametric quadrilateral elements with a mesh as shown in Fig. 1. The total width and height of the modeled soil domain is 18 m \times 18 m, including a 1 m thick layer of perfectly matched layer (PML) elements described below. The element size is approximately 0.2 m \times 0.2 m. As an approximate rule-of-thumb, a minimum of 3–4 quadratic elements are needed for proper resolution of an elastic wave. With the lowest shear wave velocity in the study, the mesh is suitable for frequencies up to around 100 Hz. While the case of a moving static load does not have a well-defined range of excitation frequencies, it was however shown in [3] that the ground response to a static load moving close to critical speed is dominated by much lower frequencies (<15 Hz).

Because the geometry is assumed invariant in the track direction, the periodicity of the sleepers cannot be accounted for. Here, the sleeper stiffness is disregarded in the track direction, and considered rigid in the lateral direction. This is enforced by constraining the displacements in the topmost nodes of the embankment located within a distance of 1.3 m from the symmetry line (assuming a sleeper width of 2.6 m). In addition, the sleeper mass is lumped to these nodes.

The rail is represented by a Bernoulli–Euler beam of infinite length, with bending stiffness $(EI)_r$ and mass m_r , continuously supported by distributed springs with stiffness k_p representing the rail pads. The governing equation for the rail can be written as

$$(EI)_r \frac{\partial^4 u_r}{\partial x^4} + m_r \frac{\partial^2 u_r}{\partial t^2} + k_p (u_r - u_s) = P(x, t). \quad (2)$$

Here, $u_r = u_r(x, t)$ is the vertical displacement of the rail and $u_s = u_s(x, t)$ is the vertical displacement of the sleeper. Furthermore, $P(x, t)$ is the load on the rail.

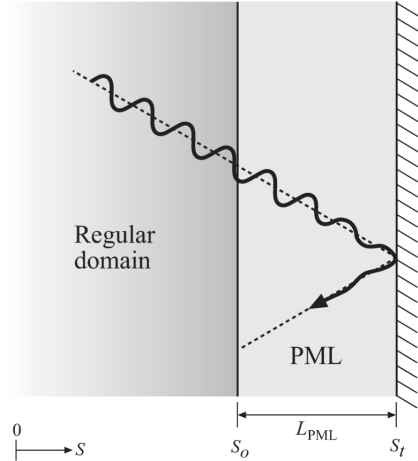


Fig. 2. An incident wave being attenuated inside the PML.

In frequency–wavenumber domain this equation becomes

$$(EI)_r k_1^4 u_r - \omega^2 m_r u_r + k_p (u_r - u_s) = P(k_1, \omega), \quad (3)$$

where $u_r = u_r(k_1, \omega)$ and $u_s = u_s(k_1, \omega)$ now represent the displacement quantities in (k_1, ω) -domain.

A one-dimensional element, similar to a simple Kelvin–Voigt element, can be formulated for the rail and rail pad as

$$\begin{bmatrix} (EI)_r k_1^4 - \omega^2 m_r + k_p & -k_p \\ -k_p & k_p \end{bmatrix} \begin{bmatrix} u_r \\ u_s \end{bmatrix} = \begin{bmatrix} P \\ f_s \end{bmatrix}, \quad (4)$$

where f_s is the force exerted onto the element from the sleeper node. The element is assembled into the global dynamic stiffness matrix for the whole soil–track system in a standard manner.

Furthermore, a harmonic load oscillating with the frequency Ω , moving at constant velocity v along the x -axis, is represented in time–space domain by $p(x, t) = P_0 \times \delta(x - vt) \times e^{i\Omega t}$. In frequency–wavenumber domain the load is given by $p(k_1, \omega) = P_0$ where $\omega = \Omega - k_1 \times v$. Hence, a moving constant (non-oscillating) load, $\Omega = 0$, is analyzed by setting the frequency to $\omega = -k_1 \times v$.

To reduce spurious reflections at the fictitious boundaries of the FE model, the soil domain is truncated by a layer of PML elements. With PML, a so called stretched coordinate is introduced. Consider an elastic domain extending from $s = 0$ to $s = s_0$, and a PML region extending from $s = s_0$ to $s = s_r$, see Fig. 2.

The stretched coordinate can be written as [39]

$$\tilde{s} = \int_0^s \lambda(s) ds = s_0 + \int_{s_0}^s \lambda(s) ds, \quad (5)$$

where $\lambda(s)$ is a complex valued stretch function, chosen as [39,37]

$$\lambda(s) = 1 + f^e(s) - i \frac{f^p(s)}{a_0}. \quad (6)$$

The functions $f^e(s)$ and $f^p(s)$ are attenuation functions, attenuating evanescent (e) and propagating (p) waves, respectively. The “perfectly matching” property of the PML is obtained by selecting $f^e(s_0) = f^p(s_0) = 0$ so that $\lambda(s) = 1$ at the interface between the regular domain and the PML domain. Further, $a_0 = \omega L_p / C_s$ is a dimensionless frequency, with L_p chosen as the thickness of the PML and C_s is the shear wave velocity of the medium. It is demonstrated in [37] that the gradual stretch of the coordinate s , implied by the real part of the stretch function, modifies

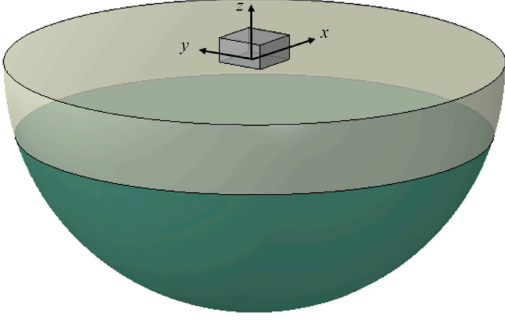


Fig. 3. Rectangular load moving along the x -axis on the soil surface of a layered half-space.

Table 1
Ground properties.

Layer	Property	Value
Soil	Depth (m)	6
	Young's modulus (MPa)	16.6
	Poisson's ratio	0.48
	Density (kg/m^3)	1500
	Loss factor $\eta = 2\zeta$ (-)	0.08
Half-space	Depth (m)	∞
	Young's modulus (MPa)	45.0
	Poisson's ratio	0.48
	Density (kg/m^3)	1500
	Loss factor $\eta = 2\zeta$ (-)	0.10

the apparent wavelength $\lambda'(s)$ inside the PML as $\lambda'(s) = \lambda(s)/(1 + f^e(s))$, i.e. an increasing value of f^e decreases the apparent wavelength. Here, f^e is chosen as

$$f^e(s) = \frac{2\pi}{\text{abs}(a_0)} \frac{(s - s_0)}{L_{\text{PML}}}, \quad (7)$$

where L_{PML} is the thickness of the PML, see Fig. 2. This choice yields a gradual decrease of the apparent shear wavelength from $\lambda'(s = s_0) = \lambda_s$ to $\lambda'(s = s_t) = \lambda_s/(1 + \lambda_s)$ inside the PML. For example, for a shear wavelength of $\lambda_s = 3$ m (implying a frequency of 20 Hz, which is considered high in the present study), the apparent shear wavelength is gradually decreased to $\lambda' = 0.75$ m at the end of the PML layer. The value of the imaginary part of the stretch function, $f^p(s)$, is based on recommended values in literature [39,37]:

$$f^p(s) = 20 \left(\frac{s - s_0}{L_{\text{PML}}} \right)^2. \quad (8)$$

When $a_0 = 0$, i.e. for the case $\omega = k_1 = 0$, the stretch functions are set to $\lambda = 1$, i.e. the PML elements behave like regular 2.5D FE elements. This choice of attenuation functions provides satisfactory attenuation as demonstrated in the next subsection. The stretched coordinate is incorporated into the 2.5D FE equations as described in [37].

Model validation

In order to validate the 2.5D FE model and the effectiveness of the PML, an example problem for which a semi-analytical solution can be found, is analyzed. In the example problem, the track is disregarded and instead a moving, rectangular, uniform traction load is applied directly on the soil surface, see Fig. 3. The semi-analytical solution is calculated using the Thomson and Haskell layer transfer matrix approach, as proposed by Sheng [6,7], using software developed by the present first

author [40].

The rectangular load distribution is $2.6 \text{ m} \times 2.6 \text{ m}$. The load is moving along the x -axis of a layered ground, consisting of a 6 m deep soft clay layer with a shear wave velocity of $C_s \approx 60 \text{ m/s}$ overlaying a half-space with a shear wave velocity of $C_s \approx 100 \text{ m/s}$. The ground properties are shown in Table 1. The soil surface response is studied for various load speeds at three different y -coordinates: $y = 0, y = 8$ and $y = 16 \text{ m}$, see Fig. 4. In the figure, the load is located centered at $x = y = 0$.

Generally, very good agreement is found between the two models. There are, however, some deviations, especially at $y = 16 \text{ m}$ for the load speed $v = 80 \text{ m/s}$, i.e. for a load speed between the shear wave speeds (C_s) of the two materials. These deviations between the two models are caused by reflections at the fictitious boundaries in the FE model, i.e. due to imperfect settings for the PML, which has been confirmed by an analysis using a larger FE model with a greater distance to the fictitious boundaries. However, the discrepancies are limited and deemed insignificant for the further studies in the paper. Furthermore, it is observed that the maximum displacement directly underneath the load ($y = 0$) is obtained for the velocity $v = 60 \text{ m/s}$ which is close to C_s of the clay layer. However, at a greater distance ($y = 16 \text{ m}$) maximum displacement is obtained for the velocity $v = 100 \text{ m/s}$, close to the C_s of the underlying half-space. This effect is further studied in the next section.

Effect of soft layer depth

Load applied directly on the soil surface

The stiffness and depth of the soil layers largely affect the vibration of the soil surface and the load speed at which the maximum response is obtained. For a homogeneous half-space, the critical speed corresponds to the Rayleigh wave speed C_R of the soil material. However, with the presence of multiple soil layers with different stiffness values, the critical velocity can either tend to the wavespeed in the upper or lower layer(s), depending on their depth and stiffness, as demonstrated in the following.

Here, a soil configuration is considered where again a soft clay layer overlays a stiffer half-space, with properties as presented in Table 1. In this model the depth of the soft top layer is varied. Fig. 5 shows the maximum soil surface vertical displacement for a rectangular load ($2.6 \text{ m} \times 2.6 \text{ m}$) moving at varying speeds, for various thickness values of the top layer, calculated using the semi-analytical model. Subfigures (a) and (b) show the maximum response at $y = 0$, i.e. under the load path, and at $y = 16 \text{ m}$, respectively. As can be seen in Fig. 5 (a), the speed for which the highest displacement response is obtained corresponds to the Rayleigh wave speed of either the soft or the stiff material, when the thickness of the top layer is infinite (i.e. a soft homogeneous half-space) or non-existing (i.e. a stiff homogeneous half-space), respectively. The maximum displacement is considerably higher for the softer homogeneous half-space, for all load speeds in the studied range. For a thin soft layer, the peak displacement is less pronounced. For increasing values of the soft layer thickness, the critical speed approaches that of the soft homogeneous half-space. For a layer thickness $> 4 \text{ m}$ the maximum response at $y = 0$ for speeds higher than C_s in the layer, is very similar to the response of a homogeneous half-space. However, this is not true for the response at $y = 16 \text{ m}$, as shown in Fig. 5 (b). At this distance, a sharp rise in the displacement response when approaching the shear wave speed of the clay layer is observed for all layer depths $h \geq 4 \text{ m}$, but the maximum response is observed for speeds closer to the shear wave speed of the underlying half-space.

Load applied on a railway track

When the load acts on the rail of a railway track, the track properties influence the railway response as well as the free-field ground surface response. Here, the 2.5D model with the ballasted track shown in Fig. 1

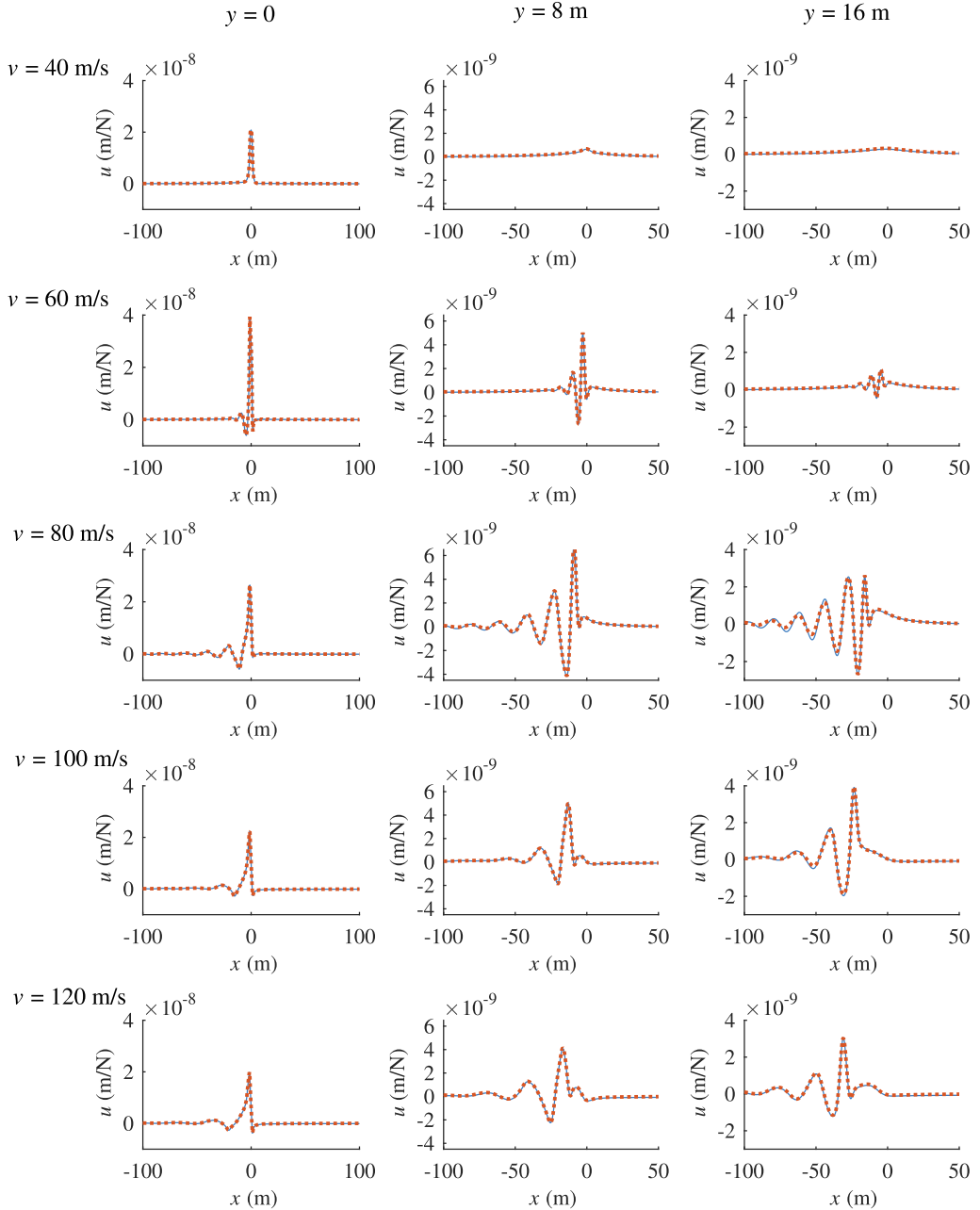


Fig. 4. Comparison of the responses obtained with the FE-PML model (blue solid line) and the semi-analytical model (red dotted line). The vertical displacement u of the soil surface is plotted against the x -coordinate, with the load being centered around $x = 0$, for three different y -coordinates.

is used for calculating the track and free-field vibration. The properties of the track are shown in Table 2. The mechanical properties of the embankment were adapted from [2].

In the following, the load is applied as a concentrated unit load on the rail (0.5 N per rail). Fig. 6 (a) shows the rail displacement at different speeds, for a half-space underlying a soft soil layer with varying thickness. When the soft clay layer is absent ($h = 0$), the critical speed is

approximately corresponding to the Rayleigh wave speed of the half-space material. For an increasing soft clay layer depth, the critical speed decreases and approaches the Rayleigh wave speed of the soft clay material, similarly to the case of a uniform traction acting directly on the soil surface. This can be explained by the dispersive properties of P-SV waves in the layered half-space, and in particular in relation to the dispersive properties of the bending waves in the track.

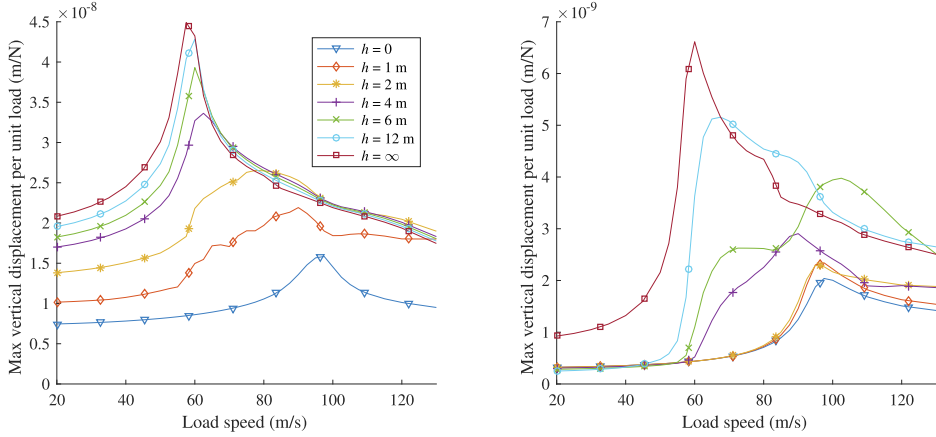


Fig. 5. Maximum soil surface displacement for different depths h of the soft clay layer, due to a moving rectangular load. Left: $y = 0$, right: $y = 16$ m.

Table 2

Track properties.

Property		Value
Rail	Mass (kg/m)	60
	Young's modulus (GPa)	210
	Second moment of inertia (m^4)	3.217×10^{-5}
	Loss factor (-)	0.01
	Track gauge (m)	1.435
Rail pads	Stiffness (MN/m^2)	250
	Loss factor (-)	0.1
Sleepers	Width (m)	2.6
	Mass (kg/m)	535
Embankment	Density (kg/m^3)	1800
	Young's modulus (MPa)	189
	Poisson's ratio	0.19
	Loss factor (-)	0.08
	Width, top/bottom (m)	6.0/ 8.6
Height (m)	1.2	

Kausel et al. [5] recently presented a methodology to establish the dispersion spectrum for a fully coupled system of a railway track on a layered half-space, from which the critical speed can be obtained as the smallest stationary point. However, a common approach, also used here, is to calculate the dispersion spectra of the two separate systems, soil and track, and obtain an approximation of the critical speed at the intersection point between the two spectra [41–43]. To find the dispersive properties of P–SV waves in the layered half-space an eigenvalue problem is formulated from the Thomson and Haskell layer flexibility matrices. The solution to this eigenvalue problem reveals the wavenumbers and frequencies of propagating P–SV modes. The details on how to formulate this eigenvalue problem from the layer flexibility matrices can be found in [41]. To obtain the dispersion spectrum of the track, the embankment is modeled as a Bernoulli–Euler beam, with bending stiffness $(EI)_e$ and mass m_e . The second moment of inertia $I_e = 1.04 m^4$ and mass $m_e = 15770 kg/m$ are calculated from the cross-section geometry detailed in Table 2, and the Young's modulus is accordingly $E = 189 MPa$. Combining the embankment beam with the rail and railpad, c.f. Eq. (4), with properties according to Table 2, provides a system of equations for the unconstrained track as

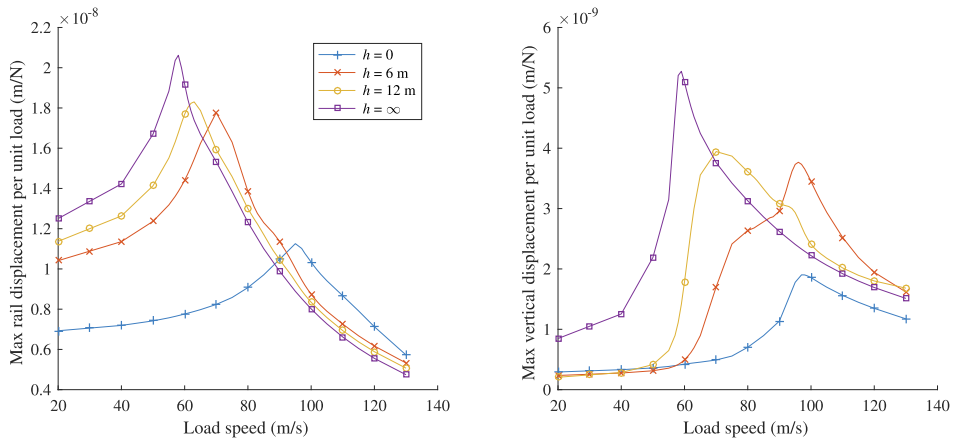


Fig. 6. Maximum vertical displacement of the rail (left) and soil surface at $y = 16$ m (right) for different depths of the soft clay layer.

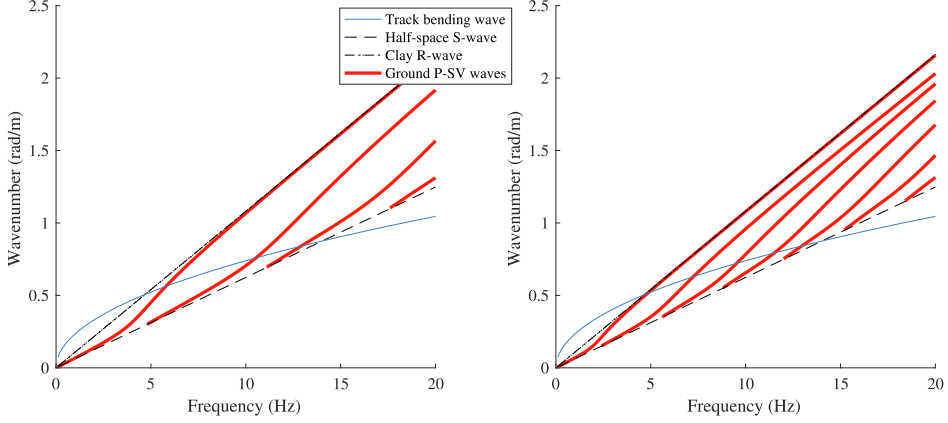


Fig. 7. Dispersion spectrum showing the P-SV modes of the ground (red solid line) and the bending wave dispersion of the track (blue solid line). The shear wave of the half-space material and the Rayleigh wave of the top soil material is indicated by a black dashed and dash-dotted line, respectively. In the left figure, the depth of the clay layer is $h = 6$ m. Right figure: $h = 12$ m.

$$\begin{bmatrix} (EI)_r k_1^4 - \omega^2 m_r + k_p & -k_p \\ -k_p & (EI)_e k_1^4 - \omega^2 m_e + k_p \end{bmatrix} \begin{bmatrix} u_r \\ u_e \end{bmatrix} = \begin{bmatrix} P \\ f_e \end{bmatrix}. \quad (9)$$

The dispersion spectrum is defined by combinations of frequency ω and wavenumber k_1 yielding a singular system matrix in Eq. (9), for which a mode of free vibration exist in the track. The intersection point between the dispersion curves of the track and the fundamental P-SV mode defines a point in (ω, k) -space for which waves propagate freely in both the ground and the track. The inverse of the slope given by the line from the origin to this intersection point, $c = \omega/k$, gives an approximation of the critical speed, i.e. a speed for which the track response reaches a maximum.

In Fig. 7, the P-SV dispersion curves are shown in red. The blue curve represents the dispersion curve of the unconstrained track. The black dashed and dotted lines correspond to the shear wave of the half-space material and the Rayleigh wave of the clay material, respectively. The left and right subfigures pertain to the ground with a 6 m and 12 m deep clay layer, respectively. The track dispersion curve is identical in both subfigures, but due to the different clay layer depths, the P-SV modes differ. The fundamental P-SV wave is aligned close to the shear wave of

the half-space material for low frequencies ($< 2-4$ Hz) and then gradually approaches the Rayleigh wave of the clay material. The reason for this is that for low frequencies, the wavelengths are much longer than the depth of the clay layer and the properties of the layer has a diminishing effect on the wave propagation. On the contrary, for increasing frequencies the wavelengths become in the order of the clay layer depth and instead the half-space properties become less significant.

For the two cases presented in Fig. 7, the increased clay layer depth in the right subfigure causes the so called cut-on frequency, where the fundamental P-SV mode approaches the Rayleigh mode of the top material, to tend to a lower frequency. In turn, the intersection point with the track dispersion curve occurs at a lower frequency which, given the dispersion curve for the track, implies that the critical speed is lower. From the intersection points in the two subfigures the critical speeds can be approximated as $v = 65$ m/s and $v = 59$ m/s, respectively, which obviously differs from those obtained by the 2.5D FE calculation presented in Fig. 6 ($v = 70$ m/s and $v = 63$ m/s respectively). In the detailed calculation, however, effects of cross section deformation and continuity of strains in the interface between the embankment and the ground are accounted for. Considering the embankment as a beam is a less accurate

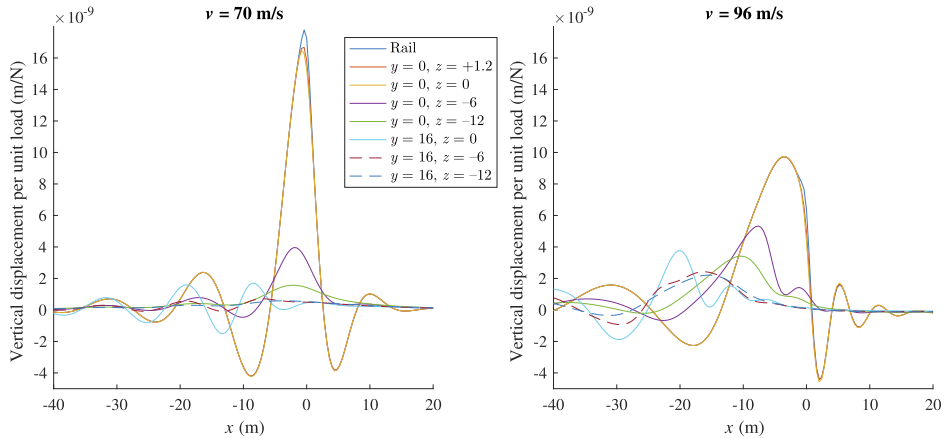


Fig. 8. Vertical displacement response in different locations of the model at the load speed $v = 70$ m/s (left) and $v = 96$ m/s (right), for the case with a $h = 6$ m deep clay layer.

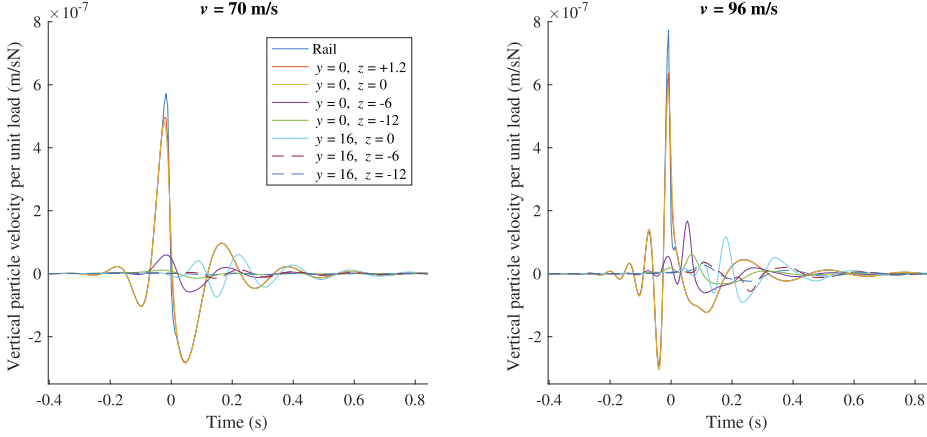


Fig. 9. Vertical particle velocity response in different locations of the model at the load speed $v = 70$ m/s (left) and $v = 96$ m/s (right), for the case with a $h = 6$ m deep clay layer.

approximation but serves as an efficient mean to estimate the dispersion characteristics for the track and explaining the trends regarding the maximum rail displacement observed in Fig. 6 (a).

In Fig. 6 (b) the maximum soil surface displacement 16 m from the track is shown for various speeds. These curves share some characteristics with the corresponding curves for the case with a load acting directly on the soil surface, c.f. Fig. 5 (b). When the load speed is well below the wave speeds in the underlying ground, no propagating waves are generated. A deflection shape, similar to that caused by a non-moving static load, moves with the load. However, when the load speed is increased towards the Rayleigh wave speed of the ground material, propagating waves are generated that cause the displacement amplitudes to increase significantly also far away from the load. The dispersion diagram analysis (see Fig. 7) indicates that the critical speed (i.e. speed of maximum rail displacement) occurs for a load speed corresponding to the track-soil intersection point (ω, k_1) where both track and soil exhibits free propagating waves; i.e. similar to a resonance frequency of a coupled system. This explains also why the response in the far-field exhibits a sharp increase when the load speed approaches critical speed. For $h = 12$ m, the displacement increases drastically when the load speed approaches the shear wave velocity of the top layer, reaching a maximum at around $v = 70$ m/s. Increasing the speed further yields a lower response, and no sharp amplification is observed for speeds around the shear wave velocity of the half-space. On the other hand, for the case with $h = 6$ m, the maximum displacement 16 m from the track is obtained for a load speed close to the shear wave velocity of the half-space. However, a sharp rise in the response is obtained already at speeds near C_s of the top layer. The vertical displacement in different points of the model is shown in Fig. 8 for the load speeds $v = 70$ m/s (maximum rail response) and $v = 96$ m/s (maximum response at $y = 16$ m), plotted against the distance along the x -axis. The load is located at $x = 0$. In both cases, the vertical displacement in the embankment is almost identical to that of the rail. The vertical displacement at the interface between the clay layer and the half-space, at $z = -6$ m, is considerably higher for the higher load speed. This is also true for deeper levels, i.e. at $z = -12$ m. At $y = 16$ m, the displacement at the depths $z = -6$ m and $z = -12$ m, respectively, are very similar and of considerable magnitude in comparison with the surface response, indicating that the free-field response is indeed governed by a mode involving the half-space. The corresponding vertical particle velocity time-histories are shown in Fig. 9.

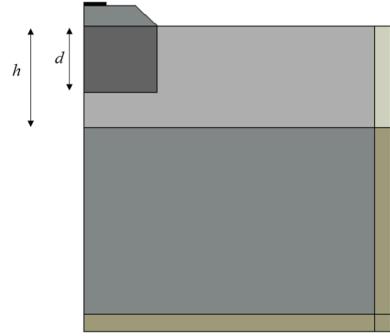


Fig. 10. Schematic cross-section of a track on a layered soil. Note that symmetry is assumed around the leftmost vertical line of the model.

Table 3

Improved soil properties. Values in brackets are for partial soil improvement.

Property	Value
Young's modulus (MPa)	320 (160)
Poisson's ratio	0.33 (0.40)
Density (kg/m^3)	1600 (1550)
Loss factor (-)	0.08 (0.08)

Soil improvement effects

The effect of soil improvement is first studied by assuming that the entire soil volume underneath the track, to a certain depth, is stiffened as schematically shown in Fig. 10. The soil improvement block shares nodes with the surrounding soil and the embankment along its interface, i.e. full interaction is assumed. For the improved soil the assumed mechanical properties are given in Table 3. These properties approximately correspond to a twentyfold increase of the shear modulus and a fivefold increase of the shear wave velocity compared to the unimproved clay.

In addition, the effect of a soil improvement block having a lower stiffness is compared. These lower stiffness properties, specified within brackets in Table 3, have been calculated considering a replacement ratio within the block of 50% and can therefore be considered as a "smeared" approach of simulating an arbitrary column pattern

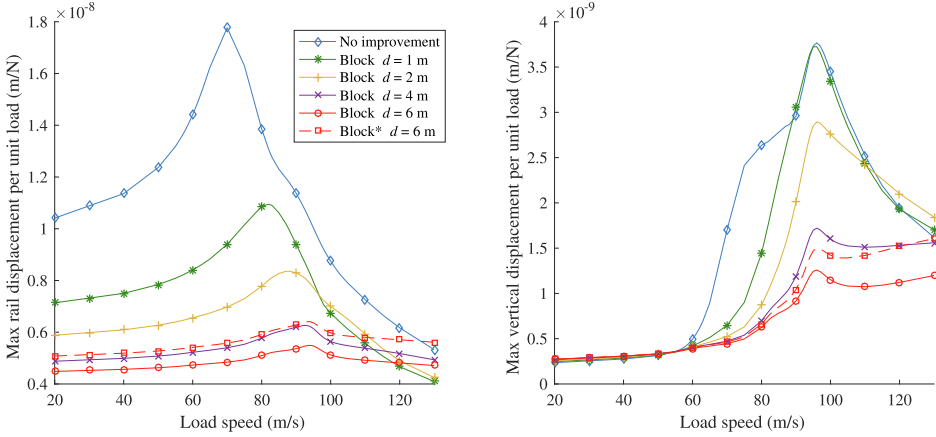


Fig. 11. Maximum vertical displacement of the rail (left) and soil surface at $y = 16$ m (right) for different depths of the soil improvement. The depth of the soft soil layer is $h = 6$ m. Dashed line corresponds to a partial soil improvement using the smeared material properties.

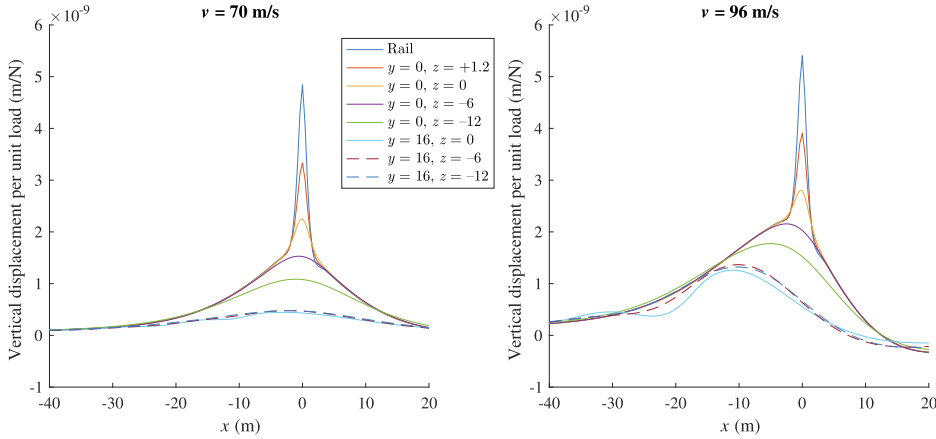


Fig. 12. Vertical displacement response in different parts of the model at the load speed $v = 70$ m/s (left) and $v = 96$ m/s (right), for the case with a $h = 6$ m deep clay layer and a $d = 6$ m deep soil improvement block under the track.

occupying half the volume of the block. Despite the approximation of using a smeared model, the analyses indicate how the lower stiffness of the improvement block affect the rail and free-field response.

Soil improvement depth

For the case with a $h = 6$ m deep soft clay layer, Fig. 11 shows the maximum vertical rail displacement (left) and soil surface displacement at $y = 16$ m (right) for different speeds and various depths of the soil improvement. It is observed that the maximum response decreases and the critical speed increases and approaches the wavespeed in the underlying half-space, for an increasing depth of the soil improvement. The change of the maximum rail response and the critical speed are greater for shallow improvement depths. An improvement depth of $h = 2$ m provides an increase in the critical speed from $v \approx 70$ m/s to $v \approx 90$ m/s. For an increasing improvement depth, the critical speed slowly approaches C_R of the half-space material, and the maximum rail response continues to decrease. The peak in the rail displacement in Fig. 11 becomes less pronounced as the depth of the improvement increases. It should be added that the stabilized soil, having a higher stiffness than

the underlying half-space, produces an inversely dispersive soil profile. Such a soil profile, with a stiffer top layer, implies that the wave speed increases with frequency as the wavelengths become of the order of the top layer depth. The rail response, when plotted against the load speed, may then exhibit two peaks where the first peak occurs when the load speed is similar to C_R of the half-space material, and the second peak occurs when the load speed is similar to C_R of the top layer (improvement) material. Which peak is the larger is dependent on the depth of the top layer, see e.g. [42]. This implies that the "true" critical speed may occur for load speeds near the wavespeeds of the soil improvement material, which is outside the studied speed range in the present case.

The displacement response 16 m from the track is significantly reduced in the speed range of about 60 to 85 m/s for a shallow improvement of $d = 1$ m. When increasing the speed further and approaching C_R of the half-space material, such a shallow improvement does not affect the maximum free-field displacement. For an increasing improvement depth, a reduction of the maximum free-field displacement is also obtained for load speeds around C_R of the half-space material. When the entire top layer soil volume is improved ($d = 6$ m) the maximum displacement response, at the load speed around C_R of the

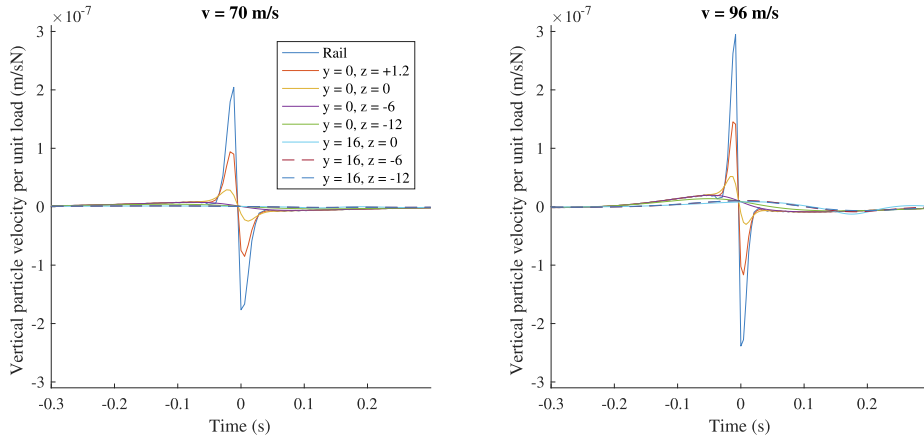


Fig. 13. Vertical particle velocity response in different parts of the model at the load speed $v = 70$ m/s (left) and $v = 96$ m/s (right), for the case with a $h = 6$ m deep clay layer and a $d = 6$ m deep soil improvement block under the track.

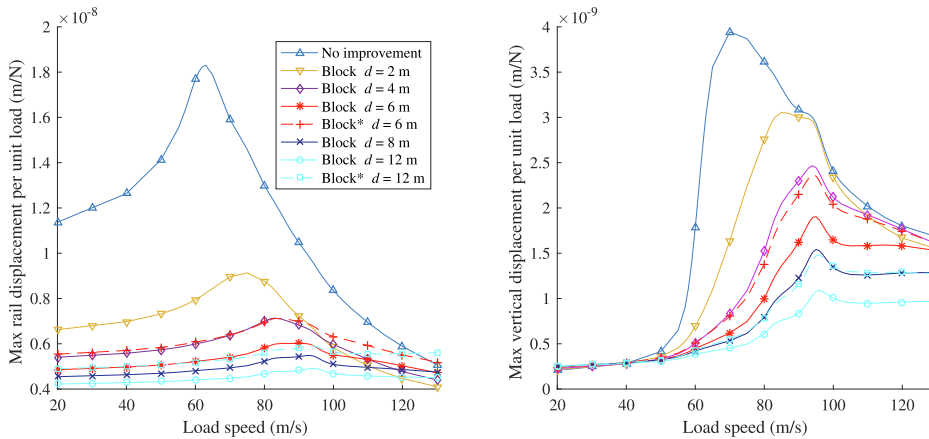


Fig. 14. Maximum vertical displacement of the rail (left) and soil surface at $y = 16$ m (right) for different depths of the soil improvement. The depth of the soft soil layer is $h = 12$ m. Dashed lines correspond to a partial soil improvement using the smeared material properties.

half-space material, is reduced to about 1/3. For this improvement depth, the vertical displacement in different points of the model is shown in Fig. 12 for the load speeds $v = 70$ m/s and $v = 96$ m/s, plotted against the distance along the x -axis. The load is located at $x = 0$. Comparing with the unimproved case (c.f. Fig. 8) it is evident that with the stiffer subsoil, a relatively larger part of the total rail displacement now occurs in the railpads and the embankment. For the lower speed ($v = 70$ m/s), the displacement pattern along the x -axis has a quasi-static appearance and is almost symmetric around the load $x = 0$. For the higher speed ($v = 96$ m/s) the displacement pattern is clearly affected by the speed being higher. Further, the displacements in the free-field increases. As in the unimproved soil case, the soil surface displacement 16 m from the track is strongly governed by the motion in the half-space. The corresponding vertical particle velocity time-histories are shown in Fig. 13. The dashed line in Fig. 11 shows that the maximum displacements obtained with a $d = 6$ m deep block of partial improvement (smeared stiffness properties assuming 50% stabilized soil) are comparable with those obtained for a $d = 4$ m deep block of fully improved soil, in the entire studied load speed interval.

For the case with a $h = 12$ m deep soft clay layer, the maximum

vertical rail displacement and soil surface displacement at $y = 16$ m for different speeds and various depths of the soil improvement are shown in Fig. 14. These curves show trends corresponding to those discussed above for the shallower clay layer depth. The free-field response for the case with unimproved soil has a global maximum for load speeds near C_S of the clay material, and a local maximum at C_R of the half-space material. A shallow improvement of $d = 2$ m shifts the speed of maximum response towards C_R of the half-space material. For load speeds around C_S of the clay material, the reduction of the response is around 50%, whereas the maximum response for load speeds around half-space C_R are unaffected. With an increasing soil improvement depth, the maximum free-field response occurs around C_R of the half-space, with a stronger reduction in maximum response.

Soil improvement pattern

Instead of stiffening the entire soil volume under the track, it may be more economical and practical to stiffen a limited soil volume. A common technique for accomplishing this is by installing lime-cement columns, by use of techniques such as deep soil mixing. Such columns may

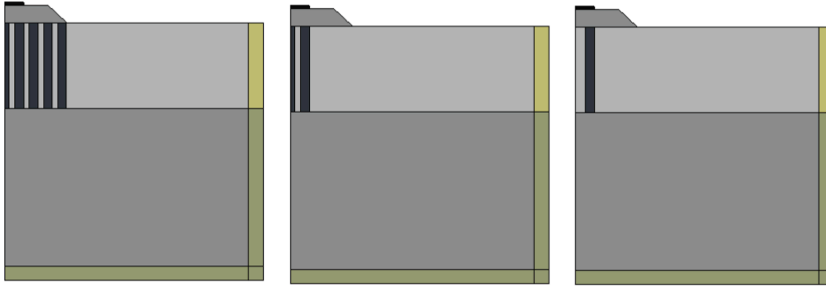


Fig. 15. Panel configurations with a total of 9, 3 and 2 panels, respectively. Note that symmetry is assumed around the leftmost vertical line of the model.

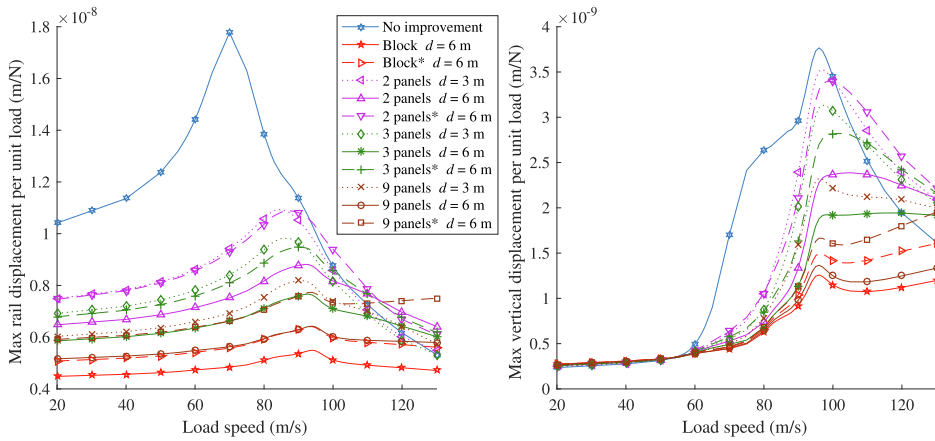


Fig. 16. Maximum vertical displacement of the rail (left) and soil surface at $y = 16$ m (right) for different patterns of the soil improvement. The depth of the soft soil layer is $h = 6$ m. Dashed lines correspond to a partial soil improvement using the smeared material properties. Dotted lines correspond to an improvement to half the soil layer depth i.e. $d = 3$ m.

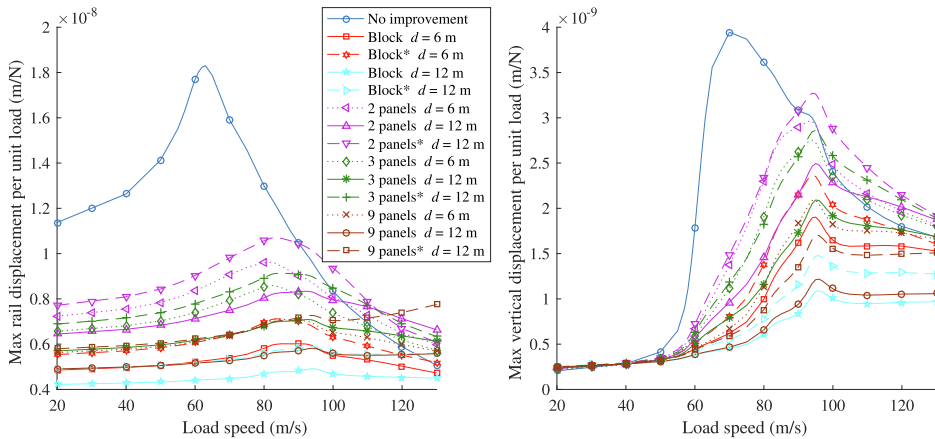


Fig. 17. Maximum vertical displacement of the rail (left) and soil surface at $y = 16$ m (right) for different patterns of the soil improvement. The depth of the soft soil layer is $h = 12$ m. Dashed lines correspond to a partial soil improvement using the smeared material properties. Dotted lines correspond to an improvement to half the soil layer depth i.e. $d = 6$ m.

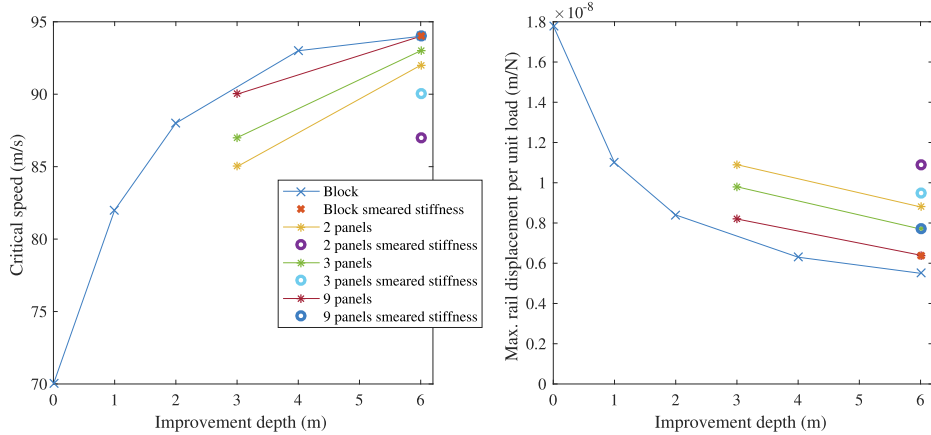


Fig. 18. Critical speed (left) and corresponding rail displacement (right) for various soil improvement patterns and depth. The depth of the upper clay layer is $d = 6$ m.

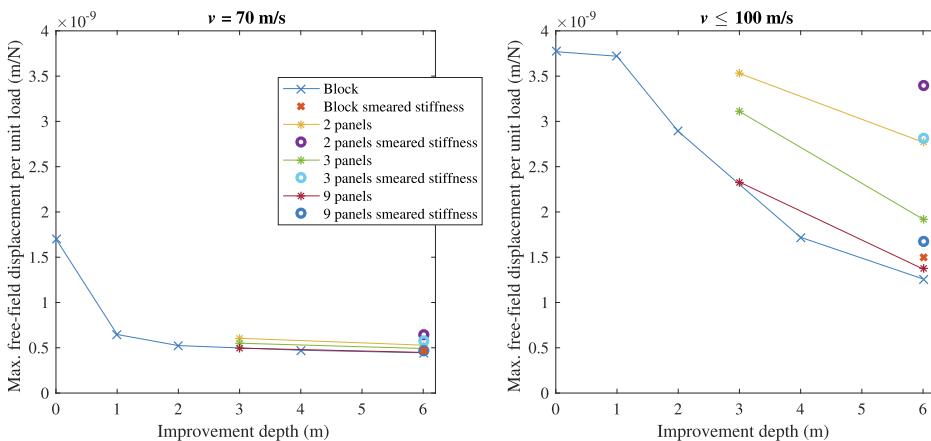


Fig. 19. Maximum free-field displacement 16 m from the track for the load speeds $v = 70$ m/s (left) and $v \leq 100$ m/s (right) for various soil improvement patterns and depth. The depth of the upper clay layer is $d = 6$ m.

be installed in various patterns resulting in various amounts of soil being stiffened. Apart from installing single discrete piles, overlapping piles can be installed to form long-stretched panels.

Here, the effects in terms of the rail and free-field vertical displacements are evaluated for three different panel configurations, for the cases with $h = 6$ m and $h = 12$ m, respectively, deep soft clay layer on top of a half-space. In each configuration, the panels extend either to the interface between the clay layer and the half-space ($d = 6$ m and $d = 12$ m, respectively) or halfway through the clay layer ($d = 3$ m and $d = 6$ m, respectively). The configurations are shown in Fig. 15 and involve 9, 3 and 2 panels on the track, respectively. The panels are $t = 0.6$ m thick and infinitely long, having the same elastic properties as the improvement block considered in the previous subsection. In addition, panels extending to the half-space interface are also evaluated using the smeared material properties shown in Table 3. In practice, differential settlements may develop between the soft soil and the improvement panels, leading to soil arching. This redistribution of stresses is not accounted for. The linear-elastic stress distribution due to the different stiffness of the unimproved and improved soil, however, is naturally accounted for in the model since the track shares nodes with both

unimproved and improved soil at the interface.

Fig. 16 and Fig. 17 show the maximum vertical rail displacement (left) and soil surface displacement at $y = 16$ m (right) for various speeds for a constant unit load acting on the rail, for the three panel configurations and the solid block improvement, for the $h = 6$ m and $h = 12$ m deep clay layer, respectively. For load speeds near C_S of the clay material, a substantial reduction of both the maximum rail and the free-field response is obtained with all panel configurations. For load speeds around C_R of the half-space material the reduction obtained with the panels is smaller, and for even higher speeds the soil improvement can have an adverse effect, i.e. yielding a higher response than obtained in the unimproved case which makes the comparison less relevant for practical purposes.

Fig. 18 shows the critical speed and the corresponding rail displacement vs. improvement depth, for the various analyzed improvement types, for the case with a $h = 6$ m deep clay layer. In Fig. 19 (left) the maximum free-field displacement at $y = 16$ m is plotted for various soil improvement patterns and depths, for a load speed $v = 70$ m/s, i.e. at the critical speed of the unimproved soil. In Fig. 19 (right)

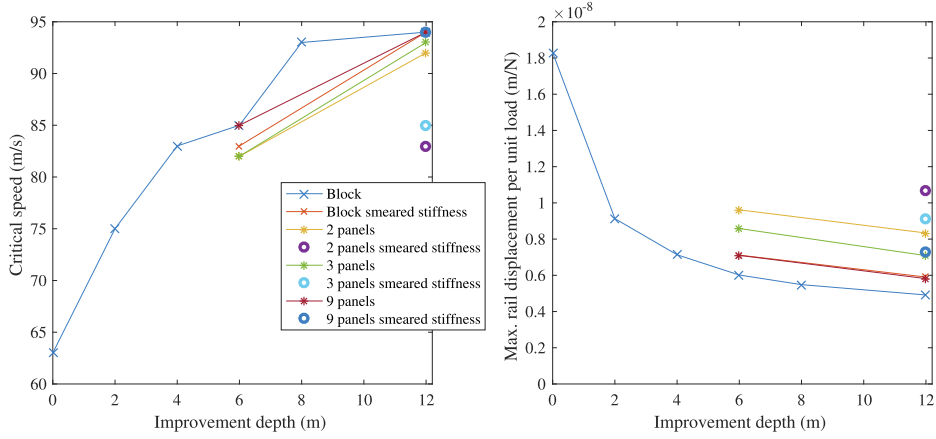


Fig. 20. Critical speed (left) and corresponding rail displacement (right) for various soil improvement patterns and depth. The depth of the upper clay layer is $d = 12$ m.

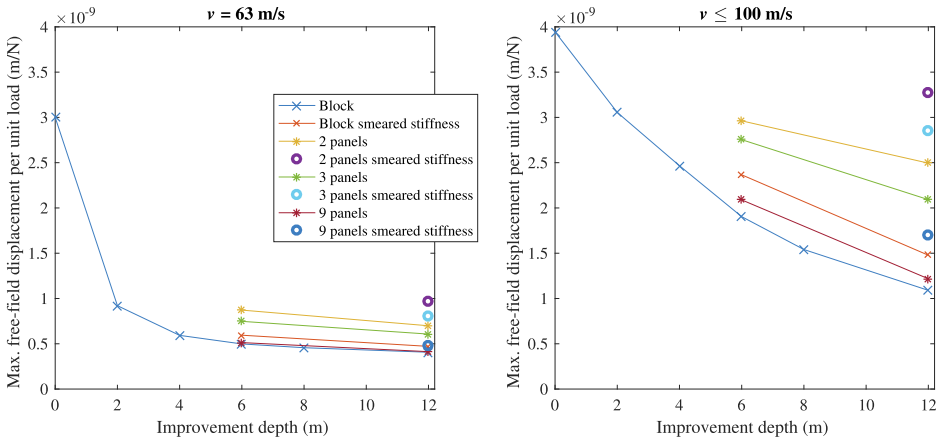


Fig. 21. Maximum free-field displacement 16 m from the track for the load speeds $v = 63$ m/s (left) and $v \leq 100$ m/s (right) for various soil improvement patterns and depth. The depth of the upper clay layer is $d = 12$ m.

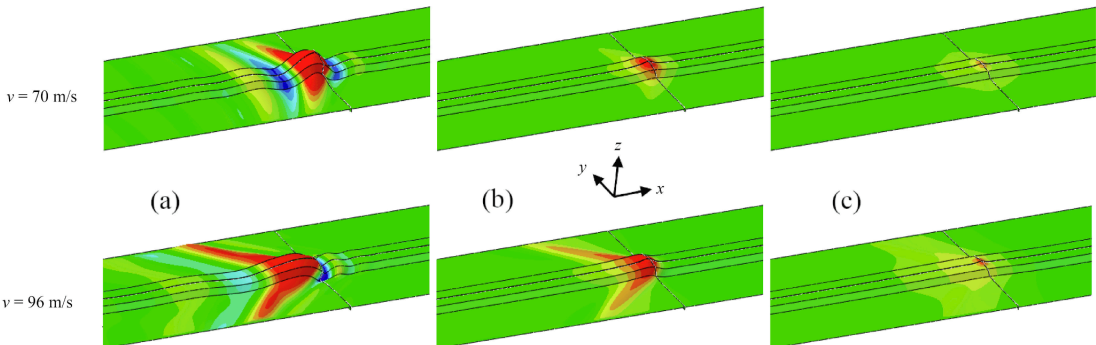


Fig. 22. Contour plot of the vertical displacements of the track and the soil surface at $v = 70$ m/s and $v = 96$ m/s for (a): no improvement (b): two panels (c): block improvement. The load is applied as a concentrated load on the rails (not shown), in the positive z -direction (upwards). Red color indicates a positive vertical displacement amplitude and blue color indicates a negative amplitude.

the maximum displacement is shown for any load speed ≤ 100 m/s. The corresponding results for the case with a $h = 12$ m deep clay layer are shown in Figs. 20 and 21. In these figures, the upper speed limit has been chosen as $v = 100$ m/s ($= 360$ km/h), so in fact the critical speed can become higher due to the inversely dispersive character of the ground with improved soil, as previously discussed. This is, for example, visible in Fig. 17 (left) where, for the case with 9 panels of smeared material properties, the rail response has a local peak around the half-space material C_R , but continues to increase at the end of the studied speed interval. From Fig. 18 (right) and Fig. 20 (right) it is observed that all analyzed soil improvements reduce the rail response by 39–73% at the critical load speed. Furthermore, Fig. 19 (left) and Fig. 21 (left) show that the maximum free-field ground displacements are significantly reduced by 68–86% when the load moves at the critical speed of the unimproved case (70 m/s and 63 m/s, respectively). At higher load speeds similar to C_R of the half-space, see Fig. 19 (right) and Fig. 21 (right), the effect of the improvement depth and stiffness is stronger with larger variations in the free-field response.

Through Python scripting, the model data and results from the calculations are written to an Abaqus output database, allowing for convenient post-processing of the results in Abaqus/Viewer [44]. Fig. 22 shows a contour plot of the vertical displacements of the track and the surrounding soil surface, for the case with $h = 6$ m, for three configurations: (a) no improvement, (b) improvement by two panels and (c) block improvement. The contour plots are shown for the load speeds $v = 70$ m/s and $v = 96$ m/s, that for the unimproved case cause maximum rail and free field displacements, respectively. For the unimproved case (a), the V-shaped mach cone is clearly visible with trailing oscillations behind the load. A significant “bow wave” is also seen ahead of the load. For the two improved cases, the displacements are significantly lower, and the response appears nearly quasi-static for the load speed $v = 70$ m/s. For the load speed $v = 96$ m/s, the high-speed effect is visible also for the improved cases, however significantly lower than for the unimproved case.

Conclusions

In the paper, the mitigation of large rail and free-field displacements at high speeds by subsoil stiffening was studied numerically for a railway track on soft soil. A very soft clay layer with a shear wave velocity $C_S = 60$ m/s overlaying a homogeneous half-space with a shear wave velocity $C_S = 100$ m/s was considered.

The soil surface response was studied for a uniform traction load moving at various speeds on the soil surface, for varying depths of the clay layer. It was found that the speed at which the maximum displacement response occurs under the load, the critical velocity, is clearly dominated by the shear wave velocity of the top layer material for depths greater than 4 m, with a speed–response curve similar to that of a soft homogeneous half-space. For shallower depths (< 2 m) large displacement amplification under the load was found for load speeds near the shear wave velocity of the top layer material, but with a less pronounced maximum between the shear wave velocities of the top layer and the half-space. For such shallow depths, however, the response in the free-field (16 m from the load) was shown to be almost unaffected by the top layer with a speed–response curve similar to that of a homogeneous half-space of the stiffer material. With the load acting on the rail of a ballasted railway track, similar behavior was found regarding the maximum displacement under the load and in the free field. The critical velocity, i.e. the velocity at which maximum rail displacement occurs, was also estimated using a dispersion diagram approach in good agreement with what was found using the 2.5D FE model.

The reduction of the displacement by subgrade stiffening was studied by modeling a stiff block underneath the track, simulating locally improved soil conditions. This was found to have an immediate effect on both maximum rail response and critical speed already at modest improvement depths (1–2 m). The displacements 16 m from the track

were also found to be significantly reduced for load speeds near C_S of the clay layer material. However, at load speeds near the C_C of the underlying half-space material, such shallow improvement was found to yield insignificant reduction of the free field response. With deeper soil improvement, stronger reduction of both rail and free field response was obtained, as well as an increasing critical velocity. Finally, soil improvement by panels along the track was considered. It was found that efficient mitigation can be obtained both regarding rail displacement and free field response, with a relatively low volume of soil improvement, especially for load speeds around the original (unimproved) critical velocity. For higher load speeds, close to C_R of the half-space material, the efficiency of the soil improvement in reducing the free-field ground vibrations is more strongly depending on the improvement depth and stiffness.

Declaration of Competing Interest

The authors declare that they have no known competing financial interests or personal relationships that could have appeared to influence the work reported in this paper.

Acknowledgments

The authors gratefully acknowledge financial support from the Swedish Innovation Agency (Vinnova) under Grant No. 2018–04159.

References

- [1] Kaynia AM, Madhus C, Zackrisson P. Ground vibration from high-speed trains: prediction and countermeasure. *J Geotech Geoenviron Eng* 2000;126(6):531–7.
- [2] Alves Costa P, Calçada R, Silva Cardoso A, Bodare A. Influence of soil non-linearity on the dynamic response of high-speed railway tracks. *Soil Dynam Earthquake Eng* 2010;30(4):221–35.
- [3] Shih JY, Thompson DJ, Ntotsios E. Analysis of resonance effect for a railway track on a layered ground. *Transport Geotech* 2018;16:51–62.
- [4] Connolly DP, Alves Costa P. Geodynamics of very high speed transport systems. *Soil Dynam Earthquake Eng* 2020;130:105982.
- [5] Kausel E, Estaire J, Crespo-Chacón I. Proof of critical speed of high-speed rail underlain by stratified media. *Proc Roy Soc A* 2020;476:20200083.
- [6] Sheng X, Jones CJC, Petyt M. Ground vibration generated by a harmonic load acting on a railway track. *J Sound Vib* 1999;225(1):3–28.
- [7] Sheng X, Jones CJC, Petyt M. Ground vibration generated by a load moving along a railway track. *J. Sound Vib.* 1999;228(1):129–56.
- [8] Yang Y, Hung H. A 2.5D finite-infinite element approach for modelling visco-elastic bodies subjected to moving loads. *Int. J. Numer. Meth. Eng.* 2001;51:1317–36.
- [9] Sheng X, Jones CJC, Thompson DJ. Prediction of ground vibration from trains using the wavenumber finite and boundary element methods. *J. Sound Vib.* 2006; 293:575–86.
- [10] François S, Schevenels M, Galvin P, Lombaert G, Degrande G. A 2.5D coupled FE-BE methodology for the dynamic interaction between longitudinally invariant structures and a layered halfspace. *Comput. Methods Appl. Mech. Eng.* 2010;199: 1536–48.
- [11] Galvin P, François S, Schevenels M, Bongini E, Degrande G, Lombaert G. A 2.5D coupled FE-BE model for the prediction of railway induced vibrations. *Soil Dynamics and Earthquake Engineering* 2010;30:1500–12.
- [12] Alves Costa P, Calçada R, Silva Cardoso A. Track-ground vibrations induced by railway traffic: In-situ measurements and validation of a 2.5D FEM-BEM model. *Soil Dynamics and Earthquake Engineering* 2012;32(1):111–28.
- [13] Thompson DJ, Jiang J, Toward MGR, Hussein MFM, Djckmans A, Coulier P, Degrande G, Lombaert G. Mitigation of railway-induced vibration by using subgrade stiffening. *Soil Dynamics and Earthquake Engineering* 2012;32(1): 111–28.
- [14] Andersen L, Nielsen SRK. Reduction of ground vibration by means of barriers or soil improvement along a railway track. *Soil Dynamics and Earthquake Engineering* 2005;25(7–10):701–16.
- [15] Persson P, Persson K, Sandberg G. Numerical study of reduction in ground vibrations by using barriers. *Eng. Struct.* 2016;115:18–27.
- [16] Djckmans A, Ekblad A, Smekal A, Degrande G, Lombaert G. Efficacy of a sheet pile wall as a wave barrier for railway induced ground vibration. *Soil Dynamics and Earthquake Engineering* 2016;84:55–69.
- [17] With C, Bahrekazemi M, Bodare A. Wave barrier of lime-cement columns against train-induced ground-borne vibrations. *Soil Dynamics and Earthquake Engineering* 2009;29(6):1027–33.
- [18] G. Holm, B. Andreasson, P. Bengtsson, A. Bodare, H. Eriksson, Mitigation of track and ground vibrations by high speed trains at Ledsgard, Sweden. Report 10. Svenskt Djuptabilisering, 2002.

- [19] Noren-Cosgriff KM, Bjornara TI, Dahl BM, Kaynia AM. Advantages and limitation of using 2-D FE modelling for assessment of effect of mitigation measures for railway vibrations. *Appl. Acoust.* 2019;155:463–76.
- [20] J. Fernandez-Ruiz, M. Miranda, J. Castro, Improvement of the critical speed in high-speed ballasted railway tracks with stone columns: A numerical study on critical length. *Transportation Geotechnics*, 100628, 2021.
- [21] Coulier P, François S, Degrande G, Lombaert G. Subgrade stiffening next to the track as a wave impeding barrier for railway induced vibrations. *Soil Dynamics and Earthquake Engineering* 2013;48:119–31.
- [22] Alves Costa P, Calçada R, Silva Cardoso A. Ballast mats for the reduction of railway traffic vibrations. Numerical study. *Soil Dynamics and Earthquake Engineering* 2012;42:137–50.
- [23] Lombaert G, Degrande G, Vanhauwere B, Vandeborghht B, François S. The control of ground-borne vibrations from railway traffic by means of continuous floating slabs. *J. Sound Vib.* 2006;297:946–61.
- [24] Takemiya H, Fujiwara A. Wave propagation/impediment in a stratum and wave impeding block (WIB) measured for SSI response reduction. *Soil Dynamics and Earthquake Engineering* 1994;13:49–61.
- [25] Takemiya H. Field vibration mitigation by honeycomb WIB for pile foundations of a high-speed train viaduct. *Soil Dynamics and Earthquake Engineering* 2004;24: 69–87.
- [26] Peplow AT, Jones CJC, Petyt M. Surface vibration propagation over a layered elastic half-space with an inclusion. *Appl. Acoust.* 1999;56:283–96.
- [27] Gao G, Chen J, Gu X, Song J, Li S, Li N. Numerical study on the active vibration isolation by wave impeding block in saturated soils under vertical loading. *Soil Dynamics and Earthquake Engineering* 2017;93:99–112.
- [28] Connolly D, Giannopoulos A, Forde MC. Numerical modelling of ground borne vibrations from high speed rail lines on embankments. *Soil Dynamics and Earthquake Engineering* 2013;46:13–9.
- [29] Gao G, Bi J, Chen J. Vibration mitigation performance of embankments and cuttings in transversely isotropic ground under high-speed train loading. *Soil Dynamics and Earthquake Engineering* 2021;141:106478.
- [30] Peplow AT, Kaynia AM. Prediction and validation of traffic vibration reduction due to cement column stabilization. *Soil Dynamics and Earthquake Engineering* 2007; 27(8):793–802.
- [31] Dong K, Connolly DP, Laghrouche O, Woodward PK, Alves Costa P. The stiffening of soft soils on railway lines. *Transportation Geotechnics* 2018;17:178–91.
- [32] Dong K, Connolly DP, Laghrouche O, Woodward PK, Alves Costa P. Non-linear soil behaviour on high speed rail lines. *Comput. Geotech.* 2019;112:302–18.
- [33] Shih JY, Thompson DJ, Zervos A. The influence of soil nonlinear properties on the track/ground vibration induced by trains running on soft ground. *Transportation Geotechnics* 2017;11:1–16.
- [34] Connolly DP, Dong K, Alves Costa P, Soares P, Woodward PK. High speed railway ground dynamics: a multi-model analysis. *International Journal of Rail. Transportation* 2020;8:324–46.
- [35] Intel, *Intel Fortran Compiler 19.0, Reference Manual*, 2019.
- [36] Intel, *Intel Math Kernel Library 2019, Reference Manual*, 2019.
- [37] François S, Schevenels M, Lombaert G, Degrande G. A two-and-a-half dimensional displacement-based PML for elastodynamic wave propagation. *Int. J. Numer. Meth. Eng.* 2015;79:89–103.
- [38] Malmberg J. Numerical modeling of train-induced ground vibrations. Licentiate dissertation. Report TVSM-3080. Lund University; 2020.
- [39] Basu U, Chopra AK. Perfectly matched layers for time-harmonic elastodynamics of unbounded domains: theory and finite-element implementation. *Comput. Methods Appl. Mech. Eng.* 2003;192(11–12):1337–75.
- [40] Malmberg J, Persson P, Persson K. Effects of modeling strategies for a slab track on predicted ground vibrations. *Soil Dynam Earthquake Eng* 2020;136:106254.
- [41] Sheng X, Jones CJC, Thompson DJ. A theoretical study on the influence of the track on train-induced ground vibration. *J Sound Vib* 2004;272:909–36.
- [42] Alves Costa P, Colaço A, Calçada R, Silva Cardoso A. Critical speed of railway tracks. Detailed and simplified approaches. *Transport Geotech* 2015;2:30–46.
- [43] Mezher SB, Connolly DP, Woodward PK, Laghrouche O, Pombo J, Alves Costa P. Railway critical velocity - Analytical prediction and analysis. *Transport Geotech* 2016;6:84–96.
- [44] Dassault Systèmes SIMULIA. *Abaqus 6.14*.

Paper E



Numerical study of train-induced vibrations in light and heavy building systems

J. Malmberg, O. Floden, P. Persson, K. Persson
Department of Construction Sciences, Lund University
P.O. Box 118, SE-22100 Lund, Sweden
jens.malmberg@construction.lth.se

Abstract

This paper deals with the numerical prediction of building vibrations induced by a passing train on an adjacent railway track. The calculations are based on a sub-structure approach, where a sequence of different models are used to predict the train-track interaction forces, the free-field ground vibrations due to these forces, and the building-on-soil response when subjected to the incident wave field. The free-field ground vibrations and the track receptance are calculated using a so called 2.5D technique where the railway track is represented by finite elements that couple to a dynamic stiffness of the underlying soil, which in turn is obtained from the Green's function of a horizontally layered half-space using a layer transfer matrix approach. A planar multi-body model of the train, coupled to the track receptance, is used for calculating the train-track interaction forces as the train runs over an uneven rail. Finally, the building response to the incident wavefield is calculated using a 3D finite element model, accounting for the soil dynamic stiffness. This sequence of models and calculations are applied to evaluate the vibrations in two buildings with identical layout, one lightweight wooden building and one heavyweight concrete building, due to a passenger train passing by at two different speeds. It was found that the difference in response between the two buildings were small, with slightly higher response in terms of root-mean-square (RMS) velocity in the lightweight building. Compared to the incident wavefield, an amplification of the response inside the building was found in frequency bands around the fundamental natural frequencies of the slabs; however for higher frequencies and in terms of the 1s running RMS velocity the building response was reduced. Further, it was found that accounting for soil-structure-interaction, as opposed to simply enforcing the free-field displacements at the building foundations, significantly reduced the building response in terms of 1s RMS velocity.

Keywords: Train-induced ground vibration, building vibration, soil-structure interaction, 2.5D finite elements, Green's function.

1. Introduction

The trend towards an expanding train infrastructure in the European Union may lead to increasing vibrations and noise in buildings located in the vicinity of railways. Studies have shown that vibrations from rail transport can be a significant source of annoyance. In [1], the association between distance to the railway track and annoyance from vibrations were studied, finding increased annoyance for closer distances, with significant annoyance reported for distances up to 400 m. Being subjected to environmental noise may lead to negative health effects as pointed out by the WHO evidence review on annoyance [2].

When new buildings are erected close to existing railway lines, or when new railway lines are constructed, measures to reduce the noise and vibrations may be required. In order to adequately design such measures, models are needed that can properly represent the physics of the vibration problem. In numerical modeling of train-induced vibrations, a large number of simplifications are usually necessary due to the complexity of the problem and the large quantity of unknown parameters involved. The size of the computational domain, including the track, surrounding soil and adjacent buildings, involved in the vibration problem poses challenges to reduce the computational effort. While 3D finite element (FE) and boundary element (BE) models have been used by some researchers to study both the vibration generation at the track and the wave propagation through the surrounding soil [3, 4, 5, 6], so called 2.5D models operating in frequency domain have become a popular choice. In 2.5D models, the track and soil properties are assumed invariant in the track direction but providing the full 3D response, potentially at a much cheaper computational cost than with 3D models. Such models have been formulated and developed by a large number of researchers using semi-analytical and/or numerical methods such as FE and BE methods [8, 13, 11, 17, 21, 26, 27, 22, 19]. A drawback of the 2.5D modeling technique is that it is not possible to directly include a stationary building next to the track, due to the assumed geometrical invariance in the track direction. The most common approach to evaluate building vibrations is therefore to assume a weak coupling between the source and receivers, i.e. to assume that the presence of the building does not affect the vibrations generated at the source. This allows for calculating the free-field ground vibrations in a separate (e.g. 2.5D-) model and then apply them in a 3D model to excite the building structure. To the authors knowledge, the first to utilize such a formulation in the field of traffic induced building vibrations was Pyl et al [15] who used a subdomain formulation where the free-field vibrations due to road traffic, obtained from a separate 2.5D BE model, were applied to a 3D FE model of the building where the soil was modeled using BE. This approach was later used by Fiala et al [16] to study the vibration and noise in a multi-story portal frame building due to the passage of a high-speed train. Lopes et al [22, 23] used a 2.5D FE model with Perfectly Matched Layers (PML) to calculate the free-field ground vibration to an underground train. The building response was then obtained in a separate 3D FE/BE model of the building structure including the soil impedance. Connolly et al [19] calculated the wheel-rail interaction forces due to a rail defect using a planar FE model of the track in time domain. These forces were then transformed to frequency domain and applied in a 2.5D FE/BE model of the track and the surrounding soil to obtain the free-field ground surface response. The ground surface response was then transformed back to time domain, and the responses of a 4-story and an 8-story, respectively, building was calculated using a modal dynamic procedure,

accounting for the soil using springs and dampers under the building. Lopez-Mendoza et al [20] proposed a scoping model to predict train-induced vibrations in buildings using either a measured or a calculated free-field spectrum as input to a building model. Using a FE model of the building, the building response was then obtained using a response spectrum calculation. Recently, Colaço et al [29] used a substructure approach to calculate the building response due to a passing train, where a calculation model based on 2.5D FEM and Method of Fundamental Solutions (MFS) was used to obtain the free-field ground vibrations which were applied to a 3D FE model of the building. In the building model, the soil dynamic stiffness was accounted for in a simplified manner by a Lumped Parameter Model (LPM). Measurements from an experimental campaign was used to validate the models with satisfactory agreement.

In Sweden, lightweight wooden buildings are becoming increasingly popular, not only for residential buildings but also for office buildings etc. However, there is a lack of knowledge how lightweight buildings perform, compared to traditional heavyweight concrete buildings, with respect to ground-borne vibrations, e.g. from railway traffic. The choice of building system has to be dealt with in an early building design stage. Numerically predicting vibration levels in buildings from railway traffic is not easily done using commercially available FE software. The purpose of this paper is therefore to present a numerical prediction model for train-induced vibrations and to demonstrate its use to assess the dynamic responses of two buildings with identical layout but with different materials in the load bearing structure. A lightweight and a heavyweight 3-slab building, supported by surface footings, excited by ground vibrations caused by a passing train running over an uneven rail, is considered. The computational chain is based on a substructure approach, where a 2.5D model is first used to obtain the free-field ground response due to the passing train. This free-field response is then applied in a 3D FE model of the building, where the soil dynamic stiffness is accounted for.

The paper is structured as follows. In Section 2 the computational approach is presented; the numerical models developed for calculating the free-field ground motion caused by a passing train and for imposing the wave field onto the building structure are described. The ground, track, train and building properties assumed for the study are presented in Section 3 together with the calculated responses. A discussion of the results is provided in Section 4, and the most important findings are highlighted in Section 5.

2. Computational model

In the present paper, a substructuring approach is followed to analyze the building response due to the ground motion caused by a passing train. The different steps in the calculation scheme are summarized in Figure 1. In the first step, detailed in Section 2.1, the track receptance and the free-field ground displacements due to a moving harmonic unit load acting on the rails, is calculated for a range of excitation frequencies and a specific vehicle speed. For this purpose a 2.5D FE model of the track is coupled to a dynamic stiffness representing the surrounding soil. In the second step the track receptance, calculated in Step 1, is combined with a 2D multi-body vehicle model to calculate the dynamic axle loads accounting for rail unevenness, as described in Section 2.2. The free-field ground displacements due to a unit load, calculated in Step 1, is then scaled with these dynamic axle

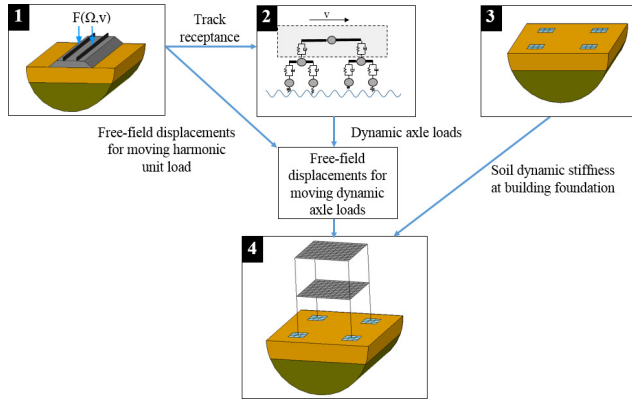


Figure 1: Analysis steps to calculate the building vibrations due to a passing train.

loads to yield the actual dynamic response of the free-field ground surface due to the passing train. In Step 3, the dynamic stiffness of the building footings on the layered ground is calculated using a semi-analytical approach, which is added to the FE model of the building structure in Step 4 to calculate the building response due to the incoming wavefield, see Section 2.3.

The code is developed by the first author. The most computationally demanding parts, Step 1 and Step 3, are written in Fortran [33] and utilizes Intel MKL [34] for mathematical operations. The remaining parts are written in MATLAB.

2.1. Track and ground model

To calculate the rail and ground surface response due to a moving load acting on the railway track a 2.5D technique is employed, where the track is modeled by finite elements and the underlying soil is accounted for through a dynamic stiffness matrix calculated from the Green's function of a horizontally layered half-space. The geometry is assumed invariant in the track direction. The 3D time-domain problem is solved via a sequence of frequency-domain analyses of the 2D cross-section, through a double Fourier transformation of the governing equations with respect to time and the track coordinate. Each such 2D analysis corresponds to a specific wavenumber k_1 in the track direction.

For each wavenumber k_1 , the resulting system of equations can be written as:

$$\left(-\omega^2 \mathbf{M} + \mathbf{K}_0 + ik_1 \mathbf{K}_1 + k_1^2 \mathbf{K}_2 + \mathbf{D}_g(k_1, \omega) \right) \mathbf{a}(k_1, \omega) = \mathbf{f}_1(k_1, \omega), \quad (1)$$

where the 2.5D FE stiffness matrices \mathbf{K}_0 , \mathbf{K}_1 , \mathbf{K}_2 and the mass matrix \mathbf{M} are independent of the wavenumber k_1 . Detailed expressions for these matrices can be found in e.g. [11, 18, 25]. Further, the matrix $\mathbf{D}_g(k_1, \omega)$ is the dynamic stiffness matrix of the ground, as further discussed below. The vector $\mathbf{a}(k_1, \omega)$ represents the nodal displacements and $\mathbf{f}_1(k_1, \omega)$ is the load vector.

The soil dynamic stiffness matrix $\mathbf{D}_g(k_1, \omega)$ is calculated using the Green's function of a horizontally layered

half-space. The Green's function, $G_{ij}(k_1, k_2, \omega)$ is obtained with a layer transfer matrix approach [7, 8, 10]. The soil-track interface is discretized into n strips, with n being the number of finite elements of the track at the interface. Within each strip, a constant traction is assumed. For a strip, having a width Δ , centered around $y = 0$, the traction is described in wave number domain as

$$p(k_1, k_2) = \frac{\sin(k_2 \frac{\Delta}{2})}{k_2 \frac{\Delta}{2}}. \quad (2)$$

The displacement u in direction i at an arbitrary position y , due to a unit load in direction j of the strip centered around $y = 0$, is expressed by an inverse Fourier transform from wavenumber k_2 to coordinate y as

$$u_{ij}(k_1, y, \omega) = \frac{1}{2\pi} \int_{-\infty}^{\infty} G_{ij}(k_1, k_2, \omega) p(k_1, k_2) e^{ik_2 y} dk_2. \quad (3)$$

This expression is used for establishing a flexibility matrix $\mathbf{H}(k_1, \omega)$ involving the center points of all the strips, and its inversion leads to a dynamic stiffness matrix for these points, $\tilde{\mathbf{D}}(k_1, \omega) = \mathbf{H}^{-1}(k_1, \omega)$. Hence, the strips can be regarded as 2.5D boundary elements, with one node and three DoFs, having constant traction field and its displacement evaluated at the element center point. This approach has previously been suggested by Alves Costa et al [21]. The soil dynamic stiffness matrix $\tilde{\mathbf{D}}(k_1, \omega)$ cannot readily be attached to the FE system matrix, due to the differing node positions. Applying the linear transformation [21, 24]

$$\mathbf{D}_g(k_1, \omega) = \mathbf{T}_q \tilde{\mathbf{D}}(k_1, \omega) \mathbf{T}, \quad (4)$$

yields a dynamic stiffness matrix $\mathbf{D}_g(k_1, \omega)$ defined at the nodes of the FE mesh, which is the one used in Eq. (1). The matrix \mathbf{T} relates the displacements in the boundary element nodes to the displacements in the adjacent FE nodes, and \mathbf{T}_q describes the transfer of forces on the boundary elements to the FE nodes, through integration of the FE shape functions. The details of these matrices can be found in [24]. In the case considered here, with linear FE shape functions and an assumed constant traction field over the boundary element, $\mathbf{T}_q = \mathbf{T}^T$.

The rail is represented by a Bernoulli–Euler beam of infinite length, with bending stiffness $(EI)_r$ and mass m_r , continuously supported by distributed springs with stiffness k_P representing the rail pads. The governing equation for the rail can be written as

$$(EI)_r \frac{\partial^4 u_r}{\partial x^4} + m_r \frac{\partial^2 u_r}{\partial t^2} + k_P (u_r - u_s) = P(x, t). \quad (5)$$

Here, $u_r = u_r(x, t)$ is the vertical displacement of the rail and $u_s = u_s(x, t)$ is the vertical displacement of the sleeper. Furthermore, $P(x, t)$ is the load on the rail.

In frequency–wavenumber domain this equation becomes

$$(EI)_r k_1^4 u_r - \omega^2 m_r u_r + k_P (u_r - u_s) = P(k_1, \omega), \quad (6)$$

where $u_r = u_r(k_1, \omega)$ and $u_s = u_s(k_1, \omega)$ now represent the displacement quantities in (k_1, ω) -domain.

A one-dimensional element, similar to a simple Kelvin–Voight element, can be formulated for the rail and rail

pad as

$$\begin{bmatrix} (EI)_r k_1^4 - \omega^2 m_r + k_P & -k_P \\ -k_P & k_P \end{bmatrix} \begin{bmatrix} u_r \\ u_s \end{bmatrix} = \begin{bmatrix} P \\ f_s \end{bmatrix}, \quad (7)$$

where f_s is the force exerted onto the element from the sleeper node. The element is assembled into the global dynamic stiffness matrix for the whole soil–track system in a standard manner.

Solving Eq. (1) yields the displacements in all the nodes of the FE mesh, which allows for calculating the individual soil–strip tractions. The displacement response at an arbitrary y -coordinate of the soil surface is then obtained by summing the responses from each individual strip traction (c.f. Eq (3)):

$$u_i(k_1, y, \omega) = \frac{1}{2\pi} \sum_{n=1}^N \int_{-\infty}^{\infty} G_{ij}(k_1, k_2, \omega) p_j^n(k_2) e^{ik_2(y-y_n)} dk_2, \quad (8)$$

where p_j^n represents the traction in direction j of strip n , whose midpoint is located at $y = y_n$.

Furthermore, a harmonic load P_0 oscillating with the frequency Ω , moving at constant velocity v along the x -axis, is represented in time–space domain by $p(x, t) = P_0 \times \delta(x - v \times t) \times e^{i\Omega t}$. In frequency–wavenumber domain the load is given by $p(k_1, \omega) = P_0$ where

$$\omega = \Omega - k_1 \times v. \quad (9)$$

For a given load speed v and excitation frequency Ω , Eq. (1) is solved for a range of wavenumbers k_1 with the corresponding material point frequency ω from Eq. (9) and this then corresponds to a change of reference frames, to one following the load at speed v [8]. The inverse Fourier transform of the displacement $u_i(k_1, y, \omega)$ w.r.t. wavenumber k_1 , then yields the displacement in spatial domain:

$$u_i(\tilde{x}, y, \Omega) = \frac{1}{2\pi} \int_{-\infty}^{\infty} u_i(k_1, y, \omega) e^{ik_1 \tilde{x}} dk_1, \quad (10)$$

where a tilde on \tilde{x} is used to emphasize that the response is in the moving frame of reference. In the moving reference frame the response is harmonic with the excitation frequency Ω . A fixed point next to the track, however, experiences a transient response as the harmonic load on the track passes by. It is shown in [8] that the displacement spectrum of a fixed point can be expressed as

$$S_{u_i}(x, y, f) = \frac{1}{v} e^{ik_1 x} u_i(k_1, y, \omega), \quad (11)$$

where the frequency ordinate $f = \omega/2\pi$. Hence, different points along the x -axis located at equal distance y from the track have the same spectrum magnitude.

2.2. Train–track interaction

The forces exerted on the rail from the train wheels are static and dynamic. The static part simply corresponds to the dead weight of the train whereas the dynamic part is much more complex and come from various phenomena such as spatially varying track stiffness, wheel out-of-roundness and rail unevenness [12]. The dynamic excitation by the moving train is here assumed to result exclusively from rail unevenness.

Assuming that the wheel is in constant contact with the rail, the condition between the displacements of the wheel contact point u_w and rail u_r can be written as

$$u_w(x) = u_r(x) + \Delta u(x) + \frac{P}{k_H}, \quad (12)$$

where $\Delta u(x)$ denotes the rail unevenness amplitude at position x along the rail, P the wheel–rail contact force and k_H a Hertzian contact spring stiffness. The solution procedure, used by many authors, combines a two-dimensional multi-body vehicle model with the track compliance in frequency domain, in a frame of reference following the vehicle moving at constant speed. The rail unevenness is decomposed into a finite number of harmonic components, and the contact forces are calculated separately for each such component. In [9] it is shown that the wheel–rail contact forces for a train of M wheelsets, moving over a sinusoidal rail profile with wavelength λ , can be calculated as

$$\mathbf{P}(\Omega) = -(\mathbf{F} + \mathbf{F}^H + \mathbf{A})^{-1} \mathbf{\Delta u}(\Omega), \quad (13)$$

where $\mathbf{P}(\Omega)$ is a vector of length M containing complex valued contact forces at the frequency $\Omega = 2\pi v/\lambda$. The vector $\mathbf{\Delta u}(\Omega)$ contains the complex valued rail unevenness for each of the M contact points. The magnitude of the unevenness, A , is the same for each contact point, but the fact that different wheels are in different phase is accounted for by $\Delta u_j(\Omega) = A e^{i(2\pi/\lambda)a_j}$, where a_j denotes the coordinate of wheel j . Furthermore, $\mathbf{F}(\Omega)$ is the receptance matrix of the train at the contact points with the rail, and \mathbf{F}^H is a diagonal matrix containing the flexibility of the contact springs at the wheel–rail contact points, $1/k_H$. The matrix $\mathbf{A}(\Omega)$ is the rail receptance matrix, with A_{ij} containing the displacement at wheel–rail contact point i due to a unit load at point j . The details regarding this formulation can be found in e.g. [9, 13, 21]

Hence, the time-varying dynamic contact forces between the wheels and the rail are decomposed into a discrete number of harmonic force components, each associated with a single rail unevenness wavelength component. Since the complete system (train–track–soil–building) is assumed linear, the total response is obtained from a summation of the partial responses due to each unevenness component. In the present paper, a number of artificial rail unevenness profiles are generated from a power spectral density (PSD) function, as further described in Section 3.1.

2.3. Soil–structure interaction

In the approach followed here a so-called weak coupling to the soil–structure interaction (SSI) problem is considered, i.e. it is assumed that the presence of the building does not affect the wheel–rail contact forces and the resulting wave-field generated in the ground around the track. Hence, the building response to the incoming wave field may be determined by applying a formulation in which the building is excited by a set of fictitious forces at the soil–structure interface. These fictitious forces are calculated from the free-field response at the soil–structure interface. Kausel et al [30, 31] refer to this as the substructure theorem,

$$\begin{bmatrix} \mathbf{D}_{bb} & \mathbf{D}_{bi} \\ \mathbf{D}_{ib} & \mathbf{D}_{ii} + \mathbf{Z} \end{bmatrix} \begin{bmatrix} \mathbf{u}_b \\ \mathbf{u}_i \end{bmatrix} = \begin{bmatrix} \mathbf{0} \\ \mathbf{Z}\mathbf{u}_i^* + \mathbf{p}_i^* \end{bmatrix}, \quad (14)$$

where $\mathbf{D} = \mathbf{D}(\omega)$ refers to the dynamic stiffness matrix of the building structure, partitioned so that the subscript i refers to DoFs along the soil–structure interface and b refers to all other DoFs of the building. Furthermore $\mathbf{Z} = \mathbf{Z}(\omega)$ refers to the dynamic stiffness matrix of the soil along the soil–structure boundary, and vectors \mathbf{u}_i^* and \mathbf{p}_i^* refer to the free-field displacements and tractions, respectively, at the soil–structure boundary. Here, the structure foundation is composed of surface footings, assumed to be placed on top of the soil surface. Hence, in Eq. (14) the term $\mathbf{p}_i^* = \mathbf{0}$ because a free surface is traction free.

The dynamic stiffness of the foundation, $\mathbf{Z}(\omega)$, is calculated using the Green’s function of the layered half-space previously discussed in Section 2.2. Each soil–footing interface is discretized by a number of elements, each in which constant traction is assumed. The displacements are evaluated at the mid-point of each element. This technique was previously used by Lopes et al [22, 23]. The soil–footing interface, of each of the N footings, is discretized into $m \times n$ elements. Each element has three translational DoFs (x, y, z), resulting in a total of $s = (3 \times N \times m \times n)$ DoFs. A flexibility matrix $\mathbf{H}(\omega)$ ($s \times s$) is established using the Green’s function of the layered half-space, where element H_{ij} is the displacement in DoF j due to a unit load in DoF i , applied as a constant traction over the element associated to DoF i . The inverse of this flexibility matrix provides a dynamic stiffness matrix of the discretized soil–structure interface, $\mathbf{Z}(\omega) = \mathbf{H}^{-1}(\omega)$. Now, each footing is assumed rigid and its motion may therefore be fully described by three translational and three rotational DoFs, i.e. a total of $6 \times N$ DoFs. A linear transformation matrix \mathbf{T} ($s \times 6N$) that kinematically relates the original footing DoFs to the reduced system DoFs is applied to the dynamic stiffness matrix so that

$$\tilde{\mathbf{Z}}(\omega) = \mathbf{T}^T \mathbf{Z}(\omega) \mathbf{T}. \quad (15)$$

The set of fictitious forces, $\mathbf{f}_i = \mathbf{Z}\mathbf{u}_i^*$, acting on the original DoFs of the soil–footing interface is likewise transformed to the reduced system DoFs by $\tilde{\mathbf{f}}_i = \mathbf{T}^T \mathbf{f}_i = \mathbf{T}^T \mathbf{Z}\mathbf{u}_i^*$. In the present case, the footings are not actually modeled by finite elements, and the columns attached to the footings are modeled by beam elements. Hence, for the current case Eq. (14) can be written as

$$\begin{bmatrix} \mathbf{D}_{bb} & \mathbf{D}_{bi} \\ \mathbf{D}_{ib} & \mathbf{D}_{ii} + \tilde{\mathbf{Z}} \end{bmatrix} \begin{bmatrix} \mathbf{u}_b \\ \mathbf{u}_i \end{bmatrix} = \begin{bmatrix} \mathbf{0} \\ \tilde{\mathbf{f}}_i \end{bmatrix}, \quad (16)$$

where a subscript i now refers to the $(6 \times N)$ DoFs at the bottom of the columns. It is emphasized that although each footing is regarded rigid and modeled solely by a single node with six DoFs, the excitation due to the incoming wave field is calculated with respect to the actual footing surface area, accounting for the free–field motion in the $(3 \times m \times n)$ original footing DoFs. The free–field motion of each such DoF is obtained by Eq. (11). It is also emphasized that the matrix $\tilde{\mathbf{Z}}(\omega)$ is full, accounting for through-soil interaction between different individual footings.

3. A comparative study of vibrations in a light and a heavy building

A study that compares the resulting vibrations in a heavyweight concrete building and a lightweight wooden building from a passing train is presented here. The building models are adapted from [32], and although the buildings are fictitious, the structural members were chosen to fulfill the static design criteria in accordance with Eurocode. In Section 3.1 the track, ground and train properties are presented together with the calculated free-field response. The properties of the buildings and their vibration response are presented in Section 3.2.

3.1. Track, ground and train

The track considered here is a ballasted track with properties according to Table 1. Since the geometry is assumed invariant in the track direction with the 2.5D approach, discrete sleepers and rail pads are modeled with distributed properties by dividing the discrete properties with the assumed sleeper spacing, 0.66 m. The sleepers are regarded rigid in the plane of the track cross-section, enforced by constraining all the nodes on top of the ballast layer within the sleeper width (see Figure 2). Furthermore, the (distributed) sleeper mass is lumped to these nodes. The ground consists of a $h = 4$ m deep sand layer, with a shear wave velocity $C_s = 173$ m/s, overlying a stiffer half-space. The soil material properties are shown in Table 2.

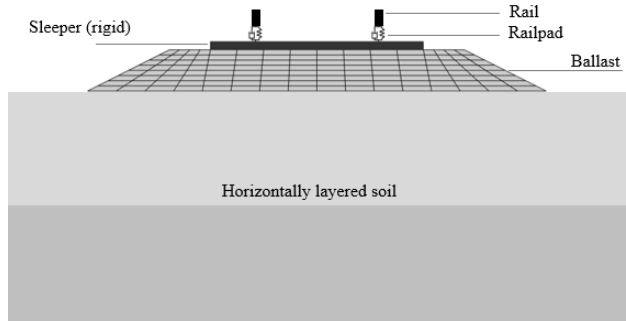


Figure 2: Track 2.5D analysis model.

Alves Costa et al [28] studied the effect of modeling approaches regarding the train, on the calculated wheel-rail contact forces and the resulting free-field vibrations, concluding that a multi-body vehicle model involving the unsprung and semi-sprung masses, i.e. the wheelsets and the bogies, are sufficient and that the sprung mass (car body) can be disregarded. Therefore, such a model is adopted here to simulate the passage of a high-speed train. The train properties, representing a Portuguese Alfa-Pendular high-speed train, are taken from [29] where a detailed description of the model properties can be found. The train consists of 6 carts, each cart having a bogie-to-bogie center distance of 19.0 m, and a bogie width of 2.7 m. The bogie-to-bogie center distance between two neighbouring carts is 6.9 m. The distance between the first and last wheelsets of the train is 151.2 m. Each bogie has a mass and a rotational inertia in the range $m_b = 4712 - 4932$ kg and $I_b = 5000 - 5150$ kg·m², respectively. The primary suspension stiffness and damping values are $k_p = 3200$ kN/m and $c_p = 35$ kN·s/m, respectively.

Table 1: Track properties.

	Property	Value
Rail	Mass (kg/m)	60
	Young's modulus (GPa)	210
	Second moment of inertia (m ⁴)	3.217 × 10 ⁻⁵
	Loss factor (-)	0.01
Rail pads	Stiffness (MN/m ²)	250
	Loss factor (-)	0.1
Sleeper	Width (m)	2.6
	Mass (kg/m)	540
Ballast	Density (kg/m ³)	2000
	Young's modulus (MPa)	200
	Poisson's ratio	0.33
	Loss factor (-)	0.04
	Width, top/bottom (m)	3.6 / 5.6
	Height (m)	0.5

Table 2: Ground properties.

Layer	Property	Value
Soil	Depth (m)	4
	Young's modulus (MPa)	160
	Poisson's ratio	0.33
	Density (kg/m ³)	2000
	Loss factor $\eta = 2\zeta$ (-)	0.06
Half-space	Depth (m)	∞
	Young's modulus (MPa)	800
	Poisson's ratio	0.33
	Density (kg/m ³)	2000
	Loss factor $\eta = 2\zeta$ (-)	0.06

Each wheelset has a mass in the range $m_w = 1538 - 1884$ kg. The static axle loads are in the range 128.8 – 136.6 kN.

In the present study, a number of artificial rail profiles were generated from a power spectral density (PSD) function $S(k_1)$ for the track unevenness as given by:

$$S(k_1) = S(k_{1,0}) \left(\frac{k_1}{k_{1,0}} \right)^{-w}, \quad (17)$$

where $k_{1,0} = 1$ rad/m, $w = 3.5$ and $S(k_{1,0}) = 1 \times 10^{-8}$ m²/(rad/m) [14, 23]. The PSD function describes how the unevenness amplitude is distributed over different wavelengths. An artificial rail profile (sample) is generated by selecting a discrete number of wavelengths, with the corresponding unevenness amplitudes from the PSD function, and assigning a random phase angle to each discrete wavelength. Figure 3 shows the PSD function and a number of rail profile samples.

For a moving vehicle on the rail, each discrete unevenness wavelength corresponds to a harmonic excitation frequency $f = v/\lambda$, and the corresponding dynamic axle loads between the wheels and the rail are calculated

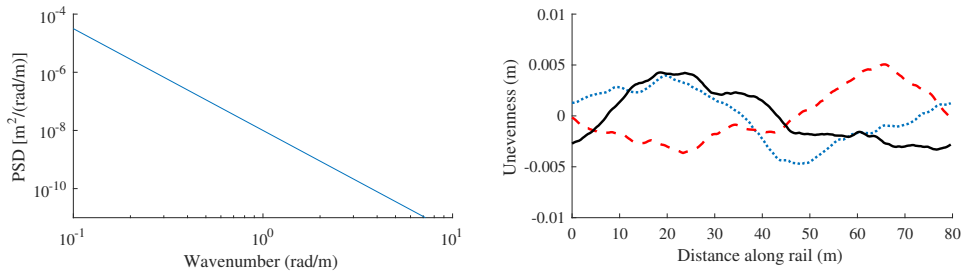


Figure 3: Left: One-sided PSD of rail unevenness. Right: Three realizations (samples) of rail unevenness.

as described in Section 2.2. The rail receptance, calculated as the rail response due to a harmonic unit load on the rails (0.5 N per rail), is shown in Figure 4 (left) for different speeds of the load. The load speed affects the rail receptance only to a small extent. Most notably, it can be observed that the peak around 15 Hz is shifted to slightly lower frequencies for increasing speeds, which is due to the Doppler effect [13]. Figure 4 (right) shows the dynamic wheel–rail contact forces in 1/3 octave bands, for the first axle of the train, for train speeds $v = 30$ m/s and $v = 60$ m/s. These spectra are dependent on the PSD function (Figure 3) but not the actual sample. Although the spectra appear to be increasing monotonously in the higher frequency bands, there is a maximum at around 90 Hz corresponding to the “resonance” frequency of the vehicle and track on the layered ground, which however is outside the studied frequency range. The peak around 6 Hz corresponds to the resonance frequency of the bogie on the primary suspension.

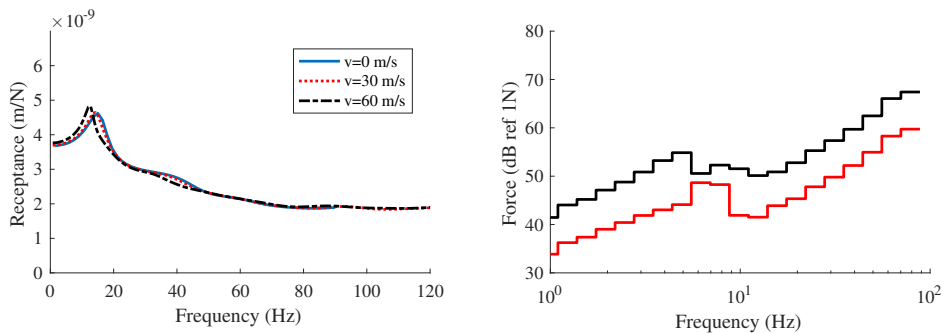


Figure 4: Left: Rail receptance for different load speeds. Right: 1/3 octave band spectra of wheel–rail contact force for speeds $v = 30$ m/s (red) and $v = 60$ m/s (black).

Figure 5 shows the time-history response and the frequency content of the vertical vibration velocity in the free-field, at distances $y = 10$ m and $y = 18$ m from the track, due to a train passing at $v = 30$ m/s, for one rail profile sample. The x -axis in the left figure is set so that $t = 0$ corresponds to the time instant when the middle of the train is passing the receiver point. Figure 6 shows the corresponding results for the train speed $v = 60$ m/s. In both cases, the maximum frequency of excitation is $f = 80$ Hz, corresponding to a minimum rail

unevenness wavelength of $\lambda = v/f$. Due to the Doppler effect, the moving load at frequency f excites a range of frequencies in the free-field, governed by the slowest moving wave in the soil as $[f/(1+v/C), f/(1-v/C)]$. This explains why the spectra in Figures 5 and 6 show frequency content beyond the maximum excitation frequency 80 Hz. The jagged shape of the frequency spectra is a result of modulation due to the superposition of several axle loads with similar values with a time-delay corresponding to v/L where L is the distance between axles within or between bogies/carriages [13]. Although the complex response magnitude for a fixed point in the free-field, due to the train running over one particular rail unevenness wavelength, is independent of its coordinate along the track, c.f. Eq. (11), this is no longer the case when the response spectrum from several unevenness wavelengths are superimposed, i.e. when considering a full rail profile sample. The summed response for a fixed point in the free-field is strongly affected by the phase angles of the individual unevenness wavelengths. Figure 7 (left) shows the running RMS, calculated over a 1 s window, of the vertical velocity in points located 10 m and 18 m from the track due to a train passing at $v = 30$ m/s, for 100 different rail profile samples. The average value, calculated as the mean value from the 100 simulations at each time instant, are indicated by thick black lines. Figure 7 (right) shows the max/min envelopes of velocity spectra in 1/3 octave band, calculated over the time it takes for the train to pass a fix point, $T = L/v$ where L is the total train length. The corresponding results for a train speed $v = 60$ m/s are shown in Figure 8. Figure 9 shows the ensemble average of the running RMS and the 1/3 octave band spectra, for both train speeds. It can be observed from the spectra that the vibration levels increase significantly in the frequency bands around 15 Hz, associated with the cut-on frequency of the upper soil layer, i.e. the frequency above which the dominant P-SV wave propagates in the upper soil layer with little influence of the underlying half-space. For the frequency bands below about 5 Hz the quasi-static response, i.e. the response due to the moving dead load of the train, dominates the total response and the difference between the two vehicle speeds is mainly due to the modulation resulting from the superposition of the static axle loads with different time-delays.

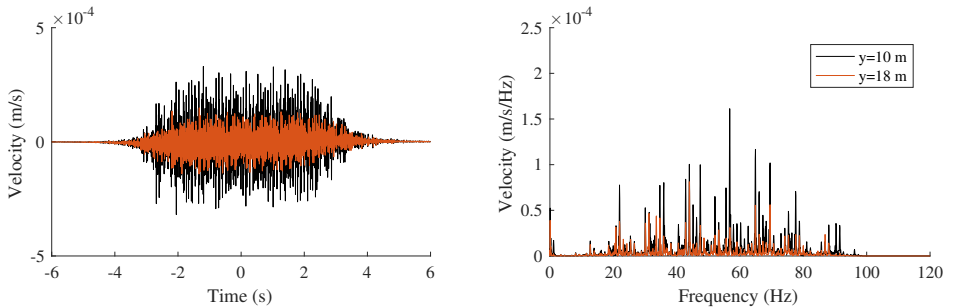


Figure 5: Left: Vertical free-field response 10 m and 18 m from the track for one rail profile sample, for a train speed $v = 30$ m/s. Right: Corresponding frequency spectra.

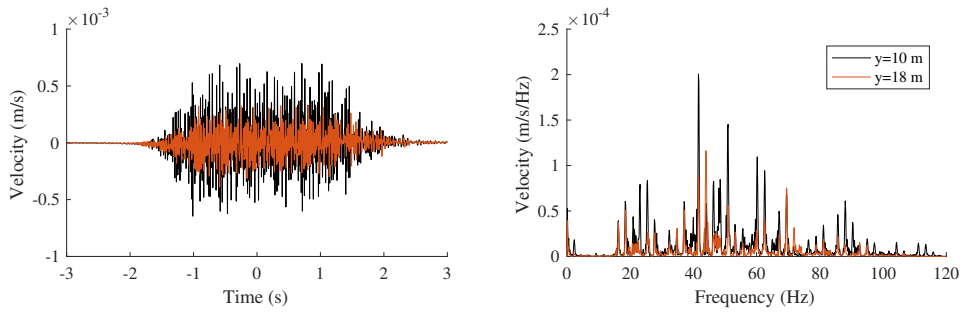


Figure 6: Left: Vertical free-field response 10 m and 18 m from the track for one rail profile sample, for a train speed $v = 60$ m/s. Right: Corresponding frequency spectra.

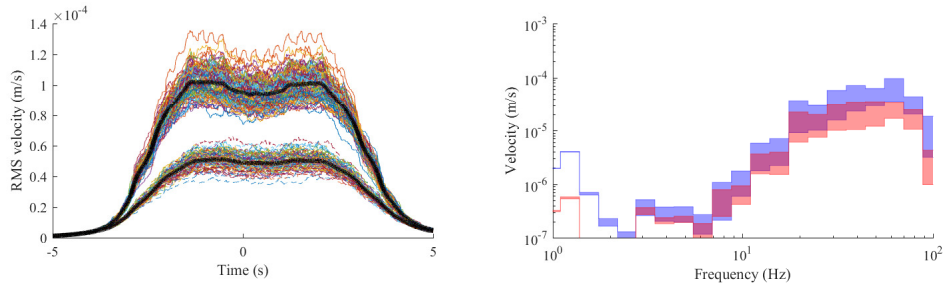


Figure 7: Left: Running RMS of the free-field velocity at 10 m and 18 m from the track for 100 rail profile samples, for a train speed $v = 30$ m/s. Thick lines indicate ensemble average. Right: Max/min envelopes of velocity spectra in 1/3 octave bands at 10 m (blue) and 18 m (red).

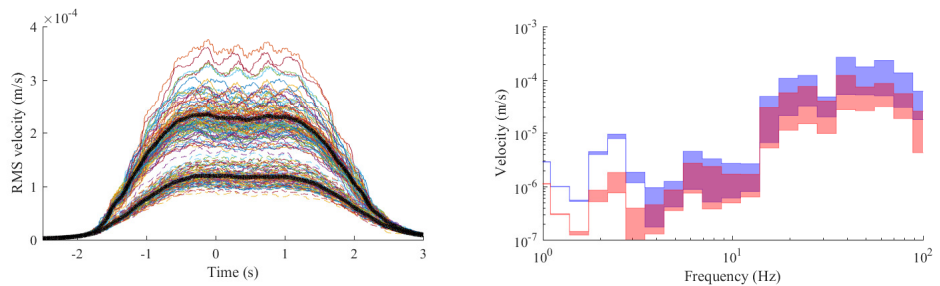


Figure 8: Left: Running RMS of the free-field velocity at 10 m and 18 m from the track for 100 rail profile samples, for a train speed $v = 60$ m/s. Thick black lines indicate ensemble average. Right: Max/min envelopes of velocity spectra in 1/3 octave bands at 10 m (blue) and 18 m (red).

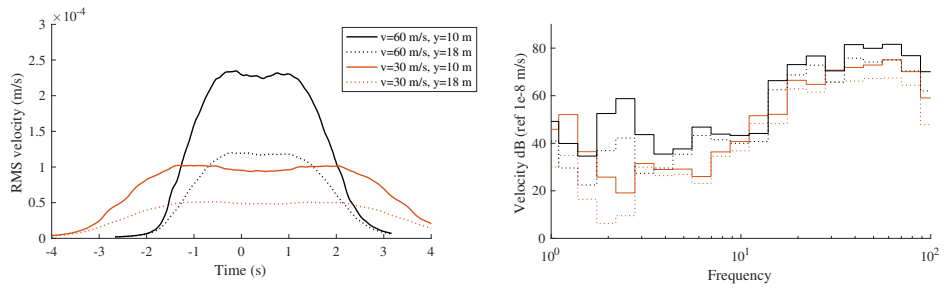


Figure 9: Left: Ensemble average of running RMS of the free-field velocity at 10 m and 18 m from the track, for train speeds $v = 30$ m/s and $v = 60$ m/s. Right: Ensemble average of velocity spectra in 1/3 octave bands at 10 m and 18 m.

3.2. Building model

The previously described calculation procedure is applied here to calculate the train-induced vibrations in two different buildings; a heavyweight concrete building and lightweight wooden building. The building models are adapted from [32]. Although the buildings are fictitious, the structural members were chosen to fulfill the static design criteria in accordance with the European structural design codes (Eurocode) to provide realistic resonance frequencies. The geometry and FE mesh of both buildings are identical and shown in Figure 10. The building, founded on surface footings, consists of two frames with slabs. In the heavyweight building, both frames and slabs are of concrete, whereas for the lightweight building, the frames are composed of glued laminated timber (glulam) beams and columns and the slabs are of cross-laminated timber (CLT). The wood material was modeled as orthotropic, with stiffness parameters Young's moduli E_i and shear moduli G_{ij} , and Poisson's ratios ν_{ij} , where the subindices refer to the longitudinal (1), transverse (2) and radial (3) directions. Material properties and structural member dimensions are specified for both buildings in Table 3 and Table 4, respectively.

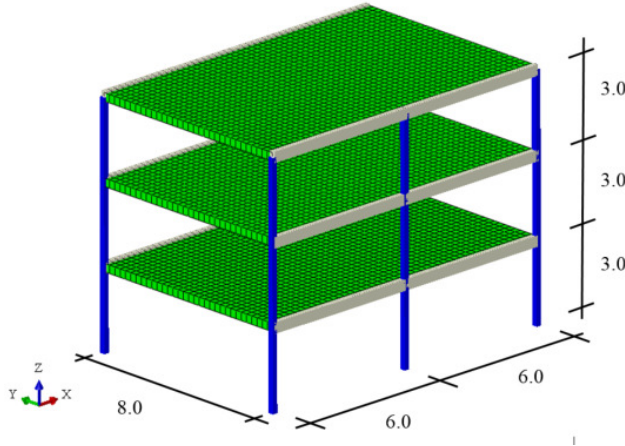


Figure 10: FE mesh used for both building types.

The FE models of the buildings were created in Abaqus [35], assuming linear-elastic material models. For the CLT slabs, a composite layup of 7 layers in a cross-wise pattern was assumed, with the two outermost layers on both sides of the slab positioned to provide a high stiffness in the Y -direction. The frames are modeled using 2-node linear beam elements, denoted B31 in Abaqus, whereas the slabs are modeled by 4-node shell elements with reduced integration, denoted S4R. An element size of 0.25 m is used throughout the model. The total mass of the lightweight and heavyweight buildings are 42 500 kg and 235 700 kg respectively. In Figure 11 and Figure 12 a selection of eigen-mode shapes are presented for the two buildings. The presented mode shapes include the fundamental slab modes. The fundamental sway/torsion modes of both buildings are in the frequency range 1–5 Hz, but are not presented due to their diminishing contribution to the the vertical vibration of the slabs.

Table 3: Building material properties [32].

Concrete	Density (kg/m^3)	2500
	Young's modulus E (GPa)	32
	Poisson ratio ν	0.2
	Loss factor $\eta = 2\zeta$ (-)	0.04
Wood	Density (kg/m^3)	500
	E_1 (MPa)	8500
	E_2 (MPa)	350
	E_3 (MPa)	350
	ν_{12}	0.2
	ν_{13}	0.2
	ν_{23}	0.3
	G_{12} (MPa)	700
	G_{13} (MPa)	700
	G_{23} (MPa)	50
	Loss factor $\eta = 2\zeta$ (-)	0.06

Table 4: Structural member dimensions.

Member	Heavyweight building	Lightweight building
Column	$0.2 \times 0.2 \text{ m}^2$	$0.16 \times 0.16 \text{ m}^2$
Beam	$0.2 \times 0.4 \text{ m}^2$	$0.115 \times 0.36 \text{ m}^2$
Slab	$t = 0.3 \text{ m}$	$t = 0.28 \text{ m}$ (7 layers)

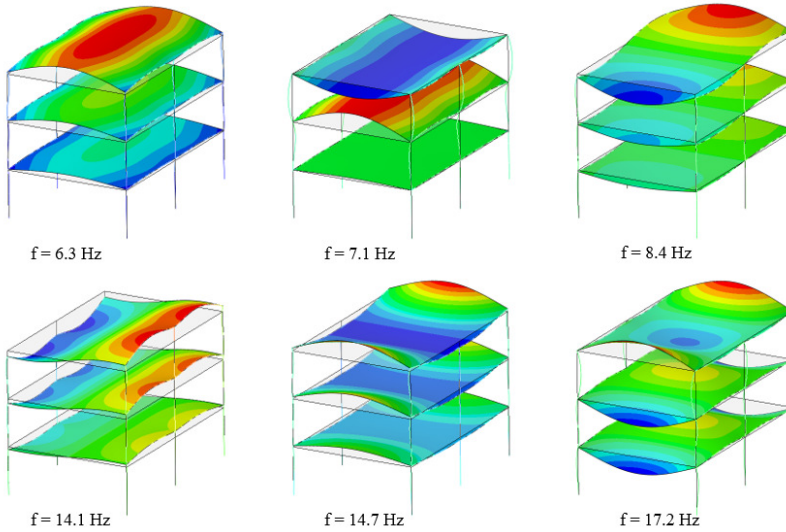


Figure 11: Mode shapes for the isotropic heavyweight building.

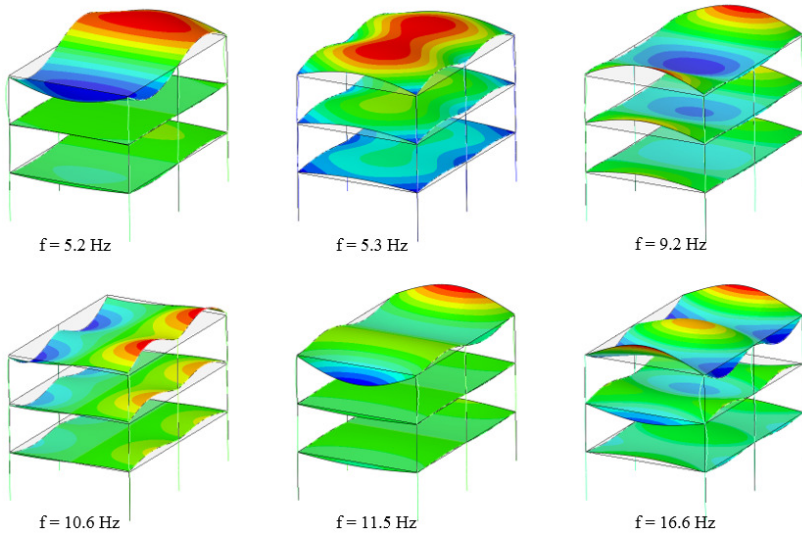


Figure 12: Mode shapes for the orthotropic lightweight building.

The mass and stiffness matrices of the buildings, \mathbf{M}_b and \mathbf{K}_b , respectively, were exported from Abaqus and imported into Matlab for integration in the computational model. For a given frequency ω , the dynamic stiffness of the building is calculated as

$$\mathbf{D}_b(\omega) = -\omega^2 \mathbf{M}_b + (1 + i\eta) \mathbf{K}_b. \quad (18)$$

In the present case, footings with a surface area $2.0 \times 2.0 \text{ m}^2$ were assumed. The dynamic stiffness of the footings, $\tilde{\mathbf{Z}}(\omega)$, calculated as described in Section 2.3 using a discretization of 8×8 elements per footing, was then added to the building dynamic stiffness in accordance with Eq. (16). As discussed in Section 3.1, for a moving vehicle a single excitation frequency due to a discrete rail unevenness wavelength excites a range of frequencies for a fixed point on the ground. For each discrete rail unevenness wavelength, i.e. for each excitation frequency, the building response due to a unit load on the rail is calculated by applying Eq. (16) for each response frequency. The total building response due to a passing train is then obtained by superposition to account for 1) all the train axle loads calculated from Eq. (13) and 2) all the rail unevenness wavelengths included in the artificial rail profile. This allows for efficient evaluation of many different rail profiles and potentially various train configurations. If only one or a few rail profiles were to be evaluated, it would be more efficient to first calculate the total ground response from all the discrete rail unevenness wavelengths and dynamic axle loads, and then apply Eq. (16).

The building is oriented along the track such that the footings are located at $y = 10 \text{ m}$ and $y = 18 \text{ m}$ from the track. The building response is calculated for each of the 100 rail profile samples for which the free-field response was presented in the previous sub-section. The response, in terms of vertical vibration, is calculated in 5×5 evenly distributed points per floor, as indicated in Figure 13.

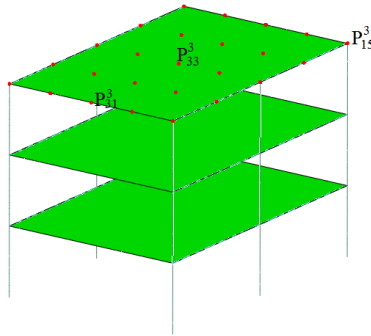


Figure 13: Output points for the roof marked by red dots. The naming convention is illustrated for a few points. The super-index indicates floor level, and the sub-index indicates row (along X) and column (along Y).

The building response varies strongly between different rail profile samples, much like the free-field response. Furthermore, a comparison between the vertical response levels in different locations within a floor for a particular rail profile sample also shows significant variation, because of the buildings' eigen-mode shapes, as can be seen in Figure 14 where the time-history response of three different points of the roof of the lightweight building is shown for one rail profile sample.

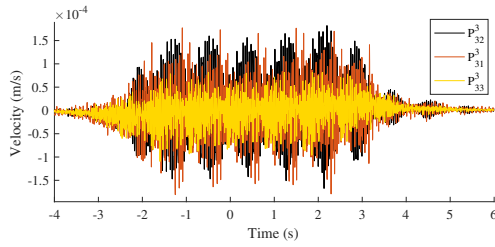


Figure 14: Vertical velocity in three points of the roof of the lightweight building, due to a train passing at $v = 30$ m/s.

To compare the vibration levels between floors and between the two buildings, a floor vibration value is calculated. For each output point on a floor, an ensemble mean spectrum is calculated by averaging the spectra from the different rail profiles, and an average floor spectrum is then calculated by averaging these ensemble mean spectra over the output points.

Figure 15 shows the floor average of the vertical RMS velocity, and the floor average velocity spectrum in 1/3 octave bands, for a train speed of $v = 30$ m/s. The corresponding results for the train speed $v = 60$ m/s are shown in Figure 16.

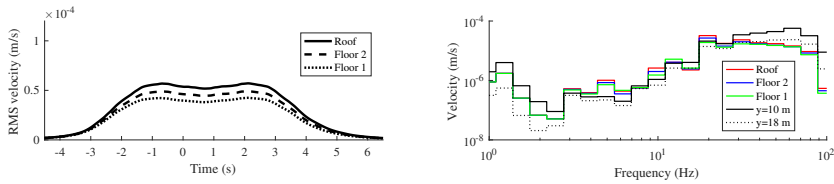


Figure 15: Average floor RMS velocity (left) and 1/3 octave band spectra (right) for the lightweight building, for a train speed $v = 30$ m/s.

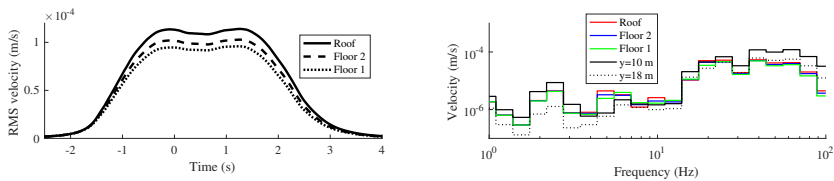


Figure 16: Average floor RMS velocity (left) and 1/3 octave band spectra (right) for the lightweight building, for a train speed $v = 60$ m/s.

Figure 19 shows a comparison between the average floor responses between the lightweight and the heavy-weight building for a train passage at $v = 60$ m/s. The responses are very similar, with a slightly higher RMS observed for the lightweight building. In terms of the 1/3 octave band spectra, the heavyweight building displays a higher response around the frequencies of its fundamental slab modes (6–8 Hz) and also in the frequency bands 11–18 Hz. Although not presented here, the same trends are seen for the lower train velocity.

For both building types, analyses have shown that the soil has a strong attenuating effect on the building

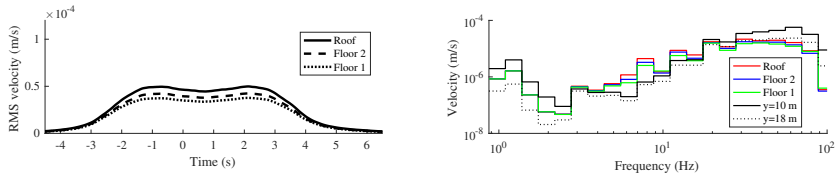


Figure 17: Average floor RMS velocity (left) and 1/3 octave band spectra (right) for the heavyweight building, for a train speed $v = 30$ m/s.

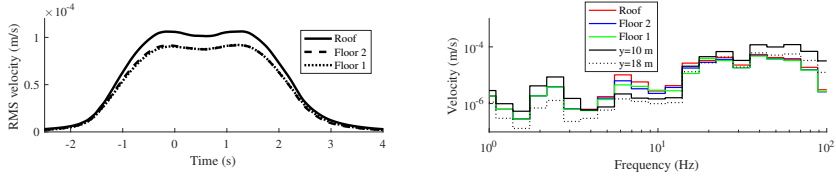


Figure 18: Average floor RMS velocity (left) and 1/3 octave band spectra (right) for the heavyweight building, for a train speed $v = 60$ m/s.

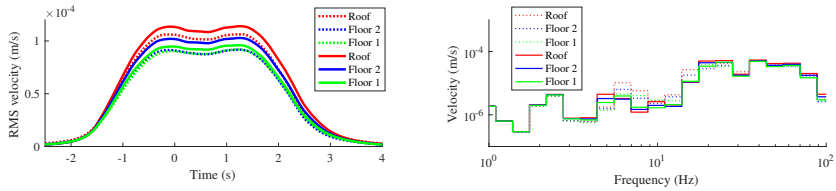


Figure 19: Average floor RMS velocity (left) and 1/3 octave band spectra (right) for a train speed $v = 60$ m/s. Solid lines: Lightweight building. Dotted lines: Heavyweight building.

response. This has previously been concluded by Lopes et al [23] who studied building response due to an underground train. Figure 20 shows a comparison of the response for the lightweight building, when disregarding the soil dynamic stiffness, and instead exciting the building supports directly with a prescribed motion identical to the incident wave field, for the case with $v = 30$ m/s. Including the soil effects significantly reduces the slab response for frequencies over 20 Hz.

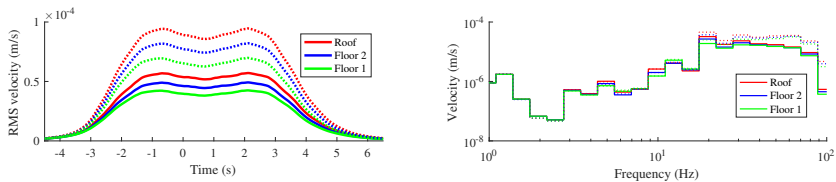


Figure 20: Average floor RMS velocity (left) and 1/3 octave band spectra (right) for the lightweight building, for a train speed $v = 30$ m/s. Solid lines: With SSI. Dotted lines: Without SSI.

4. Discussion

In the paper, the slab vertical vibration levels due to a passing train, were calculated for a lightweight (wooden) and a heavyweight (concrete) building using numerical simulations. The simulation strategy, based on a sub-structuring technique, involves calculating the dynamic contact forces between the train wheels and the rail due to an uneven rail profile, and applying these forces to a 2.5D track–ground model to establish the free-field ground motion. This free-field ground motion, i.e. the so-called incident wave field, is applied to the base of a FE building model accounting for the soil dynamic stiffness and through-soil coupling between individual footings. Referring to Figure 1, the most computationally demanding parts are Step 1 (to calculate the free-field displacements and track receptance using the 2.5D model), and Step 3 (to calculate the soil dynamic stiffness of the footings). However, since both these steps involve looping over a range of (uncoupled) wavenumbers, using parallel computing and exploiting the multi-core CPUs of standard desktop computers significantly reduces the computational time so that for both Step 1 and Step 3 the computational times for a single frequency are measured in seconds instead of minutes.

It was demonstrated that an increased train speed generally increased the vibrations levels in the free-field ground surface, and hence also in the buildings. The running RMS of the vertical velocity for the building slabs were found to be lower than in the free-field, i.e. the buildings were found to reduce the overall RMS vibration values. However, comparing the frequency spectra between the slabs and the free-field, a significant amplification of the response were found for the slabs in the frequency range around the fundamental slab bending modes. Furthermore, it was found that the soil–structure interaction had a reducing effect on the slab vibration levels for both the concrete building and the wooden building.

Noise levels were not evaluated in this paper. However, an acoustic evaluation could be appended to the calculation procedure presented herein. In many cases a weak coupling between the structural parts and the acoustic volume inside the building can be assumed [36, 37], i.e. it can be assumed that the structural vibrations are not affected by the acoustic pressure variations. The acoustic pressure would then be calculated with a (e.g. FE-) model of the acoustic medium, excited by the vibrations of the surrounding structural parts as calculated using the methodology presented in the paper. However, in early design stages the use of such detailed models may not be necessary or even meaningful. In [38], a velocity based structural vibration metric was suggested for predicting structure-borne noise in timber buildings. The vibration metric represented a spatial average of the normal-to-surface-direction velocities in the receiver room, which was found to have a high degree of correlation with a noise metric representing the spatial average of the sound pressure. Adopting such a vibration metric does not produce results of absolute noise levels in the building, but may be useful to qualitatively compare different design alternatives, with very low computational effort.

5. Conclusions

The following conclusions can be drawn for the studied case:

- Increased train speed increased the vibration in the free-field and in the adjacent building.

- The building slab vertical response, in terms of 1s running RMS velocity, was lower than the free-field ground response.
- Significant amplification of the slab response was observed, compared to the free-field response, in the frequency ranges around the fundamental slab bending modes. The amplification was higher for the heavy-weight concrete building.
- Similar vibration response, in terms of 1s running RMS velocity, for the lightweight wooden building and the heavyweight concrete building.
- Accounting for SSI effects lead to significantly reduced vibration response in the buildings for frequency bands over 20 Hz.

In terms of 1s running RMS velocity, a slightly higher response was observed for the lightweight building, whereas the heavyweight building provided higher response in the frequency bands between 6 and 20 Hz of the 1/3 octave band spectra. Hence, the results presented here suggests that a lightweight building does not necessarily perform worse than a heavyweight building in terms of vibration response when subjected to train-induced ground vibrations.

Acknowledgments

The authors gratefully acknowledge financial support from the Swedish Innovation Agency (Vinnova) under Grant No. 2018–04159.

References

- [1] L. Maclachlan, M. Ögren, E. van Kempen, L. Hussain-Alkhateeb, K. Persson Waye, Annoyance in response to vibrations from railways. *International journal of environmental research and public health* **15(9)**. p.1887, 2018.
- [2] R. Guski, D. Schreckenberg, R. Schuemer, WHO environmental noise guidelines for the European region: A systematic review on environmental noise and annoyance. *International journal of environmental research and public health* **14(12)**. p.1539, 2017.
- [3] L. Andersen, S.R.K. Nielsen, Reduction of ground vibration by means of barriers or soil improvement along a railway track. *Soil Dynamics and Earthquake Engineering* **25**. 701–716, 2005.
- [4] P. Galvin, A. Romero, J. Dominguez, Fully three-dimensional analysis of high-speed train-track-soil-structure dynamic interaction. *Journal of Sound and Vibration* **329**. 5147–5163, 2010.
- [5] D. Connolly, A. Giannopoulos, M.C. Forde, Numerical modelling of ground borne vibrations from high speed rail lines on embankments. *Soil Dynamics and Earthquake Engineering* **46**. 13–19, 2013.
- [6] G. Kouroussis, D.P. Connolly, G. Alexandrou, K. Vogiatzis, The effect of railway local irregularities on ground vibration. *Transportation Research Part D: Transport and Environment* **39**. 17–30, 2015.
- [7] X. Sheng, C.J.C. Jones, M. Petyt, Ground vibration generated by a harmonic load acting on a railway track. *Journal of Sound and Vibration* **225(1)**. 3–28, 1999.
- [8] X. Sheng, C.J.C. Jones, M. Petyt, Ground vibration generated by a load moving along a railway track. *Journal of Sound and Vibration*, **228(1)**. 129–156, 1999.
- [9] X. Sheng, C.J.C. Jones, D.J. Thompson, A theoretical model for ground vibration from trains generated by vertical track irregularities. *Journal of Sound and Vibration*, **272**. 937–965, 2004.
- [10] R. Wang, A simple orthonormalization method for stable and efficient computation of Green's functions *Bulletin of the Seismological Society of America*, **89(3)**. 733–741, 1999.
- [11] X. Sheng, C.J.C. Jones, D.J. Thompson, Prediction of ground vibration from trains using the wavenumber finite and boundary element methods. *Journal of Sound and Vibration*, **293**. 575–586, 2006.
- [12] G. Lombaert, G. Degrande, S. François, D.J. Thompson, Ground-borne vibration due to railway traffic: a review of excitation mechanisms, prediction methods and mitigation measures. *Noise and vibration mitigation for rail transportation systems*. 253–287, 2015.
- [13] G. Lombaert, G. Degrande, J. Kogut, S. François, The experimental validation of a numerical model for the prediction of railway induced vibrations. *Journal of Sound and Vibration*, **297**. 512–535, 2006.

- [14] G. Lombaert, G. Degrande, Ground-borne vibration due to static and dynamic axle loads of InterCity and high-speed trains. *Journal of Sound and Vibration*, **319**. 1036–1066, 2009.
- [15] L. Pyl, G. Degrande, D. Clouteau, Validation of a source-receiver model for road traffic induced vibrations in buildings. ii: receiver model. *Journal of Engineering Mechanics*, **130(12)**. 1394–1406, 2004.
- [16] P. Fiala, G. Degrande, F. Augusztinovicz, Numerical modelling of ground-borne noise and vibration in buildings due to surface rail traffic. *Journal of Sound and Vibration*, **301**. 718–738, 2007.
- [17] Y. Yang, H. Hung, A 2.5D finite-infinite element approach for modelling visco-elastic bodies subjected to moving loads. *International Journal for Numerical Methods in Engineering*, **51**. 1317–1336, 2001.
- [18] S. François, M. Schevenels, G. Lombaert, G. Degrande, A two-and-a-half dimensional displacement-based PML for elastodynamic wave propagation. *International Journal for Numerical Methods in Engineering*, **79**. 89–103, 2015.
- [19] D.P. Connolly, P. Galvín, B. Olivier, A. Romero, G. Kouroussis, A 2.5D time-frequency domain model for railway induced soil-building vibration due to railway defects. *Soil Dynamics and Earthquake Engineering*, **120**. 332–344, 2019.
- [20] D. López-Mendoza, A. Romero, D.P. Connolly, P. Galvín, Scoping assessment of building vibration induced by railway traffic. *Soil Dynamics and Earthquake Engineering*, **93**. 147–161, 2017.
- [21] P. Alves Costa, R. Caçada, A. Silva Cardoso, Track-ground vibrations induced by railway traffic: In-situ measurements and validation of a 2.5D FEM-BEM model. *Soil Dynamics and Earthquake Engineering*, **32**. 111–128, 2012.
- [22] P. Lopes, P. Alves Costa, M. Ferraz, R. Caçada, A. Silva Cardoso, Numerical modeling of vibrations induced by railway traffic in tunnels: From the source to the nearby buildings. *Soil Dynamics and Earthquake Engineering*, **61**. 269–285, 2014.
- [23] P. Lopes, P. Alves Costa, R. Caçada, A. Silva Cardoso, Influence of soil stiffness on building vibrations due to railway traffic in tunnels: Numerical study. *Computers and Geotechnics*, **61**. 277–291, 2014.
- [24] C. Bode, R. Hirschauer, S.A. Savidis, Soil-structure interaction in the time domain using halfspace Green's functions. *Soil Dynamics and Earthquake Engineering*, **22**. 283–295, 2002.
- [25] J. Malmberg, Numerical modeling of train-induced ground vibrations. Licentiate dissertation. Report TVSM-3080, Lund University, 2020.
- [26] S. François, M. Schevenels, P. Galvin, G. Lombaert, G. Degrande, A 2.5D coupled FE-BE methodology for the dynamic interaction between longitudinally invariant structures and a layered halfspace. *Computer Methods in Applied Mechanics and Engineering*, **199**. 1536–1548, 2010.

- [27] P. Galvin, S. François, M. Schevenels, E. Bongini, G. Degrande, G. Lombaert, A 2.5D coupled FE-BE model for the prediction of railway induced vibrations. *Soil Dynamics and Earthquake Engineering*, **30**. 1500–1512, 2010.
- [28] P. Alves Costa, R. Calçada, A. Silva Cardoso, Vibrations induced by railway traffic: influence of the mechanical properties of the train on the dynamic excitation mechanism. In: EURODDYN 2011, Leuven, Belgium, 2011.
- [29] A. Colaço, P. Alves Costa, P. Amado-Mendes, R. Calçada, Vibrations induced by railway traffic in buildings: Experimental validation of a sub-structuring methodology based on 2.5D FEM-MFS and 3D FEM. *Engineering Structures*, **240**. 112381, 2021.
- [30] E. Kausel, R.V. Whitman, J.P. Morray, F. Elsabee, The spring method for embedded foundations. *Nuclear Engineering and Design*, **48(2-3)**. 377–392, 1978.
- [31] E. Kausel, Advanced structural dynamics. *Cambridge University Press*, 2017.
- [32] R. Torndahl, T. Svensson, Methodology for analysis of traffic-induced building vibrations. Report TVSM-5000, Lund University, 2017.
- [33] Intel, Intel Fortran Compiler 19.0, Reference Manual, 2019.
- [34] Intel, Intel Math Kernel Library 2019, Reference Manual, 2019.
- [35] Dassault Systèmes SIMULIA. Abaqus 6.14.
- [36] L.V. Andersen, P.H. Kirkegaard, K.A. Dickow, N. Kiel, K. Persson, Influence of wall surface and air modelling in finite-element analysis of sound transmission between rooms in lightweight buildings. In *Noise Control and Acoustics Division Conference*, American Society of Mechanical Engineers, **45325**. 393–404, 2012.
- [37] O. Floden, A. Peplow, P. Persson, L. Mangliar, L.V. Andersen, Effect of modelling the air in rooms on the prediction of vibration transmission in cross-laminated timber buildings. In *8th International Conference on Structural Engineering, Mechanics and Computation (SEMC 2022)*.
- [38] O. Floden, P. Persson, Robust prediction metrics for structure-borne noise in timber buildings. In *50th International Congress and Exposition of Noise Control Engineering, INTER-NOISE 2021*, The Institute of Noise Control Engineering of the USA, Inc., 2021.
- [39] J. Lysmer, R. Kuhlemeyer, Finite dynamic model for infinite media. *Journal of the engineering mechanics division*, **95(4)**. 859–877, 1969.

Appendix

To show that the 2.5D model presented in Sections 2.1 and 3.1 provides reasonable results, comparisons are here made with a 3D FE model created with the commercial FE software Abaqus [35], for a stationary harmonic load on the track. The 3D FE model, shown in Figure 21, comprises a part of the track and the surrounding soil. The radius of the model is 30 m, and the soil is modeled to a depth of 10 m. The track and the soil was modeled using twenty node brick elements with reduced integration, denoted C3D20R, with an approximate maximum element length of 0.5 m. Symmetry boundary conditions were used around the XZ- and YZ-planes. At the fictitious boundaries, at the bottom and along the curved boundary of the model, so-called “infinite” elements denoted CIN3D12R were used, which for dynamic analyses implies that impedance boundary conditions with “tuned” dashpots [39], are inserted. The sleepers were not explicitly modeled, but were assumed rigid in the YZ-plane using kinematic couplings to tie the nodes on the top of the track. The sleeper mass was added using distributed mass elements. The rail was modeled using Timoshenko beam elements, denoted B31, with an element length of 0.2 m. The rail pads were modeled using springs at each beam node, with the same distributed properties as in the 2.5D model. Material properties of the soil and the track are presented in Tables 1 and 2. Figure 22 shows a comparison of the rail point receptance calculated with the 2.5D model and the Abaqus model, showing good agreement. Figure 23 shows the rail displacement for an excitation frequency of $f = 40$ Hz, as obtained with both models. Further, the free-field vertical ground motion along a line 10 m from the track, is shown for both models in Figure 24. Good agreement between the models are observed both concerning the rail and free-field ground displacements.

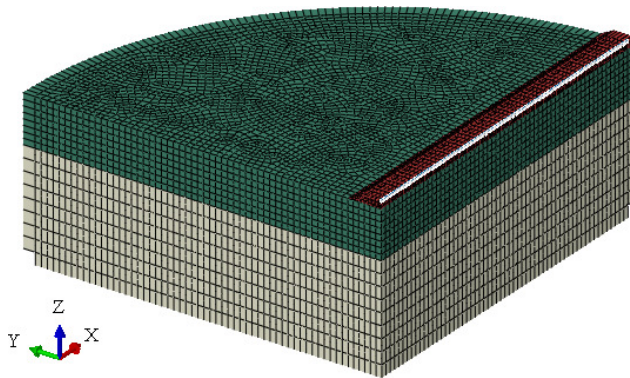


Figure 21: Abaqus model used for verification of 2.5D model response for a stationary load.

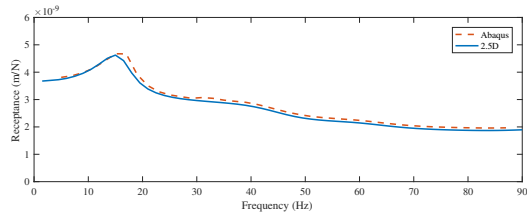


Figure 22: Rail point receptance. Displacement to a unit load on the rails (0.5 N per rail).

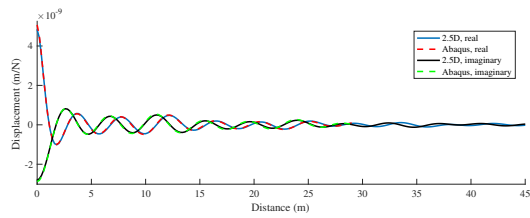


Figure 23: Displacement along rail for a loading frequency $f = 40$ Hz.

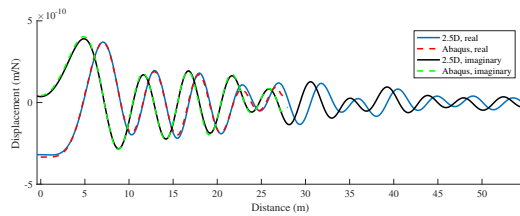


Figure 24: Free-field ground motion 10 meters from the track, for a loading frequency $f = 40$ Hz.

Paper F



Numerical modelling applied to wave-propagation analysis for arbitrary frequency and layer depths within infinite elastic media

Andrew Peplow, Jens Malmborg, Peter Persson

Engineering Acoustics and Structural Mechanics, Department of Construction Sciences, Lund University, P.O. Box 118, SE-221 00 Lund, Sweden

Abstract

There are well-known methods for deriving natural frequencies and mode shapes of displacement for layered elastic media of finite depth which have classical stress-free or rigid boundary conditions. There are also methods for the more complex problem with particular boundary conditions, such as several finite layers resting on a halfspace. However, these expressions permit the evaluation of only the first few modes. Surprisingly, then, there is not a method which has determined the natural frequencies and mode shapes for all frequencies and layer depths. This paper describes a new method to achieve this, by writing the dynamic stiffness matrices of attached layers strategically. The main advantages of this strategy to the modeller include arbitrary frequency, depth and number of layer strata over an elastic halfspace. Naturally, there are limitations with computational accuracy and capacity but for a general study of free or forced vibration this methodology is straightforward to program and to compute relevant response outputs. Computation of wavenumber dispersion diagrams, phase velocity plots and response data in the frequency and time-domains are presented here to highlight the methodology for two case-studies in earthquake assessments for plane-strain and axisymmetry. Numerical evidence of a layer resonance due to the presence of a ZGV (zero group velocity) mode phenomena via a case-study for a ground profile where layers are hundreds of metres in depth, with solutions both in the frequency and time-domains illuminating this special case. The framework is especially favorable for engineers and modellers solving problems with application to ground vibration and seismic problems under small strains.

Keywords: Wave propagation, linear-elastic material, scaling, zero group velocity

Email address: andrew.peplow@construction.lth.se (Andrew Peplow, Jens Malmborg, Peter Persson)

Contents

1	Introduction	4
2	Computational model	7
2.1	Two-dimensional models	7
2.2	Free vibration	12
2.3	Forced vibration	13
2.4	Numerical evaluation of the dynamic stiffness matrix	14
2.5	Root finding	15
3	Numerical examples	17
3.1	Free vibration - Dispersion relations	17
3.1.1	Verification of model, Strobbia (2003): Example 1.	18
3.1.2	Verification against orthonormalisation technique, Latur earthquake: Example 2.	19
3.2	Modal evaluation, Latur earthquake: Example 2.	21
3.3	Forced vibration - frequency domain, Latur earthquake, Example 2.	21
3.4	Forced vibration - time domain, Latur earthquake, Example 2.	24
4	Conclusions	27

List of Tables

1	Material properties for Example 1 referenced in Kumar and Naskar (2017).	18
2	Material properties for Example 2, referenced in Wang (1999).	19

List of Figures

1	A layered halfspace model geometry. The parameters of the model are shear and pressure wave velocities C_s , C_p respectively, mass density ρ and layer thickness, h_i	7
2	A comparison between the dispersion phase velocity curves calculated by the present method, solid colored lines, with Kumar and Naskar (2017), (\circ) and Kausel and Roesset (1981), (\square). The ground profile comprises four layers of depth 4.0 km each situated over an elastic halfspace, Table 1, referenced as Profile C in Kumar & Naskar, Kumar and Naskar (2017).	19

3	Dispersion curves of the present method for ground profile, Table 2 in Wang (1999) where \rightarrow indicates a ZGV (zero group velocity) location and the circles, \bullet , indicate frequencies (28.5 Hz and 38.8 Hz) and wavenumbers where modal shapes are displayed for each, see Fig.4.	20
4	Modes evaluated two frequency related to Latur earthquake ground-profile, Table 2. All modes are real-valued evaluated at (a) $f = 28.5$ Hz (b) 38.8 Hz., see Fig. 3.	22
5	Radial and vertical displacement amplitude at five receiver postions 5, 10, 20, 40 and 60 m from centre of disk-load. Ground profile represented in Table 2.	23
6	A Ricker-wavelet time-profile, which applies to a uniform pressure over a rigid disk in Example 2.	25
7	For a Ricker-wavelet load over a rigid disk, responses at 5, 10, 20, 40 and 60 m from centre of disk-load. Upper (a) and lower (b) solutions compared for two ground-profiles.	26

1. Introduction

The main aim in the paper is the study of elastic waveguide propagation from a rigid strip-load or rigid disk-load at the surface of a two-dimensional or axisymmetric three-dimensional layered semi-infinite space without the need to perform necessary subdivisions of layers due to their increased depth.

The ground is modelled as a soil profile which consists of multiple elastic, homogeneous, isotropic layers. This problem has seen much activity in the past but this formulation contains a novel approach to determine a dynamic stiffness matrix. What is new, but comparable to previous studies in this area, is the computation of natural modes of free vibration for very deep strata which may be computed easily and used for further physical analysis. These are usually used to help explain a forced response calculation due to harmonic or seismic loads in the body of the ground whereas an example related to a harmonic rigid surface disk-load is presented. Since the formulation is related primarily to P-SV wavetypes we will drop most references pertaining to either the plane-strain or axisymmetric problems, where it is understood the formulations can be applied to both cases. At the end of the paper, a forced vibration result presented in terms of the time and frequency domains are presented for an axisymmetric problem.

Ground vibration literature contains a wealth of publications with much work on the natural propagating modes in a layer over a half-space. The case of a fluid layer over a higher-velocity fluid half-space is less complicated than the elastic wave problem, and was first investigated by Pekeris (1948), and is well-known as one of the first attempts into the study of wave propagation through layers which overly infinite domains. Although the domains lack shear wave coupling his thorough analysis showed that unattenuated propagation of sound would occur in a slower fluid-layer characterised by the minimisation of something called the group velocity. The group velocity basically indicates the speed at which the amplitude or envelope wave “groups” progresses in a medium. Importantly, if the group velocity is constant then the wave propagation is commonly called non-dispersive which means that all waves progress at the same speed. In layered media, where wave speeds vary between layers, group velocity is clearly non-constant and wave propagation analysis, although linear in nature is complicated to analyse.

Currently, elastic wave propagation analysis is usually performed via the Kausel and Roesset (1981) stiffness matrix method (SMM). This approach was devised based on the earlier transfer matrix method (TMM) proposed originally over 70 years ago by Thomson (1950) and later corrected and elaborated by Haskell (1953) and iterated further by Wang (1999) relatively re-

cently. Dunkin (1965) has also obtained the modal solutions by using the TMM. As was pointed out by Kausel and Roesset, the SMM has several advantages over the TMM approach: (i) the global stiffness matrix becomes symmetric in the SMM and as a result lesser storage is required and also fewer operations are required for executing the analysis, (ii) various loading profiles can be easily treated, and (iii) sub-structuring techniques become readily applicable. In these exact approaches, while forming the global stiffness matrix, the contribution of each layer is duly incorporated without making any approximation. However, while obtaining the solution, since the exact approach contains a number of hyperbolic and transcendental functions, the solution can be obtained only by trial and iterative procedure. In this work, we shall also employ the SMM approach for horizontal wavenumber searching.

This model considered here demonstrates the effect of a harmonic finite load over layered strata, Ewing (1957). The results derived by Fourier transform are valid for any frequency and importantly any depth of layer. In principle, following traditional methods, Jones and Petyt (1991), we could use displacement and stress–continuity boundary conditions at the bottom of the layer with equations at the ground surface to generate equations for four subsequent unknowns of stress and displacement. However, this direct approach leads to formidable numerical problems. The reason for this work is in part due to fundamental expressions for the characteristic wave functions, such as \cosh or \sinh , which, when employed, can have a dramatic effect on the numerical evaluation of solutions. Moreover problems can arise due to the cancellation or division of either very small or very large numbers, Kausel (2006). To overcome this Karasalo (1994) also derived a well–conditioned propagator matrix (TMM) for radially symmetric problems. In this work, though, we construct a single stiffness matrix (SMM) for the physical layer for plane–strain problems which conveniently avoids these difficulties. We therefore proceed in the establishment of an original global dynamic stiffness matrix using expressions that do not cause numerical problems. This approach has been successfully applied to Euler and Timoshenko beams, Gonçalves et al. (2018), Khasawneh and Segalman (2019) and Gonçalves et al. (2019).

Hence, a *scaled* dynamic stiffness matrix for an arbitrary thick layer is derived. To achieve this the vibration components in the wavenumber domain for the layer depths and the half–space are considered and arranged into a single matrix formulation. For a forced response calculation, where a load is modelled as an infinite rigid strip on the ground surface, so that the problem is plane–strain, the response may be calculated by an inverse Fourier transform. For an axisymmetric case where a rigid uniform disk loading is applied the vertical and radial responses can also

be calculated by an inverse double Fourier transform noting that for numerical purposes a single Hankel transform is computed in the axisymmetric case. Except for some small differences in a few entries in the matrices the 2D plane-strain and the 3D axisymmetric problems are almost identical. Nevertheless, the overall purpose of the present study is to present a computational method which does not suffer numerical evaluation difficulties when predicting vibration transmission, in particular its attenuation on the surface of a deep layer. The usefulness of the method is illustrated by presenting numerical results from potentially computationally intensive application examples.

This paper, which determines the free and forced solutions for wave-propagation problems, is organised as follows: in Section 2 we establish the scaled formulation of the problem for plane-strain and axisymmetric coordinates in the wavenumber domain which includes a brief reminder of the root finding methodology. This is then followed by a numerical example which establishes a verification of the free vibration formulation derived by previous researchers and in a second example we also determine the existence of zero group velocity modes related to a well-known example on an earthquake study. Section 3 includes frequency and time-domain simulations for a stationary rigid-disk load and Section 4 draws the article to a conclusion with some discussion.

2. Computational model

In this section the methodology related to free and forced vibration are formulated for plane-strain or axisymmetric cases.

2.1. Two-dimensional models

A generic model considered is shown in Figure 1. A strip-load has width $2b$, and is aligned with respect to the z -axis. It rests on an homogeneous, isotropic, elastic layer, with material properties E (Young's modulus), ρ (mass density) and ν (Poisson's ratio). An harmonic vertical rigidly supported load acts uniformly over a strip situated above elastic layers. The elastic layers of finite depth consist of homogeneous and isotropic material, overlying an infinite halfspace of flexible material. The model is two-dimensional, and the co-ordinate system and parameters are shown in Figure 1. Although two-dimensional, the methods used here cover plane-strain and axisymmetric cases. This figure shows a generalized example of a semi-infinite stratified soil profile with the linear elastic layers. For computation of theoretical dispersion curves corresponding to the assumed layer structure the problem is assumed plane-strain in the (x, z) plane. The x -axis is taken parallel to the layers, with the x -axis in the horizontal direction to surface wave propagation. The positive z -axis is directed downwards. To develop the axisymmetric model, we refer the reader to the book by Verruijt (2010) for inspiration.

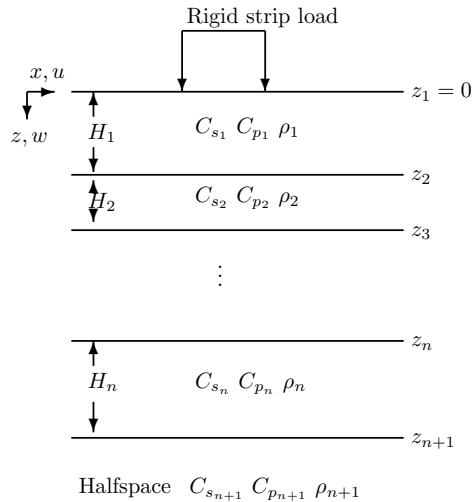


Figure 1: A layered halfspace model geometry. The parameters of the model are shear and pressure wave velocities C_s , C_p respectively, mass density ρ and layer thickness, h_i .

For plane-strain conditions much of the analysis necessary for the derivation of the dynamic stiffness matrix has been presented before in references Ewing (1957), Jones and Petyt (1991) and Jones and Petyt (1993), so this will only be briefly summarized. For small strains the behaviour of the elastic material is described by Navier's elastodynamic equations, Ewing (1957) and without loss of generality, in the absence of body forces, these equations apply to any layer and are written in vector form as follows:

$$(\lambda + \mu)\nabla(\nabla \cdot \mathbf{u}) + \mu\nabla^2\mathbf{u} = \rho\ddot{\mathbf{u}}, \quad (1)$$

where $(u) = (u, w)$ represent the components of the displacement in the x and z directions and λ , μ are the Lamé constants. For the free-vibration problem the boundary conditions for the layered problem are as follows; zero stresses at the surface, so on $z = 0$,

$$\sigma_{zz} = 0, \quad \sigma_{xz} = 0. \quad (2)$$

and continuity of displacement and stress at internal interfaces, with displacements decaying in the far-field, $u \& w \rightarrow 0$ as $z \rightarrow \infty$. The quantities C_p and C_s are respectively the pressure (P) and shear (S) wave speeds respectively, given by:

$$C_p^2 = \frac{\lambda + 2\mu}{\rho} = \frac{E(1 - \nu)}{\rho(1 + \nu)(1 - 2\nu)}, \quad C_s^2 = \frac{\mu}{\rho} = \frac{E}{2\rho(1 + \nu)}. \quad (3)$$

Note that the conditions are almost identical for an axisymmetric problem in (r, z) , but on the surface $\sigma_{zz} = -(P/\pi b^2)$ over a disk of radius b . For each layer, the displacement field can be obtained from potentials as:

$$\begin{aligned} u &= u(x, z, t) = \frac{\partial\Phi}{\partial x} + \frac{\partial\Psi}{\partial z}, \\ w &= w(x, z, t) = \frac{\partial\Phi}{\partial z} - \frac{\partial\Psi}{\partial x}, \end{aligned} \quad (4)$$

where the potentials $\Phi = \Phi(x, z, t)$ and $\Psi = \Psi(x, z, t)$ are the solutions of two-dimensional wave equations for each elastic layer,

$$C_p^2\nabla^2\Phi = \ddot{\Phi}, \quad \text{and} \quad C_s^2\nabla^2\Psi = \ddot{\Psi}. \quad (5)$$

For the sake of argument we assume a single-layer has depth $H > 0$ and the z -coordinate for the layer is locally specified, $0 \leq z \leq H$. In this region the corresponding stress fields $\sigma = [\sigma_{xz}, \sigma_{zz}]^T$

are subsequently obtained as:

$$\begin{aligned}\sigma_{xz} &= \tau = \mu \left(2 \frac{\partial^2 \Phi}{\partial x \partial z} + \frac{\partial^2 \Psi}{\partial z^2} - \frac{\partial^2 \Psi}{\partial x^2} \right), \\ \text{and} \\ \sigma_{zz} &= \sigma = \mu \left(\frac{C_p^2}{C_s^2} \frac{\partial^2 \Phi}{\partial z^2} + \left(\frac{C_p^2}{C_s^2} - 2 \right) \frac{\partial^2 \Psi}{\partial x^2} - 2 \frac{\partial^2 \Psi}{\partial x \partial z} \right).\end{aligned}\tag{6}$$

The pair of equations (5) are transformed into the Fourier domain, with respect to x , via the transform pair

$$\bar{f}(k) = \frac{1}{2\pi} \int_{-\infty}^{+\infty} f(x) e^{-ikx} dx, \quad f(x) = \int_{-\infty}^{+\infty} \bar{f}(k) e^{ikx} dk.\tag{7}$$

For the sake of completeness the Fourier transform pair in the case of radial symmetry are

$$\bar{f}(k) = \int_0^{+\infty} f(r) r J_0(kr) dr, \quad f(r) = \int_0^{+\infty} \bar{f}(k) k J_0(kr) dk.\tag{8}$$

This introduces the Fourier component k which is also commonly known as the *wavenumber* in the horizontal direction. Upon the transformation we obtain differential equations in the z - direction which now includes frequency ω and the wavenumber k as parameters. Much of the analysis of this problem is identical to the solution of similar problems, Jones and Petyt (1991, 1992) where a dynamic stiffness matrix $[\mathbf{T}]$ is derived, such that

$$\{\bar{\tau}\} = [\mathbf{T}] \{\bar{u}\},\tag{9}$$

where $\{\bar{\tau}\}$ are the transforms of the stress functions, \bar{u} are the transforms of the displacements. Note that it is common practice to write solutions to the subsequent homogeneous ordinary differential equations in terms of cosh and sinh functions. However, this choice of characteristic functions is not convenient for problems involving a spatial domain of arbitrary size. Hence, the general solutions in the Fourier domain may be written in the *scaled formulation*, after introducing wavenumber pairs $k_p = \omega/c_p$ and $k_s = \omega/c_s$.

$$\begin{aligned}\Phi(r, z, t) &= \left(A e^{-\alpha_1 z} + B e^{\alpha_1(z-H)} \right), \quad \alpha_1 = \sqrt{k^2 - k_p^2} \\ 0 < z < H \\ \Psi(r, z, t) &= \left(C e^{-\alpha_2 z} + D e^{\alpha_2(z-H)} \right), \quad \alpha_2 = \sqrt{k^2 - k_s^2}\end{aligned}\tag{10}$$

where the branch-cuts are chosen so that $\text{Re}(\alpha_{1,2}) \geq 0$. The reason for choosing the scaled exponential characteristic functions over hyperbolic functions is clear if you attempt to evaluate and manipulate these functions on a personal computer, as commented by Kausel in his compendium Kausel (2006), section 10.2.2. Basically, this choice of basis ensures the characteristic functions do not grow unbounded with layer depth, as $z \rightarrow H$, which would occur with unscaled elementary functions. Subsequently, it is evident the displacements (u, w) also will not grow unbounded with depth. Now, by inserting the scaled *ansatz* into the equations (4) this yields the element displacements on the upper and lower interfaces respectively for layer (e, i)

$$\{\bar{u}_{(e,i)}\} = [\mathbf{C}] \{A\}. \quad (11)$$

where $\bar{u}_{(e,i)} = [\bar{i}w_i, \bar{u}_i, \bar{i}w_{i+1}, \bar{u}_{i+1}]^T$ and the 4×4 complex-valued matrix $[\mathbf{C}]$ is given by

$$[\mathbf{C}] = \begin{bmatrix} -i\alpha_1 & i\alpha_1 e^{-\alpha_1 H} & -k & -k e^{-\alpha_2 H} \\ ik & i k e^{-\alpha_1 H} & \alpha_2 & -\alpha_2 e^{-\alpha_2 H} \\ -i\alpha_1 e^{-\alpha_1 H} & i\alpha_1 & -k e^{-\alpha_2 H} & -k \\ i k e^{-\alpha_1 H} & ik & \alpha_2 e^{-\alpha_2 H} & -\alpha_2 \end{bmatrix}. \quad (12)$$

To derive a dynamic stiffness matrix for element (e, i) we need the transformed stress equations which can be developed by equation (6),

$$\{\bar{\sigma}\}_{(e,i)} = [\mathbf{S}] \{A\}, \quad (13)$$

where $\bar{\sigma}_{(e,i)} = [-i\bar{\sigma}_i, -\bar{\tau}_i, i\bar{\sigma}_{i+1}, \bar{\tau}_{i+1}]^T$ and

$$[\mathbf{S}] = \begin{bmatrix} -i\alpha_1^2 (\lambda + 2\mu) + i\lambda k^2 & (-i\alpha_1^2 (\lambda + 2\mu) + i\lambda k^2) g_1 & -2\mu k \alpha_2 & 2\mu k \alpha_2 k g_2 \\ 2i\mu k \alpha_1 & -2i\mu k \alpha_1 k g_1 & \mu (\alpha_2^2 + k^2) & \mu (\alpha_2^2 + k^2) g_2 \\ i (\alpha_1^2 (\lambda + 2\mu) - \lambda k^2) g_1 & i (\alpha_1^2 (\lambda + 2\mu) - \lambda k^2) & 2\mu k \alpha_2 g_2 & -2\mu k \alpha_2 \\ -2i\mu k \alpha_1 g_1 & 2i\mu k \alpha_1 & -\mu (\alpha_2^2 + k^2) g_2 & -\mu (\alpha_2^2 + k^2) \end{bmatrix} \quad (14)$$

with the decaying functions $g_i = e^{-\alpha_i H}$, $i = 1, 2$. We are now in a position to combine equations (11) and (13), to obtain at a single matrix formulation which expresses the displacements and stresses at the interfaces. The general dynamic stiffness matrix, for any global domain thus

$2n \times 2n$ matrix, but remembering the matrix is transcendental in wavenumber, k . The right-hand side now only involves transformed stresses at the ground surface, since the neighbouring interface values have cancelled each other as discussed earlier,

$$[\mathbf{K}]_G \{\bar{u}\}_G = \{\bar{\tau}\}_G. \quad (19)$$

Kausel and Roesset previously presented the alternative formulation from a transfer-matrix approach using stiffness matrices which are similar to those frequently used in discrete structural dynamics multi-dimensional models. An element stiffness matrix, $[\mathbf{K}_i]$ is obtained for each layer in the geodynamic model. This matrix, for a distinct layer, relates the stresses at the upper and lower interfaces of the layer to the corresponding displacements. For a multi-layered model, the system stiffness matrices could then be used, with the prescribed load vectors, to solve for the displacements with techniques analogous to the standard finite element method. Given a prescribed load on the surface – Equation (2) is no longer zero – the transformed stress $\{\bar{\tau}\}_G$ is non-zero hence the matrix equation (19) may be solved for each wavenumber k relevant quadrature for either equations (7) or (8).

Apart from a slight change in the transformed values for the displacements, identical expressions are obtained in the axisymmetric P-SV case. Hence it is straightforward to compute plane-strain propagating and axisymmetric P-SV propagating modes in the free-vibration case.

2.2. Free vibration

To consider free vibration for the layered halfspace problem the right-hand side of equation (19) is zero, and hence we have the following expression,

$$[\mathbf{K}]_G \{\bar{u}\}_G = 0 \quad (20)$$

where the matrix has been defined above, see equation (18) and the unknowns are the displacements on interfaces. Non-trivial solutions of equation (20) are found by equating the determinant of the matrix to zero. The non-zero solutions or eigenvectors of this solution give, indirectly through equations (4) and (10), the actual (real-valued) u and w displacements representing the propagating modes through a vertical cross-section.

For calculations where the response of a layered half-space to a surface loading, the transformed loads in the plane-strain and axisymmetric P-SV are not identical nor are the inverse transforms

which need to be evaluated.

2.3. Forced vibration

In the plane–strain case, the transformed load on the surface is represented as a traction. In both cases of plane–strain and axisymmetry, responses at points on the surface of the ground can be recovered by employing suitable quadrature to the products of the displacements in the wavenumber domain and the transform kernel. The solution of the system of equations (19) yields the transformed displacements $\bar{u}(k, z, \omega)$ at the surface and hence by suitable inverse transformations solutions can be obtained. The response in the space–frequency domain is obtained by an inverse transformation from the wavenumber to the spatial domain as outlined in Verruijt (2010), where

$$\sigma_{zz} = \begin{cases} -\frac{P}{\pi b^2} e^{i\omega t}, & |r| < b, \\ 0, & \text{elsewhere.} \end{cases} \quad (21)$$

$$\sigma_{rz} = 0. \quad (22)$$

2.4. Numerical evaluation of the dynamic stiffness matrix

Generally, for non-dimensional wavenumbers $k_s h \geq 36$, where k_s is the shear wavenumber, the conventional approach "breaks down". That is, for depths greater than around six shear wavelengths, $h \geq 6\lambda_s$ a numerical bottleneck problem arises when solving the linear system of algebraic equations. Equally for high frequency computations can become ill-conditioned. Note that we cannot show results where "bottleneck" occurs, or is about to occur, as matrix entries become unbounded so solutions are not presentable.

As an alternative to the global coordinate system, a set of local coordinate systems are introduced to characterize the vibration within the layered media with the intention of avoiding the bottleneck problems, Kausel (2006). This choice of projected method permits a stable numerical evaluation for entries in the stiffness matrix. This avoids numerical round-off errors especially division of large numbers by small numbers and the subtraction of very large numbers. For example due to round-off errors it can be shown that the relative error for the evaluation of the difference between functions, such as $|\cosh(s_1) - \cosh(s_2)|$ can grow like $\exp(|s|)$, $s_1 < s < s_2$ where the difference $|s_1 - s_2|$ is small. In themselves the numerical evaluation of hyperbolic functions \cosh and \sinh can also be problematic for large values of their arguments.

Now, each of the entries in the stiffness matrix $[\mathbf{K}_G]$ are nonlinear functions with respect to the spatial wavenumber k , and hence the overall problem is a multi-dimensional nonlinear root finding exercise. We shall not study any deeper into the function itself but focus on finding the roots. So, on this basis the method described below is used to find the singular eigenvalues or equivalently the roots of the determinant, $\det[\mathbf{K}_G]$. This is a standard method which provides the solution for the natural frequencies of the system which correspond to a given real wavenumber and also as a consequence the phase-velocity for any propagating mode.

2.5. Root finding

A root finding routine has been implemented using the complex-plane winding number integral to check for the number of real roots. Using the roots of the characteristic equations the wave propagation wavenumbers and the modes - which carry the energy - can be determined easily from.

Many methods exist which are capable of finding roots or zeroes of nonlinear functions in one or many variables. The root-finding algorithm presented in this work is based on the procedure developed by Ivansson and Karasalo (1992). These routines for root-finding in the complex plane are based upon the use of the complex argument principle. Consider a function $f(z)$ that is analytic, without any poles, within a simple, closed, positively oriented contour Γ that lies on the complex plane. Let N be the number of complex roots of $f(z)$ within Γ . Then, the winding number argument principle states that

$$\frac{1}{2\pi i} \int_{\Gamma} \frac{f'(z)}{f(z)} dz = N.$$

With this arrangement the winding integral gives the **number** of complex roots (which of course can include the real roots we seek in our case) within a closed contour. This is an important stepping stone towards finding all the real wavenumber (roots) for a given frequency. The first step in the numerical root finding routine is to define the contour, Γ . Any simple closed contour can be chosen, where circular disks are the most common, and these were used in the current work. Since we are interested in determining only the real-valued roots (for zero damping) of the function we divided the wavenumber real-axis into a number of intervals and ensured each disk did not overlap but enveloped the integration path adequately. Due to parameterization it is a straightforward task to modify the contour in the complex-plane to an integration over $(0, 2\pi)$. In this work a Gauss-Quadrature scheme was used in evaluating the integrals numerically. Any scheme could be employed but this scheme provided adequate accuracy against speed. Once the number of roots and the disks, which included a root, were determined, a numerical nonlinear solver (Secant method) was employed to further isolate the roots to a desired accuracy. The strategy employed is similar to the approach by Ivansson and Karasalo (1993), by which large disks are chosen in a coarse division.

Although it is possible to find the roots of the dispersion equation at each frequency separately, we found it more effective and robust to trace any dispersion curves by a parametric continuation

approach. This is only effective where each frequency corresponds to a single root. As we shall see later any folds in a branch encountered can lead to non-uniqueness of solutions. A forward approach, then is the only suitable procedure where folds in dispersion curves may be encountered. This method simply used extrapolation from previous roots, in frequency, as starting values for new solutions of the set of equations. Convergence and speed-time improved dramatically using this approach. But clearly an initial set of solutions was necessary to initiate the continuation scheme. The number of wavenumbers were determined for the highest frequency of interest, then frequency was reduced by a suitable frequency-step using previous root as initial estimates and seeking a root along a tangent or quadratic arc. However, this approach, although extremely fast, does have it's own shortcomings, which we will see in a later section.

3. Numerical examples

All surface waves, except Rayleigh waves on an isotropic half-space, exhibit dispersion, with the apparent velocity along the surface depending on frequency. Almost any seismic source excites waves that comprise a continuous spectrum of frequencies, each harmonic component having a velocity, $c(\omega)$, that is called the phase velocity. If a monochromatic wave were somehow excited, only the phase velocity for that frequency would be needed to characterize the disturbance fully. However, when a spectrum of frequencies exists, the wave disturbances interfere, producing constructive and destructive patterns that influence the total ground motion. Constructive interference patterns behave as wave packets, which themselves propagate as disturbances along the surface with well-defined group velocities, $U(\omega)$. Thus, the phase velocity is directly controlled by the medium parameters (scale lengths of layering, intrinsic P and/or S velocities, rigidity, etc.) and the geometric “fit” of a particular harmonic component into the associated boundary conditions, as seen in the last section. The group velocity depends on the medium parameters through their influence on the phase velocity, but it also depends on the variation of phase velocity with frequency, which controls the interference between different harmonics. The group velocity is very important in that energy propagates mainly in the constructively interfering wave packets, which move with the group velocity rather than the individual phase velocities. The backward waves are guided waves with opposite phase and group velocities, in which the phase moves to the wave source. The history of their study, which spans more than a hundred years, starting with the pioneering work of Lamb in 1904, Lamb (1904). A backward-wave mode is indicated by a typical bend of the dispersion curve with a negative slope resulting in the negative group velocity of the corresponding guided wave. The physics of the problem where a negative group velocity is shown will not be discussed in detail but will be exemplified through the results of an example in both time and frequency domains taken from the literature.

The accuracy of the method through the examples is demonstrated via comparisons for a couple of scenarios. These are not benchmark solutions, as none such exist to the best of the author’s knowledge, but highlight the formulation with respect to increased computational speed. Soil characteristics values used are presented for two examples.

3.1. Free vibration - Dispersion relations

An application of the free vibration, Section 2.2, is to aid understanding of characteristics that show up for a forced response case. In this respect Figs. 2 & 3 show the principal results for the

Soil	Layer 1	Layer 2	Layer 3	Layer 4	Halfspace
Depth (km)	1.0	1.0	1.0	1.0	∞
E (Pa)	1.04×10^{11}	0.81×10^{11}	1.60×10^{11}	1.30×10^{11}	1.94×10^{11}
ρ (kgm^{-3})	2700	2500	3100	2900	3300
ν	0.33	0.33	0.33	0.33	0.33
C_r (ms^{-1})	3542	3262	4100	3821	4380
C_s (ms^{-1})	3800	3500	4400	4100	4700
C_p (ms^{-1})	7544	6948	8735	8140	9331

Table 1: Material properties for Example 1 referenced in Kumar and Naskar (2017).

ground-profiles, Tables 1 & 2. Verification of the method in the first and demonstration in the second figure of “unusual” ZGV behaviour mentioned above is presented. To show the accuracy and effectiveness of the proposed technique, we proceed to evaluate the phase velocity spectra and for the two ground profiles.

3.1.1. Verification of model, Strobbia (2003): Example 1.

A ground profile was chosen in the thesis by Strobbia (2003) which has been further evaluated by Kumar and Naskar (2017), Table 1 using various popular approaches. The ground profile is made up from four different layers each 1.0 km depth and a semi-infinite space, with the second and fourth softer layers sandwiched by stiffer layers. Generally the stiffness of the layer and mass density vary non-uniformly with depth and shear wavespeeds vary from $C_s = 2700$ m/s to $C_s = 4700$ m/s for the halfspace.

There is little physical information included in this referred example but the computations are quite extensive due to the depths of layers involved, the present method requiring inversions of a 10×10 matrices, hence this example was chosen for computational reasons. Figure 2 was produced by the root solver described in Section 2.5 and by digitization of the curves presented in Kumar & Naskar it was possible to reproduce the phase velocity curves presented.

To compare accuracy or computation times between Kumar & Naskar with Kausel methods is not available for this single example but working on an i5 processor 32MB RAM machine running MATLAB 2020A calculation software the tasks were clocked. Here wavespeed variation with frequencies, at 140 frequency steps, between 0 and 9 Hz, for the first nine natural modes were computed. Adopting the root finding method beginning at 9 Hz and ending at 0.1 Hz, the method adopted here took approximately 12.0 seconds to complete the 140 frequency step analysis. The half-space shear wavespeed is shown as a line across the graph, to show the limit of the solution. It is clear that all three methods agree well.

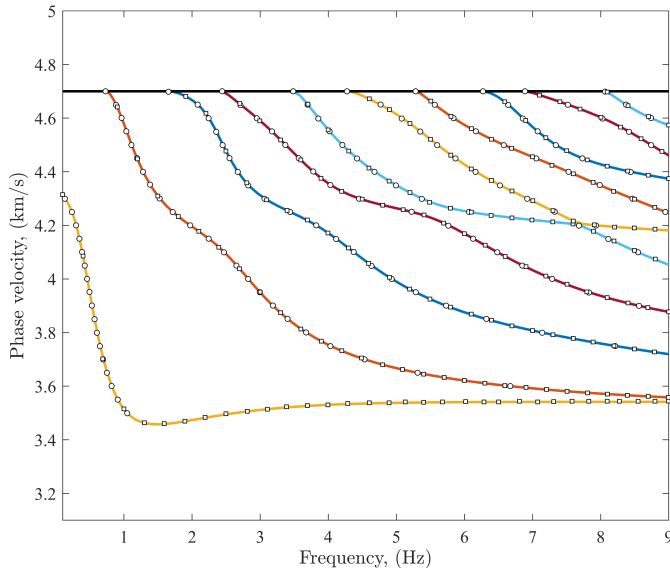


Figure 2: A comparison between the dispersion phase velocity curves calculated by the present method, solid colored lines, with Kumar and Naskar (2017), (\circ) and Kausel and Roesset (1981), (\square). The ground profile comprises four layers of depth 4.0 km each situated over an elastic halfspace, Table 1, referenced as Profile C in Kumar & Naskar, Kumar and Naskar (2017).

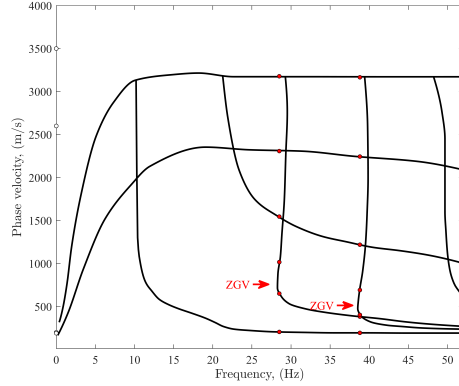
3.1.2. Verification against orthonormalisation technique, Latur earthquake: Example 2.

A ground model site, Table 2 used for synthetic seismograms observed as aftershocks of the Latur earthquake, 1993 has been evaluated in the paper Wang (1999). It consists, simply, of two layers overlying an elastic halfspace. Although Fig. 3 is a more conventional dispersion diagram for wavenumbers and phase velocities and suitable for physical interpretation, such as cut-on frequencies and Leaky modes, etc. Fig. 3(a) however does not feature characteristics which allow straightforward interpretation. Two modes have real wavespeeds or wavenumbers at all frequen-

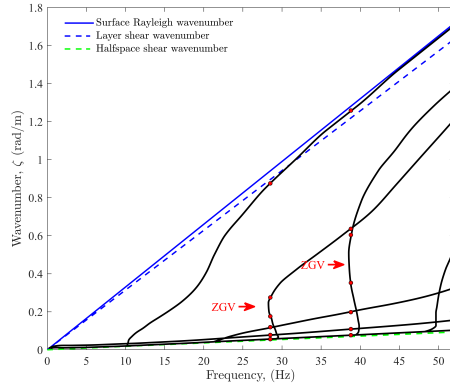
Soil	Layer 1	Layer 2	Halfspace
Depth (m)	5	300	∞
E (Pa)	1.55×10^8	4.22×10^{10}	8.22×10^{10}
ρ (kgm^{-3})	1300	2500	2700
ν	0.486	0.250	0.240
C_r (ms^{-1})	190	2392	3216
C_s (ms^{-1})	200	2600	3500
C_p (ms^{-1})	1200	4500	6000

Table 2: Material properties for Example 2, referenced in Wang (1999).

cies, but only one of which, we shall call the second mode, tends toward the Rayleigh wavespeed for the upper layer at low frequencies (190 m/s). At low frequencies or large wavelengths, the layer depth should become negligible and wavespeeds should tend towards the half-space Rayleigh wavespeed (which would exist without the two layers). At higher frequencies the modes do tend toward the upper-layer wavespeed as expected



(a) Phase velocity plotted against frequency for ground profile, Table 2. Zero Group velocity detected at 28.4 Hz and 38.7 Hz.



(b) Propagating wavenumber plotted against frequency for ground profile, Table 2. Zero Group velocity detected at 28.4 Hz and 38.7 Hz.

Figure 3: Dispersion curves of the present method for ground profile, Table 2 in Wang (1999) where \rightarrow indicates a ZGV (zero group velocity) location and the circles, \bullet , indicate frequencies (28.5 Hz and 38.8 Hz) and wavenumbers where modal shapes are displayed for each, see Fig.4.

It is well-known in the non-destructive inspection community that Lamb modes can possess backward-wave phenomena for certain values of Poisson's ratio or combinations of layer and substrate. A backward-wave mode is indicated by a typical bend of the dispersion curve with

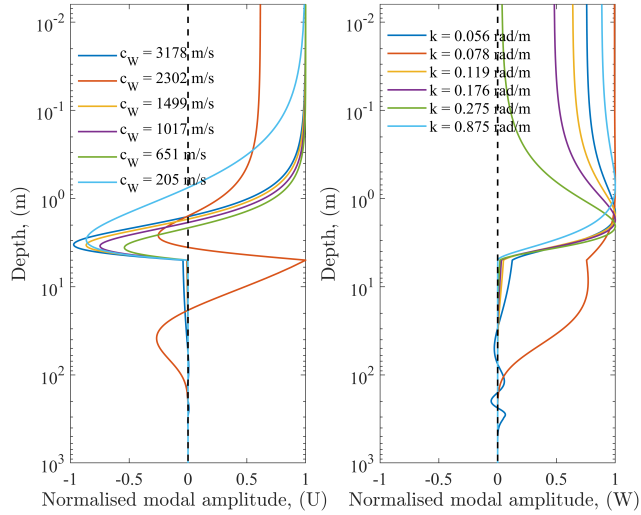
a negative slope resulting in the negative group velocity of the corresponding guided wave. At the minimum frequency of the backward-wave range, the group velocity becomes zero while the wavenumber remains nonzero; the corresponding wave is referred to as a ZGV mode, which occurs twice in the frequency range used here, Fig. 3(b). Besides the opposite phase movement, which detection is a rather challenging task, the backward wave is considered to manifest itself by a surface displacement resonance at the ZGV frequency. The red dots in Fig. 3 depict the positions at which the propagation modes are computed in the next section.

3.2. Modal evaluation, Latur earthquake: Example 2.

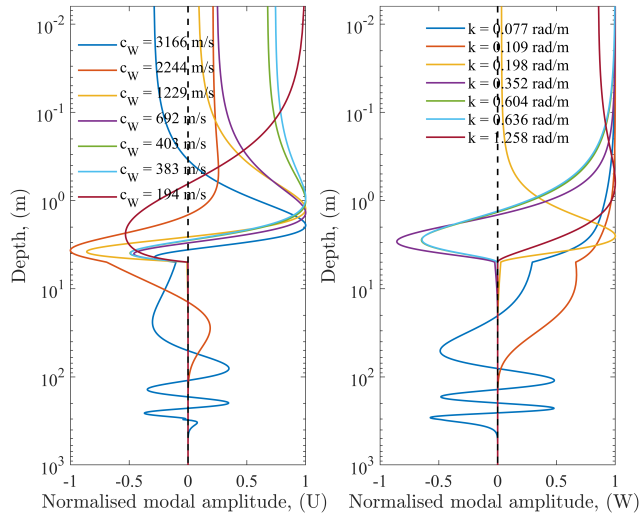
Figure 4 shows the variation of amplitude (to within an arbitrary amplitude factor) of the vertical and horizontal motion components of the first few modes, plotted against depth up to 1000 m into the ground at frequencies in the vicinity of the appearance of the zero group velocity (ZGV) mode. The depth scale is logarithmic which highlights the modal behaviour nearer the surface. The legends in this figure show the phase velocity and the wavenumber related to individual mode shapes. In Fig. 4(a) the variation of the radial mode (U) with depth, adjacent to the first ZGV frequency $f = 28.5$ Hz, shifts from maximum to minimum within the top 5 m layer then attenuates quickly to zero through the lower strata in the ground. At the surface it appears each modal wavetype can equally contribute to a surface vibration response, except at the *second* mode $c_W = 2302$ m/s, $k = 0.078$ rad/m where it appears contrary this second mode dominates in carrying the vertical surface wave energy for vertical mode shapes (W). At this frequency mode shapes in the vicinity of the ZGV turning point were not remarkably different to other modes corresponding to other waves. At the second ZGV turning point mode shapes were evaluated at an adjacent frequency, 38.8 Hz, Fig. 4(b). Contributors to potential surface waves are evenly distributed through the lowest phase velocity modes across all seven mode shapes displayed here. Interestingly the mode which relates to the halfspace shear wave dispersion curve shows a potential significant contribution in the lower depths of the strata, up to around 600 m below the surface.

3.3. Forced vibration - frequency domain, Latur earthquake, Example 2.

In this section the results displayed in Fig. 5 were obtained with the proposed solution strategy determined by the axisymmetric model, Section 2.3 and are compared with those of obtained with a methodology proposed in Wang (1999), a method which has been adopted widely by many researchers in ground vibration and seismic scientific communities. This approach evolves from the Thomson–Haskell layer transfer matrix methods with an orthonormalization procedure to



(a) Six mode shapes plotted against depth on a logarithmic scale at frequency, $f = 28.5$ Hz, see Fig. 3.



(b) Six mode shapes plotted against depth on a logarithmic scale at frequency, $f = 38.8$ Hz, see Fig. 3.

Figure 4: Modes evaluated two frequency related to Latur earthquake ground-profile, Table 2. All modes are real-valued evaluated at (a) $f = 28.5$ Hz (b) 38.8 Hz., see Fig. 3.

overcome numerical stability issues with the original propagation algorithm. The basic steps of this approach are discussed in Appendix II. In the following, responses to a harmonic surface load

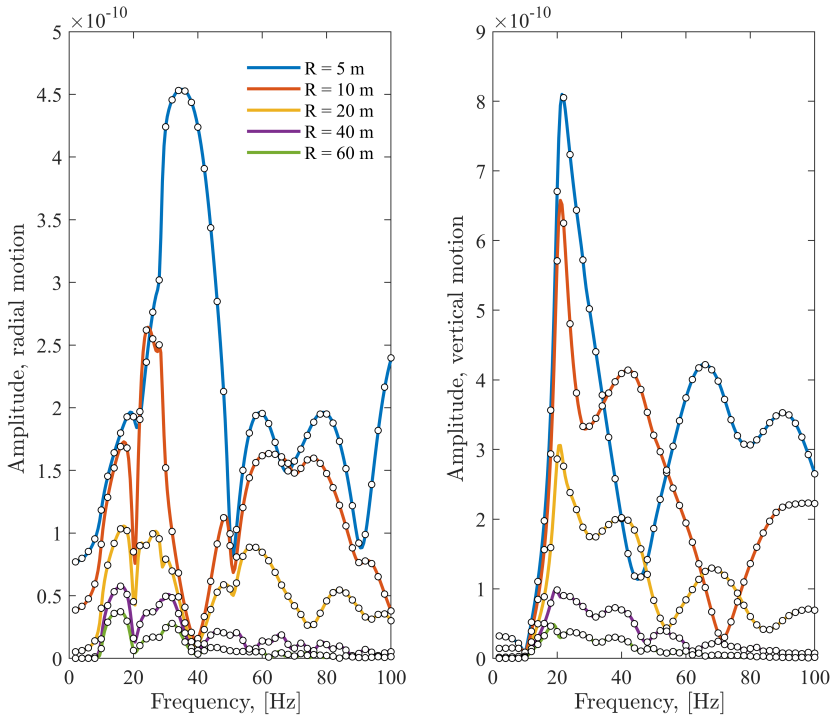


Figure 5: Radial and vertical displacement amplitude at five receiver positions 5, 10, 20, 40 and 60 m from centre of disk-load. Ground profile represented in Table 2.

were calculated using hysteretic damping values established in Wang (1999). To conduct this a circular uniform traction load with radius $b = 1$ m, equation (21) was applied on the surface of a layered soil deposit. The deposit consists of a $h = 5$ m soft soil layer on top of a 300 m deep stiffer layer which overlays a homogeneous halfspace. The soil layer properties are shown in Table 2. Figure 5 shows the vertical and horizontal displacement magnitude at five response points located on the soil surface at distances $d = 5, 10, 20, 40, 60$ m from the disk centre, as obtained with the proposed solution strategy and the flexibility approach using the stabilizing scheme from Wang Wang (1999). The two solution procedures provide virtually identical responses for the studied case. Relative differences at furthest distance and highest frequency, where quadrature errors are expected to be highest, were around 1.0 %. Attenuation of radial and vertical displacement with distance is evident throughout the frequency range. At 10 m and beyond it is clear that the greatest response features close to frequencies 18 and 38 Hz for radial component and 20 and 40

Hz for vertical component beyond 10 m. Although this is not strong evidence of resonance due to the existence of a ZGV mode, increased amplitude is clear and verifies conclusions in Wang (1999).

Comparing solution times between the two methods directly is not justified since we are comparing essentially a 2D method against a 3D solution technique. For interest, the axisymmetric solution using the present scheme involved a one-dimensional numerical inverse transform, which to a relative error $1E-13$ by a Gauss-Kronrod quadrature at the highest frequency (involves most oscillatory integrals) took approximately 2.0 seconds per frequency on the i5 processor on a desktop computer. The size of the dynamic stiffness matrix was fixed at 6×6 for all frequencies. Using the Wang orthonormalisation method (Appendix II), the 3D solution was obtained from a two-dimensional inverse FFT of 2048×2048 wavenumbers. The code, implemented in Fortran 95 and utilizing the OpenMP API for parallelizing the computations, took approximately 12.0 seconds per frequency on the i7 processor with 4 cores on a desktop computer. Although not exploited here, the 3D solution for rotationally symmetric loads may be obtained in a more efficient manner by transforming the wavenumber solution of the Green's function to polar coordinates, effectively reducing the required integration to one dimension, as shown e.g. by Andersen and Clausen (2008). The significant difference in computational cost demonstrated above suggests essential savings if axisymmetry can be exploited.

3.4. Forced vibration - time domain, Latur earthquake, Example 2.

To study the behaviour of a time-dependent force located on the surface of the layered half-space we used the numerical fast Fourier transform (FFT) to convert solutions from the frequency domain to the time-domain. This technique gives the displacements in the space-time domain, taking a source whose temporal variation is provided by a Ricker wavelet, as defined below. To reduce the computational time we used quadrature in space to calculate responses at a few selected receiver points and also since the Ricker wavelet decays rapidly, in both time and frequency, this also allows a computed time-domain solution to be calculated in a reasonable time for interpretation.

The Ricker wavelet function is given by,

$$w(\tau) = W_0 \left(1 - \frac{1}{2}\tau^2 \right) \exp\left(-\frac{1}{4}\tau^2\right)$$

where W_0 is the amplitude, $\tau = (t - t_d)/t_0$; t_d is the time delay at which maximum occurs and

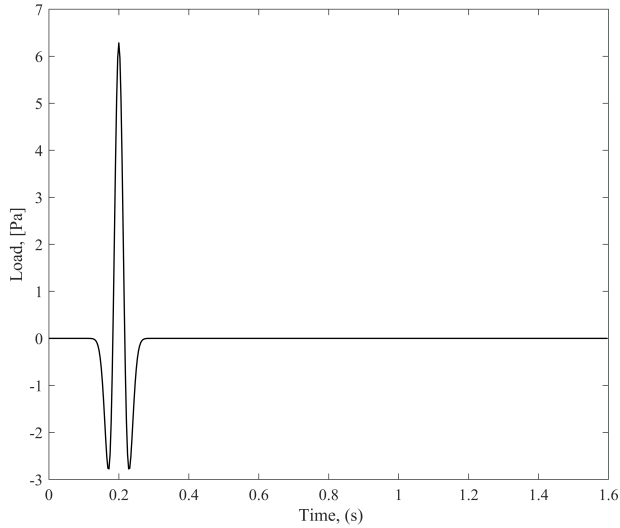
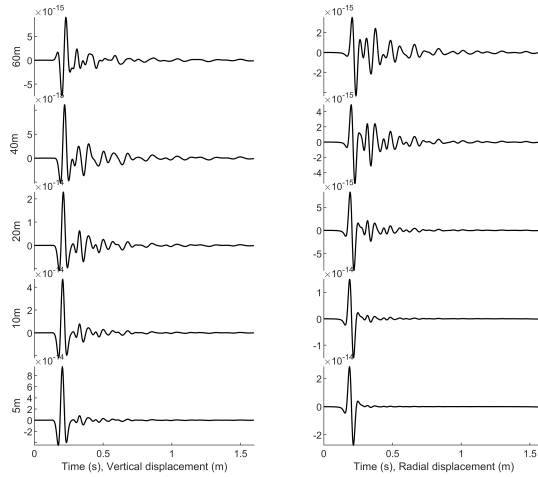
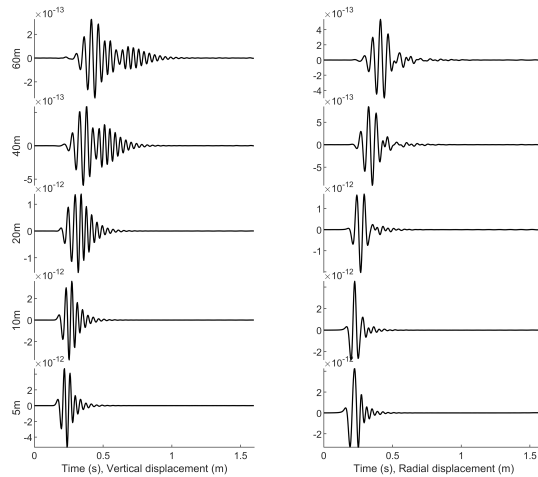


Figure 6: A Ricker-wavelet time-profile, which applies to a uniform pressure over a rigid disk in Example 2.

t_0 is related to the “natural frequency” of the Ricker wavelet $1/t_0 = 2\pi f_0$, see Fig. 6. In our calculations we have chosen the width of the input pulse as $f_0 = 14$ Hz, somewhat arbitrarily but to allow at least the cut-on of a few propagating modes. By applying exponential windowing with damping terms equivalent to the frequency domain, time domain responses were calculated using a FFT with 512 frequency steps up to the Nyquist frequency around 250 Hz.



(a) Ground profile represented in Table 2, without the top 5 m layer.



(b) Ground profile represented in Table 2.

Figure 7: For a Ricker-wavelet load over a rigid disk, responses at 5, 10, 20, 40 and 60 m from centre of disk-load. Upper (a) and lower (b) solutions compared for two ground-profiles.

The two sets of results highlight the difference between a model including a soft top layer, see Fig. 7b. Both sets of solutions naturally exhibit a strong dispersive nature as the envelope of the solution wave-packet propagates along the surface. This is especially evident for the soft 5 m layer result: there appears a second wave-packet in the vertical response at distances that

develops from 40 m, which is due to the soft layer response. As reported in Wang (1999) the “slow” speed of two wave-packets are clearly evident which are effected by ZGV dispersion.

4. Conclusions

A uniformly valid model has been developed for investigating the propagation of surface vibration over arbitrary depth elastic-layers. The model consists of an elastic, isotropic and homogeneous layer which overlies a half-space. A well-conditioned dynamic stiffness matrix has been developed for this model, which is derived by projecting the characteristic functions onto the end-points in the depth dimension. To study the behaviour of the natural propagating modes in the layers, for zero surface stress, singular values of the dynamic stiffness were computed. The characteristic equation was then also used to find the solution shapes of these propagating modes. For an example a ground profile with a high Poisson’s ratio in the top layer over a deep strata, a zero group velocity mode was found, where it has been observed previously that a layer resonance exists. Vibration responses due to a fixed disk load in the frequency were obtained suggesting resonances at cut-on frequencies. Time-domain results were determined which establish the existence of non-dispersive wave packets suggested by earlier researchers.

Given the general validity of this formulation for dynamic stiffness matrices many new problems may be modelled, where plane-strain conditions apply, are within easy reach. This method may also be easily developed to take into account sub-layers of different material within the strata and extended to three-dimensional problems where entries to an exact 6×6 dynamic stiffness matrix could be established.

The following conclusions have been drawn:

- A well-conditioned dynamic stiffness matrix has been developed for arbitrary layer depths.
- Determination of a characteristic equation has been found by expressing unknowns only at material layer nodal points: so that no subdivision of strata is necessary.
- A known ground profile which has been used to investigate large amplitude deflections has been shown to reveal the existence of zero group velocity modes. Examples producing time histories and frequency domain response have also been provided.
- Future development to 3D dynamic stiffness, which involves analytic determination of 36 entries could lead to dramatic reductions in full model computational costs.

Acknowledgements

The final author gratefully acknowledges the Swedish Innovation Agency Vinnova for financial support 485 (Grant ref. no. 2018-04159).

References

- Andersen, L., Clausen, J., 2008. Impedance of surface footings on layered ground. *Computers and Structures* 86, 72–87. doi:<https://doi.org/10.1016/j.compstruc.2007.05.030>.
- Dunkin, J.W., 1965. Computation of modal solutions in layered, elastic media at high frequencies. *Bulletin of the Seismological Society of America* 55, 335–358. doi:10.1785/BSSA0550020335.
- Ewing, W., 1957. *Elastic Waves in Layered Media*. McGraw-Hill.
- Gonçalves, P.J.P., Brennan, M.J., Peplow, A., Tang, B., 2019. Calculation of the natural frequencies and mode shapes of a euler–bernoulli beam which has any combination of linear boundary conditions. *Journal of Vibration and Control* 25, 2473–2479. doi:10.1177/1077546319857336.
- Gonçalves, P.J.P., Peplow, A., Brennan, M.J., 2018. Exact expressions for numerical evaluation of high order modes of vibration in uniform euler-bernoulli beams. *Applied Acoustics* 141, 371–373. doi:<https://doi.org/10.1016/j.apacoust.2018.05.014>.
- Haskell, N., 1953. The dispersion of surface waves on multilayered media. *Bulletin of the Seismological Society of America* 43, 17–34. doi:10.1785/BSSA0430010017.
- Ivansson, S., Karasalo, I., 1992. A high-order adaptive integration method for wave propagation in range-independent fluid–solid media. *The Journal of the Acoustical Society of America* 92, 1569–1577. doi:10.1121/1.403898.
- Ivansson, S., Karasalo, I., 1993. Computation of modal wavenumbers using an adaptive winding-number integral method with error control. *Journal of Sound and Vibration* 161, 173–180. doi:[https://doi.org/10.1016/0022-460X\(93\)90410-D](https://doi.org/10.1016/0022-460X(93)90410-D).
- Jones, D., Petyt, M., 1991. Ground vibration in the vicinity of a strip load: A two-dimensional half-space model. *Journal of Sound and Vibration* 147, 155–166. doi:[https://doi.org/10.1016/0022-460X\(91\)90689-H](https://doi.org/10.1016/0022-460X(91)90689-H).

- Jones, D., Petyt, M., 1992. Ground vibration in the vicinity of a strip load: An elastic layer on a rigid foundation. *Journal of Sound and Vibration* 152, 501–515. doi:[https://doi.org/10.1016/0022-460X\(92\)90483-E](https://doi.org/10.1016/0022-460X(92)90483-E).
- Jones, D., Petyt, M., 1993. Ground vibration in the vicinity of a strip load: An elastic layer on an elastic half-space. *Journal of Sound and Vibration* 161, 1–18. doi:[https://doi.org/10.1016/0022-460X\(93\)90257-C](https://doi.org/10.1016/0022-460X(93)90257-C).
- Karasalo, I., 1994. Exact finite elements for wave propagation in range-independent fluid-solid media. *Journal of Sound and Vibration* 172, 671–688. doi:<https://doi.org/10.1006/jsvi.1994.1205>.
- Kausel, E., 2006. *Fundamental Solutions in Elastodynamics: A Compendium*. Cambridge University Press. doi:10.1017/CBO9780511546112.
- Kausel, E., Roesset, J., 1981. Stiffness matrices for layered soils. *Bulletin of the Seismological Society of America* 71, 1743–1761. doi:10.1785/BSSA0710061743.
- Khasawneh, F.A., Segalman, D., 2019. Exact and numerically stable expressions for euler-bernoulli and timoshenko beam modes. *Applied Acoustics* 151, 215–228. doi:<https://doi.org/10.1016/j.apacoust.2019.03.015>.
- Kumar, J., Naskar, T., 2017. A fast and accurate method to compute dispersion spectra for layered media using a modified kausel-roësset stiffness matrix approach. *Soil Dynamics and Earthquake Engineering* 92, 176–182. doi:<https://doi.org/10.1016/j.soildyn.2016.09.042>.
- Lamb, H., 1904. On group - velocity. *Proceedings of the London Mathematical Society* s2-1, 473–479. doi:<https://doi.org/10.1112/plms/s2-1.1.473>.
- Pekeris, C., 1948. Theory of propagation of explosive sound in shallow water. *Geological Society of America Memoir* doi:10.1130/MEM27-2-p1.
- Sheng, X., Jones, C., Petyt, M., 1999. Ground vibration generated by a harmonic load acting on a railway track. *Journal of Sound and Vibration* 225, 3–28. doi:<https://doi.org/10.1006/jsvi.1999.2232>.
- Strobbia, C., 2003. *Surface wave methods: acquisition, processing and inversion*. Ph.D. thesis. Dottorato di Ricerca in Geoingegneria Ambientale. Politecnico di Torino.

Thomson, W., 1950. Transmission of elastic waves through a stratified solid medium. *Journal of Applied Physics* 21, 89–93. doi:10.1063/1.1699629.

Verruijt, A., 2010. *An Introduction to Soil Dynamics*. Springer Dordrecht. doi:10.1007/978-90-481-3441-0.

Wang, R., 1999. A simple orthonormalization method for stable and efficient computation of Green's functions. *Bulletin of the Seismological Society of America* 89, 733–741. doi:10.1785/BSSA0890030733.

Appendix I

We follow the notation that the element in the i^{th} row and j^{th} column is denoted K_{ij} . The matrix $[K]$ is, however, not symmetric but we have $K_{31} = K_{13}$, $K_{32} = -K_{14}$, $K_{33} = K_{11}$, $K_{34} = -K_{12}$, $K_{41} = -K_{23}$, $K_{42} = K_{24}$, $K_{43} = -K_{21}$ and $K_{44} = K_{22}$. The remaining elements of the matrices are as follows:

$$K_{11} = -\alpha_2 (\lambda + 2\mu) k_p^2 \left((k^2 - \alpha_1 \alpha_2)^2 \left(e^{-2(\alpha_1 + \alpha_2)H} - 1 \right) + (k^2 + \alpha_1 \alpha_2)^2 \left(e^{-2\alpha_1 H} + e^{-2\alpha_2 H} \right) \right) / D, \quad (23)$$

$$K_{12} = k \left\{ (k^2 - \alpha_1 \alpha_2) \left((\lambda + 2\mu) \alpha_1^2 - 2\mu \alpha_1 \alpha_2 - \lambda k^2 \right) \left(e^{-(\alpha_1 + \alpha_2)2H} + 1 \right) + 4\alpha_1 \alpha_2 \left((\lambda + 2\mu) \alpha_1^2 - (\lambda - 2\mu) k^2 \right) e^{-(\alpha_1 + \alpha_2)H} - (k^2 + \alpha_1 \alpha_2) \left((\lambda + 2\mu) \alpha_1^2 + 2\alpha_1 \alpha_2 - \lambda k^2 \right) \left(e^{-2\alpha_1 2H} + e^{-2\alpha_2 H} \right) \right\} / D, \quad (24)$$

$$K_{21} = -\mu k \left\{ (k^2 - \alpha_1 \alpha_2) \left(k^2 + \alpha_2^2 - 2\alpha_1 \alpha_2 \right) \left(e^{-2(\alpha_1 + \alpha_2)H} + 1 \right) + 4\alpha_1 \alpha_2 \left(\alpha_2^2 + 3k^2 \right) e^{-(\alpha_1 + \alpha_2)H} + (k^2 + \alpha_1 \alpha_2) \left(k^2 + 2\alpha_1 \alpha_2 + \alpha_2^2 \right) \left(e^{-2\alpha_1 H} + e^{-2\alpha_2 H} \right) \right\} / D, \quad (25)$$

$$K_{22} = \mu \alpha_1 k_s^2 \left\{ (k^2 + \alpha_1 \alpha_2) \left(e^{-2\alpha_1 H} - e^{-2\alpha_2 H} \right) - (k^2 - \alpha_1 \alpha_2) \left(e^{-2(\alpha_1 + \alpha_2)H} - 1 \right) \right\} / D \quad (26)$$

$$K_{13} = 2\alpha_2 k_p^2 (\lambda + 2\mu) \left\{ k^2 e^{-\alpha_2 H} \left(e^{-2\alpha_1 H} - 1 \right) + \alpha_1 \alpha_2 e^{-\alpha_1 H} \left(1 - e^{-2\alpha_2 H} \right) \right\} / D, \quad (27)$$

$$K_{14} = -2\alpha_1 \alpha_2 k k_p^2 (\lambda + 2\mu) \left\{ e^{-\alpha_1 H} \left(e^{-2\alpha_2 H} + 1 \right) - e^{-\alpha_2 H} \left(e^{-2\alpha_1 H} + 1 \right) \right\} / D, \quad (28)$$

$$K_{23} = 2\mu k \alpha_1 \alpha_2 k_s^2 \left\{ e^{-\alpha_1 H} \left(e^{-2\alpha_2 H} + 1 \right) - e^{-\alpha_2 H} \left(e^{-2\alpha_1 H} + 1 \right) \right\} / D, \quad (29)$$

$$K_{24} = -2\mu \alpha_1 k_s^2 \left\{ k^2 e^{-\alpha_1 H} \left(1 - e^{-2\alpha_2 H} \right) - \alpha_1 \alpha_2 e^{-\alpha_2 H} \left(1 - e^{-2\alpha_1 H} \right) \right\} / D. \quad (30)$$

Here

$$\begin{aligned} D = & (k^2 - \alpha_1\alpha_2)^2 (\exp(-2(\alpha_1 + \alpha_2)H) + 1) - \\ & (k^2 + \alpha_1\alpha_2)^2 (\exp(-2\alpha_1H) + \exp(-2\alpha_2H)) + \\ & 8k^2\alpha_1\alpha_2 \exp(-(\alpha_1 + \alpha_2)H) \end{aligned} \tag{31}$$

Appendix II

In Section 3.3 displacement magnitudes were compared by two methods, the present approach and the method devised in Wang (1999). The latter approach uses the Thomson-Haskell layer transfer matrices, with an orthonormalization procedure to overcome numerical stability issues with the original propagation algorithm. In the Thomson-Haskell transfer matrix algorithm, the displacements and tractions are placed in a vector:

$$\mathbf{S} = \begin{bmatrix} U_1 & U_2 & U_3 & P_1 & P_2 & P_3 \end{bmatrix}^T. \quad (32)$$

For a homogeneous layer j of depth h , the solution \mathbf{S} at any coordinate z of the layer can be written in the form

$$\mathbf{S}^j = \mathbf{A}^j \mathbf{E}^j \mathbf{b}^j \quad (33)$$

where \mathbf{A} is a 6×6 layer matrix (for its entries, see e.g. Sheng et al. (1999)), \mathbf{E} is a 6×6 diagonal matrix with the terms

$$E_{11} = e^{\alpha_p z}, E_{22} = E_{33} = e^{\alpha_s z}, E_{44} = e^{-\alpha_p z}, E_{55} = E_{66} = e^{-\alpha_s z}, \quad (34)$$

and \mathbf{b} is a 6×1 vector of integration constants

$$\mathbf{b}^j = \begin{bmatrix} a_1 & b_1 & c_1 & a_2 & b_2 & c_2 \end{bmatrix}^T. \quad (35)$$

With the notation $\mathbf{E}^{j,0} = \mathbf{E}^j(z=0) = I$ and $\mathbf{E}^{j,1} = \mathbf{E}^j(z=h)$, the solution at the top ($z=0$) and at the bottom ($z=h$) of layer j can be written as

$$\mathbf{S}^{j,0} = \mathbf{A}^j \mathbf{E}^{j,0} \mathbf{b}^j = \mathbf{A}^j \mathbf{b}^j \quad (36a)$$

$$\mathbf{S}^{j,1} = \mathbf{A}^j \mathbf{E}^{j,1} \mathbf{b}^j \quad (36b)$$

By combining the above expressions, the integration constants \mathbf{b}^j can be eliminated so that

$$\mathbf{S}^{j,1} = \mathbf{A}^j \mathbf{E}^{j,1} (\mathbf{A}^j)^{-1} \mathbf{S}^{j,0} = \mathbf{T}^j \mathbf{S}^{j,0} \quad (37)$$

expresses a relationship between the solution at the top and at the bottom of the layer through the Thomson-Haskell propagator matrix $\mathbf{T}^j = \mathbf{A}^j \mathbf{E}^{j,1} (\mathbf{A}^j)^{-1}$. Continuity of displacements and

traction requires that the solution at the top of layer j equals the solution at the bottom of layer $j - 1$, i.e.

$$\mathbf{S}^{j,0} = \mathbf{S}^{j-1,0}. \quad (38)$$

Hence, the solution at the bottom of layer j may be related to the solution at the surface (top of layer 1), as

$$\mathbf{S}^{j,1} = \mathbf{T}^j \mathbf{T}^{j-1} \mathbf{T}^{j-2} \dots \mathbf{T}^1 \mathbf{S}^{1,0}. \quad (39)$$

However, due to the limited precision of computers, this approach often leads to stability issues for deep layers and/or high frequencies caused by operations between different increasing exponentials. Wang (1999) proposed a scheme where the propagation is carried out layer by layer for a set of base solution vectors. For each layer and solution base vector, the corresponding vector of integration constants is explicitly calculated. Before the propagation to the next layer is carried out for the current solution base vectors, an additional procedure is followed. In short, this additional procedure makes the solution base vectors orthonormal, so as to avoid propagation or pollution of the solution accuracy due to coupling of P- and SV-waves at the layer interfaces. The solution for an arbitrary load is then obtained by superposition of the fundamental solutions so as to satisfy the source condition. For full details of the scheme, the reader is referred to Wang (1999).